RHEOLOGICAL STUDY OF MAGNETORHEOLOGICAL POLISHING FLUIDS

A Dissertation

by

NAVEEN THOMAS

Submitted to Graduate and Professional School of
Texas A&M University
in partial fulfillment of the requirements for the degree of

DOCTOR OF PHILOSOPHY

Chair of Committee,	Arun R. Srinivasa
Co-Chair of Committee,	Satish T.S. Bukkapatnam
Committee Members,	Kumbakonam R. Rajagopal
	N.K. Anand
Head of Department,	Guillermo Aguilar

December 2021

Major Subject: Mechanical Engineering

ABSTRACT

The aim of this work is to study the flow behavior of magnetorheological polishing fluids/ slurries, with specific focus on answering the following two research questions: a) What is the suitable model for a polishing slurry in the absence of magnetic fields? and how to select a model from among a class of possible models in an objective manner?, b) What causes segregation and brush formation in MR polishing fluids in the presence of magnetic fields? and how does shearing affect the segregated structure?

In the first half of the work, an experimental study was conducted to find appropriate models for polishing slurries. In the later half of the work, a mixture theory based model was used for the segregation and rheological behavior of the magnetorheological (MR) polishing mixture. Then numerical studies are conducted to study the segregation behavior of the mixture under stationary and couette type bulk flow conditions in the presence of magnetic fields.

In the work for identifying rheological models for polishing fluids, a novel means for obtaining rheological properties of polishing slurries for a given class of models by combining CFD and measurements of Torque vs Speed Data is discussed. Experiments were conducted using a custom-built torsional rheometer that subjects the polishing fluid to conditions that are similar to polishing. Comparison with the analytical solution indicates that side wall and inertial effects (ignored in the analytical solution) significantly affect the values of the parameters of any given model even under nominally slow rates of rotation. This significantly affects model selection as described below.

Using statistical inference techniques (the Akaike Information Criterion), among the three rheological models, namely the Bingham fluid model, the Power-law model and the Herschel-Bulkley model, considered for the fluid, the Herschel-Bulkley model seems to be

a significantly better fit compared to other models for the slurry. The results suggest that a systematic combination of computational-statistical-data science approach is necessary for identifying model parameters even for slow flows as compared to currently used data reduction methods based on analytical solutions for torsional flow that ignore inertial and side-wall effects.

Segregation and flow behavior of the MR polishing mixture is modeled using mixture theory. The dipole-current circuit approach was used to model the magnetic behavior of the polishing fluid. Balance equations for the bulk mixture fluid and the relative flow of the magnetic component are derived. Thermodynamically consistent constitutive models were developed for the fluid to exhibit segregation through diffusion and flow of the bulk mixture during the polishing process. A mixture model for the bulk flow velocity, formulated using the volume concentrations of the component as weights, is observed to enforce the incompressibilty constraint directly on the bulk velocity. Thus, this approach can easily accommodate the simple incompressible models used to experimentally characterize the mixture.

A polishing mixture with a magnetic component concentration of 50 % is considered in simulations. Decoupled and coupled simulations of stationary mixture under different magnetic field boundary conditions were performed. The results showed that coupling the magnetic field equations with the convection-diffusion equations is necessary to capture the segregation and formation of brushes in the mixture. A non-dimensionalized study of simulations of a perturbed stationary fluid identifies that the segregation behavior of the mixture depends upon the magnetic coefficient and the initial brush width of the perturbation in the fluid.

Evolution of the magnetic component's concentration in a segregated fluid while undergoing a couette type flow in the presence of uniform magnetic field is simulated. It is observed that, at low shear rates, the mixture is able to segregate periodically as the

brushes are reformed after breaking. But, at higher shear rates, the segregated mixture mixes completely.

DEDICATION

To my family and my teachers who have always supported me.

ACKNOWLEDGEMENTS

My PhD work has been the most daunting project that I have taken in my limited career as a student of mechanics. Without the sincere support of the many individuals this journey would have been impossible for me to complete.

I wish to express the deepest gratitude to my Chair, Prof. Arun R. Srinivasa for the opportunity to pursue this research work. I thank him for his trust in me to pursue and complete this research. He provided me with motivation, support and guidance at the most difficult moments in my research. His mentorship was extremely helpful in gaining experience and knowledge in research, teaching and academic writing.

I wish to convey sincere thanks to my Co-Chair, Prof. Sathish T. Bukkapatnam for constantly conveying his spirit of enthusiasm in regard to my research. I am deeply thankful for the amount of time spent in teaching me about MR polishing. I am also thankful for the lab facilities that he provided for me to conduct my experimental studies on polishing fluids. I am also grateful to him for providing me with an opportunity to co-author a chapter on polishing.

My sincere thanks to my Committee Member, Dr. K. R. Rajagopal, for providing me with his equipment to conduct my experimental investigations. His book on the Mechanics of Mixtures was very helpful in my research work on modeling. I also thank him for teaching me the basics in continuum mechanics through his courses.

My sincere thanks to my Committee Member, Dr. N. K. Anand, for teaching me numerical methods which were very helpful at every point in my PhD research. Heartfelt thanks to my labmates Dr. Ashif Iquebal, Dr. Nazanin Afsar, Dr. Jayavel Arumugam, Dr. Jason Wang, Dominic Jarecki and Bamidele for a wonderful time working together on different fields of mechanics. My time at Texas A&M was made memorable by my friends

and roommates Richards C. Sunny, Alwin Jose and Jobin K. Joy.

I am also grateful to my wife, parents and brother for their constant support in the last few years. I thank God for blessing me with all these people in my life.

CONTRIBUTORS AND FUNDING SOURCES

Contributors

This work was supported by a dissertation committee consisting of Professor Arun R. Srinivasa (advisor), Professor K. R. Rajagopal and Professor N. K. Anand of the Department of Mechanical Engineering and Professor Satish T. Bukkapatnam (co-advisor) of the Department of Industrial Engineering.

All other work conducted for the dissertation was completed by the student independently.

Funding Sources

The experimental research study conducted in Chapter 6 was supported by a fellowship by the National Science Foundation through the Grant CMMI 1538501.

NOMENCLATURE

ρ, A, α, β ...	scalars
$\mathbf{v}$, $\mathbf{h}$, $\mathbf{Q}$ ...	tensors (1^{st}, 2^{nd} and higher orders) (boldface)
ρ^m, $\mathbf{v}^m$	variables associated with the magnetic constituent
ρ^a, $\mathbf{v}^a$	variables associated with the abrasive constituent
v_x^a, v_y^a	x and y component of the vector $\mathbf{v}^a$
$\mathbf{p} \otimes \mathbf{v}$	tensor product ($\mathbf{p}_i \mathbf{v}_j \hat{\mathbf{e}}_{ij}$) of tensors $\mathbf{p}$ and $\mathbf{v}$
$\mathbf{A} \cdot \mathbf{B}$	scalar product ($A_{ij...} B_{ij...}$) of tensors $\mathbf{A}$ and $\mathbf{B}$ of equal dimensions
$\mathbf{AB}$	product ($A_{i...j} B_{j...k}$) of tensors $\mathbf{A}$ and $\mathbf{B}$
$\mathbf{A}^T$	transpose of tensor $\mathbf{A}$
$\frac{\partial a}{\partial t}$, $\frac{\partial \mathbf{p}}{\partial t}$ or $a_{,t}$, $\mathbf{p}_{,t}$	local time derivative of the scalars (a) or tensors ($\mathbf{p}$)
$grad(\rho)$, $grad(\mathbf{v})$	gradient of scalars (ρ) or tensors ($\mathbf{v}$) $grad(\rho)_i = \rho_{,i}$ and $grad(\mathbf{v})_{ij} = \mathbf{v}_{i,j}$
$div(\mathbf{v})$, $div(\mathbf{T})$	divergence of tensor ($\mathbf{v}$, $\mathbf{T}$) $div(\mathbf{v}) = \mathbf{v}_{i,i}$ and $div(\mathbf{T})_i = \mathbf{T}_{ij,j}$
$curl(\mathbf{A})$	curl of the vector $\mathbf{A}$ $curl(\mathbf{A})_i = \epsilon_{ijk} \mathbf{A}_{j,k}$

TABLE OF CONTENTS

Page

LIST OF FIGURES

FIGURE Page

LIST OF TABLES

1. INTRODUCTION

Polishing Fluids are primarily used in achieving nanoscale finish on workpieces. There are a variety of mechanical polishing methods currently in vogue, including Jet Polishing, Chemical Mechanical Polishing, Abrasive Flow Finishing, Magnetorheological (MR) Finishing, etc. The advantages to using a fluid media for polishing is the ability to easily carry the abrasives to the workpiece surface and carry the abraded chips back after polishing as opposed to using a solid abrasive surface. In Jet Polishing, Abrasive Flow Finishing and MR finishing the flow of the abrasive-laden fluid relative to the workpiece is utilized to polish the surface of the workpieces. Moreover, in MR finishing the segregation of the fluid determines the regions of polishing and forces in the polishing process. As a result, the rheological properties of the fluids play a crucial role in determining the Material Removal Rate of the process and the final roughness of the workpiece polished through MR finishing.

Generally, all these methods have been widely successful in global polishing of surfaces that are easily accessible. With the advancement of technology, increasingly complicated structures with complicated (and sometimes inaccessible) shapes are used for different applications. One such case is biomedical implants where complex shapes and joints are used to bring out close structural behavior as that of the joints being replaced. These implants need two different types of surfaces for their application. A rough surface at the regions where they are in contact with the bone and a smooth surface at the regions of joint where they need to slip against each other. These implants with these complicated shapes need to be polished differently at these localized regions.

For such cases, MR finishing (slurries of magnetic and non-magnetic abrasive particles) is one of the popular techniques where magnetic fields are used to segregate and

increase the viscosity of a abrasive-laden MR fluid for polishing as well as drive the flow in a controlled manner. This controllability using magnetic fields help in localized polishing of surfaces. This method is suitable for polishing irregular geometries as the "polishing pad" easily conforms to the shape of the workpiece during the process.

The normal and shear forces applied at the surface of the workpiece play an important role in determining the material removal and roughness of the workpiece. The segregated structure of the fluid under flow determine the regions of polishing and the rheological properties of the mixture. In this thesis (Chapter) we at first identify appropriate models through experimentation, modelling and simulation for polishing fluid with high concentration of particles. Later we discuss the development of a multi-phase mixture theory based model for MR polishing mixture. And numerical simulations are performed to study the segregation behavior of the fluid under different flow conditions and magnetic fields.

2. NANOFINISHING OF BIOMEDICAL IMPLANTS[1]

2.1 Need and Significance of biomedical implant polishing

Biomedical implants are manufactured medical devices that are augmented to human (or animal) bones and tissues to support or replace an existing structure and/or enhance an organ's performance. The market for implants is growing at 5% annually and expected to exceed $35B by 2019 [16, 17]. Among these, dental, orthotic implants (including those for hip, knee, spine and foot joints), and heart pacemakers share the bulk of the current market. Moreover, in the near future, the use of artificial heart, cranium, and spinal implants is set to experience over 5 % growth rate. In particular, orthotic implants serve as structural aids when augmented to the bone. They are normally secured to the bones using nuts and bolts, or just placed in the cavity as structural fillers [18]. These are mostly made of materials such as stainless steel (316L SS), Cobalt-Chromium alloys (CoCrMo), Titanium (Ti), Titanium alloys (Ti6Al4V, Ti6Al7Nb, TiNi), a variety of ceramic materials with or without acrylic cement [19], and soft polymers, such as Ultra High Molecular Weight Polyethylene (UHMWP) and polyurethane. These materials are chosen to promote bio-acceptance, i.e., (a) implantation is not known to cause undesirable mechanical, chemical or biological stress, and (b) the implant bonds well and promotes the growth of the bone and the nearby tissues.

A collection of different orthotic implants is given in figure 2.1. Here, we can observe that every implant is primarily composed of two types of surfaces. A textured surface on the regions which bond and mesh with the bone, and an ultrasmooth surface ($Ra < 100$ nm) at the locations where the components slide against each other (i.e., bear-

[1]Reproduced with permission of The Licensor through PLSclear from Naveen Thomas, Ashif Iquebal Sikandar, and Satish Bukkapatnam. "Nanofinishing of biomedical implants." Nanofinishing Science and Technology. CRC Press, 2016. 569-616. Copyright[2016] by Taylor and Francis

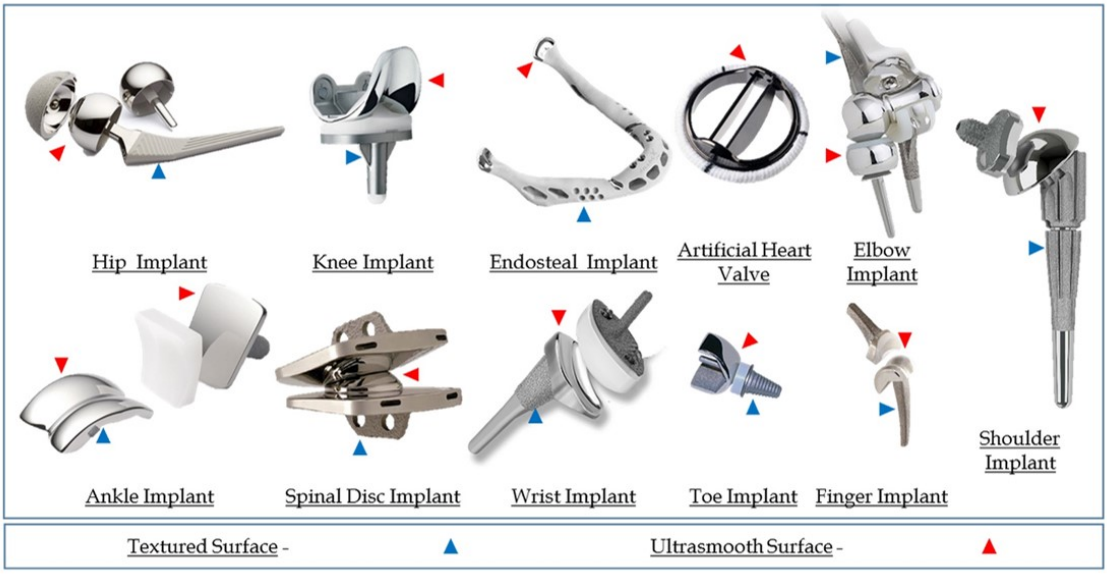

Figure 2.1: A montage of orthotic implants showing the different surface texture requirements at different areas.

ing surfaces). Furthermore, these surfaces have complex shapes, sizes and form factors to match a patient's anatomy. Formation of a positive bond between the bone, nearby hard tissue and the implant over the course of the healing time is referred to as bone integration or osseointegration. Osteointegration is necessary whenever an implant is inserted into regions where a cavity needs to be filled, a broken bone needs to be restored, or a joint is replaced [20]. The following factors play a primary role in osseointegration: (a) growth of bone tissue on the implant surface [21], (b) adsorption of the proteins onto the surface of the implant (bioactivity) that leads to adhesion [22], (c) tissue growth through the pores of the implant to form a strong bond with the bone. Local biological, mechanical, surface compatibility and finishing determine the durability of the moving parts in the joints as well as the speed and the strength of osseointegration along the bonding surfaces. Statistical analysis of Shalabi et al. [21] suggests that higher surface roughness results in a higher bone to implant contact area and higher torque resistance. They noted that a

roughness Ra of 0.5 – 8.5 μm was most conducive for osseointegration. This generalizes an earlier finding of Alberktsson et al. [23] that Ra of 1-1.5 μm is needed for the growth of the bone cells. Gotz et al. [24] found that titanium alloy (Ti6Al4V) implants, which were Laser-blasted to produce surfaces with pores of the order of 200 μm and a surface roughness of Ra 7.5 μm, promoted surface integration through deposition and in-growth of the bone tissue. Aniket et al. [25] conducted experiments to study the early osteoblast growth on titanium alloy (Ti6Al4V) implants versus similar alloy implants coated with bioactive silica-calcium phosphate nanocomposite (SCPC50). They observed that the surface roughness of the coating promoted the attachment of the cells to the implant surface, but the uncoated surface promoted the growth of the cell. This is because uncoated surface enhances the concentration of a linear polymer microfilament called Factin near the surface which promotes cell growth. Lundgren et al.'s [26] investigations on the growth of bone tissue suggests that the extent of bone growth was not significantly different between a turned smooth surface (Sa = 0.48 ± 0.3 μm) and a titanium oxide blasted surface (Sa = 1.54 ± 0.3 μm), but more mineralized bone was in direct contact with titanium oxide blasted implant. In this context, Anselme et al.'s [22] investigations with titanium implants and Deng et al.'s [27] with hydroxyapatite based composites suggest that (a) the adhesion power of the cells were higher on rougher surfaces, and (b) surface roughness plays an important role in the integration of bone.

As noted in the foregoing, while microscopic roughness is essential for bone growth, ultrasmooth finish Ra < 0.5 μm is necessary on the bearing surfaces (e.g., at hip and knee joints) to ensure performance as well as durability under dynamic loading. As the world population ages, the challenges associated with realizing ultrasmooth finish on the bearing surfaces of joints are set to grow. For example, joint replacement surgeries are growing at over 15 % annual rates, especially in the developed countries, to address issues with arthritic complications and permanent damage to bones and bearing surfaces in old age.

Implants for these applications contain surfaces that slide and bear during their functioning.

Joint implants possess components that are in continuous relative motion with each other throughout their life. This relative motion of implant surfaces can lead to surface erosion, chipping, and deformation of the geometry of the implants over time. Deformed and worn implants cause debilitation of functions, squeaky noises, stiffening and dislocation of the joints, as well as significant inconvenience and pain to the patient. Smooth finishing of these surfaces is essential to minimize wear. Primary material combinations employed for joint surfaces include polymer linings, metal on polymer, ceramic on polymer, metal on metal, and ceramics. Pertinently, polymer liner materials include acrylic, nylon, ultra high molecular weight polyethylene, polyurethane, and polypropylene. Metals used for joint implants include medical grade titanium, and cobalt chromium while ceramics includes Alumina, Zirconia, and Diamond thin films [28]. The first generation implant materials were metallic with appropriate surface treatments. Metal-on-metal components offer strong wear resistance of below 0.05 mm/year. However, the abraded asperities are known to dissolve into and contaminate the bloodstream causing some health concerns and known hazards such as metallosis, where the worn-out debris deposit and aggregate in the soft tissues causing pain. While polymer linings allow economic generation of ultra-smooth surfaces, they are prone to chipping and create micrometer-scale debris. The issue of debris and high rate of wear (> 0.1 mm/year for most common materials) has been noted to be a significant limiter of an implant life. Ceramic and advanced polymeric implants are under investigation for various applications, and many of their variants are in various stages of clinical testing and regulatory approval process.

From a tribological standpoint, these implant surfaces are designed to have a lower coefficient of friction [29],[30],[31]. Consequently, very low surface roughness ($Ra < 1$ μm) is needed for implant bearing surfaces to ensure smooth slipping [30] The ease of

sliding between the surfaces can be measured using a factor known as lambda ratio (Λ) [32]

$$\Lambda = \frac{h_{min}}{\sqrt{R^2_{a(head)} + R^2_{a(cup)}}} \tag{2.1}$$

where, h_{min} is the theoretical film thickness of the lubricating film, and, $R_{a(head)}$ and $R_{a(cup)}$ are the roughness parameters associated with the two relatively sliding surfaces of the joint. It is suggested that higher the lambda ratio (Λ) of the bearing surfaces, lower is the wear rate in the implants.

Thus, finish requirements for biomedical implants tend to be localized—certain parts of the implant would require rough porous surfaces to facilitate osseointegration. Certain other regions, notably the ones whose surfaces are under relative sliding motion, would require a smooth surface finish, in order to reduce friction, and hence wear. This differential surface finish requirement restricts the use of several traditional as well as advanced finishing processes, including Chemical Mechanical Polishing (CMP), Electro Chemical Mechanical Polishing (ECMP) and Electro Chemical Polishing (ECP) to finish. The remainder of this chapter discusses various techniques reported in the literature for polishing biomedical implant surfaces, with emphasis placed on the techniques employed to achieve sub-micrometer scale finish, referred to as ultrasmooth finish in the biomedical implant parlance.

2.2 Classification of finishing methods for biomedical implants

Surface finishing processes for biomedical implants can be mainly classified into (a) mechanical, (b) chemical, (c) electrochemical, (d) vacuum deposition, (e) laser and thermal treatment techniques [33]. It may be noted that some of these techniques aim to

impart specific surface texture on a smooth surface, and others aim to create ultrasmooth surfaces with nanometric scale finish. Conventionally, the industry has been employing handheld polishers for finishing bio-medical implants, especially to achieve differential, localized polishing. Such processes tend to be laborious and demand extreme dexterity. Alternatively, localized electro-chemo-mechanical etching methods have been investigated [34],[35]. However, they require elaborate masking to achieve localization of material removal. Many of the methods investigated focus on providing surface texture conducive for osseointegration. Limited techniques have been investigated for nanofinishing of implant surfaces. However, as stated in the foregoing, localized finishing of free-form geometries remains an open issue. The remainder of this section will introduce and provide a critical review of various approaches for polishing implant surfaces.

2.2.1 Fine Abrasive based Nanofinishing

Mechanical finishing methods mainly include using fine abrasive particles to treat and polish the surface of the implant. These techniques, as mentioned earlier may be used to create specific textures and/or to provide an ultrasmooth finish.

2.2.1.1 Sandblasting

Sandblasting is used primarily to create sub-micrometer textures on ultrasmooth finished surfaces to promote osseointegration. Here, abrasive beads ($\phi \approx$ 70-900 μm) made of alumina, carborundum (SiC), or glass [36],[37],[38] are impinged onto the desired regions of the surface. For example, Taga et al. [37] employed this process to create textured surfaces with roughness Ra in the range of 0.5 – 2.5 μm. Their investigations also suggested that carborundum would provide an effective performance both in terms of achieving texture control as well as improving the structural properties, such as fracture resistance [36]. It was also noted in literature that the hardness and brittleness (alternatively, toughness) of the abrasive particle, the blast-head power, abrasive powder flow rate, pulse

intervals and finishing time are the main parameters that determine the surface characteristics. The process is however limited to finishing external surfaces that are in direct line of vision to the blast-heads.

2.2.1.2 Abrasive Flow Finishing

Abrasive flow finishing (AFF) uses a slurry consisting of fine abrasive particles mixed into a viscoelastic medium (henceforth referred to as the medium) to flow under pressure on the target surface to create an ultrasmooth finish [2]. For example, Subramanian et al. [39] employed AFF technique to polish a hip implant to nano-scale roughness to create ultrasmooth-slipping surfaces. This process can be tuned to polish a variety of rough, porous implants to the required micro-roughness to promote adhesion to the bone.

The key process parameters in this technique are the pressure in the medium, number of cycles, flowrate and rheology of the medium, and the abrasive particle size and concentration. Increase in pressure, the number of cycles or the flow rate of the medium increases the material removal rate (MRR) in the process. The medium's viscosity has a high influence on the final roughness and MRR. The viscosity, however, is hard to control during the process as it is dependent on factors, such as flow rate and temperature. Generally, a higher viscosity in the medium results in a higher removal rate [2]. The roughness of the workpiece is dependent on the size of the abrasive particles as well. The major limitation in this approach is that local polishing cannot be achieved without the use of masks and elaborately designed confinements. Moreover, as the flow of the abrasive particles on the surface is unidirectional and reciprocative, a uniform surface finish is not assured in all the directions along the surface.

2.2.1.3 Bonnet Polishing

The "Precession" tooling for bonnet polishing was first introduced by Walker et al. [40],[41] for polishing glass surfaces. It uses a flexible bonnetshaped inflated membrane

(cf. figure 2.2) pressed onto a target surface in such a way that the axis of the head is at an angle to the normal on the surface of the workpiece. This angle is called as precess angle. The bonnet is rotated about both the H axis (see figure 2.2) and the normal (A axis) to achieve the precessions movement for smooth finishing. The compliance of the bonnet helps in conforming to the freeform shape of the surface being polished. Slurry formed by mixing fine abrasive particles [7, 42, 43] in deionized water with a specific surfactant [44],[45] is used at the interface. Automated tool motion (CNC control) is used to ensure that the workpiece is finished to the desired surface quality and form. Pertinently, Zeng et al. [42] employed bonnet polishing method to produce a multi-radius hip joint implant made of CoCr material using alumina 3µm abrasives. A roughness level of $Sa \approx 16.1$ nm was achieved by the process.

The MRR in bonnet polishing is dependent on the machine parameters, such as precess angle, head speed, tool offset, the down pressure, and the slurry composition[7, 46]. These parameters bear a nonlinear relationship to the surface roughness of the implant. While versatile in term of the surface forms that can be bonnet polished, the process is limited to polishing only the outer surfaces of the workpiece and it is not suitable to polish internal surfaces and narrow pathways. The radius of curvature of concave workpieces that can be polished by using this technique is limited by the size of the bonnet and the form of the target surface on the workpiece.

2.2.1.4 Magnetic Polishing

Most common variants of magnetic polishing processes for biomedical implants use a magnetic or magnetorheological fluid (MR fluid) mixed with abrasive particles. The performance of the process largely depends on the magnetorheological properties of the fluid in terms of the variation of the stiffness and other elastic properties of the fluid with magnetic field strengths. In particular, higher elastic modulus of the stiffened fluid helps

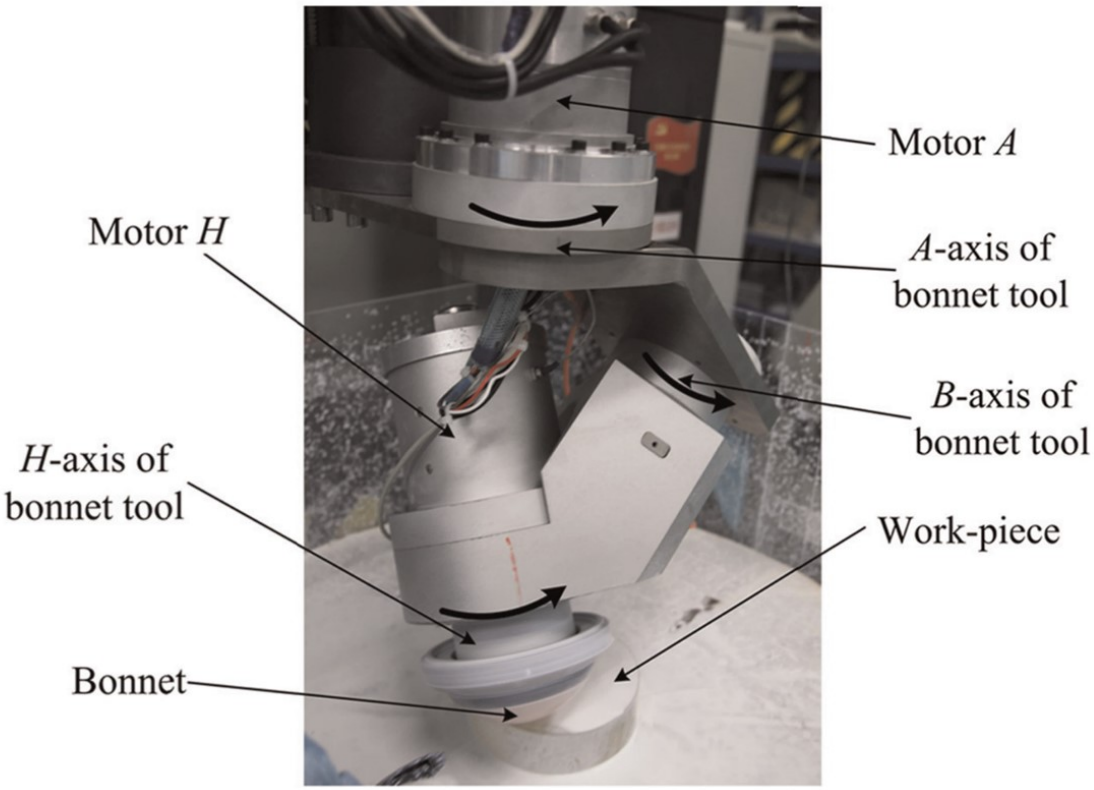

Figure 2.2: Bonnet polishing machine for polishing optical surfaces [1]

in abrading the surface, but at the same time conforming to the free-form surface of a workpiece [10]. The magnetic field can also be used to control the relative motion as well as the down force required for polishing. However, in some cases, a physical tool may be employed to generate the down force. For example, Sidpara et al. [47] developed a MR fluid based ball end tool to polish the free-form surface of a knee implant. Other parameters that influence the surface finish include abrasive particle size, fluid concentration and hardness as well as the strength of the magnetic field. The advantage of using MR fluids is its ability to conform to the shape of the workpiece which is primarily helpful in polishing free-form surfaces of different materials such as glass, CoCr and titanium alloys.

2.2.2 Non-Abrasive based Nanofinishing

The main non-traditional finishing methods reported in the literature include chemical, electrochemical and laser finishing techniques. The commonality among these methods is that the main material removal mechanism is not mechanical abrasion or deformation of surface asperities.

2.2.2.1 Chemical Etching

Several chemical methods have been employed to treat and prepare the surface of an implant to make it suitable for insertion into the human body [33]. Chemical etching methods have been employed to achieve varied purposes, including cleaning the surface to remove grease and chemicals, texturing the surface for subsequent finishing or patterning, and passivation of the surface to improve in-use corrosion resistance performance of mechanical finishing processes. Acid etching processes are by far the most common chemical etching processes reported for finishing biomedical implants.

Acid etching, as the name suggests, employs a mixture of highly concentrated acids to erode the surface of an implant to achieve the desired texture. This treatment involves washing the surface of the implant with the acids, including nitric, sulphuric and/or phos-

phoric acids at pH < 0.1 and oftentimes with negative pH to create micro-pits for roughening the surface. For example, Sittig et al. [48] employed concentrated nitric acid with hydrogen fluoride to etch the surface of titanium and titanium alloys to produce a surface roughness of around 3-5 μm. The surface dissolution rate in the workpiece is dependent on key parameters, such as the pH of the acid and the concentration of complexing agent. The choice of chemicals relative to the implant material plays a vital role because of diverse mechanisms involved in an etching process. For example, nitric acid by itself has no effect on the surface roughness of titanium and its alloys, but instead nitric acid with hydrofluoric acid (HNO_3-HF) increases the surface roughness of titanium through grain-structure and lattice orientation-dependent dissolution of the surface. In Ti6Al7Nb and Ti6Al4V alloys HNO_3-HF increases the surface roughness through selective dissolution of α–phase alloy.

2.2.2.2 Electrochemical Treatment

Electrochemical polishing methods aim to selectively remove material from surfaces of the electrode or a workpiece via electrolytic reactions [33]. Two variants of this process are electropolishing and anodic oxidation. Electropolishing is primarily used to treat the surface of stainless steel and can be extended to titanium alloys. The workpiece surface is dissolved into the electrolyte in a controlled manner through an electrochemical reaction. It uses a mixture of strong acids as electrolyte. The metallic workpiece (anode) is dissolved into the acid through oxide formation [49]. Most of the surface can be smoothened through this process except the pits that are present at the grain boundaries of the micro-structure [33]. Latifi et al., [50] discovered that if electropolishing is followed by acid dipping the surface roughness could be further improved. They achieved a surface roughness of $Sa \approx 0.96 \pm 0.29$ nm in 316L stainless steel by employing this procedure. Larsson et al. [49] showed that when electropolishing of titanium was followed by anodic oxidation, the oxide layer may exhibit the texture conducive for the growth of osteoblasts

on the surface. Hryniewicz et al. [51] studied magnetoelectropolishing, a variant of electropolishing. They reported that the dissolution rate and micro-roughness characteristics of the workpiece are dependent on the strength of the magnetic field.

2.2.2.3 Laser Treatment

This process employs pulsed Nd:YAG [24] lasers to create tiny surface pores that serve as nucleation sites for subsequent growth of bone structure that interlocks itself onto the implant. A unique advantage of this technique is that the microscale pores created in this process support the ingrowth of bone [24]. Also, as it is a non-contact process it provides a better control over the patterns desired on the surface. For example, Faeda et al. [52] showed that titanium implants textured using a laser beam ($Ra \approx 1.38 \pm 0.23 \mu$m) resulted in better bonding with the bone in terms of the torque required to break the implant free from the bone.

While localization is hard to achieve with free-abrasive methods, many geometric features are inaccessible to hand-held polishers. On the other hand, bulk polishing methods based on chemical and/or electrochemical effects need some kind of masks or physical barriers to confine material removal to desired regions. Table 1 summarizes various techniques for finishing biomedical implants. Among these, Bonnet, AFF and magnetic polishing are most promising approaches for achieving nanoscale finish on implant surfaces. In particular, recent advances in magneto-viscoelastic fluids offer an interesting opportunity for localized polishing at drastically reduced times [53],[54]. These methods are described in more detail in the following sections.

2.3 Advances in Abrasive Flow Finishing

Abrasive flow based polishing was first introduced by McCarty in 1960s [55] as a method to deburr and polish metal products at difficult to reach regions. The AFF methods employ a medium made up of fine abrasive particles mixed with polyborosiloxane,

commonly referred to as the silly putty [56]. The abrasion occurs when the pressurized medium flows along the surface of the workpiece. These methods can be applied to polish internal as well as external surfaces of a biomedical implant [56]. AFF technique is normally used in aircraft and automobile industry to finish complex shapes and extremely small orifices, such as fuel injector nozzles, which are not normally amenable to conventional polishing [57]. Recently, these techniques have been further advanced to polish biomedical implants to fine tolerances and finish [39]. The key advantage of AFF is its deformable medium which conforms to the surface during the finishing process. The MRR and surface finish of the final product depends on different process parameters including the pressure in the medium, concentration and geometrical properties of the abrasive particles and the flow characteristics of the medium such as viscosity.

2.3.1 Process setup and mechanism

An AFF setup consists of two hydraulic cylinders filled with abrasive medium connected to hydraulic systems that reciprocatively pump the medium between the cylinders [58]. For internal polishing, the workpiece is mounted between the cylinders in such a way that there is a leak proof pathway for the medium to flow along the surface of the work-piece between the cylinders. As illustrated in schematic of internal polishing setup shown in figure 2.3(a) & 2.3(c), the abrasive medium is pushed through the workpiece to achieve material removal. For external polishing, the workpiece is mounted inside a cylinder which is again connected to the two cylinders(figure, 2.3(b)) [39]. The medium primarily consists of a viscoelastic carrier fluid with suspended abrasive particles. The percentage of abrasive particles may vary from 5% to 75% by volume [2]. Generally, the viscosity of the polymer medium is chosen based on the viscosity that is desired of the abrasive medium. The composition may vary as per the size and complexity of the surface being polished. The medium is pumped through the workpiece at pressures, ranging from

7-220 bars according to the requirements of surface finish and component materials [56].

Generally, there are three types of AFF methods, namely, one-way, two-way and orbital AFF depending on the relative motion between the abrasive medium and the target surface. In one way AFF, the abrasive medium is passed through the workpiece in only one direction and is collected on outflow into a reservoir. Figure 2.3(a) illustrates a typical one-way AFF setup indicating the flow of the medium through the workpiece. In such a flow finishing, the finishing process is faster as fresh medium without any microchips or broken abrasive particles, is passed through the workpiece every cycle [59]. In a two way AFF, as shown in figure 2.3(b), the abrasive medium flows back and forth through the workpiece shearing the surface during both the motions. Here, the same medium with the abraded chips from the workpiece are repeatedly used, thus decreasing its effectiveness over time. But, higher number of cycles can be achieved in a short time as the need for a reservoir is avoided. This is the most popular technique of AFF. Orbital finishing method is used for polishing external surfaces and edges. This method differs from the other two methods, in that additional small orbital eccentric oscillations are applied on the workpiece while the medium is flowing through, as shown in figure 2.3(c) [60]. Small vibrations of the order of 0.5 – 5 mm cause the medium to locally compress very close to the edges, increasing the down pressure generated for finishing the edge [56],[61].

As with all finishing processes, the MRR and the finish depend mainly on two parameters, namely, the normal down force acting on the surface and the relative motion between the polishing medium and the workpiece. In AFF, the bulk pressure of the medium generates the required normal force onto the surface for polishing. The relative motion between the medium and the surface is achieved by the flow of the medium. The preference for a viscoelastic material as opposed to a viscous fluid is attributed to the fact that the former restricts the rotation of the abrasive particles during the abrasive action, thereby creating a rubbing action to achieve a finer finish. Gorana et al. [61] stated that this rubbing mech-

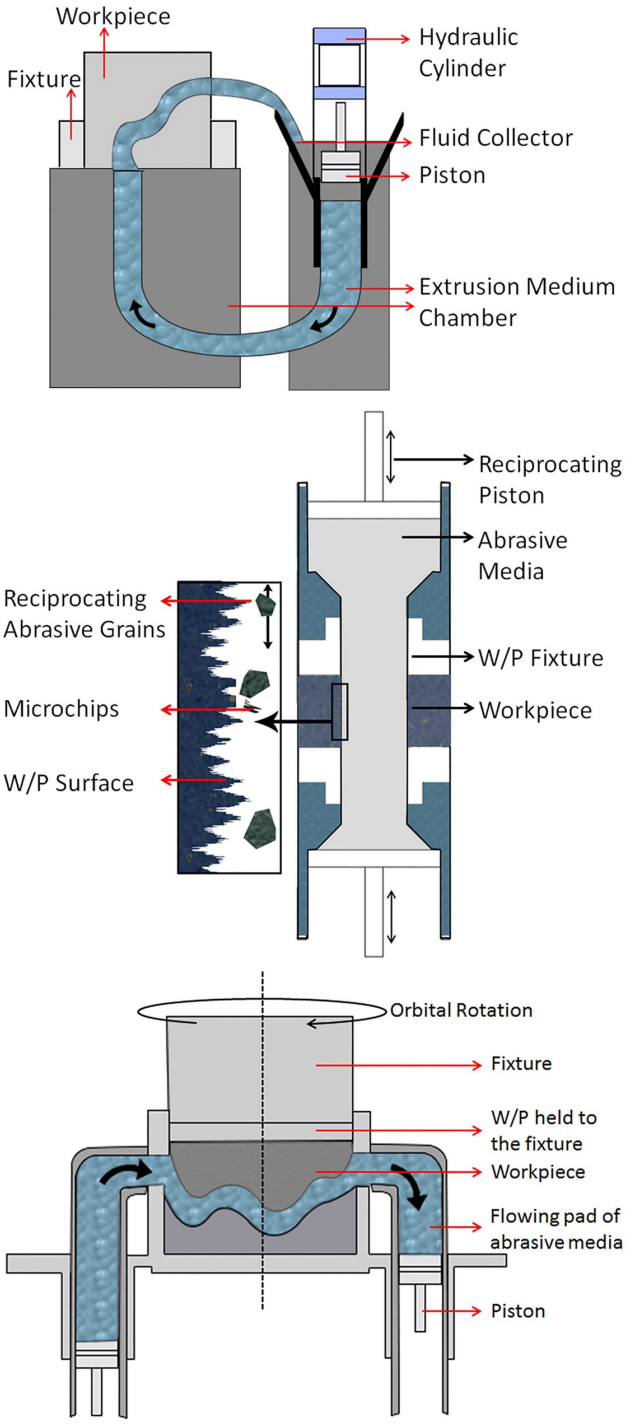

Figure 2.3: Schematic showing different setups in AFF (a) One way AFF (b) Two way AFF (c) Orbital AFF [2]

anism of polishing dominates in AFF, but the effect of ploughing is also evident on the surface.

2.3.2 Materials

As discussed in the earlier sections, the abrasive medium consists of polymeric viscoelastic material and fine abrasive particles thoroughly mixed into a homogeneous mixture. The commonly reported polymer medium used in AFF are of two types, Silicon-based polymers and Rubber-based polymers. Among these, polyborosiloxane is the most popular silicon-based medium used in AFF processing [62]. The rubber based polymers being studied in the literature include natural rubber, butyl rubber, or styrene butadiene derivatives. The most commonly used abrasives in AFF are silicon carbide (SiC) and Alumina (Al2O3) with an average size of 10-200 μm in concentrations of 5-75 % of the medium [2].

2.3.3 Process Parameters

The main process parameters that influence the MRR and the surface quality in the AFF process are (a) the bulk pressure in the medium, (b) flowrate of the abrasive fluid, (c) rheology of the medium, (d) the abrasive particle size and concentration, and (e)the number of flow cycles.

2.3.3.1 Pressure in the Medium

The pumping pressure in AFF relates directly to the normal force applied during the lapping process. An average pressure of at least 4 MPa is needed in the medium to observe significant polishing in the workpiece [63]. Figure 2.4(a) summarizes the variation of material removal in a unit time with pressure [3]. Here, we can observe that in all cases the MRR increases with increase in extrusion pressure. Though the MRR and the amount of material chipped increases with increase in medium pressure, the same cannot be deduced

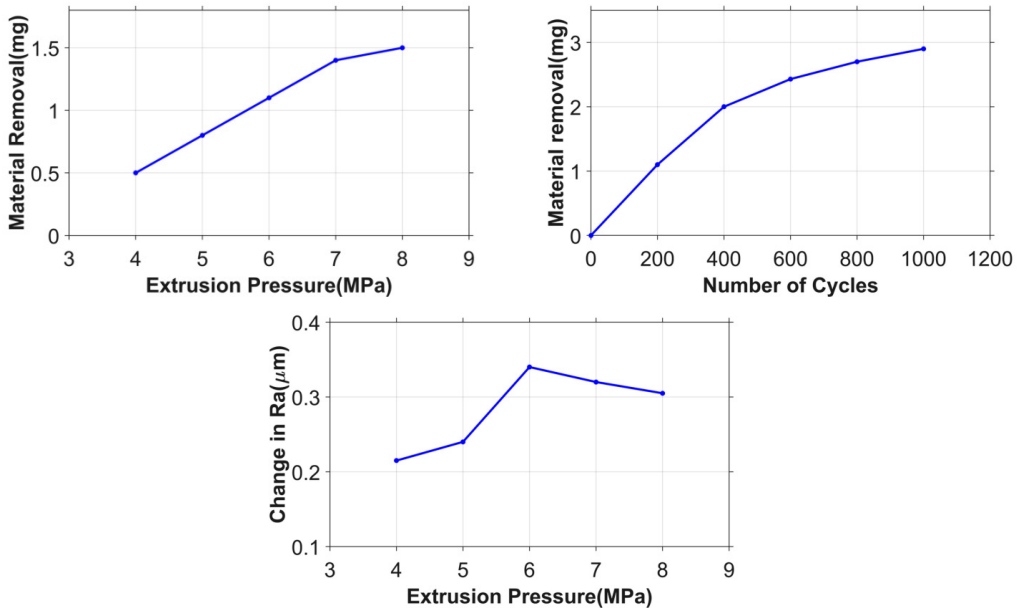

Figure 2.4: (a) Variation of material removal with Extrusion Pressure (b) Variation of the change in roughness with extrusion pressure (c) Variation of material removal with number of cycles[3]

for the surface finish. Figure 2.4(b) describes the effect of increasing pressure on the change in surface roughness. It shows that the Sa initially increases to a certain limit and then decreases with the increase in pressure.

2.3.3.2 Medium Flowrate

The flowrate of the abrasive medium affects primarily the uniformity of the finish during the process. This is calculated using the volume of medium pumped during any particular cycle and dividing it by the processing time. It is reported that the lower flow rates of the medium, although would slow the process, leads to a very uniform finish [57][61]. On the other hand, faster flow rates result in increased MRR. An exception to this effect is observed in brass where the flow rate of the medium has almost no effect on the material removal [57].

2.3.3.3 Rheology of the Medium

The apparent viscosity of the fluid has a high impact on the polishing effect of the process. It is of primary importance in internal polishing of macro and micro channels. Medium with low viscosity is preferred for channels with small cross section and long lengths. Generally, higher viscosity is preferred for shorter channel lengths. The viscosity of the final medium is largely dependent on the size and the concentration of the abrasive particles along with the viscosity of the polymer. It is independent of the pressures acting on them, thereby maintaining a constant viscosity for different working pressures [3]. Moreover, rheological studies suggest that increase in shear rate, induced by the flowrate in the medium, reduces the viscosity of the material [3],[64].

2.3.3.4 Abrasive Particle Size and Concentration

The characteristics of the abrasive particles have direct as well as indirect effects on the finishing process. The concentration of the abrasive enhances the MRR and surface finish. However, post a certain amount of concentration, the finishing depends on the particle size and the mechanical properties of the medium. A further increase in concentration does not have a significant effect on the finishing process [57]. The particle size of the abrasive particles affect the finishing process in two ways, it affects the cutting characteristics such as the width of cut during polishing and indirectly affects the depth of cut during the finishing process [57]. It is observed that the flexible medium with large particles results in a smooth surface finish as the depth of cut is low.

2.3.3.5 Number of Cycles

As every cycle results in abrasion of the workpiece to some extent, we can observe that the total material removed, increases with increase in the number of cycles the medium is passed through the workpiece. The MRR is normally higher in the initial cycles and de-

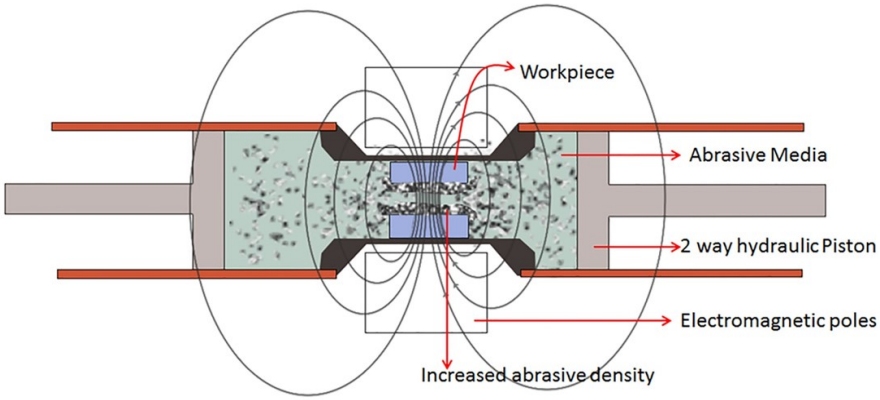

Figure 2.5: Schematic of MFA-AFF setup[4]

creases in the later cycles which can be observed from the slope of the graphs as illustrated in figure 2.4 [3]. This is partially attributable to the degradation of the medium.

2.3.4 Variants

In order to improve the process efficiency and the final finish numerous hybrid polishing processes have been developed. These different variants of AFF are, (a) Magnetic AFF, (b) Centrifugally Assisted AFF, (c) Ultrasonic Flow Polishing. These variants tend to enhance different aspects of the polishing process, and they need to be chosen as per the workpiece and polishing requirements.

2.3.4.1 Magnetic Abrasive Flow Finishing

In magnetic AFF, Carbonyl Iron Particles (CIP) are added to the medium. An external magnetic field is applied to increase the down force imparted to the workpiece by the medium or control its flow characteristics. There are two variants of magnetic AFF based on the medium and functionalities, (a) Magnetically Assisted AFF and (b) Magnetorheological AFF.

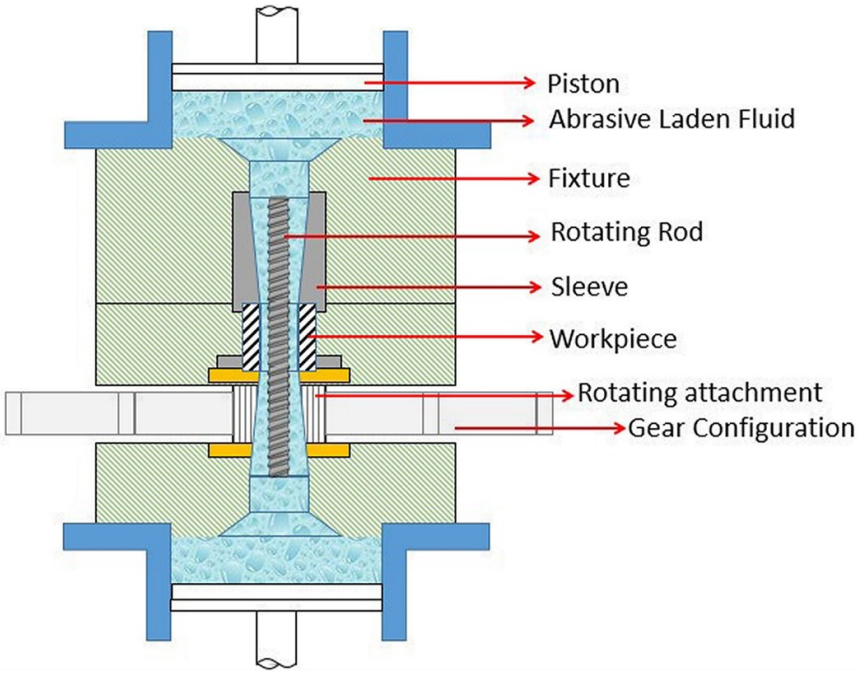

Figure 2.6: Schematic of an experimental setup of a Centrifugally Assisted AFF [5]

2.3.4.1.1 **Magnetically Assisted AFF:** Here, the magnetic field is applied to attract the CIP towards the workpiece as shown in figure 2.5. This causes an increase in the density of abrasive particles close to the finishing surface and increase in the normal force onto the surface resulting in improved MRR during the finishing process. This method is not very effective for workpieces made of ferromagnetic materials, but are effective in finishing materials, such as Brass and Aluminum. This is because of the shielding and reverberation effects from the ferromagnetic workpieces.[4]

2.3.4.1.2 **Magnetorheological AFF:** Here, the magnetic field is instead applied to primarily manipulate the rheological properties of the medium. The application of magnetic field results in the formation of a thick network of the CIP that restrict the rotation of the abrasive particles while flowing. This improves the cutting action of the particles, hence increasing the MRR and rate of the finishing.

2.3.5 Ultrasonic Flow Polishing

This process was invented in 1998 by Cheema and Jones [2],[65]. In this technique, the medium flowing through the workpiece during the process, is excited using an ultrasonic probe. This excitement of the medium activates the abrasive particles to interact more with the peaks on the surface resulting in faster finishing.

2.3.6 Relevance to Biomedical Implants

Biomedical implants are normally made to match the shape of bones, teeth, etc. with complex 3D surfaces. Polishing of these free form surfaces generally require specialized tools that can adapt to the shape of the implant. AFF is very conducive for polishing these implants as the abrasive medium can assume the shape of the workpiece being polished. Subramanian et al. [39] experimented and achieved a surface roughness Ra of 11 nm on hip prosthesis using AFF.

2.3.7 Limitations

Although the abrasive medium is flexible to reach inaccessible regions in the part, and can conform to complex shapes, its flow is generally reciprocative in nature. Because of such a flow pattern the polishing lay lines at any point are unidirectional in nature. Hence, even though the process yields a fairly smooth finish, one can observe significant differences in the roughness values along different directions. Also, localized polishing is hard to achieve unless the undesired regions are masked. Working pressures of the process also tend to be high (7-220 bars). Consequently, expensive and massive setups are needed to run the process.

2.4 Advances in Bonnet Polishing

Bonnet polishing is a widely used polishing method for finishing aspheric surfaces of lenses and mirrors. This method can also be used for finishing freeform bioimplants.

Bonnet polishing was introduced by Walker et al. [40],[66] at Zeeko Ltd. as Precessions tooling for optical surfaces. This technique employs a multi-axis CNC machine with a polishing bonnet attached to an end.

2.4.1 Process Setup and Mechanism

A bonnet (see figure 2.6) is made up of an inflatable membrane filled with pressurized fluid (eg. air) to serve as a flexible polishing pad [66]. This construction of a bonnet helps in conforming to the shape of the surface to be polished. This flexible pad is attached to the rotating head of a multi-axis CNC machine for polishing. As shown in figure 2.2, the arms connected to the CNC machine are oriented in different directions with motor controls. This gives the machine the freedom to reach complicated surfaces at different angles as required. An abrasive slurry consisting of sub-micrometer scale abrasive particles mixed with surfactants and other ingredients is introduced onto the surface to be bonnet polished [44]. During polishing, the bonnet head is brought in contact with the surface of the workpiece such that the axis of the Head (H-axis) is at an angle to the normal to the surface of the workpiece which is called as precess angle (α in figure 2.7). While polishing, the bonnet is rotated about these two different axes (H-axis and A-axis in figure 2.7) to generate the rubbing action for polishing. This technique of rotating the bonnet in multiple directions is called as Continous Precession. This method can also be used for very low scale form correction of workpieces [67]. As the process is computer controlled, localized polishing to any required roughness level is possible. It also offers a high MRR for fast polishing to achieve nanometric surface finish ($Sa \approx 16.1$ nm) on implants [42].

2.4.1.1 Mechanism

The mechanism of bonnet polishing is very similar to that of lapping and other mechanical fine-abrasive finishing processes [68],[69]. These models attempt to predict the MRR by modifying the Preston equation [70] to accommodate the process behavior pe-

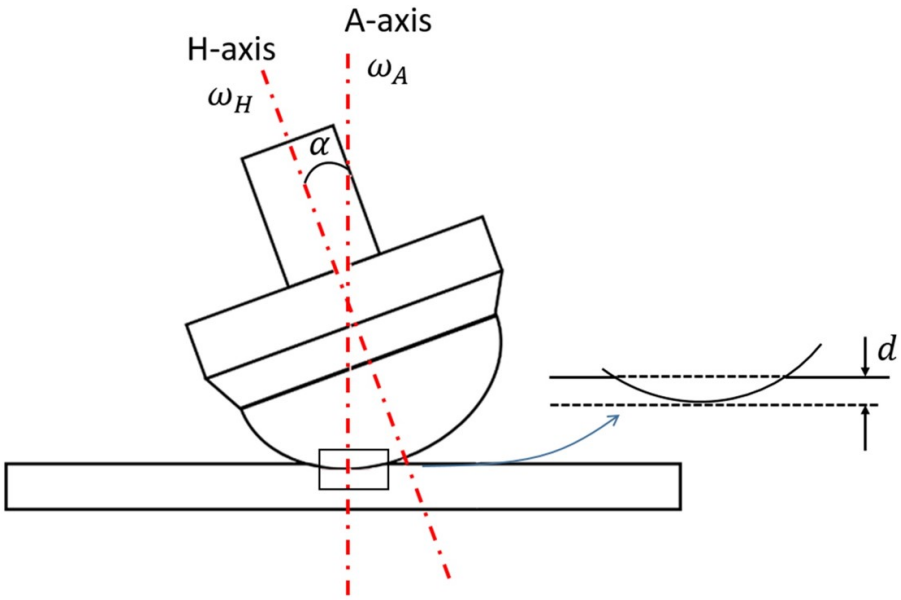

Figure 2.7: Schematic of an experimental setup of a Centrifugally Assisted AFF [5]

culiar to bonnet polishing. For conventional polishing processes, material removal rate ($MRR = \Delta h / \Delta t$ where Δh is a notional reduction in the asperity height after a period, Δt, of polishing time) is predicted by Preston equation [70],

$$MRR = C_p P v \tag{2.2}$$

where, C_p is the Preston coefficient, which includes the effects of the process parameters affecting the interaction between the workpiece and the tool (e.g., pH, slurry, type of abrasive, etc.), P is the down pressure applied (i.e., normal force, F per unit contact area, A_c, on the workpiece being polished), and v is the relative velocity between the part and the tool. This equation indicates that for conventional polishing MRR is controlled by the applied normal load and the relative velocity between the workpiece and the polishing tool/pad.

The key difference in the behavior can be attributed to the spherical (balloon like)

shape of the bonnet which gives a non-uniform pressure distribution on the surface of the workpiece. Through experimentation under static conditions, this pressure distribution on the contact surface of the workpiece was found to be near-Gaussian as illustrated in figure 2.8 [6]. This is modeled using a modified Gaussian equation. Hence, the height of material removed varies locally at the polishing spot. The equation for the computation of the material removal at a point B in the polishing spot, modeled by Cheung et al. [68], is given by,

$$M_B = kP_m exp(\frac{-1}{2}(\frac{r_B}{b})^{\lambda})V_B t_d \tag{2.3}$$

where, M_B is the height of the material removed at B, k is the Preston coefficient, P_m is the maximum pressure observed at the center of the spot, r_B is the distance from the center of the spot O to B, b and λ are the parameters of the pressure distribution, V_B is the relative velocity at B and t_d is the dwell time of the tool. Eq. (3) is also known as the Tool Influence Function (TIF) of the polishing process as it gives the material removal from the polishing area as a function of r_B. This function can be used to predict the shape of the surface for form correction during polishing [46],[6]. The integral of TIF over the polishing spot gives the material removal from the region of the workpiece. The material removal rate can be computed as the material removal per unit dwell time on the surface.

It is important to note that the relative velocity at the point is dependent on the rotational speeds of the bonnet about both the H and A axes and the precess angle between them. Precessions rotation of the bonnet is needed as the polishing cuts from only the rotation about H-axis are unidirectional in nature. In order to achieve a uniformly polished surface, the bonnet needs to be rotated about the A-axis at the precess angle also to constantly change the direction of cutting in the polishing spot. This process of polishing

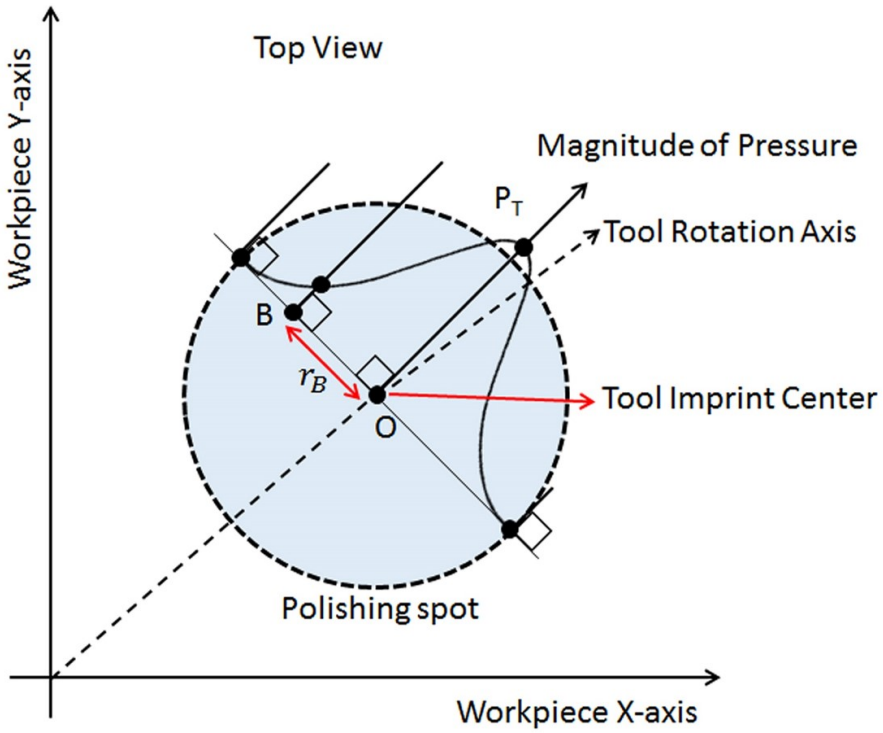

Figure 2.8: Distribution of pressure on the surface of the workpiece in static conditions [6]

using both the head axis rotations and A-axis rotations is called as continuous precession polishing and was first suggested by Bingham et al. [71]. Pan et al. [1] suggested that a random abrasive path during continuous precessions results in a more uniform surface finish as compared to single precession polishing.

2.4.2 Materials

Bonnet polishing employs a variety of abrasives, such as alumina, diamond powder, and cerium oxide for polishing different types of materials. For example, cerium oxide with a particle size of < 1 µm is suitable for polishing glass surfaces such as lenses [44],[72]. Metals such as cobalt chromium alloys [42],[46]and metal plated surfaces are usually polished with harder abrasives, such as diamond or alumina with particle sizes ranging from 2 µm to 9 µm depending on the desired finish of the polished sur-

face [73],[74][81]. Soft materials that can trap the abrasive particles such as polyurethane and polishing "microcloth" are used for manufacturing bonnets.

2.4.3 Process Parameters

The process parameters such as precess angle, bonnet offset, head speed and tool pressure directly affect the efficiency of the process and the quality of the final surface. The final surface roughness of the workpiece is also dependent on the size and hardness of the abrasive particles. The following subsections describe the effects of these parameters for finishing CoCr surfaces with a GR35 polyurethane bonnet and 3 μm alumina abrasive particles on a 7-axis bonnet polishing machine [7].

2.4.3.1 Precess Angle

In bonnet polishing, precess angles from 5º to 30º are generally used for the polishing process. Figure 2.9(a) shows the variation of the MRR with respect to the precess angle of the bonnet. It shows that an increase in precess angle increases MRR. A six-fold increase in MRR was observed by increasing the precess angle from 5º to 30º. This increase in MRR can be attributed to the increase in both contact area and the relative speed at the polishing spot.

2.4.3.2 Bonnet Tool Offset

The tool offset is the distance by which the surface of the bonnet is compressed by the workpiece during the polishing process which is indicated as d in figure 2.7. An increase in the offset of the polishing tool increases the contact area of the polishing tool on the workpiece. As shown in figure 2.9(b), the increase in the contact area and the pressure at the surface resulting from increasing the tool offset leads to an initial increase in MRR. The MRR peaks at a limit and is then followed by a decreasing trend. This is due to the drop in contact pressure at high tool offset of the bonnet.

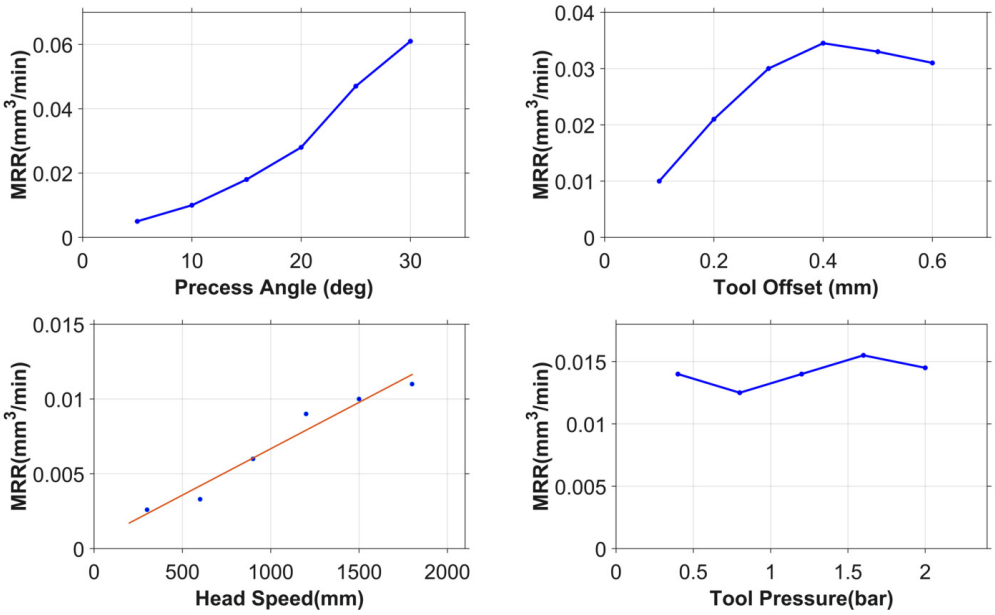

Figure 2.9: Variation of the MRR in Bonnet Polishing with respect to different process parameters such as (a) Precess Angle (b) Tool offset (c) Head Speed and (d) Tool Pressure [7]

2.4.3.3 Head Speed

Head speed refers to the rotational speed of the bonnet head about the H-axis. The effect of the increase in the head speed on the MRR is the same as that of the speed of rotation in lapping. As summarized in figure 2.9(c), the MRR increases linearly with the head speed. This is in agreement with the Preston equation [70] in the context of lapping. The linear relationship between the material removal rate and the relative velocity shown in Eq. (3) is validated through the experimental results in figure 2.9(c).

2.4.3.4 Bonnet pressure

The bonnet pressure refers to the bulk pressure of the fluid filled inside the bonnet. Under static tool conditions with constant tool offset, an increase in tool pressure would increase the contact pressure on the workpiece [6]. However, under dynamic working

conditions TIF of the process is not affected significantly with increase in bonnet pressure. As a result, only a slight increase in MRR is observed when bonnet pressure is increased. Hence, as shown in figure 2.9(d), the effect of bonnet pressure on MRR is not significant in comparison with the other parameters such as the precess angle, tool offset and head speed.

2.4.3.5 Tool Path

Tool Path plays a vital role on the surface roughness and the uniformity of the polishing surface. As the TIF suggests, MRR over the polishing spot is not constant. Moreover, the polishing spot is generally much smaller in size than the workpiece. This can result in a non-uniform local polishing if the bonnet is kept stationary at the spot. Hence, the tool is moved along the surface at a certain feed rate for polishing the whole surface. The path followed by the tool too plays a vital role in determining the uniformity of the finish. Dunn et al. [8] experimented with a randomized unicursal tool path on the surface as opposed to raster tool paths (see figure 2.10). These images suggest that periodic structures are formed on the surface from raster tool paths. These surfaces have a high Rt with low Ra. On the other hand, randomized tool paths yield a more uniform surface with less periodic structures and Rt values comparable with Ra.

2.4.4 Variants

Bonnet polishing is a secondary finishing process that is best suited for creating ultrasmooth finish on surfaces that are already prefinished to a certain extent via grinding and other primary finishing processes. This process is not effective with unfinished initial surfaces. Hence, a variant to the basic bonnet polishing method based on using an abrasive jet to prepolish a machined surface has been investigated [73],[74]. This process variant was found to drastically reduce bonnet wear and more efficiently achieve an ultrasmooth surface [73],[74].

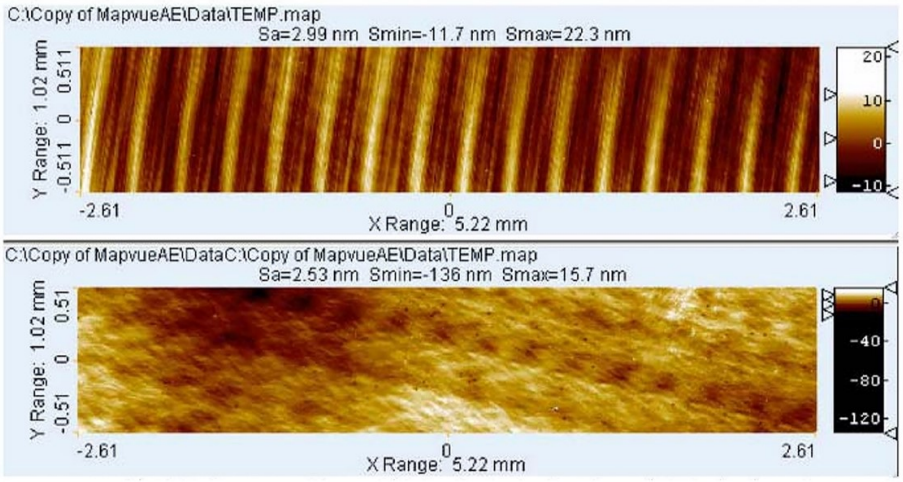

Figure 2.10: Surface images of the workpiece after regular straight path and unicursal path [8]

2.4.5 Limitations

One of the primary drawbacks with bonnet polishing is that it is a contact polishing process, making it necessary to use mechanical arms and links to reach the polishing spot. This restricts the use of bonnet polishing only to external surfaces and accessible to internal locations of a biomedical implant. Also, the concavity of the surface that can be efficiently polished is limited by the dimensions of the bonnet and the range of precess angles achievable in the equipment. Concave surfaces with curvatures higher than that of the bonnet are often difficult to polish using this technique.

2.5 Advances in Magnetic Polishing

Magnetic field assisted polishing processes are based on applying a magnetic field on abrasive-mixed magnetic fluid for surface finishing. In the presence of magnetic fields, magnetic particles in the fluid align themselves in the direction of the magnetic field. This increases the apparent stiffness of the Bingham fluid to provide the desired elastic properties to facilitate polishing, expose the abrasive particles to the workpiece surface, and/or

exert the desired down force.

The use of a magnetic field for polishing was first reported in 1940 for cleaning oxide scales and polishing welded joints [75]. Later efforts focused more on developing improved process designs and fluid compositions to achieve improved polishing results with different workpiece geometries. For example, Shimada et al. [76] developed a magnetic compound fluid to increase the apparent viscosity as well as the stability of the dispersed particles. Their work greatly overcomes the earlier limitations of magnetic and MR fluids. Shinmura et al. [77] employed bonded magnetic abrasive particles to polish steel and silicon nitride cylinders. Subsequently, Fox et al. [78] investigated the effects of using unbounded magnetic abrasive particles in a cylindrical magnetic abrasive finishing process. Their experimental results suggested an increase in MRR and surface roughness compared to bonded abrasives. They have also observed that imparting axial vibration to the workpiece resulted in a better surface finish due to the improved flow pattern and tribological regimes and increasing the magnetic flux density yielded higher MRR and better surface finish [78].

Kim et al. [79] used a pressurized jet of magnetic abrasive particles through a nozzle to finish internal surfaces of a workpiece with non-circular cross sections. While the magnetic field is used to attract the abrasive particles towards the workpiece surface, they are dragged along the cylinder's surface via the pressurized jet simultaneously to facilitate polishing. More recently, Wang et al. [80],[81] employed a gel with magneto-rheological properties to finish a cylindrical workpiece. The steel workpiece was treated as a pole of the magnet and was rotated at high speeds to create a relative motion between the asperities and abrasive particles. An axial vibration was introduced to impart a uniform surface finish.

2.5.1 Process Setup and Mechanism

The mechanism of a magnetic polishing process is primarily governed by the behavior of the magnetic (mostly MR) fluid in the presence of magnetic field. MR fluids are particularly attractive for polishing because they can (a) transport the abrasive particles to the cutting zone and remove abraded chips and heat to prevent scratching and thermal damage, respectively, (b) reach internal surfaces and profiles that are inaccessible to conventional polishing tools, (c) mitigate abrasive and process degradation as the fluid can be continuously recycled, monitored and conditioned, (d) provide optimal stiffness to meet various polishing needs, and (e) augment other polishing processes (e.g., abrasive flow/jet polishing) to improve the process efficiency, especially for optical surfaces [9].

2.5.1.1 Setup

Over the past few decades, several magnetic polishing setups have been designed and customized to meet the needs of a variety of workpiece materials and geometries. Among these, a schematic of a commercial machine tool, originally invented by Kordonski [9] for polishing aspheric surface of lenses [82] is shown in figure 2.11. In the setup, nozzle delivers the MR fluid charged with abrasive particles onto the vertical rotating wheel. The rotary wheel carries the fluid to the converging work zone between the lens (workpiece) and the wheel. An electromagnet placed transversely to the carrier wheel magnetizes the MR fluid, thus increasing its viscosity and yield stress. Upon the application of magnetic fields, the material stiffens and abrasive particles segregate to the surface of the fluid to promote material removal (along the exposed face of the fluid) [10]. This switching of the rheological properties of the fluid to a higher apparent viscosity and stiffness in the presence of magnetic field is associated with the formation of Flexible Magnetic Abrasive Brushes (FMAB) [10]. These brushes change profile according to the surface form, as well as employing magnetic jigs that form chains of abrasive particles, resulting in material re-

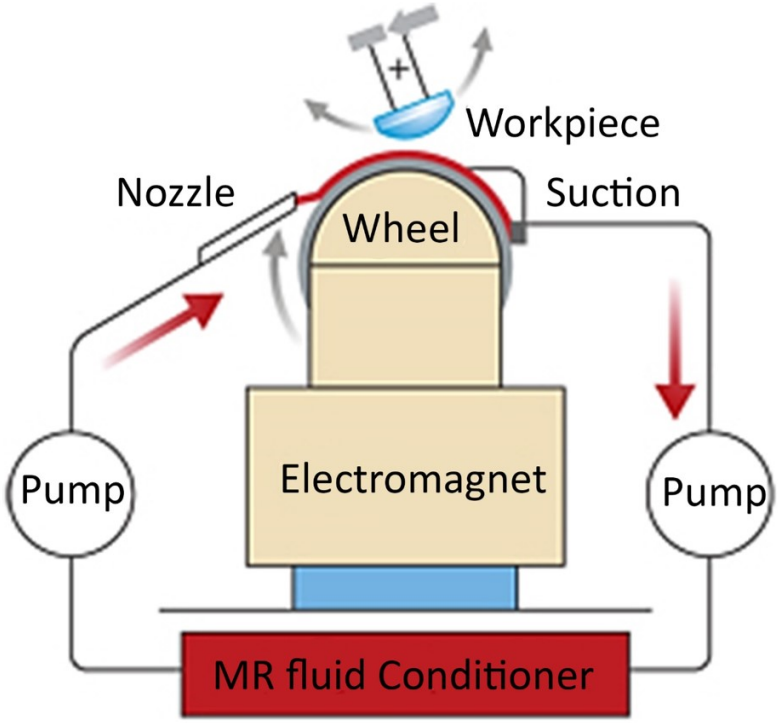

Figure 2.11: Magnetorheological Finishing [9]

moval from both external [10] as well as internal surfaces [83]. Whereas in cases where bonded abrasives are used, the magnetic forces in these magnetically active bonded abrasive particles provide the required down force and relative motion in the abrasive particles for finishing. As the wheel rotates, the used MR fluid is collected by a suction system which is then conditioned and recycled for the next cycle [9].

2.5.1.2 Mechanism

The material removal mechanism in this process is illustrated in figure 2.12. Figure 2.12(a) shows the randomly arranged abrasive and iron particles in a non-magnetized MR fluid. Figure 2.12(b) shows the alignment of carbonyl iron particles along the magnetic lines of force with abrasive particles suspended on the top. Figure 2.12(c) shows the

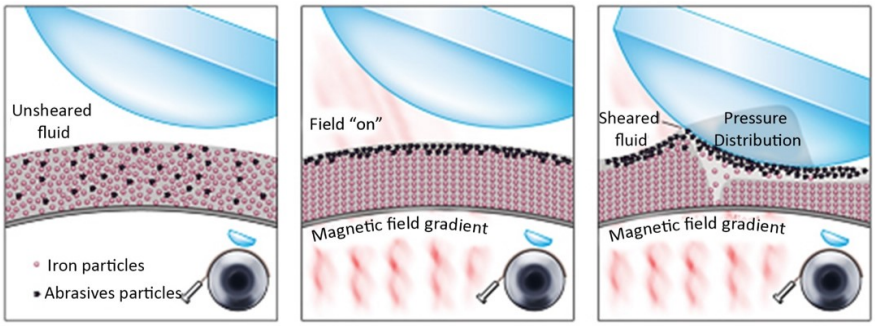

Figure 2.12: Schematic of material removal process in Magnetorheological Finishing [10]

sheared fluid with abrasive particles in contact with the workpiece surface while abrading the surface, thus removing material. Here the relative motion is caused by the rotation of the carrier wheel and the sweeping motion of the lens. The magnetic force provides the normal component of the force while the tangential component of the force is generated by the rotation of the carrier wheel. The sweeping motion of the lens contributes to both the normal as well as the tangential force components. The relative motion between the workpiece and the abrasive-mixed MR fluid removes the material in the form of micro and nano-chips [10].

Mori et al. [11] suggested that the down force influences the indentation of the abrasive particle on the surface of the workpiece. The tangential force contributes to restoring particles to their equilibrium chain structures from the disturbances as the workpiece rotates, asperity removal, and to spinning the abrasive particles to help climb off the valleys.

Studies have been on the different aspects of magnetorheological polishing such as the force causing the segregation of the abrasive particles in the fluid. Tani et al. [84] described a method that uses several permanent magnets of alternating poles to set up a spatial field gradient both vertically and horizontally with MR fluid comprised of unbonded abrasives. The non-uniform field has a strength of the order of 50-350 kA/m. The magnetic fluid is

composed of 10-15 nm ferrocolloid-magnetite (Fe3O4) in eicosyl naphthalene and 40 vol % 4 μm SiC. The part is rotated over the fluid and the workpiece is polished due to the relative motion of the part with respect to the “lap" created by the levitational buoyancy force. The removal rate for an acrylic resin was approximately 2 μm/min over the part surface. Here, it is suggested that, the horizontal field gradient prevent the abrasive particles from “rolling away” along with the workpiece. And the vertical gradient causes the magnetic particles to move downward towards the permanent magnets in turn driving the abrasive particles up to the region between the magnetic particles and the workpiece. These magnetic levitation forces which allow the abrasive particles stay afloat is proportional to the gradient in the magnetic field [85],[86] and is given by,

$$\frac{F_z}{V} = (\rho_f - \rho_s)g - \mu_o(\mathbf{M} \cdot \nabla \mathbf{H})_z \tag{2.4}$$

where, F_z is the levitational buoyant force, V is the volume of abrasive particles, ρ_f is the mass density of magnetic fluid, ρ_s is the mass density of abrasive particles, g is the acceleration due to gravity, μ_o is the permeability of free space, M is the ferric induction of magnetic fluid, and ∇H is the gradient in the magnetic field. Studies[84] also suggest an increase in MRR with increasing magnetic fields. This is attributed to the increase in buoyancy force resulting from the application of the magnetic field.

Shorey et al. [87] and Miao et al. [88] have studied the mechanism of material removal in the MR finishing process. Contrary to relating levitation forces to material removal, they stated that the material removal in MR fluids is primarily due to shear forces and not due to normal forces. This was based on the fact that the normal forces due to magnetic levitation (buoyant) (1×10^{-9} N) and the normal stress due to bulk deformation and/or hydrodynamic pressure due to flow of MR fluid into converging gap (1×10^{-7} N) [87] are negligibly low in comparison with the forces obtained in conventional polishing (0.007 N

and 0.065 N) [89], while the MRRs are still comparable. Miao et al. [88] reported the following expression for MRR in magnetorheological finishing processes

$$MRR_{MFF} = C'_{p(MRF(\tau,FOM))} \frac{E}{K_c H_V^2} \cdot \tau \cdot v \tag{2.5}$$

where, MRR_{MFF} is the material removal rate for MR Finishing, $C'_{p(MRF(\tau,FOM))}$ is the modified Preston's coefficient which in turn is a function of the shear stress τ and the material's Figure of Merit FOM, E is the elastic modulus of the workpiece, K_c is the fracture toughness of the workpiece, H_V is the Vicker's Hardness of the workpiece and v is the relative velocity of the MR fluid with respect to the workpiece. This expression is consistent with hydrodynamic models reported in literature for material removal in polishing processes.

Other studies on magnetic fluid polishing include finishing of edges based on forming a converging gap between the edge and the magnetized MR fluid [90], MR fluid flow, viscosity and temperature are controlled [91]. Augmented abrasive jet finishing has been developed to enhance MRR (magnetic field is used to pull and collimate abrasive jet, thus reducing the load on the fluid pump). Studies have also been conducted on finishing of deep concave surfaces [92], polishing of elastic workpieces in freezing medium [93], as well as chemo-mechanical polishing of ceramic balls [94]. The prior investigations have also provided evidence of interesting coupling between hydrodynamics and magnetic effects that affect polishing performance [95].

2.5.2 Materials

A magnetic polishing medium primary includes three major components (a) the magnetic fluid, (b) the abrasive particles, and (c) supplementary components (e.g. surfactants, such as oleic acid, tetramethylammonium hydroxide) that may be employed to increase colloidal stability of the fluid. In unbonded magnetic polishing medium, alumina, SiC

and CeO2 particles of the order of 1-25 μm size are mixed with magnetic fluids to form the abrasive medium. The nonmagnetic nature of these abrasive particles produces the required magnetic levitating force which results in the formation of the FMAB for polishing. The magnetic fluids used for polishing can belong to one of the following four categories: (a) magnetic fluids or ferrofluids which comprise of nanometric-sized carbonyl iron particles suspended in a carrier fluid such as water, oil, and eicosyl naphthalene with the help of stabilizers [84]. (b) MR fluids use larger ferromagnetic particles of the order of micrometers which are suspended in oil or water-based medium using suitable stabilizers or polymers. (c) Magnetic compound fluid suggested by Shimada et al. [76] includes both micro- and nano-scale particles where α-cellulose particles are used to stabilize the fluid. (d) Magnetic abrasive gels where the magnetic and abrasive particles are suspended in silicone gel which acts as a viscoelastic medium to suspend the particles [81].

Apart from these, the bonded abrasive particles can also be used with proper solvents and stabilizers. Mori et al. [96],[93] reported the application of sintered magnetic abrasives where small abrasive particles (alumina $\sim 5\mu$m [11]) are attached to the surface of large carbonyl iron particles (70-170 μm [11]). Bando et al. [97] have also reported the use of bonded magnetic abrasive particles synthesized through electroless plating of diamond abrasives onto ferrous particles for polishing alumina ceramic tubes [98].

2.5.3 Process Parameters

The MRR and surface finish of magnetic polishing processes are dependent on process parameters such as (a) strength of the magnetic field, (b) abrasive particle properties and type of magnetic particles, (c) down force, and (d) the relative motion of the particles.

2.5.3.1 Magnetic field strength

With an increase in the magnetic field strength, the yield stress (based on Bingham model) of the magnetic fluid increases [99]. This results in an increase in the pressure

exerted by the magnetic particles on the abrasive particles and the workpiece thereby increasing the MRR. One of the main advantages in magnetic field assisted finishing processes is the ability of the method to continuously recycle abrasive particles. However, if the magnetic field strength is increased beyond a critical point the abrasive particles are not recycled as they are held against the workpiece surface under high pressure, thus resulting in worn out edges of the active abrasive particles and progressively lower MRR.

2.5.3.2 Abrasive and magnetic particle properties

Geometrical and physical properties of the abrasive and the magnetic particles play a major role in influencing the surface finish. For example, when a steel grit is used as the ferromagnetic particles (FP), surface finish and MRR are better than with an iron grit [100]. This is because a steel grit was able to distribute the pressure more uniformly to the abrasive particles because of its polyhedron shape, compared to a spherical iron grit. Additionally, the hardness of the steel grit was much higher than that of the iron grit. This leads to more surface abrasion and hence increased MRR. Also, larger FP yielded higher MRR and surface roughness [100] because magnetic forces on the particles are directly proportional to their volume. Thus, larger FP had higher magnetic forces acting on them. This increased the average pressure on each abrasive particle, thereby increasing the MRR [85]. However, excessively high magnetic force prevented the rolling of the FP which resulted in decreasing the pressure on the abrasive particles, thereby lowering the MRR [100]. ask them

Also, larger the abrasive particle size, higher was the MRR. However, large particle sizes also lead to higher surface roughness. Smaller abrasive particles yielded better surface roughness but low MRR. This is because the smaller the size of the particles, the lower was the average pressure and shear stress exerted by the FP on each abrasive particle. Thus, as the average pressure on the abrasive particles decreases, lesser material is

removed and better surface roughness is obtained [100].

2.5.3.3 Down Force

Down force is one of the most crucial parameters for polishing. In magnetic field assisted polishing, down force on the workpiece can be applied broadly in two ways: (a) using a physical tool to push the magnetic fluid against the workpiece or vice-versa, and (b) using the magnetic fields itself to attain the required down force. The first case is mostly used for polishing the external geometries, curved surfaces, etc. For example, down force in curved and free-form geometries can be applied using a CNC controlled magnetic ball end tool covered with the magnetic fluid [101]. Here, the radius of the ball end tool becomes a limiting factor for polishing small geometrical features. Magnetic fields, on the other hand, provide an inherent advantage of flexibility in polishing hard to reach areas as well as internal geometries, for example, pipes and capillary tubes. An appropriate combination of electromagnets may be needed to adjust the magnetic fields at the target spot to create the required down force. For internal geometries, Yamaguchi et al. [102] developed a magnetic configuration to polish the internal surfaces of a thin capillary tube. The tube was initially filled with the magnetic fluid and then an external magnetic configuration was used to agitate the abrasive particles and provide the down force necessary for polishing.

2.5.3.4 Effect of relative motion

The motion of the abrasive particles relative to the surface plays a vital role in material removal. The relative motion between the workpiece and the MR fluid can be achieved through different methods. In most cases, the fluid is agitated relative to the surface of the workpiece either mechanically with the help of wheels, jets, magnetic ball, etc., or using magnetic field itself. Yamaguchi et al. [103],[102] reported the use of magnetic fields to move the abrasive mixed fluid relative to the workpiece.

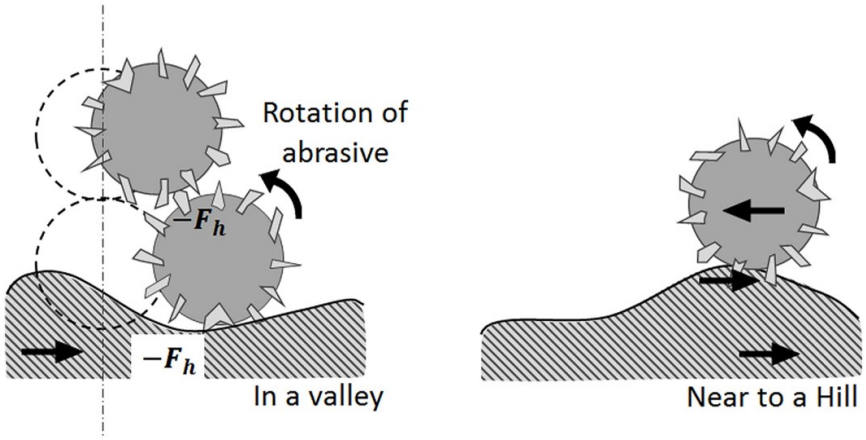

Figure 2.13: Schematic showing the motion of abrasive particles and the forces at the interface during polishing at peaks and valleys [11]

Since the pressure in this process is very low, an abrasive particle moving along the surface of the workpiece is free to rotate on the target area. But, in the presence of magnetic field the chains formed by the FP trap the abrasive particles and stop them from rotating while in contact with the surface of the workpiece. Hence, it is the shearing forces created by the abrasive particles trapped by the magnetic chains that result in finishing of the surface of the workpiece.

The material removal mechanism was further investigated by Mori et al. [11]. They had used sintered abrasive made by aggregating iron with alumina particles to form magnetic abrasives as shown in figure 2.13. It was noted that the normal force acting on the abrasive particle was responsible for the indentation of the abrasive particle on the surface of the workpiece. To investigate the tangential force, it was assumed that when the workpiece rotates, the balance in the chain structure of the abrasive particles was disturbed, and the abrasive particle at the edge moves a distance dx from its balanced point. As a result, a tangential (frictional) force acts to bring the particle back in the equilibrium position [11]. In figure 2.13, the dashed line represents the equilibrium location of the abrasive particle.

This equilibrium position of the abrasive particle is perturbed due to the combined effect of friction force between the workpiece surface and the abrasive particle during their relative motion, as well as the repulsive force between the abrasive particles. This results in a return force F_h. If the abrasive particle's equilibrium location is in the vicinity of a crest, the return force F_h results in an asperity material removal. On the other hand, if the abrasive particle's indenting point is in a trough, F_h acts in the center of the abrasive particle and a reaction force acts at the edge of the abrasive. Thus, a moment acts on the particle and makes it to rotate and climb the crest. This tendency of the particle to rotate and climb the hill is also due to the fact that, the cutting resistance of the material will be larger at the bottom of a crest owing to larger volume of material to be removed. Hence, the material climbs along the crest with increasing F_h and ultimately cuts material from the top of the hill, where there is minimal cutting resistance.

Among the process parameters, tangential speed v and strength of the magnetic field $\mathbf{B}$ (that determines the down force P) are the major determinants of MRR and surface finish [104]. While the magnetic field contributes to an increase in MRR, the surface finish improves with increase in speed v as it promotes "sloshing" of abrasive particles [104]. Thus, depending on the size, form and type of material being polished, and the type and size of the abrasive particles being used, it is critical to choose optimum magnetic field strength and rotational speed to obtain the desired surface finish.

2.5.4 Variants

Different hybrid methods of polishing have been developed along with magnetic polishing to improve the performance of the polishing process. Prior efforts also investigated the use of electrochemical action (EMAF) to create a passivation layer [105], normal vibrations (VMAF) to enhance the MRR [106], and lubricants to improve fluid flow and hence finish [98]. Characteristics of the FMAB, especially the effects of rotation speeds

and magnetic field on the particle distribution, cutting forces and MRR [107], as well as the augmentation of ultrasonic vibration [108] has also been studied.

2.5.5 Relevance to Biomedical Implants

The ability of the polishing technique to achieve nanoscale finishes and conform to the shape of the workpiece is particularly useful in finishing of implants to ultrasmooth finish. Sutton et al. [109] used a setup similar to the polishing setup described in figure 2.11 to polish hip implant ball with magneto-rheological abrasive fluids. MAF was also successfully employed by Sidpara et al. [47] and Yamaguchi et al. [110] to polish a Knee Femoral implant to a surface roughness of $Ra \approx 28$ nm and $Sa \approx 5$ nm. Both the research groups used a ball shaped magnetic pole to locally focus the magnetic abrasive fluid forming the FMAB which were used to polish the implant by rotating the pole.

2.5.6 Limitations

While great progress has been made towards adapting magnetic field and MR fluid to finish various materials and geometric shapes, issues pertaining to localization, such as confining the magnetic fluid-abrasive mix to polish the desired areas by applying "optimal" time-space variation of the magnetic field has received little attention. Recent advances in electro-permanent magnets, and magneto-viscoelastic fluidics provide some interesting possibilities for localized polishing.

2.6 Summary

Biomedical implants are medical devices that are surgically placed into the body to enhance and support an organ in its functioning. A variety of metals such as stainless steel (316L SS), titanium alloys (Ti, Ti6Al7Nb, Ti6Al4V, TiNi), cobalt chromium alloy (CoCrMo), ceramics such as zirconia, sapphire, and alumina, polymers such as Ultra High Molecular Weight Polyethylene, polyurethane, nylon, and polyethylene are used to man-

ufacture orthotic implant components. An implant needs to be chemically, mechanically and biologically accepted by the body without causing any undue stress during its lifetime.

For joint implants, two broad types of surfaces need to be prepared to achieve joint objectives of bio-acceptance and functional durability. A surface with micro-roughness at the interface between the implant and the bone tissue which promotes osseointegration, including promotion of growth of bone tissue on the surface, and adsorption of the proteins onto the surface. A surface roughness Ra in the range of 0.5–8.5 μm is known to be most conducive to achieve this objective. An ultrasmooth finish (< 50 nm) on the sliding surfaces ensures high durability and smooth movement of the implant at the joints, and inhibits debris formation. The smoothness, often quantified by ease of sliding (λ) varies depending on the material combinations and application.

In order to meet these differential surface requirements in an implant, namely, textured surface to promote osseointegration and ultrasmooth finished surface for smooth sliding. Two broad categories of processes are employed to achieve these surface needs. Texturing of surfaces can be achieved using sandblasting, chemical etching and laser treatment. Nanofinishing process employed in this context include abrasive flow finishing (AFF), bonnet polishing, magnetic polishing and electrochemical treatment. Among these, mechanical methods such as AFF, bonnet polishing and magnetic polishing are best suited to finish complex 3D shapes using free abrasive particles.

In AFF, a homogenous mixture of fine abrasive particles suspended in a viscoelastic medium is pumped through the surface of the workpiece at very high pressures (7-220 bars). The high pressures and the normal stress developed as a result of the flow of the medium cause the abrasive particles to impinge onto the surface and generate a finished surface. In bonnet polishing, a deformable bonnet membrane inflated with a fluid rotates about two different axes along with the abrasive fluid to finely finish the surface of the workpiece. The two rotating axes are oriented at a precess angle. Most magnetic polishing

methods are based on creating FMAB with abrasive particles trapped in the chains of magnetic particles. An FMAB can easily conform to the shape of the implant so that the abrasive particles can polish the surface of the workpiece. External mechanical force and/or the magnetic fields are employed to apply the down force necessary for polishing.

Localization of polishing operation is hard to achieve using the current finishing methods. Most techniques are limited to bulk polishing, compelling us to rely on manual methods or the use of elaborate surface masks for polishing local regions. Some techniques are limited by the size constraints of the machine for effective polishing. Significant contributions are yet to be made for polishing local regions of different sizes in implants with complex shapes to nanoscale smoothness.

3. LITERATURE REVIEW

As discussed in section 2.5 on magnetic polishing, the behavior of the polishing process is highly dependent on the polishing fluid's rheological properties and its control by magnetic fields. For the purpose of localization of polishing, a thorough understanding of both the change in rheological properties and segregation of the fluid in the presence of magnetic fields is necessary. This behavior of the fluid is also dependent on the composition of the abrasives and the magnetic particles in the fluid and their individual properties. This motivates us to conduct a rheological characterization of the fluid to gain knowledge on behavior of the fluid in the presence and absence of magnetic fields.

3.1 Rheology of Slurries

One of the early contribution to the literature of rheology of slurries was given by Einstein in 1906 [111]. In this seminal work, he gave a theoretical development of the variation of the viscosity for suspensions with low concentration of particles in newtonian fluids. The rheological behavior was finally derived to be newtonian whose viscosity is a function of the volume fraction of the particles as shown in equation 3.2.

$$\mathbf{T} = -PI + \eta\mathbf{D} \tag{3.1}$$

$$\text{where,} \qquad \eta = \eta_f(1 + \frac{5}{2}x^p) \tag{3.2}$$

where, η is the viscosity of the suspension, η_f is the viscosity of the medium, x^p is the volume concentration of particles, $\mathbf{T}$ is the stress in the suspension and $\mathbf{D}$ is the deformation rate of the suspension.

One of the initial experimental studies on the viscosity measurement was performed by

Mooney et al. [112]. In this paper, dilute suspensions with spherical particles was studied and the results were observed to be conforming to the theoretical predictions by Einstein though his work didn't focus on particles such as glass or abrasive particles. Another early study on the rheological properties of granular fluids was conducted by Thomas et al. [113]. In this work a study of the viscosity observed through experiments for particle suspensions were conducted for different volume fractions of solids. The data of viscosity was fit using a power series with respect to volume fraction.

In another experimental work by Lewis and Neilsen [114], the rheology of the fluids were reported to be similar to the results of the work by Mooney et. al [112] where the viscosity is modeled as an exponential function of the volume fraction. In a similar experimental work conducted by Krieger [115] this viscosity is modeled as a power-law behavior with respect to the volume fraction. In these early works, the behavior of the dilute granular fluids were modeled as a newtonian fluid though viscosity were modeled with respect to the volume fraction of the particles using different models.

In the later works reported in the literature, shear thinning effects of the granular fluids were also observed, studied and reported. This behavior of the fluids were primarily observed in fluids with higher volume ratio of particles in the medium. These Non-Newtonian behavior of the fluid have been attributed to different behaviors of the particles in the fluid matrix. The factors influencing the behavior include Brownian motion, inertial effects and the volume fraction of the particles moving in the fluid. These effects for a neutrally buoyant steady state flow can been summarized in the literature to study of 3 dimensionless numbers describing the flow, namely Péclet number(Pe), Reynold's number(Re) and the volume fraction of solids in the suspension [116]. Hence, giving the effect as,

$$\frac{\mu}{\mu_0} = f(Pe, Re, \phi) \tag{3.3}$$

where,

$$Pe = \frac{6\pi\mu_0 a^3 \dot{\gamma}}{kT} \tag{3.4}$$

$$Re = \frac{\rho_0 a^2 \dot{\gamma}}{\mu_0} \tag{3.5}$$

where medium properties such as viscosity μ_0, density ρ_0, particle properties such as radius a, thermal energy kT and nominal shear rate $\dot{\gamma}$ affect the final generalized viscosity μ of the suspension.

Here the Péclet number Pe is ratio of the hydrodynamic forces from the medium flowing past the particles and diffusive forces of mixing caused by Brownian motion (thermal energy). Hence, we can observe that low particle size and high thermal energy will decrease the value of Pe in the suspension. Hence, the effect of the Brownian motion is found to be effective for $Pe \leq 10^3$ values[116]. Reynold's number is the ratio of the inertial forces of the particle to the viscous forces by the medium on the particle. Hence, the inertial effects of the particles dominate the viscosity of the suspension when $Re \geq 10^{-3}$. The inertial effects in the fluid seem to result in segregation in some viscometers such as Couette Viscometer and parallel-plate viscometers. Hence, for the cases with higher Pe value (as the size of MR particles $> 1\ \mu m$) and low Re value the fluid flow behavior is dominated by the volume fraction of particles in the slurry.

Mueller et al.[12] in a recent paper conducted a detailed study of the properties of monodisperse particle suspensions. In this study, particles of different aspect ratios and volume fractions were studied to find the flow behavior. This study was limited to only the shear stresses developed by the fluid in a parallel-plate rheometer. Upon study it was concluded that Herschel-Bulkley Model [117] was an excellent model for such suspensions. The fitting parameters or the material constants of the fluid was reported to be varying as per the model of Maron & Pierce [118]. The material parameters seem to

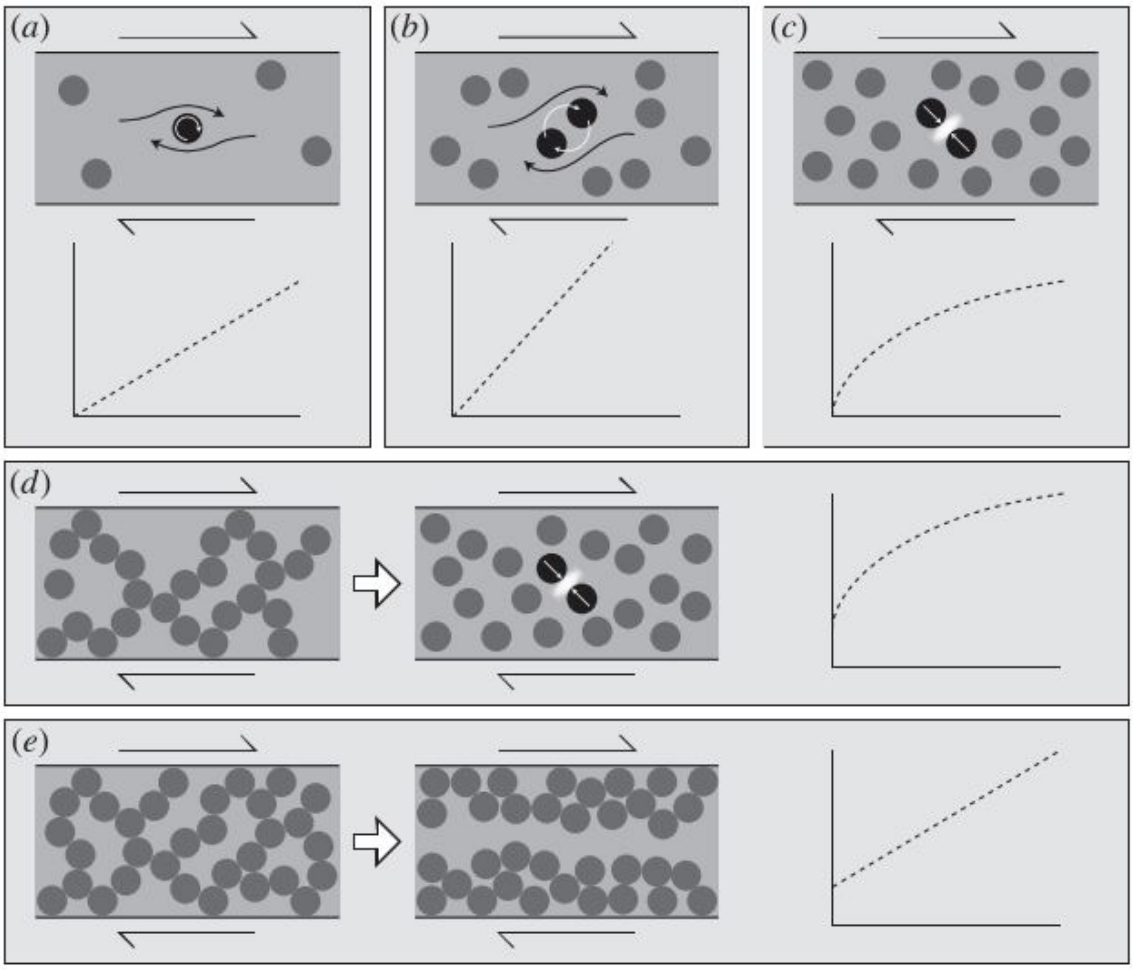

Figure 3.1: Schematic of the fluid flow and rheology at different volume fractions of particles (a) Fluid in a highly dilute suspension. (b) Fluid with low concentration showing increase in viscosity with Newtonian Behavior. (c) Fluid with higher concentration of particles with inter particle interaction showing shear thinning behavior (d) Fluid with much higher concentration of particles showing yield stress behavior at zero shear rate (e) Fluid with very high concentration of particles showing a shear band behavior with a yield stress [12]

vary differently based on the ratio of the volume fraction with the maximum possible volume fraction (ϕ/ϕ_m) for such fluids. For particle suspensions with spherical particles, with $0 \leq \phi/\phi_m \leq 0.35$ Newtonian fluid behavior is reported. For suspensions with $0.35 \leq \phi/\phi_m \leq 0.8$ shear thinning behavior is reported for such fluids. It was also reported that the fluids produced an appreciable yield stress for $\phi/\phi_m \geq 0.8$. The appreciably different behavior of the fluid at these volume ratios of particles in the fluid is due to different mechanisms of flow and particle interactions as shown in 3.1.The shear thinning behavior of the slurry at higher volume fraction of particles is due to the particle-particle interactions at low shear rates which is lost as the shear rates are increased. Most of the research in the literature model slurries as a single continua. Some attempts have also been made to model slurries as a mixture under different boundary conditions. Ravindran et al. [119] also presented a numerical study of slurry flowing down an inclined plane using mixture theory. Johnson et al. [120] solved the flow of slurry in as a mixture between two flat plates. Massoudi [121] presented a mixture model for particulate fluids where the interaction forces between the fluid and solid particles such as, drag, diffusion, slip-shear lift, spin lift, virtual mass and Basset forces were considered.

3.2 Rheology of MR fluids

MR Fluids are particle suspensions which consist of magnetic particles in a non magnetic fluid medium. The most common media used for this purpose are Newtonian Fluids such as oil and water. Due to the presence of magnetic particles in the media the rheology of the fluids can be controlled using magnetic fields. It has been observed generally that the particles tend to align along the magnetic field lines causing an increase in the viscosity of the suspension. This property of the material was first used to invent magnetic clutches, brakes and dampers [122]. Researchers studied the rheological properties of these fluids for these applications.

The experimentation on the MR fluids have been conducted in different modes such as valve mode, shear mode, squeeze mode etc [123]. Experiments in shear mode have been conducted extensively on MR fluids for its applications in clutches, brakes and polishing. These were conducted by modifying commercially available rheometers to suit the purpose. Different type of rheometers which use concentric cylinders [124], Parallel Plates [125] [126] and Cone-Plate [125] geometries have been used to study these fluids. In general it has been observed that these fluids exhibit yield stress behavior. In some cases experiments have also reported shear thinning behavior for the fluid as shown in figure3.2 and 3.3. This behavior of the fluid is highly dependent on the particle concentration and the applied magnetic fields. Note that in figure3.2 exhibited shear thinning in a relatively smaller range of rates this is because of the lower concentration of the particles in fluid. In figure3.3 the shear thinning behavior of the fluid is observed over the whole range of rates which may be due to the higher concentration of particles in the medium.

3.2.1 Modeling of MR Fluids

There have been two types of models developed for MR fluids, continuum and discrete [123]. In continuum models the whole fluid is treated as a continuum and the bulk and surface behavior is modeled whereas in discrete models the behavior of individual particles in the fluid such as particle-particle interaction (mechanical and magnetic) and particle-fluid interaction are modeled[127, 128]. Numerous models have been used to model the MR fluid out of whom Bingham fluid model and Herschel-Bulkley models are most commonly used. A list of the different models used are shown in Table 3.1.

Among the models discussed in most papers the common factor that could be observed is the presence of a yield stress (τ_y) in most. The other constants used in the models seem to vary among the models. It is reported that these parameters depend primarily upon the particle concentration (ϕ) and the magnetic field strength ($\mathbf{H}$) applied on the material[123].

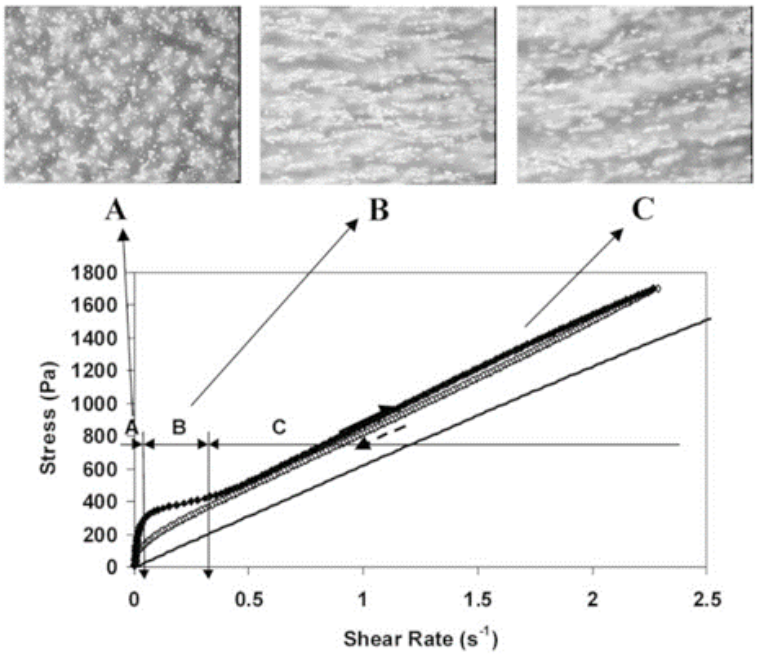

Figure 3.2: shear stress vs. shear rate graph for a MR fluid with 5 % concentration of magnetic particles suspended in silicone oil in the presence of magnetic field compared with the behavior at no magnetic field(continuous line). Note the constant viscosity of the fluid post-yield for the fluid. Pictures of microscopy of the distribution of particles at each rate, A) very low shear rates where a structure is maintained, B) low shear rates where were the structure is broken where shear thinning is observed and C) high shear rates where the viscosity is almost constant

The effect of the Péclet number and Reynolds number have been neglected in all the works as the fluids considered here have particles with sizes of the order of micrometers and bulk velocity of the fluid is maintained low. Since, the magnetic field also plays a role in determining the rheology of the fluids two other dimensionless number namely Mason number (Mn) and lambda (λ) number are also used to characterize the fluid. The equations both these number is given below,

$$Mn = \frac{8\eta_f \dot{\gamma}}{\mu_0 \mu_f \beta^2 H_0^2} \tag{3.6}$$

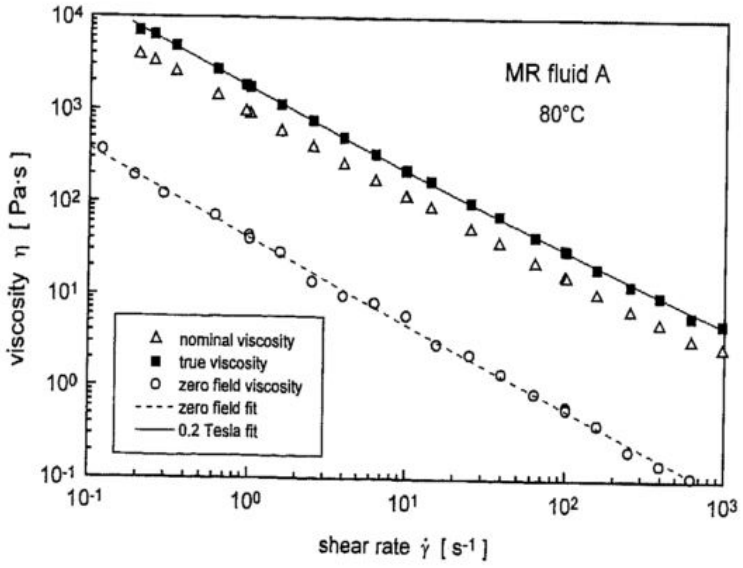

Figure 3.3: Viscosity vs. shear Rate graph for a concentrated MR fluid (55% by weight) in zero magnetic field (unfilled circle) and when 0.2 T magnetic field is applied(filled square). Note that the viscosity continues to drop with increase in shear rates suggesting shear thinning behavior

$$\lambda = 4\pi\mu_0\mu_f\beta^2 a^3 H_0^2 \frac{1}{kT} \tag{3.7}$$

$$\beta = \frac{\mu_p - \mu_f}{\mu_p + 2\mu_f} \tag{3.8}$$

where μ_f, μ_0 and μ_p are the magnetic permeability of the fluid, free space and particle, a is the size of the magnetic particles and H_0 is the applied magnetic field strength, η_f is the viscosity of the medium, $\dot{\gamma}$ is the shear rate, k is the Boltzmann constant and T is the temperature of the fluid.

Here, Mn is the ratio of the viscous forces acting on the particle to the magnetic forces in the fluid and λ is the ratio of the magnetic forces to the diffusive forces (due to thermal energy) in the fluid [129]. Here it has been observed that the secant viscosity ($\eta = \tau/\dot{\gamma}$) is dependent on the Mason number for fluids modeled as Bingham fluids. The relation

Table 3.1: Different models used to model MR fluids in the literature

Rheological Model	Equation
Bingham Fluid	$\tau = \tau_y + \mu\dot{\gamma} \quad \lvert\tau\rvert > \tau_y$
Herschel-Bulkley	$\tau = \tau_y + \mu\dot{\gamma}^n \quad \lvert\tau\rvert > \tau_y$
Casson	$\sqrt{\tau} = \sqrt{\tau_y} + \sqrt{\mu\dot{\gamma}} \quad \lvert\tau\rvert > \tau_y$
Biviscous	$\tau = \begin{cases} \mu_1\dot{\gamma} & \tau \leq \tau_1 \\ \tau_y + \mu\dot{\gamma} & \lvert\tau\rvert > \tau_1 \end{cases}$
Cross	$\tau = (\mu_\infty + \frac{\mu_0 - \mu_\infty}{1+\lambda\dot{\gamma}})\dot{\gamma}$

between the viscosity and the Mason number is given below [123],

$$\frac{\eta}{\eta_\infty} = 1 + (\frac{Mn}{Mn'})^{-1} \tag{3.9}$$

$$Mn' = \frac{C\phi\eta_f}{\eta_\infty} \tag{3.10}$$

Here the relation between the magnetic field and the viscosity is given through the Mason number. It has been generally reported that the shear stress is dependent on the magnetic field as a power law behavior as shown in equation 3.11. Literature by Ramos et al. [130] and Bosis et al. [131] suggest b = 2 for low concentrations but for similar concentrations Claracq et al. [125] and Chin et al. [132] suggest b = 1.5. The value of a varies from 0.5 (Claracq et al. [125]), 1 (Chin et al.[132]) in the literature.

$$\tau_y \propto \phi^a H^b \tag{3.11}$$

Apart from the variation in the viscosity of the material MR fluids at high concentrations have been observed to produce normal stress differences [126]. These effects of the fluid show dependency on the magnetic fields applied on the fluid. The normal force ap-

plied by the fluid on Torsional Plate varies with the applied field in both static and dynamic cases [126]. The dependency of the static normal force (F_N) is reported as follows,

$$F_N \propto |\mathbf{B}|^{2.4} \tag{3.12}$$

where, $|\mathbf{B}|$ is the magnitude of the magnetic field near the sample. The normal stress produced under shear is reported to vary linearly with the magnetic field as shown below [126],

$$N_1 = 7.2|\tau| - 42 \tag{3.13}$$

$$N_2 = 1.8|\tau| - 22 \tag{3.14}$$

where, N_1 and N_2 are the normal stress differences(primary and secondary) and τ is the shear stress experienced by the fluid

These modeling approaches are motivated from the experiments conducted on the flow behavior of the fluids. A mathematical modeling of the MR fluids was provided by Brigadnov and Dorfmann [133] where a complete model for isotropic incompressible MR fluid was suggested as given below,

$$\begin{aligned}\mathbf{T} = -P\mathbf{I} + \alpha_{21}|\mathbf{D}|^{q-1}\mathbf{B}\otimes\mathbf{B} + (\alpha_{30} + \alpha_{32}|B|^2)\mathbf{D} + (\alpha_{31} + \alpha_{33}|B|^2)|\mathbf{D}|^{q-2}\mathbf{D} \\ +(\alpha_{40} + \alpha_{41}|\mathbf{D}|^{q-2})(\mathbf{d}\cdot\mathbf{B}\otimes\mathbf{B} + \mathbf{B}\otimes\mathbf{B}\cdot\mathbf{d})\end{aligned}$$

where $\mathbf{T}$ is stress in the fluid, P is the pressure, $\mathbf{D}$ is the deformation rate tensor, $\mathbf{B}$ is the magnetic field and q is a material parameter along with the coefficients α_{ij} that depend on

temperature. Constraints on the coefficients are given below,

$$\alpha_{30} \geq 0, \alpha_{31} \geq 0, \alpha_{32} \geq 0, \alpha_{33} \geq 0,$$
$$\alpha_{32} + \frac{4}{3}\alpha_{40} \geq 0, \alpha_{33} + \frac{4}{3}\alpha_{41} \geq 0,$$
$$|\alpha_{21}| \leq \sqrt{\frac{3}{2}}[\alpha_{32} + \alpha_{33} + \frac{4}{3}(\alpha_{40} + \alpha_{41})]$$

As seen above, most of the models thus developed assume the MR fluid to be a single continua. Such an approach is not applicable to MR polishing fluids where the particle segregation under a magnetic field is a critical aspect of the behavior. In this regard, the approach we seek to follow is more akin to the mixture theory model for electro-rheologcial fluids of Rajagopal and Ruzika [134]. Here, the solid particles were assumed to be a continuum phase along with the carrier fluid as another phase.

Molecular Dynamics models have been used to develop models for segregation [135] and brush formations in MR fluids. Here the individual magnetic and abrasive particles are modeled as spheres moving in a fluid medium. Such models have been successful in modeling the chain formation of the particles and their behavior in shear flow [136]. But, these models are highly computationally expensive for modelling behaviors of fluid in macro-scale domains.

3.3 Conclusions

Most of the rheology experiments in the literature are restricted to the study of non-magnetic slurries which give a very detailed idea on the characteristics based on the particle concentration and parameters. There exists extensive literature on the rheology of MR fluids but most have been restricted to only magnetic particles with no non magnetic particles in the slurry. Moreover, there is a huge variation in the models and constants reported in the experiment may be due to different additives being added to the fluid. The literature

is very few on rheological characterization of MR polishing fluids especially discussing on the dependence of the parameters on the magnetic fields. Moreover, work needs to be performed to find the normal and shear stresses developed by the fluid upon shear on a workpiece.

The fluid has been confined inside the test cell for most experiments on concentrated granular media. But, in all these cases the fluid has been assumed to be slipping with respect to the confining wall. These assumptions would produce in consistencies in the experimentation of the bulk properties and especially the properties of the contact shear forces.

In all the research conducted in the literature it has been observed the dependence of the material constants are modeled as some power or polynomial function of the applied magnetic field. But, the magnetic forces on both the magnetic and non-magnetic particles are functions of the gradient of the magnetic fields too. The dependence of these quantities on the gradient also needs to be studied for effective simulation of the fluid behavior in the presence of the fields.

4. OBJECTIVES AND SCOPE

4.1 Objectives

The primary objective of this dissertation is to study the rheological characteristics of polishing fluids. In the literature on polishing fluids and granular media we generally find that the models were assumed apriori by the investigator while studying the properties of polishing media and MR fluids. In rheology experiments, it is observed that the fluid geometry and the boundary conditions are idealized to analytically compute the torque vs. speed (moving boundary) relationship while computing the constitutive model parameters. While simulating the behavior of magnetorheological polishing fluids, segregation and coupling of the magnetic fields with particle distribution are neglected, assuming the fields acting on the fluid. The research in this dissertation aims to study and fill these gaps in our knowledge in this field.

Thus, in this dissertation we pursue the following research objectives.

- Study the relative merits (model complexity, goodness of fit, etc) of different constitutive models for characterizing the rheology of polishing fluids.
- Study the effect of the reduction of the fluid geometry in the rheometer for analytical data fitting thorough numerical simulation.
- Model the segregation of magnetorheological polishing fluid using mixture theory.
- Study the effects of coupling the magnetic fields with the segregation process.
- Study the effect of shear flow on the segregated structure of the mixture.

4.2 Scope

In this dissertation, we study the rheology and the effect of magnetic fields on magnetorheological polishing fluids. The experiments on the polishing fluids have been conducted using a torsional rheometer at steady shear rates. The MR polishing fluid is modeled as a mixture of continua to study the segregation of the fluid. Two-dimensional simulations of the polishing fluids under different conditions are studied in this dissertation.

4.3 Structure of the Dissertation

The dissertation has been structured as follows,

- Chapter 1, 2 and 3 introduces the research topic with literature survey on different polishing methods, their mechanism, slurry rheology and rheology of magnetorheological fluids and magnetorheological polishing fluids.
- Chapter 4 discusses the objective and scope of this dissertation
- Chapter 5 discusses the design and development of the torsional rheometer used for studying polishing fluids
- Chapter 6 discusses on mixed experimental-CFD-data science approach to rheological measurement
- Chapter 7 discusses the development of a mixture theory model for simulating magnetorheological polishing fluids.
- Chapter 8 discusses the simulations performed using the mixture theory model.
- Chapter 9 concludes the dissertation with final remarks and future research directions.

5. TORSIONAL RHEOMETER

5.1 Design of the Torsional Rheometer

A rheometer is a experimental setup where the flow properties of a fluid is studied by inducing flow in the fluid and studying the forces developed by the fluid at a certain flow rate. The most commonly used rheometers include rotational rheometers , capillary viscometers and falling-ball rheometers, etc. In rotational rheometers the fluid sample is subjected to shear through the rotation of the contact surfaces and the resistance torque to the rotation is measured. Examples of rotational rheometers include cup and bob viscometers, parallel plate viscometer, cone-plate viscometer, couette type viscometer, orthogonal rheometer, etc. In capillary viscometers the fluid is flowed through a capillary or pipe using pressure or gravity and the resulting flow rate or velocity profile is measured to study the fluid. And in falling-ball rheometers the motion of a heavy ball enclosed in a fluid due to gravity is studied to evaluate the properties of the flow.

Among rotational rheometers, Couette-type viscometer where the fluid is contained between two coaxial cylinders and one of them is rotated to shear the fluid is quite popular to study viscous fluids. Another popular viscometer used for studying rheology is parallel-plate viscometer whose schematic is given in Fig 5.1. As shown in the figure, in these viscometers the fluid is contained between two parallel plates and is subjected to shear by rotating one of the plates relative to the other plate. As a result of this relative motion between the plates in the viscometer the fluid here is also subjected to simple shear. But, the relative speed between the surfaces of the viscometer varies linearly with respect to the distance from the axis of rotation of the plates. This variation of the relative speed and the constant height of the fluid results in a linearly varying shear rate in this type of viscometer with respect to the radius. Hence, the Torque sensed at either ends of the plates

is the cumulative torque from the fluid. There are 2 types of experimental modes used in these types of viscometers namely, Controlled Stress Experiments and Controlled Rate Experiments [137]. In controlled stress experiments the total torque sensed at the plate is maintained to be constant through a sensor based control loop by changing the speed of the plate while recording the sample data. Whereas in controlled rate experiments the shear rate on the fluid is maintained as constant while collecting the sample data. The mode of flow used by these viscometers are also known as Torsional Flow [138].

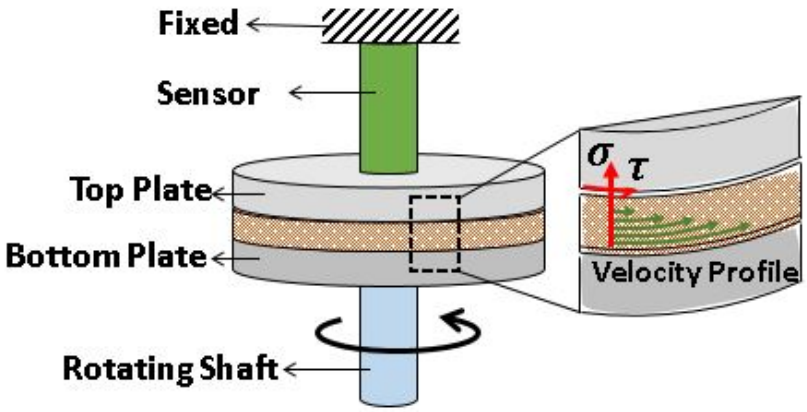

Figure 5.1: The schematic of a parallel plate viscometer showing the velocity profile and the stresses developed in the fluid. Observe that since the bottom plate is rotating the relative speed would vary with respect to the distance from the axis of rotation

Parallel plate viscometers are preferred in comparison to Couette type ones as (a)these viscometers are more versatile by being able to conduct experiments are different thicknesses of fluid [137], (b) the normal load developed by the non-newtonian fluids under shear due to normal stress differences in the fluid can also be easily studied in these types of rheometers and, (c) In case of rheology studies of magnetorheological fluids, magnetic

fields can be easily applied perpendicular to the shearing surfaces which is similar to polishing. As a result, this type of viscometer is suitable for studying polymer fluids, particle suspensions and MR fluids.

For the study of concentrated particle suspensions, the design of the parallel-plate viscometer needs to be altered with an addition of a wall around the fluid sample contained for the study. This confinement helps in holding the fluid in contact with the Top plate during the shearing of the fluid. Through this the rheometer would subject the fluid to a torsional flow and in practice have the wall also contribute to the flow induced in the setup.

5.1.1 Description of the Rheometer

For the experimental investigations a parallel plate rheometer has been developed by modifying a orthogonal rheometer to be run in the torsional mode. This orthogonal rheometer was provided by Dr. Rajagopal for conducting studies on polishing media. The schematic of the experimental setup is shown in Fig 5.2. Fig 5.3 is the photograph of the Torsional Rheometer. The setup can divided into sensing, actuating and test cell units. Controlled rate experiments are conducted in the rheometer by maintaining the shear rate using the motor actuating unit.

The setup consists of two sensing units, for measuring the torque developed by the fluid and the rate of rotations.The torque sensor, connected to the Top Plate is made up of a thin hollow cylinder onto which a strain gauge full bridge is attached. The cylinder deforms due to the torque applied at the Top Plate. This shear deformation is measured using the strain gauge bridge. The signals developed by the strain gauge bridge is calibrated using predetermined torques on the sensor. The details of the design and calibration of the sensor is given sections 5.2 and 5.3. The speed sensor in the setup consists of a encoded markings attached to the rotating shaft. These markings are read using a IR emitter-sensor for calculating the rotational speed of the shaft or the bottom cup. Details of the design of

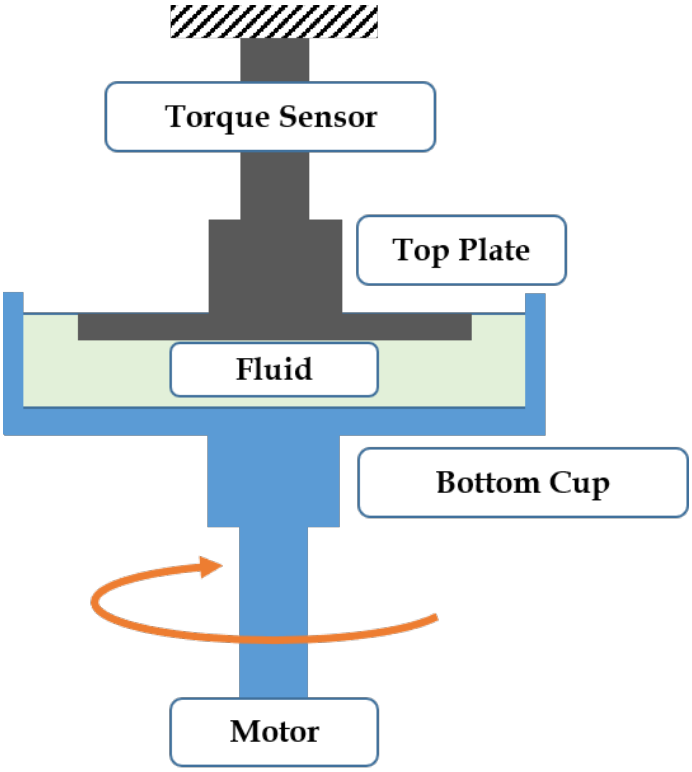

Figure 5.2: Schematic of the Torsional Rheometer. The components of the test cell are shown in detail with the abrasive sheets stuck on the contacting surfaces of the fluid.

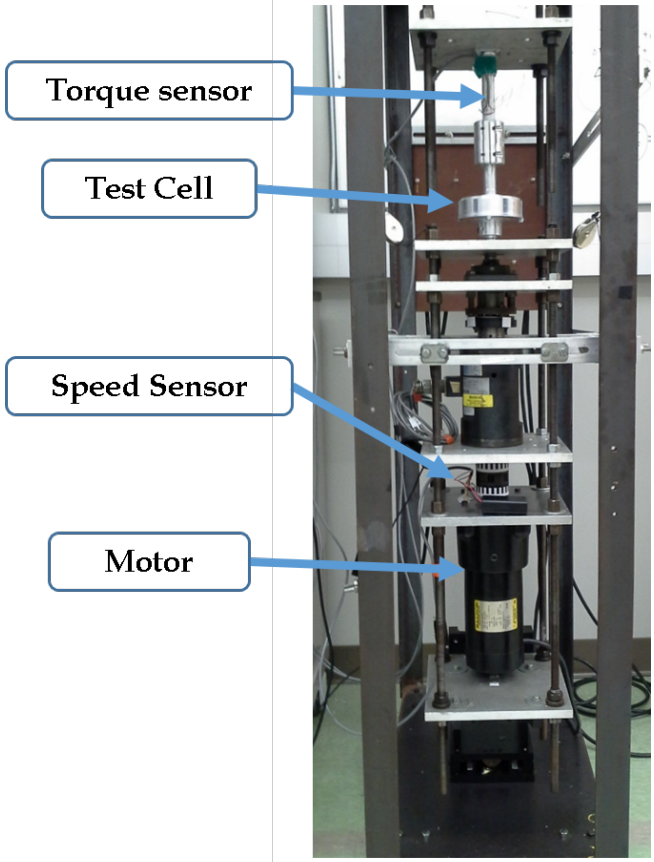

Figure 5.3: Test Equipment for Torsional Testing of Particle Suspensions

the speed sensor is given in section 5.4.

5.1.1.1 Test Cell

The setup includes a test cell, with a Top Plate and a Bottom Cup, where the fluid is contained during the experiment. In the test cell, the Top Plate is fixed to setup and the bottom cup is rotated during the experiment. As shown in the schematic in Fig 5.2, the torque developed due to traction forces at the surface in contact with Top Plate is measured by using the Torque Sensor. The bottom cup is rotated to cause the shear and the rotational speed is measured using a speed sensor. In the test cell the Top Plate and the Bottom Cup

are connected co-axially. The fluid filled in the cup and is brought in contact with the Top Plate by lifting the cup to meet the Top Plate. The excess fluid overflown above the Top Plate is removed and the test is conducted by rotating the bottom cup of the setup. In this form of setup, the height of the fluid in the chamber is set to be constant during the experiment. Hence, these experiments belong to the Constant Volume type of experiments. Here the sand papers of grit size same as the particles in the fluid are attached to the Top Plate, Bottom Cup and the walls of the Test Cell to ensure that a no-slip boundary at the contact surfaces and uniformity of surface behavior at all the boundaries. This helps us in assuming No-Slip conditions at the boundary of the fluid while fitting rheological models.

5.2 Design of the Torque Sensor: Structural and Circuit

The Torque Sensor used in this setup is based on the concept of adding a flexible torsional unit to the Top Plate that could produce considerable strains under the torque. Schematic of the torque sensor is shown in Fig 5.5. The sensor mainly consists of the flexible unit which is a hollow cylinder that produces considerable strains(easily detectable using a strain gauge) at the required range of torques, a rigid support at an end and a rigid connection for the Top Plate of the Test Chamber. The cylinder is designed with a thickness such that for the intended torque range the stresses in the cylinder is within the elastic limits of the material. As shown in the Fig 5.5, two half bridge strain gauges are attached on opposite sides of the curved face of the flexible cylinder. The gauges forming the bridge are positioned at an angle of +45°and -45°with respect to the axis of the cylinder. This full bridge is connected to a signal conditioner which applies a excitation voltage of $5\ V$ to the bridge. The signal produced by the sensor due to the applied torque of the order of mV. Hence, it is filtered and amplified by the conditioner. The conditioned signal is recorded using a Data Acquisition System.

The detailed circuit diagram of the full bridge sensor is shown in Fig 5.4. This config-

uration helps the bridge to read only the shear component of the strains with respect to the frame of reference along the axis of the cylinder. This is because the strains both along and perpendicular to the axis shall produce equal longitudinal strains in the half bridges due to symmetry and this would result in no change in potential across the signal terminals in Fig 5.4. But, the simple shear component of the stress in the cylinder shall result in a equal tension and compression stresses along the + 45 °and -45 °directions of the gauges. The difference in the axial strains thus produced is detected by the circuit. Hence, this sensor unit is able to measure the torque applied along the axis of the cylinder while remaining insensitive to the axial strains along the axis which includes the bending and axial loads. The raw signal thus produced from the torque sensor is recorded for future analysis.

This analysis and design is only a theoretical approach to the development of a good design for the sensor unit. Though the signal to torque correlation can be developed using this analysis, the relation may not be accurate due as this is sensitive to small errors that can occur in pasting the strain gauges and at the connections of the sensors. Hence, a detailed calibration of the sensor for torsional loads have been conducted to find the relation.

5.3 Calibration for Torque Load

A calibration experiment of a Torque sensor is done by recording the signals generated by known torques applied on the sensor. The signals, thus observed, is then modeled (in this case linearly) with respect to the torques to establish the relationship and the accuracy of the sensor is computed using the signals from repeated cycles of experiments.

As discussed earlier though the relation between the signal voltage and the torque applied can be calculated theoretically, the values thus computed may not be accurate enough due to discrepancies in the development of the sensor, measurement of the dimensions etc. Hence, a more accurate estimation of the relation between the signals and the Torque applied could be generated directly through calibration experiments.

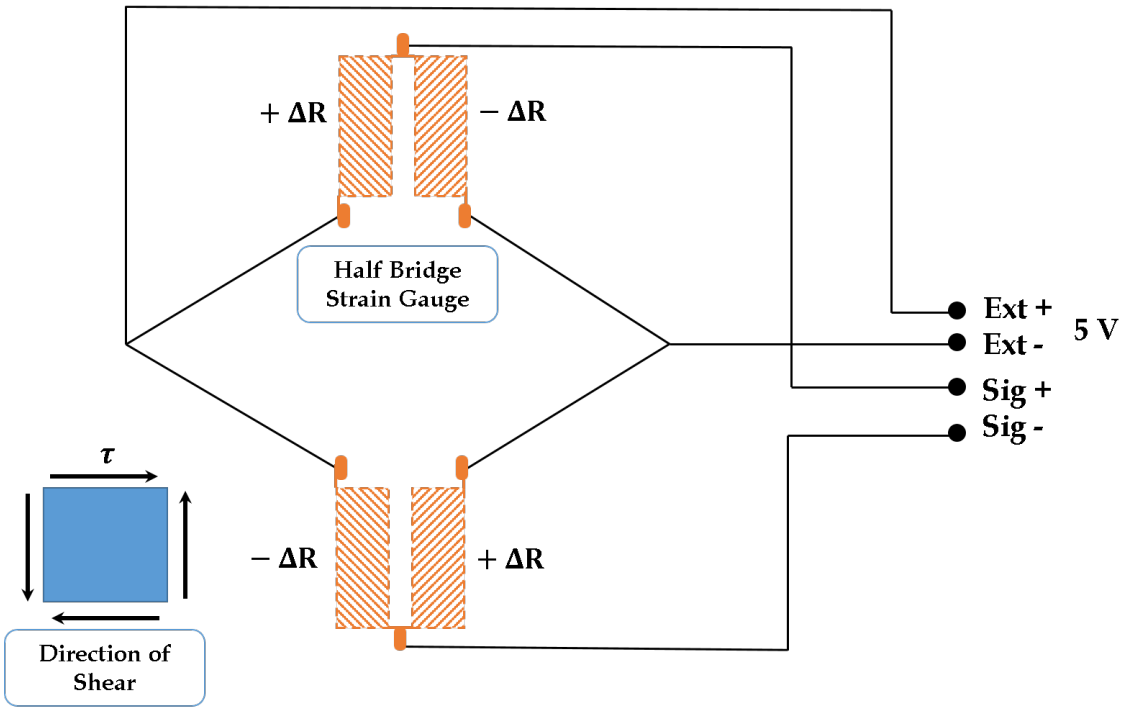

Figure 5.4: Basic Circuit Diagram for the Full Bridge of the Strain Gauges attached to the sensor. The resultant signal voltage is hence compensated for the temperature effects and the signal voltage ($\Delta V \propto \tau$)

5.3.1 Calibration Methodology

Calibration of the Torque sensor is performed by applying a known torque to the sensor with the help of calibration weights. The schematic of the Torque calibration setup is given in Fig 5.6. It consists of two strings attached and passed around a circular disk connected to the sensor that is connected to loading pans. The pulleys help in redirecting the vertical pulling force of the weights to horizontal forces. The forces generated in the strings form a couple as shown in Fig 5.6. The torque (T_{sen}) generated by these forces on the torque sensor are given below,

$$T_{sen} = mgd \tag{5.1}$$

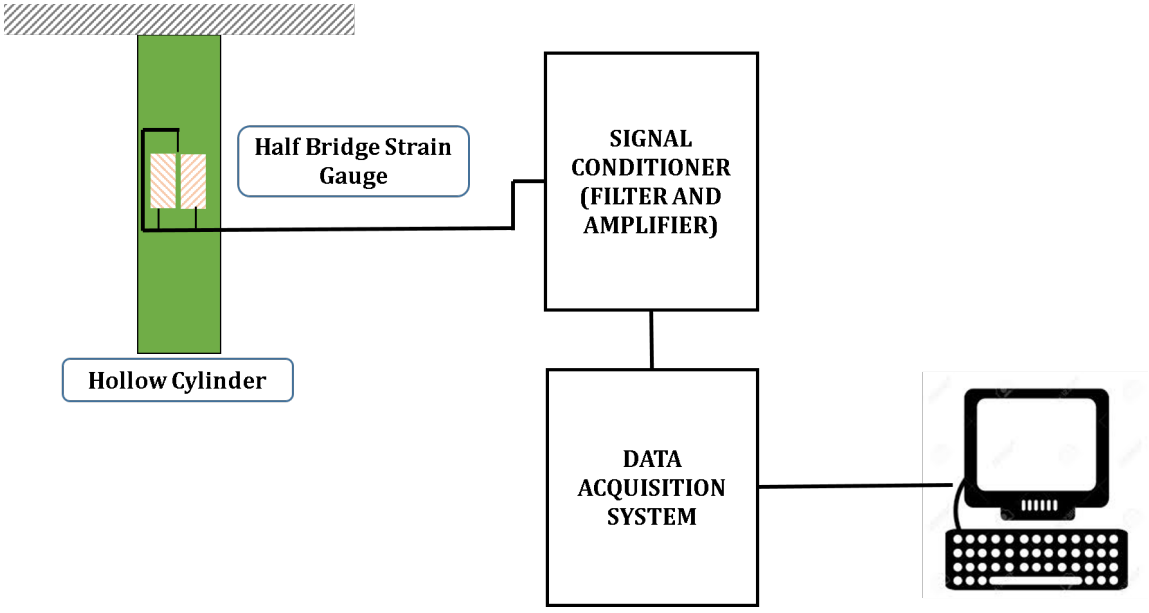

Figure 5.5: Schematic of the Torque Sensor with the Half Bridge which has two strain gauges that are oriented at 45°and -45°to the horizontal

where, m is the mass on each loading pan, g is gravitational acceleration and d is the diameter of the disk attached to the sensor.

It is to be noted that for each load setting equal masses added on each pan of the setup. The signals generated by the sensor and the mass added to the pans are recorded for the correlation which is discussed in the next section.

5.3.2 Results from the calibration experiment

The results from the calibration experiment conducted on the torque sensor is shown in Fig 5.7. The tests shown include two cycles of loading and unloading curves for loads of upto $1\ kg$ on each side. Each signal voltage is calculated by taking the average of last 2 minutes of data collected from a 3 minute data-set for each load. The model is constructed using both the unloading curves of the data is shown in the figure. The value of linear constants of the model and the accuracy of the calibration curve is calculated based on the

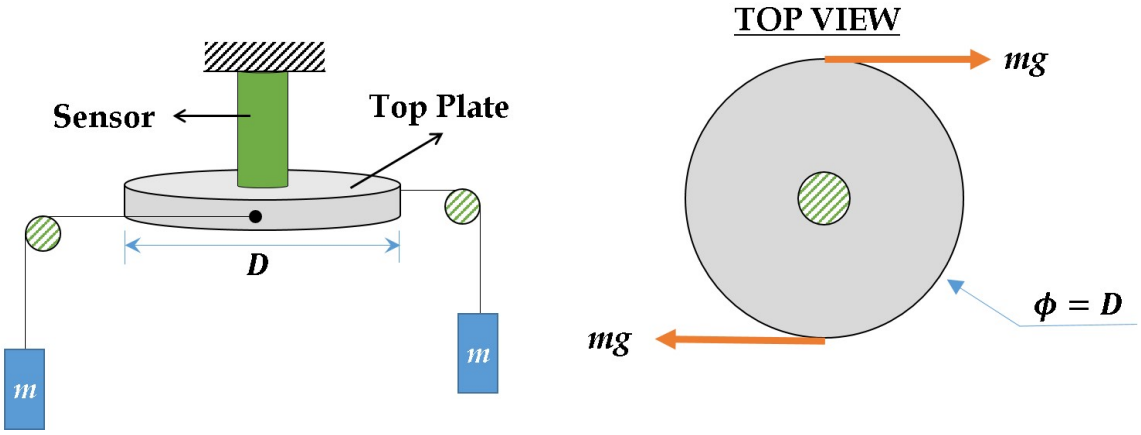

Figure 5.6: Schematic of the setup used to Calibrate the Torque Sensor. The weights on both the sides are maintained the same for the application of equal loads.

same procedure suggested by ASTM standard for Pressure sensors[139]. The final model relating the torque with the signals generated is given below,

$$T_{sen} = 0.823V_{sen} + 0.0041 \quad \text{Nm} \tag{5.2}$$

where T_{sensor} is the torque applied on the Top Plate and V_{sen} is the signal voltage in volts (V).

The accuracy in linearity for the calibration curve is $\pm 6.8\%$. The repeatability accuracy in the sensor is $\pm 1.11\%$. The Hysteresis accuracy of the sensor is observed to be lowest which is about $\pm 9.45\%$. Hence, the final accuracy of the sensor is about $\pm 9.45\%$. This accuracy in a rheometer for granular media is quite good as it has been observed in the literature that the signals recorded during the experiment on granular media vary by close to $\pm 10\%$ during experimentation.

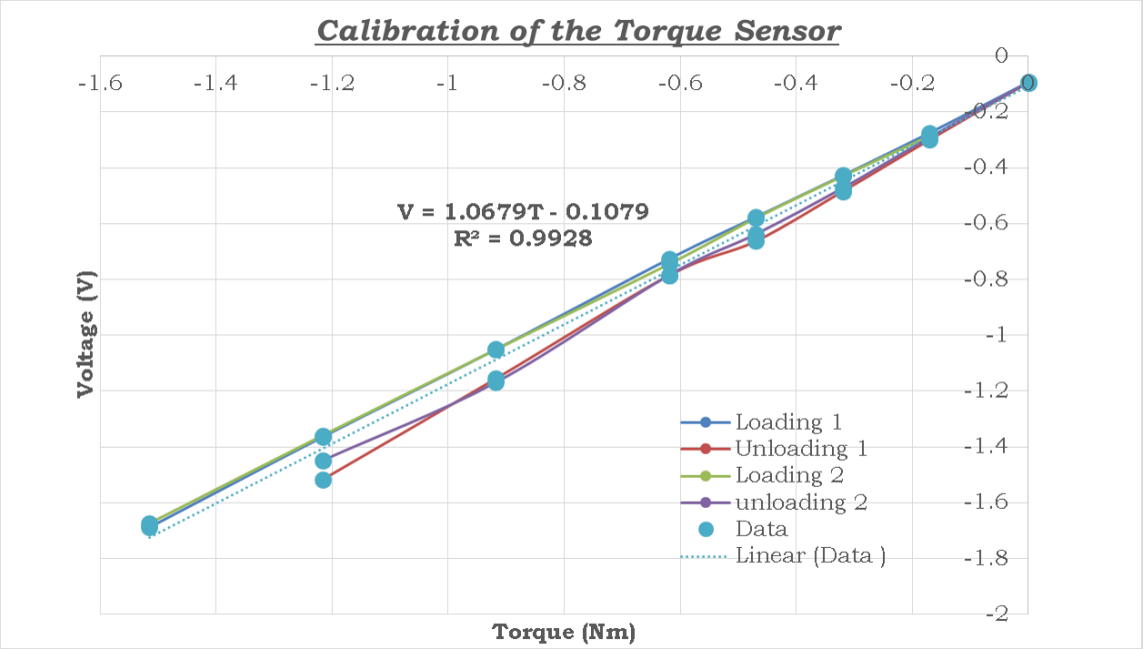

Figure 5.7: Calibration curve of Torque Sensor for the application of known torque loads.A linear model of V_{sen} vs. T_{sen} is developed for the sensor

5.4 Design of the Speed Sensor: Structural and Circuit

Since, the equipment is a controlled rate rheometer the shear rate is maintained constant throughout the collection of a signal at a single setting. And this rate of rotation of the cup is needed to be recorded for finding the material parameters. This in our case is done by finding the speed of rotations of the shaft connecting the motor to the cup using a speed sensor as shown in Fig 5.2.

The sensor for this was developed using the same idea as that is popularly used to design rotary encoder where detection of equally spaced markers of known spacing is used to calculate the speed of rotating shafts.

5.4.1 Design of the Sensor

The basic design of the sensor includes two units, a marker unit pasted to the shaft and a sensing unit connected to the ground. During the operation of the sensor the marker unit rotates along with the shaft. The sensing unit consists of an IR emitter and sensor. The marker unit has 20 black and 20 white markers of equal length placed alternatively to cover the circumference of the shaft. Hence, each marker exactly covers $\pi/20$ rotation of the shaft. The infrared rays emitted by the emitter is reflected by the marker before being sensed by the sensor which produces a voltage proportional to the intensity of the rays received. Since, different markers have different reflectivity to the rays this can be used to distinguish between the markers. During the operation the voltage produced by the voltage is recorded along with the time-stamp from the computer of that record.

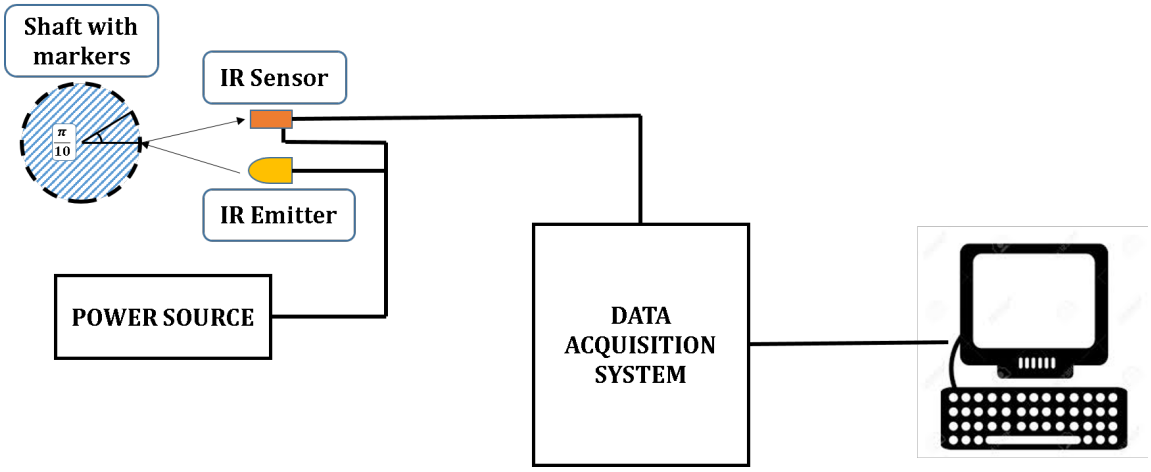

Figure 5.8: Schematic of the Speed sensor used to measure the speed of the bottom cup.

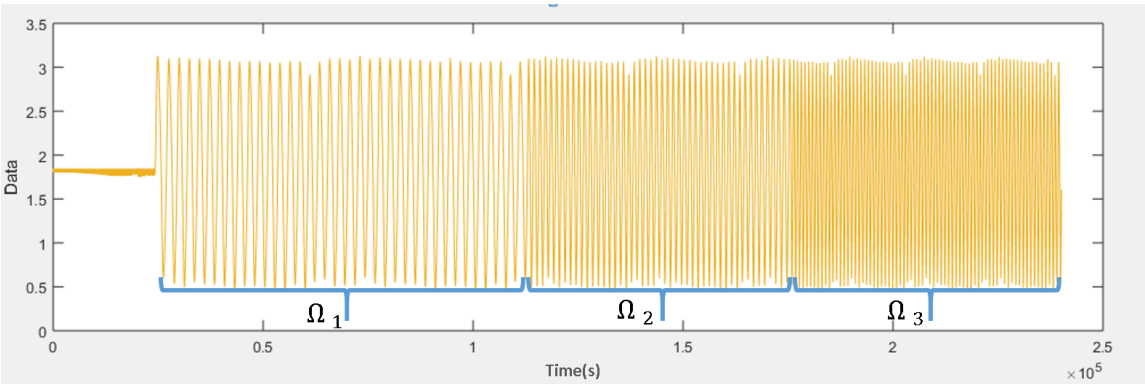

Figure 5.9: Raw Data collected for 3 different shaft speeds over time. The peaks of these signals are found the time difference between them is used to find the shaft speed.

5.4.2 Calculation of Speed from the Data

A sample raw data from the sensor is shown in Fig 5.9. From this data for each setting the time stamps associated with each peaks of the signal is calculated which are the time points of white markers being detected. Since, two adjacent white markers are at an angle of $\pi/10$ the speed of rotation (Ω) is calculated as shown below,

$$\Omega(\frac{t_i + t_{i+1}}{2}) = \frac{\pi}{10(t_{i+1} - t_i)} \quad \underline{rad/s} = \frac{3}{(t_{i+1} - t_i)} \quad \underline{RPM} \tag{5.3}$$

where t_i and t_{i+1} are timestamps of adjacent markers detected in seconds(s).

Since the result is a direct calculation of the speed there is no need for calculation though this method was independently verified by calculating the rotational speed by taking the video of the markers.

5.5 Conclusions

In this chapter, the development of a torsional rheometer has been described. The torsional rheometer was modified from an Orthogonal rheometer used to study granular

fluids. The rheometer was modified by adding a torque sensor and an encoder to collect the torque and speed data from the equipment. The sensors were calibrated to check for repeatability and reliability of signals. This equipment was used do conduct the experiments discussed in chapter 6.

6. MIXED EXPERIMENTAL-CFD-DATA SCIENCE APPROACH FOR RHEOLOGICAL MEASUREMENT[1]

6.1 Abstract

We discuss a novel means for obtaining rheological properties of polishing slurries by combining statistical inference techniques (the Akaike Information Criterion), CFD and Torque vs Speed Data. The data was obtained by using a custom built torsional rheometer that subjects the polishing fluid to conditions that are similar to polishing. Our comparison indicates that side wall and inertial effects significantly affect the values of the parameters of any given model even under nominally slow rates of rotation. When these are considered, the Herschel-Bulkley model seems to be a significantly better fit compared to two other popular other models for the slurry. The results suggest that a systematic combination of computational-statistical-data science approach is necessary for identifying model parameters even for a slow flows as compared to currently used data reduction methods based on analytical solutions for torsional flow that ignore inertial and side-wall effects.

6.2 Introduction

Polishing is one of the important tasks in the manufacturing industry while finishing components for assembly. This helps us in controlling the roughness of surfaces of a product. Reduction in the roughness of surfaces reduces the friction generated at these locations from sliding. Sometimes a certain degree of roughness is needed for the optimum functionality of the component such as medical implants [23, 140]. We are interested in polishing processes that employ an abrasive fluid composed of suspended abrasive parti-

[1]Reproduced with permission from Naveen Thomas, Arun R. Srinivasa, and Satish TS Bukkapatnam. "A mixed experimental-CFD-data science approach for rheological measurement of polishing fluids." Mechanics of Advanced Materials and Structures 27.13 (2020): 1167-1177. Copyright[2020] by Taylor and Francis

cles in a fluid medium to accomplish the polishing of the surface. The types of fluid media used with abrasives include oil or water based media used in chemical-mechanical polishing [141], Magneto-Rheological polishing [142] and dilatant media for abrasive flow polishing [143]. The rheology of the fluid medium, which is a mixture of the base fluid with fine scale particles, governs the motion of the fluid over the surface under a specified condition, and hence the polishing output in these techniques [144]. The rheology of such fluids is of interest of study in the thesis. In particular we will compare the rheological parameters for polishing fluids obtained from torsional rheometer data using analytical methods with approaches using CFD simulations.

Early experiments on solid suspensions were conducted on dilute suspensions with spherical particles like glass beads [145]. Typically, these experiments to study particulate suspensions employed different types of geometries of test cells and of relative motion, such as torsional mode [12], and pipe flows [146]. Testing particulate media especially for fluids with high concentration of particles require confinement of the sample to ensure consistency in the contact of the fluid with the surfaces and repeatibility in test results [147, 148]. Initially, the rheology of such fluids were earlier modeled as newtonian with viscosity dependent on volume fraction of particles [112]. [114] and [115] modeled this variation in viscosity as a power law function of the volume-fraction of particles. More recently, Non-newtonian models have been developed for fluids with high concentration of particles in the fluid [149]. The most common models that are employed are the Bingham fluid model, power law model and the Herschel-Bulkley model which are listed in Table 6.2. In the works that model the slurry as an effective fluid medium, the choice of the model for the behavior of the fluid is made before the analysis of the fluid and only the final parameters found using a fit for the models to the data is reported. The approach is also to idealize the geometry of the setup and the flow of the fluid such as neglecting, (a) the side wall effects in some setups and (b) the inertial effects from the fluid flow

to achieve a analytical solution to the flow problem [150]. This method of approach to experimentation of the fluid is being re-examined in this thesis.

Estimation of material parameters of non-linear solids such as tissues and polymeric materials through simulations are thoroughly discussed in the literature. [151] have provided an overview of some of these approaches. For example, the data on the displacement field collected using full field techniques such as Digital Image Correlation (DIC) is used in tandem with Finite Element Model Updating Method (FEMU) or Virtual Fields Method (VFM) to estimate the properties. In FEMU, the residuals of the measured forces with modeled forces is used to estimate the parameters through updating the finite element model. [152] uses Akaike Information Criteria (AIC) along with goodness of fit criteria in the study of myocardial tissues to rank and select appropriate models. But, here the AIC values rather than Akaike weights are used for ranking and selection of model. [153] in a recent paper has used AIC for model reduction from a large parameter model for myocardial tissue but has used ratios of AIC rather than Akaike weights to determine the reduced model. But as shown in Eq. 6.3, AIC has mixed units whose differences have can predict the likelihood for a model [154] whereas ratios as used by [153] do not have consistent units.

In contrast to these efforts, in the field of rheology, systematic model selection is has been rarely used in the experiments of rheological properties [155]. [156] recently provided a Bayesian inference approach to quantitatively select the number of modes for a multimode Maxwell model for non-Newtonian fluids. [157] have compared the coefficient of determination (R^2) and AIC in predicting computed rheological models for non-Newtonian fluids. The estimation of the material parameters in the models are conducted using a analytical approach to fit the data.

In this chapter, we show that the application of simulation based updating along with an information criteria based model selection, for constitutive parameter estimation of non-

linear materials gives significantly different results than the analytical approaches considered above. This is because, the boundary effects (which are neglected in the analytical approaches) have significant influence with non-traditional fluid geometries.

In the approach used here, a polishing slurry is subjected to torsional flow similar to its actual use in polishing and the torque versus speed characteristics are recorded. Then three different fluid models are considered and the parameters are determined by analytical methods. We then develop a special technique (based on the Nelder-Mead minimization technique [158]) to obtain parameters by using Computational Fluid Dynamics (CFD) simulation. The two methods are compared to show that there is a discrepancy between the parameters that are obtained. Furthermore, we compare the three models by using the AIC for both the Analytical and the CFD approaches and show that the results as to the most appropriate model choice may be different.

This chapter has been organized into the following sections, (a) section 6.3 describes the experimental procedure for the torsional experiments, (b) section 6.4 discusses the model class used to fit the data, (d) section 6.5 describes the different approaches of analysis used to compute the parameters and the method of comparison used for model selection, (e) section 6.6 discusses the results obtained from the analysis and (f) section 6.7 concludes about the findings from the experiments and the analysis techniques.

6.3 Experimental Procedure

6.3.1 Testing Materials

The materials used in the experiments are polishing fluids, made-up of abrasive particles mixed in a Newtonian medium. This solid suspension here consists of silicon carbide (SiC) abrasive particles (800G grit size) obtained from Panadyne Abrasives mixed with mineral oil that was procured from AniMed. The details of the quantity of ingredients used in preparing the fluids for experimentation is given below in Table 6.1. Viscosity

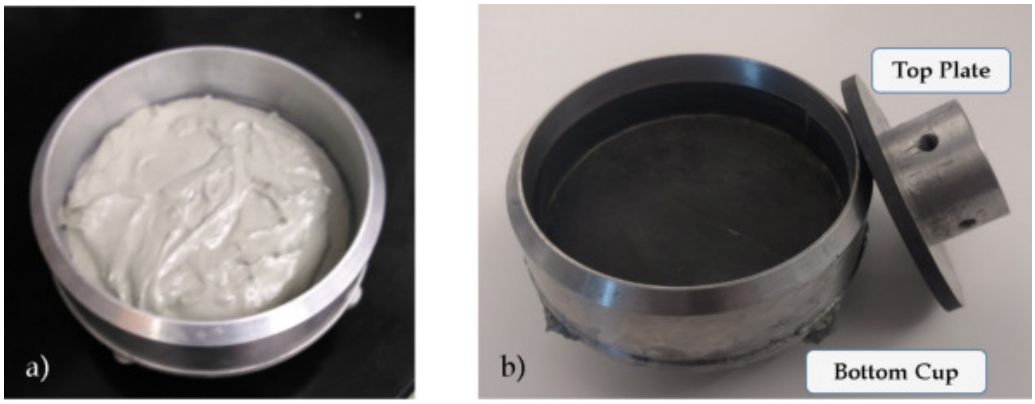

Figure 6.1: a) Particle suspension used for the experimentation. Note that the fluid doesn't form a flat top surface unlike mineral oil which is indicates the yield stress behavior of the suspension. b) Test Cell used to contain the fluid for the experimentation. Note that the surfaces in contact with the fluid is glued with sandpaper of the same grit size

of the mineral oil used is 77.18 ± 15.82 *mPas*. The final fluid sample is made by adding the abrasives in small quantities while stirring the fluid to ensure that there is no clumps formed while mixing.

Ingredient	**Density (g/cc)**	**Weight Ratio**	**Volume Ratio**
Mineral Oil	0.823	0.34	0.63
SiC	3.21	0.66	0.37

Table 6.1: Details of the Materials used in preparing the particulate fluid

The concentration of particles used in the sample is sufficient to change the characteristics of the fluid from a newtonian fluid to slurry. The final suspension is observed to not settle to a flat surface, rather retains a texture as shown in Fig 6.1a, thus indicating that there might be a yield stress behavior exhibited by the fluid. The high particle concentration also ensures very low sedimentation during the preparation and experimentation of the fluid giving consistent results upon repeated testing.

6.3.2 Torsional Rheometer

The rheological study of solid suspension is conducted in a torsional rheometer shown in Fig 6.2a. The schematic of the rheometer and the parts is shown in Fig 6.2b. It is designed to contain the fluid in a test cell, which consists of a top plate and a bottom cup, and shear it by rotating the cup at a steady rate. The torque applied by the shearing fluid on the top plate is sensed and used to characterize its properties.

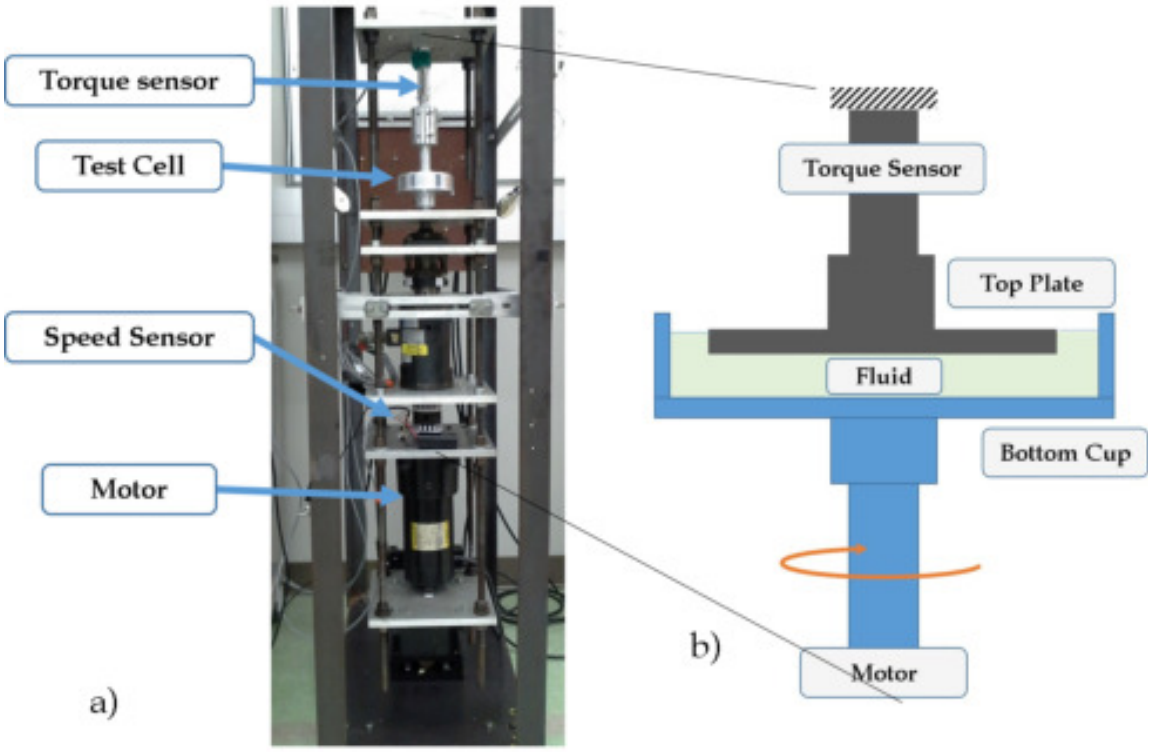

Figure 6.2: The Test Setup used to conduct rheological experiments on polishing fluids. a) Torsional rheometer during the experiment. b) Schematic of the rheometer assembly with the top plate and bottom cup with the fluid.

The test cell bottom cup is of 3.5 *in* diameter and has a wall to ensure that the fluid

is contained in the cell through-out the experiment. The top plate is of diameter of 3 *in* which ensures a gap of 0.25 *in* with the wall which is higher than the test heights for the experiments.The surfaces that come in contact with the granular fluid, in the top plate and bottom cup, are prepared by gluing sandpaper of the same grit size (800G) as the particles [147]. Fig 6.1b shows the prepared test cell that is used to conduct experiments. After adding the fluid into the test cell, the cup is connected to the motor and the top plate is connected to the torque sensor as shown in Fig 6.2.

The speed of the cup shearing the fluid, and the torque experienced at the top plate due to the fluid is measured using sensors that were built in-house. The speed is measured in between the motor and the cup and the torque sensor is connected to the top plate keeping it stationary. The speed sensor, as shown in Fig 6.3, can be divided into 2 units, a marker unit attached to the shaft of the motor and a sensing unit connected to the computer. The marker unit, designed based on rotary encoder design, consists of alternating black and white markers glued to the shaft. The sensing unit consists of an infra-red emitter and sensor which is connected to the data acquisition system and the computer. Since a total of 20 markers have been used to cover the circumference of the shaft, the time interval between sensing successive markers is be used to calculate the angular velocity of the shaft for an angle of $\frac{\pi}{10}$.

The torque experienced at the top plate of test cell is measured by a custom-built torque sensor, which consists of a thin hollow cylinder that twists considerably under the required torque range. The schematic of the Torque sensor built is shown in Fig 6.3. It consists of a hollow cylinder through which the torque at the top plate acts. The strain developed in the cylinder is sensed by a full bridge strain gauge sensor that is glued to the surface of the cylinder. The signal thus observed is conditioned and used to compute the torque experienced by the top plate due to the fluid. The torque sensor is calibrated using a predetermined torque applied using weights and recording the signals from the sensor.

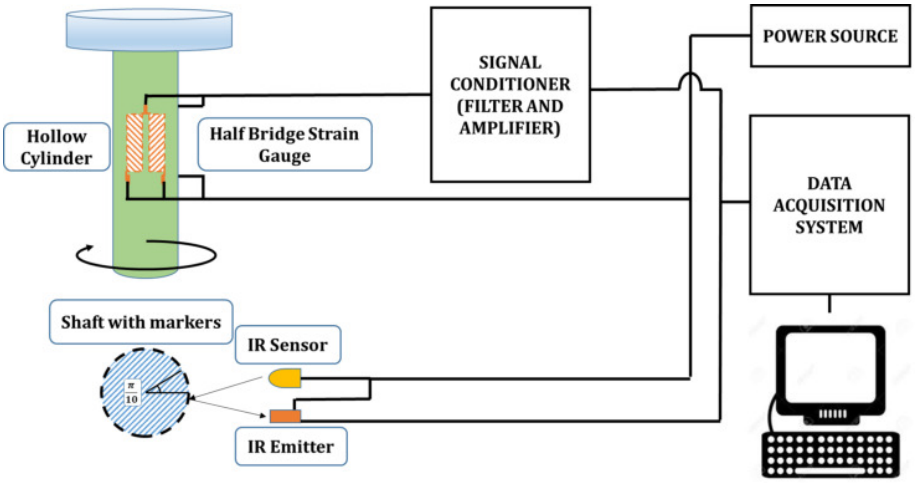

Figure 6.3: Schematic of both the torque and speed sensor in the setup. The torque sensor includes 2 half bridge strain gauges glued on diametrically opposite locations on the cylinder (only one half bridge is visible). The signal produced is conditions and amplified before acquisition. The markers on the shaft (cross-section) is read using an infra-red emitter and sensor to calculate the speed of the shaft.

The calibration experiments on the sensor indicate a calibration curve, $M = (0.8237V + 0.0041)$ *Nm* relating the torque (M) to the signal voltage (V).

6.3.3 Experimental Testing

The prepared suspension sample is added to the bottom cup. Since the particle concentration is high, this fluid doesn't easily flow forming a shape as shown in Fig 6.1a. Hence, care must be taken while bringing the top plate in contact with the fluid to not trap any air between the fluid and the surface. This is done by shaping the fluid to ensure no air is trapped, moving the cup slowly to meet the plate and by preshearing the fluid at different stages to remove the air bubbles trapped at contact. The final configuration is tested for trapped air, by checking the trend of the torque signal at a steady shear rate.

The fluid thus in contact with the test cell, is presheared for 20 *min* before conducting the actual experiment by spinning the cup at 1 *RPM* [12]. This is done to remove any initial orientation of the particles in the cup. Consistent torques are observed once the

sample is presheared before the experiment. The data for the speed and torques at different speeds are collected and evaluated to study the characteristics of fluid. In this thesis, the experimental results of only one concentration of particles is used to conduct experiments at three different heights of fluid to study the effect of experimental procedure on the calculation material properties of the fluid. At each height, controlled rate experiments were run at each setting for 180 s and the data of the last 120 s were used to calculate the torque and the speed values.

6.4 Modeling of the Flow Properties

There are a many models to choose from to model the flow of particulate suspensions, namely power law model [146], Bingham model [115], Herschel-Bulkley model [12], Casson model [146], etc. For the purpose of modeling the fluid, we have chosen a model that is pure a shear thinning fluid (power law model) and compared it with a model that has a yield stress but no shear thinning (Bingham model) and finally a model that has both yield stress and shear thinning behavior (Herschel–Bulkley model) in the set of models to be used to model the fluid. The constitutive equations for these models chosen to model the behavior obtained in the raw data have been given in Table 6.2. The best model parameters for each of these models are thus calculated using the analytical approach as well as a CFD based approach (described in section 6.5). The performance of these model parameters obtained is compared by using AIC to select the best model to describe the rheological behavior of the polishing media (described in section 6.4.1).

6.4.1 Model Selection Using Akaike Information Criterion

The goal of any constitutive model is to express the information in the fluid behavior in a compact form. The choice of an appropriate model is more of an art than science as it is difficult to identify the true model that expresses the behavior just from the raw data that includes noise from data collection. The classical approach in least squares fitting method

Model	Constitutive Equation
Power-Law	$\boldsymbol{\tau} = k\dot{\gamma}^{n-1}\mathbf{D}$
Bingham fluid	$\mathbf{D} = (1 - \frac{min(\tau_0, \|\|\boldsymbol{\tau}\|\|)}{\|\|\boldsymbol{\tau}\|\|})\frac{\boldsymbol{\tau}}{\mu}$
Herschel-Bulkley	$\dot{\gamma}^{n-1}\mathbf{D} = (1 - \frac{min(\tau_0, \|\|\boldsymbol{\tau}\|\|)}{\|\|\boldsymbol{\tau}\|\|})\frac{\boldsymbol{\tau}}{k}$ where, $\boldsymbol{\tau} = dev(\mathbf{T})$

Table 6.2: Models used for Modeling the flow properties of the solid suspension, where $\mathbf{T}$ is the stress, p the pressure, $\mathbf{D}$ is the shear rate in the fluid and $\dot{\gamma}$ being the magnitude of $\mathbf{D}$ ($\dot{\gamma} = \sqrt{\mathbf{D} : \mathbf{D}}$) with τ_0, k and n being material parameters in these different models.

is to study the goodness of fit for the data for this choice. But, this approach has a tendency to over-fit the the data. This is not a good approach as the model would be affected by the noise in the data collection.

In Information theory the information lost in choosing a particular model is quantified using the Kullback-Liebler distance (K-L distance). The K-L distance between the conceptual truth f and model g is defined for continuous function as the integral in Eq. 6.1 [154].

$$I(f, g) = \int f(x) ln(\frac{f(x)}{g(x|\theta)} dx \tag{6.1}$$

where $f(x)$ and $g(x)$ are the probability distributions the conceptual truth and the model, and θ is the parameters in the model. Akaike showed that the critical quantity for measure for model selection is the relative K-L distance for each of the models. This is used to develop the Akaike Information Criterion [159] given below,

$$AIC = -2ln(\mathcal{L}(\theta)) + 2d \tag{6.2}$$

where, $\mathcal{L}(\theta)$ is the likelihood function for parameters (θ) and d is the degrees of freedom in the model. AIC introduces a 'principle of parsimony' to the choice of model using $2d$ as a bias in the calculation. Hence, a model that minimizes this criterion is chosen to be an appropriate model that fits the data judiciously. Since we use use least squares (LS) fitting in this thesis, a corrected form of AIC, shown in Eq.6.3, which includes the effect of smaller sample set is considered for the criterion.

$$AIC_c = 2n_d\, ln(\hat{\sigma}) + 2d\frac{n_d}{n_d - d - 1} \tag{6.3}$$

where

$$\hat{\sigma}^2 = \frac{\sum \hat{\epsilon}^2}{n_d} \tag{6.4}$$

and AIC_c is the corrected AIC, $\hat{\sigma}^2$ is the maximum likelihood estimate of the variance, $\hat{\epsilon}$ is the estimated residuals for a particular model with respect to the data, n_d is the number of samples. In LS fitting, d is the total number of estimated regression parameters including the variance. Once the AIC_c values are estimated, the model with the minimum value is chosen for calculating the likelihood for each model, i, and subsequently the Akaike weights using the Eq.s 6.5 and 6.6 given below,

$$\hat{\mathcal{L}}(g_i) = exp(-\frac{1}{2}(AIC_{c,i} - min(AIC_{c,i}))) \tag{6.5}$$

$$w_i = \frac{\hat{\mathcal{L}}(g_i)}{\sum_j \hat{\mathcal{L}}(g_j)} \tag{6.6}$$

These weights are used to rank the models and select an appropriate model for the media. It should also be noted that the models can also be averaged to develop new models if we achieve significant weights for 2 or more models in this estimation.

Another criterion popularly used in the literature for model selection is Bayesian Information Criterion (BIC) developed by [160]. This information criterion used in this method is given below,

$$BIC = 2n_d \, ln(\hat{\sigma}) + 2d \, ln(n_d) \tag{6.7}$$

In this method the BIC estimated using Eq. 6.7 is used in a similar manner to develop weights and subsequently select appropriate models for estimation. This criterion is not suggested for using in estimation of rheological models for the following reasons,

(a) BIC in the development of the criterion, assumes a global set of modeling parameters from which different nested models can be created to estimate the behavior [160]. This model is referred to as the true model whose estimation is the goal of the criterion. This assumption is not appropriate here as there are no true rheological model that exists for any fluid. Moreover, we do not have a global set of parameters in rheological models from which nested models could be created for estimation as the parameters in a rheological model are not causative rather are coefficients of an equation used to fit the sample data.

(b) The primary difference in the criteria shown in Eq.s 6.3 and 6.7 are the weights used for the bias in the estimation. The weight in AIC_c is high for lower number of samples which tends to 1 as more samples are considered whereas the weight in BIC is low for smaller number of samples which tends to infinity for more samples. This means that BIC tends to under-fit or mistrust the data for higher number of samples to avoid false positives. This is not true for rheological studies as more experiments with repeatability conducted on the same material generally improves our trust on the raw data collected in the experiments[161].

6.5 Approaches to Analysis

Two different approaches to computation of the material parameters have been employed in this study. One is the traditional approach that uses an analytical expression developed for the torque experienced at the top plate for each model and other where CFD simulations are used to compute the same. In both the cases, the material parameters are computed by using the same objective function to fit the models. In the analytical approach the objective function is minimized using Least Squares fit whereas in the CFD simulation a direct search algorithm is used.

6.5.1 Objective Function

The material parameters for each model is computed through minimization of an objective function. The objective function $E(m_1, m_2, m_3)$, for a combination of parameters in a model, is calculated as a weighted L2 norm of the difference in the torques with the experimental results which is shown in Eq. 6.8.

$$E(m_1, m_2, m_3) = \sum_{i=1}^{p} W_i (M_e(\omega_i) - M_m(\omega_i, m_1, m_2, m_3))^2 \tag{6.8}$$

where, i corresponds to different data points in the experiment, W_i is the weight for each data point, ω_i is the rotational speed of the bottom cup, $M_e(\omega_i)$ is the experimental Torques observed at the speed of ω_i and $M_m(\omega_i, m_1, m_2, m_3)$ is the torque calculated for the same speed and material parameters m_1, m_2 and m_3.

The minimization of this objective function is used to find the solution for the material parameters for the models. Weighted average of the squared error is used to highlight the degree of importance that we give the data points collected at every speed setting. In this study, the weights for the data collected at zero speed is taken as zero, whereas the weights

for the other speed settings are taken as one. This is because of the huge variation of the average data that is observed at this speed of the cup. The variation of the average data for other speed settings, as shown in Fig 6.5, is within the range of variance in these individual data making it more reliable. The different material parameters for the models are given in Table 6.3.

Model	m_1	m_2	m_3
Power law	k	n	-
Bingham fluid	τ_0	μ	-
Herschel-Bulkley	τ_0	k	n

Table 6.3: The material parameters m_1, m_2 and m_3 for the models described in Eq. 6.8.

6.5.2 Analytical Approach

The analytical solutions for the torques developed at the top plate for different models are given in Table 6.4. The torques developed by these models in a CFD based analysis is computed using the simulation software and cannot be represented as a expression as given in the Table. In all the cases, the least squares objective function defined in Eq. 6.8 is used for optimization and compared to find best fit model and parameters that can be used to judge the behavior of the fluid.

6.5.3 CFD Simulation

A simulation of the test cell is created in Star CCM+ for the analysis of the fluid modeled with different models. Fig 6.4 shows the axisymmetric model for the fluid with a thickness of 0.121 *in* . The model created using the 'Axisymmetric Swirl Model' in StarCCM+ to study the torsional flow of the fluid. This model is discretized with a quadrilateral mesh. All the boundary conditions of the walls are set to no slip condition as we

Model	Torque (Analytical Solution)
Power law	$M = \frac{2\pi R^3 k(\omega R)^n}{(n+3)h^n}$
Bingham fluid	$M = \frac{2\pi R^3 \tau_0}{3} + \frac{2\pi R^4 \mu\omega}{4h}$
Herschel-Bulkley	$M = \frac{2\pi R^3 \tau_0}{3} + \frac{2\pi R^3 k(\omega R)^n}{(n+3)h^n}$

Table 6.4: Analytical Solution for the Torques developed at the Top Plate of the test setup during a Torsional Experiment for different models where, M is the torque, ω is the rotational speed of the cup, R is the Radius of the Top Plate and h is the height of the fluid in the setup.

assume at all the boundaries except air. The top plate and its wall shown in Fig 6.4 is maintained as stationary and the bottom cup and the wall set to rotate at the given angular speed for the analysis. The residual limits for convergence is chosen to be 10^{-8} for the momentum in all directions. The torque experienced by the top plate and the top plate wall is computed and reported by the simulation in every step. A grid independence study was conducted by taking a sample geometry of height 0.7 *in* the simulation and by assuming a coarse mesh to start with. In each iteration the base size was halved and the reported torque, for a rotation rate of 5 *RPM* was plotted the find that a mesh with 10,976 cells gives a grid independent output for the torque. This base size was used in the meshes of other heights for uniformity and grid independence.

Furthermore, we have verified the CFD simulations by conducting simulations mimicking the absence of the side wall by imposing the condition of no shear stress on the side walls. We observed that the Torque obtained by the CFD solution is identical to that obtained by the analytical means.

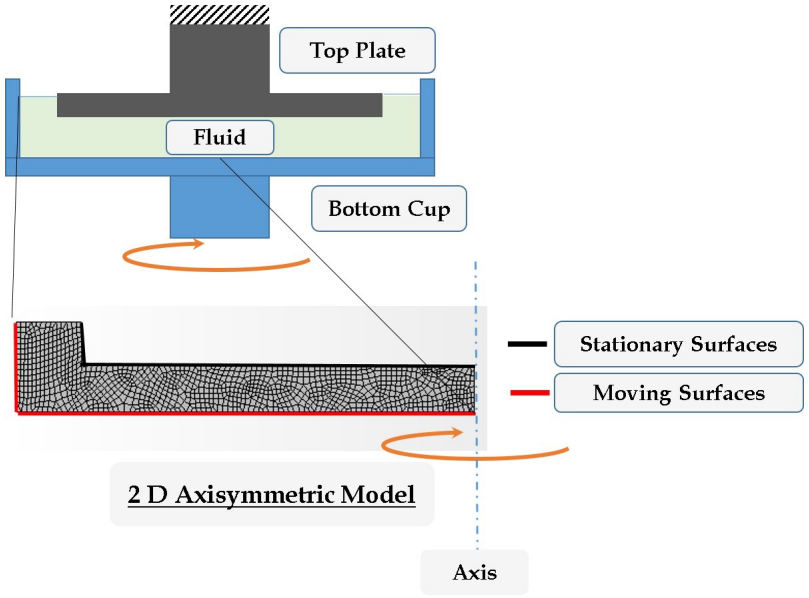

Figure 6.4: The schematic of the test setup with the 'Axisymmetric 2D model mesh' used for analysis of the fluid. The boundaries of the fluid with the cup is set to moving at the required rotational speed and the boundaries with the top plate is set stationary. The torque is calculated from the wall stresses at the top plate.

6.5.4 Direct Search Algorithm for finding the Properties

In order to compute the parameters from the experimental data using the simulation models, any direct search algorithms could be adopted. Nelder-Mead optimization method [158] has been used here to compute the parameters, since this is known to be a robust method that does not require gradient of the cost function to be computed (which is very very expensive for the CFD simulation). This method is coded into a macro in the simulation software for conducting analysis at different speeds of the cup and compute the parameters that give a minimum for the objective function.

The Nelder-Mead Optimization method uses a simplex of different points and its evaluated objective function to optimize and find the minima of the function. This method uses the value at these points to estimate the next best point in the step. In every step, the

point with the highest error gets replaced by a better point in the parameter space leading to the solution.

Direct search algorithms are quite relevant to these problems as the simulations can be used to only find the torque values for different parameters and the gradient with respect to the parameters is unknown to the user. Since it is a heuristic method to find the solution, the time taken to estimate the solution parameters for the problem will depend on the initial simplex assumed, the model for fluid behavior and the complexity of the simulation used to evaluate the torque values. In this study, the initial simplex for the problem with q number of parameters is taken by taking the set of parameters computed from the analytical approach and reducing just one parameter by 30 % to get new points, thus forming a simplex of $(q + 1)$ number of points in the parameter space.

Termination of the optimization is usually done using conditions such as a limit to the size of the simplex, improvement observed in every step, etc. For this problem, the iterations for a solution is terminated when the difference in the parameters are less than 2% of the value. The parameter set with the lowest objective function is chosen among the points in the simplex. The solution to the optimization problem is observed to achieve within 25-30 steps for each data-set of experiment.

6.6 Results and Discussion

6.6.1 Experimental Results

Experiments were conducted by shearing fluids of different heights (0.167 *in*, 0.126 *in* and 0.077 *in*) in the test cell. The raw data from the experiments conducted at a height of 0.126 *in* is given in Fig 6.5. These heights were chosen as much higher than the particle size ($> 100d_p$) to observe the bulk property of the fluid. The tests were conducted on only one concentration of the fluid as the study is to compare the outcome of different strategies of computation of material parameters. The consistency of prediction of these models for

all the heights of the experiments are used for the comparison.

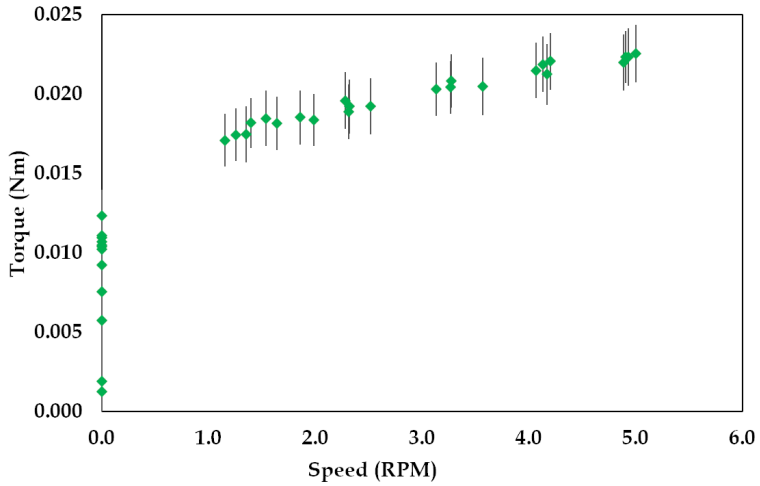

Figure 6.5: Torque vs. rotational speed data collected from the experiments at a height of 0.126 *in* which shows a typical data-set for the fluid. Note that the torque is observed at zero shear. The data for speed starts at 1 *RPM* as the motor cannot sustain lower speeds for shearing. The bars show the 95% confidence interval of the data observed at each speed.The average of the data clearly indicate a trend in the behavior of the fluid.

6.6.2 Comparison of Results for Analytical and CFD based Approach

The data obtained is fit with the three models using the objective function given in Eq. 6.8 for each height. The average of the parameters obtained for the heights is used to describe the final model in all the approaches. It is understood that the average values of the properties do not describe the average behavior of the material [162].

However our method is consistent with a Bayesian approach to parameter estimation wherein the probability distribution for the parameters is obtained from different runs and averages of the *parameters* are used to create an averaged model.

Moreover, philosophically, if the inferred “model parameters" vary with the geometry of the sample it is clear the the confidence in the model should be low (as seen from

a Bayesian perspective). For this reason, we have computed the model parameters for different heights so as to study their variations with height. The models with averaged parameters are only used to compare using the AIC_C criterion.

The values of the parameters obtained for the power law model using both the analytical and CFD simulation is given in Table 6.5. Here in both the cases, we observe that the parameters for the fluid do not vary significantly with different heights. On the other hand, we see that the inferred model parameters for the Bingham Plastic model(Table 5) varies significantly with the height . Though the consistency of the results reflect confidence in the model, the comparison of the results with other models in terms of the of the information lost in the fit will provide a quantiative judgement of the model. .

Height (*in*)	**Analytical Solution**		**CFD based Method**	
	k (*Pas*)	n	k (*Pas*)	n
0.167	135.0	0.189	88.7	0.183
0.126	139.5	0.167	92.5	0.183
0.077	127.0	0.179	88.8	0.180
Average	133.8	0.178	90.0	0.182

Table 6.5: Comparison of results of the parameters for power law model (k,n) between the Analytical and CFD based approaches of analysis

The values of the material parameters for the Bingham fluid model is given in Table 6.6. From the model parameters we can observe that the value of both the yield shear stress and the viscosity of the fluid vary from one experiment to another for the samples. Even though the values of yield shear stress (τ_0) of the fluid, considered in this model, are consistent the values of viscosity (μ) vary close to 50% between the experiments at

0.167 *in* to 0.077 *in* heights. This effect would generally indicate that the Bingham fluid model is not suitable for the fluid. This can be easily observed in the analytical approach by manipulating the equation for torque given in Table 6.8 to the equation below,

$$\tau_r = \tau_0 + \frac{3\mu}{4}\dot{\gamma} \tag{6.9}$$

where,

$$\tau_r = \frac{3M}{2\pi R^3}, \tag{6.10}$$

$$\dot{\gamma} = \frac{\omega R}{h} \tag{6.11}$$

where, τ_r is the reduced shear stress and $\dot{\gamma}$ is the apparent shear rate in the fluid. Note that, this gives only a reduced form of the data and is not directly related to the model. The data thus reduced using Eq. 6.9 is plotted and shown in Fig 6.6. This evaluation helps in judging that Bingham fluid model is not appropriate while using analytical approach as the trend is not described by the model.

But, such an illustration is not possible for a simulation based fitting of the model in the raw data. AIC based approach (discussed in section 6.6.3) to compare the models will address this disadvantage of the CFD based approach and give a more quantitative approach to the decision.

Height (*in*)	**Analytical Solution**		**CFD based Method**	
	τ_0 (*Pa*)	μ (*Pas*)	τ_0 (*Pa*)	μ (*Pas*)
0.167	121	14.3	82	7.7
0.126	131	11.3	92	6.2
0.077	131	7.1	92	4.8
Average	127.7	10.9	88.7	6.2

Table 6.6: Comparison of results for the Bingham fluid model (τ_0,μ)

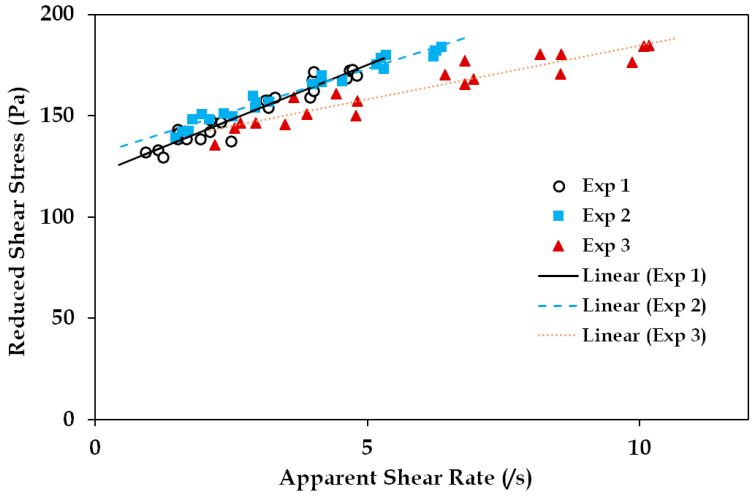

Figure 6.6: Reduced shear stress vs shear rate for the fluid built for analytical study of the properties. Note that the slopes of the data for different heights vary even though the data is quite close to each other.

For Herschel-Bulkley model, the objective function is observed to be not sensitive to the change in yield stress in the model when evaluated through curve-fitting. This results

in a huge variation in the parameters obtained from individual experiments. But, the value of the objective function for these values indicate a very good fit to ignore the model on this basis. Moreover, the value of torque data at zero shear indicate towards a yield stress behavior. Hence, the value of the yield stress is chosen from the torques observed at zero speed in the setup. The yield stress is computed to be the mode of zero shear torques observed in the experiments. The frequency distribution of the zero shear torques are given in Fig 6.7. The yield stress can be calculated from the expression for the zero shear torque for a given yield stress. Equation 6.12 is used to find the yield stress for the analytical approach.

$$\tau_{0an} = \frac{3T_{mod}}{2\pi R^3} \tag{6.12}$$

where, τ_{0an} is the yield shear stress for analytical solution, T_{mod} is the mode torque observed from the zero shear data in the experiments. The mode torque (T_{mod}) was observed to be 0.01125 *Nm* and the yield stress (τ_{0an}) to be 91.7 *Pa*.

For the CFD model, the yield stress cannot be computed directly from an expression as an analytical form doesn't exist. The stress is thus computed by running the CFD analysis for a trial low speed ($\approx 10^{-4}$ *RPM*) for a chosen yield stress for the model and finding the torque at the speed. The yield stress and torque thus computed is used to calculate the yield stress for the model as shown in Eq. 6.13 below.

$$\tau_{0cfd} = \frac{\tau_{0tr}}{T_{tr}} T_{mod} \tag{6.13}$$

where τ_{0cfd} is the yield stress for the Herschel-Bulkley Model for CFD calculations, τ_{0tr}

is the trial yield stress used in the low speed simulation, T_{tr} is the trial Torque computed for the top plate and T_{mod} is the mode of the zero shear torque data observed in the experiments. Using Eq. 6.13, the yield stress (τ_0) is obtained as 65.5 *Pa*. The material parameters, k and n calculated using this yield stress are given in Table 6.7. In the Tables 6.5, 6.6 and 6.7 we can observe that the parameters τ_0 and k estimated using both the approaches vary by 50% to 80%. This effect can be directly attributed to the side wall and inertial effects that are ignored in the analytical approach.

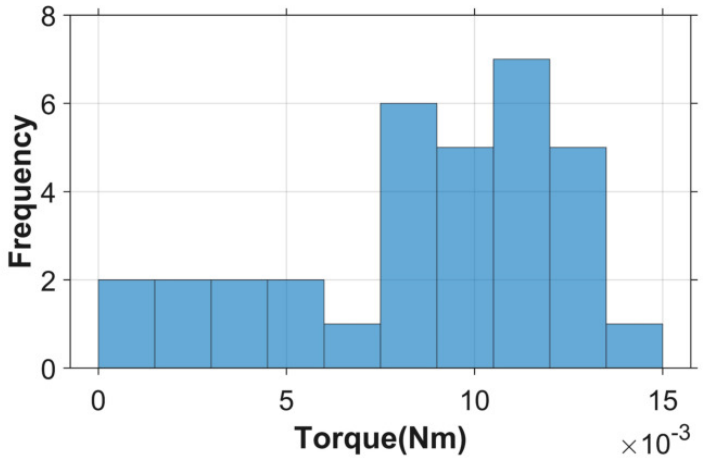

Figure 6.7: The frequency distribution of the zero shear data for all the experiments.

Height (*in*)	**Analytical Solution**			**CFD based Method**		
	τ_0 (*Pa*)	k (*Pas*)	n	τ_0 (*Pa*)	k (*Pas*)	n
0.167	91.7	42.79	0.47	65.5	20.91	0.55
0.126	91.7	48.44	0.40	65.5	26.29	0.46
0.077	91.7	45.86	0.33	65.5	24.63	0.44
Average	91.7	45.69	0.40	65.5	23.94	0.48

Table 6.7: Comparison of results for Herschel-Bulkley Fluid model (τ_0, k,n)

6.6.3 Comparison of the Models

Tables 6.8 and 6.9, list the comparison of the models for both the approaches of modeling the fluid behavior. The list includes the standard deviation, AIC_c values, Likelihood and the Akaike weights for the models. For the Herschel-Bulkley model the degrees of freedom is chosen to be 4 even though it is fixed before fitting as it is a parameter changing which will affect the fit of the model. Here, we can observe that the deviation is lowest for power law model in the analytical approach and Herschel-Bulkley in the CFD based approach. The Akaike weights, given in Table 6.8, quantify the relative probability of each model in comparison. The analytical approach indicates that the power law model accurately predicts the behavior of the fluid where as, CFD based approach gives that the Herschel-Bulkley model performs best ($w_i = 0.991$) in comparison with the other models in comparison. This suggests that the Herschel-Bulkley model performs better at describing the fluid even though it is more complex. In both the approaches the Bingham fluid model performs very poorly. The quantitative approach here gives a clear indication that even for CFD based approach Bingham model is not suitable for the model, similar to the comparison of data as shown in Fig 6.6 indicated the same for analytical approach. AIC

also provides with an opportunity to compare the results among both the approaches together which give the results given in Table 6.10. This indicates that the Herschel-Bulkley model in CFD approach is the most likely model with a weight of 99.1 %. The final standard deviation of the model estimation using a CFD based Herschel-Bulkley model is 8.24×10^{-4} *Nm*. The final model fit to the Torque data is shown in Fig 6.8. The comparison of the models in both the approaches also indicate that the analytical approach since it ignores the side wall and inertial effects models the fluid behavior poorly resulting in a very poor fit. This can be observed in the standard deviation of the data about the model as well.

Model	**Power law**	**Bingham fluid**	**Herschel-Bulkley**
$\hat{\sigma}$ (*Nm*)	8.08×10^{-4}	1.17×10^{-3}	8.20×10^{-4}
d	3	3	4
AIC_c	-962.28	-912.06	-958.06
$AIC_c - min(AIC_c)$	0	50.22	4.22
L(model)	1	1.24×10^{-11}	0.12
Akaike Weights (w_i)	**0.892**	$\mathbf{9.2 \times 10^{-12}}$	**0.108**

Table 6.8: Comparison of the different models in predicting behavior of the fluid using analytical solutions.

Model	**Power law**	**Bingham fluid**	**Herschel-Bulkley**
$\hat{\sigma}$ (*Nm*)	7.09×10^{-4}	1.09×10^{-3}	6.51×10^{-4}
d	3	3	4
AIC_c	-980.0	-921.7	-989.51
$AIC_c - min(AIC_c)$	9.50	67.79	0
$\hat{L}(model)$	0.009	1.90×10^{-15}	1
Akaike Weights (w_i)	**0.0085**	$\mathbf{1.89 \times 10^{-15}}$	**0.991**

Table 6.9: Comparison of the different models in predicting behavior of the fluid using simulation

Model	$\hat{\sigma}$ (*Nm*)	AIC_c	$AIC_c - min(AIC_c)$	$\hat{L}(model)$	Akaike Weights (w_i)
Analytical Models					
Power law	8.08×10^{-4}	-962.3	27.2	1.23×10^{-6}	1.22×10^{-6}
Bingham fluid	1.17×10^{-3}	-912.1	77.4	1.53×10^{-17}	1.52×10^{-17}
Herschel-Bulkley	8.20×10^{-4}	-958.1	31.4	1.49×10^{-7}	1.47×10^{-7}
CFD based Models					
Power law	7.09×10^{-4}	-980.0	9.50	8.66×10^{-3}	0.00858
Bingham fluid	1.09×10^{-3}	-921.7	67.8	1.90×10^{-15}	1.89×10^{-15}
Herschel-Bulkley	6.51×10^{-4}	-989.5	0	1.00	0.991

Table 6.10: Comparison among all the analysis approaches and the models in predicting behavior of the fluid.

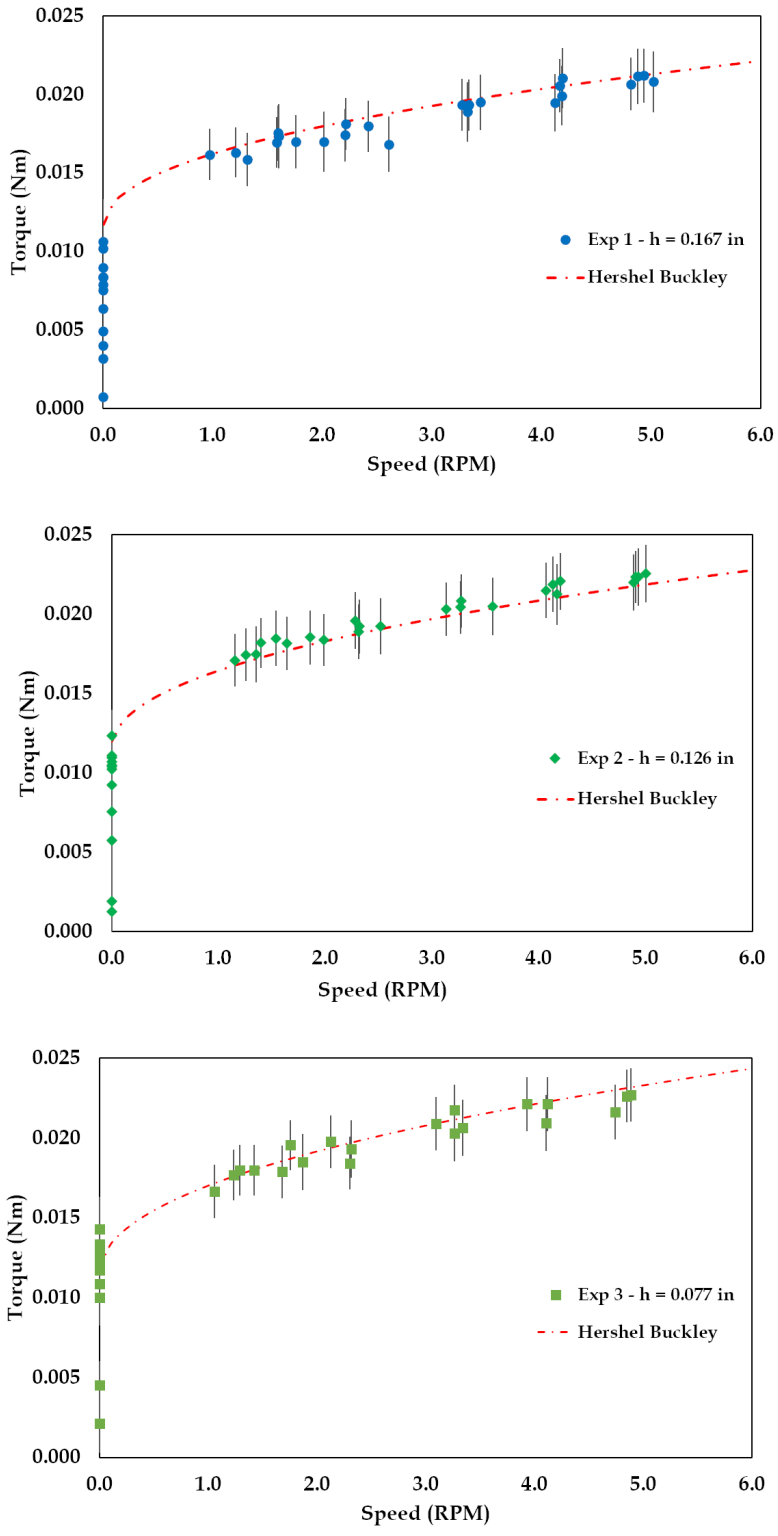

Figure 6.8: The results of the CFD based Herschel-Bulkley model fit to the data giving the final fit for the test results at 0.167 in, 0.126 in and 0.077 in of heights.

6.7 Conclusion

In this dissertation, torsional flow experiments conducted using a non-traditional test cell is modeled using analytical and CFD approaches for power law, Bingham fluid and Herschel-Bulkley models to study its rheological behavior.

When one inspects tables 6.5, 6.6 and 6.7, it becomes evident that the model parameters obtained from the analytical approach are widely different than those obtained by the CFD approach (in some cases the differences is of the order of 80%). Since we have already demonstrated that the analytical and CFD approaches agree when the side wall conditions are ignored, we infer that this difference is due to the effect of the side walls.

This indicates that, the idealization about the flow of the fluid and neglecting the flow of fluid in the gap of the setup can have a significant impact on the properties obtained for the fluid.

Moreover, Table 6.10 shows that the Akaike weights of the analytical approach were much lower in comparison to the weights in CFD based approach. The high Akaike weights and lower standard deviation in the CFD based estimation of models show the higher predictability of the fluid achieved through the CFD based analysis of the fluid behavior. Thus, the assumption that the wall effect on the fluid flow being negligible may not be a good assumption to follow in cases where experiments are conducted on non-idealistic geometries. In such cases, a method that uses the simulations will provide a more accurate estimation of the parameters for the models of the fluid.

After the complete comparison of the models as given in Table 6.10, The Herschel-Bulkley model found using the CFD based analysis is observed to represent the behavior of the fluid with a higher probability. Specifically the results suggest that compared to the other models, the Herschel-Bukley model with parameters, yield stress $\tau_0 = 65.45$ *Pa*, $k = 23.94$ *Pas* and $n = 0.48$ provides a very good approximation to the observed

experimental data. The suggested model for the rheology of the fluid for polishing is limited to low shear rates of upto $12\ s^{-1}$.

We note that, from a Bayesian perspective, it would be beneficial to provide a full probability distribution for the parameters and use that for predictions. However, we are simply using the average of the limited number of values of the parameters as a "maximum likelihood" value of the parameters.

7. FORMULATION OF SEGREGATION AND FLOW IN MAGNETIC POLISHING FLUIDS

7.1 Introduction

As we saw in the last section, the nonmagnetic response of the abrasive slurry is most readily modeled as a Herschel-Bulkley model. However, in the presence of a magnetic field, models for the fluid have to account for the segregation of the particles in the presence of a magnetic field. Given the rather high loading of the fluid (particle density exceeding 30%) and the resulting almost paste-like consistency, and the need to couple with a magnetic field, we hypothesize that a simplified mixture theory approach (where we judiciously eliminate certain terms) with a coupled magnetic field will be suitable, rather than considering individual particles. We turn to the modeling of this aspect of the fluid response next.

The slurry is made up of 2 types of particles, namely, magnetic particles suspended in oil and abrasive particles suspended in oil. In many cases, the oil is mixed with surfactants that retard the settlement of the particles in the mixture. During the polishing operation, the job and the mechanical equipment apply traction forces on the surfaces of the bulk of the fluid, whereas the magnetic forces are applied as body force on the magnetic component of the fluid. These magnetic forces will result in segregation and change in the rheological properties of the mixture. This gives the mixture a flow that can only be analyzed by studying its individual components, rather than the bulk fluid mixture as a single continuum.

In general, the mixture has three components namely, magnetic particles, abrasive particles and oil with surfactants. A typical example of a polishing scenario is shown as a schematic in Figure 7.1. In this example, the magnetic polishing fluid is held between

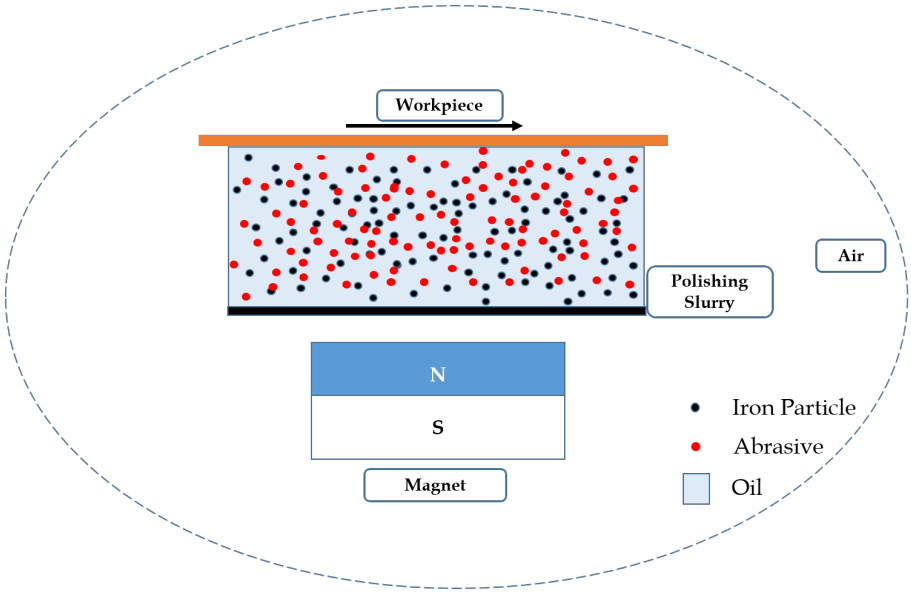

Figure 7.1: Schematic showing a typical polishing slurry in operation. Here the workpiece moves with respect to the slurry and the magnet applies a field from the bottom of the slurry. Here, the magnetic fields need to be calculated for the full field including the air, but the flow of the slurry needs to be solved within the fluid region of the slurry.

the workpiece and a stationary surface. The workpiece is then moved at a given velocity to polish the surface of the workpiece. In order to solve such a problem, we would need to solve for the magnetic fields in the entire space, including air and the magnet. Whereas, the flow and segregation of the magnetic polishing fluid needs to be solved only within the domain of the mixture. Hence, the entire problem can be subdivided into two problems, (a) Magnetics problem, which needs to be solved for the entire space and (b) Flow problem, which needs to be solved within the fluid domain. The magnetic fields in the system depend not just upon the magnet but also upon the concentration and distribution of the magnetic particles in the polishing mixture. The flow behavior of the polishing mixture is also affected by the magnetic fields, as they apply body forces onto the magnetic particles and change the rheological properties of the polishing mixture. Hence, this problem is a coupled problem.

7.2 Magnetic Field Formulation

The primary source of the stratification and diffusion in the fluid is the magnetic force that is applied on the ferrous (magnetic) particles. This is due to the presence of a magnetic field that can be applied either using electromagnetic coils or permanent magnets onto the fluid. The formulation discussed in this thesis studies with the effect of permanent magnets or magnetic field flux from the boundaries onto an abrasive magnetic fluid.

7.2.1 Maxwell's equations of Electromagnetism

The Maxwell's equations of electromagnetism for a material continua[163, 164] is shown in equations 7.1 to 7.4 given below,

$$div(\mathbf{D}_e) = \rho_e \tag{7.1}$$

$$div(\mathbf{B}) = 0 \tag{7.2}$$

$$curl(\mathbf{E}) = -\frac{\partial \mathbf{B}}{\partial t} \tag{7.3}$$

$$curl(\mathbf{H}) = \mathbf{J}_e + \frac{\partial \mathbf{D_e}}{\partial t} \tag{7.4}$$

where, $\mathbf{D}_e$ is the electric displacement, ρ_e is the charge density, $\mathbf{E}$ is the electric field, $\mathbf{B}$ is the magnetic field, $\mathbf{H}$ is the magnetic field strength and $\mathbf{J}_e$ is the current density in the media. The current density is the flux of the charges in the material giving rise to a balance law for the charges in the media as given below,

$$\frac{\partial \rho_e}{\partial t} + div(\mathbf{J}_e) + div(\rho_e \mathbf{v_e}) = 0 \tag{7.5}$$

where, $\mathbf{v_e}$ is the velocity of the media carrying the charges. The constitutive relations for

an electromagnetic media relating the magnetic and electric field [164] is given below,

$$\mathbf{B} = \mu\mathbf{H} = \mu_0(\mathbf{H} + \mathbf{M}) \tag{7.6}$$

$$\mathbf{D}_e = \varepsilon\mathbf{E} = \varepsilon_0\mathbf{E} + \mathbf{P}_e \tag{7.7}$$

Here, the magnetic permeability μ is not a constant but depends upon the concentration of magnetic particles at that location and represents the effect of the particles on the magnetic field. This is one aspect of the coupling that we will consider in the paper. The other aspect is the effect of the magnetic field on the particle segregation, which will be considered when we consider the flow problem. This results in what is usually referred to as “two-way" coupling.

When we consider the polishing of materials using magneto-rheological fluids, the fluid flows across space in the presence of magnetic field. Moreover, when the fluid segregates, the magnetic field in the space also changes inside the material. This will induce eddy currents in the magnetic particles resulting in mechanical forces in the materials, which can be inferred from equation 7.3. In this thesis, this effect in the material is ignored and may be considered in the future to study the electromagnetic effects on the polishing processes. This assumption along with the assumption that there is no polarization($\mathbf{P}_e$), free charges (ρ_e) or current ($\mathbf{J}_e$) in the whole system simplifies equations 7.1 to 7.4 to the following,

$$div(\mathbf{D}_e) = 0 \tag{7.8}$$

$$curl(\mathbf{E}) = 0 \tag{7.9}$$

$$div(\mathbf{B}) = 0 \tag{7.10}$$

$$curl(\mathbf{H}) = 0 \tag{7.11}$$

$$where, \mathbf{D}_e = \varepsilon_0 \mathbf{E} \tag{7.12}$$

$$\mathbf{B} = \mu_0(\mathbf{H} + \mathbf{M}) \tag{7.13}$$

This assumption reduces the problem to a scenario similar to magnetostatics. Considering equations 7.8, 7.9 and 7.12 along with the condition that the infinity boundary conditions for $\mathbf{E}$ and $\mathbf{D}_e$ to be zero would lead to a solution of zero electric field and electric displacement throughout the space. Considering equation 7.11, the H-field in the media can be assumed to be the gradient of a scalar potential (ϕ) satisfying the equations naturally. The B-field can be calculated through this potential and used to set up a Poisson equation for the potential (ϕ) as shown in 7.15. This method of using a scalar potential along with other formulation for magnetostatic problems is discussed by Dular et al. [165]. The potential is thus computed using the electromagnetic equations 7.14 and 7.15 as follows.

$$\mathbf{H} = grad(\phi) \tag{7.14}$$

$$div(\mathbf{B}) = div(\mu grad(\phi)) = 0 \tag{7.15}$$

The constitutive equation for the magnet is given by the following equation,

$$\mathbf{B} = \mu_0(\mathbf{H} + \mathbf{M}_{mag}) \tag{7.16}$$

where $\mathbf{M}_{mag}$ is the permanent magnetization of the magnet. Here, the permanent magnetization of the magnet acts as a source for the magnetic fields in the system. All the materials in the system that are non-magnetizable (e.g., air, workpiece, etc.) will have a permeability same as the permeability of free space($\mu_0 = 4\pi \times 10^{-7}$). Another material of interest to the problem is the magnet polishing fluid in the polishing process. Here,

the permeability of the fluid (μ), relating the H-field and the B-field in the mixture, is a function of the concentration of the magnetic component in the mixture. The permeability of the mixture is represented as a function of the permeabilities of the magnetic slurry component(μ^m) and abrasive slurry component (μ^a) using rule of mixtures as given below.

$$\begin{aligned}\mu(x^m) &= x^m\mu^m + (1-x^m)\mu^a \\ &= x^m\mu_0 + x^m\chi^m\mu_0 + (1-x^m)\mu_0 \\ &= (1+x^m\chi^m)\mu_0 \end{aligned} \tag{7.17}$$

where, x^m is the volume fraction and χ_m is the magnetic susceptibility of the magnetic component in the polishing mixture. This formulation for the permeability of the polishing mixture is inferred from the experimental results published by Simon et al. [13]. The experimental results for the effective permeability of MR fluids are given in Fig 7.2. In the literature, the effective permeability for MR fluids are modelled using nonlinear relationships. But, in the context of this study, the particle concentrations of the polishing fluids are around 0.3-0.4 as discussed in Chapter 6. Hence, this relationship gives a good estimate for the effective permeability of the polishing mixture, as the concentration of magnetic particles will never be above 0.4.

7.2.2 Interface Conditions

Since we have a system where a permanent magnet is used outside the fluid in air, the solution of the magnetic field and potential is to be calculated across all these multiple materials. Continuity of these field across all materials is to be considered in the formulation. The continuity of the fields are as follows, on the boundary of a material.

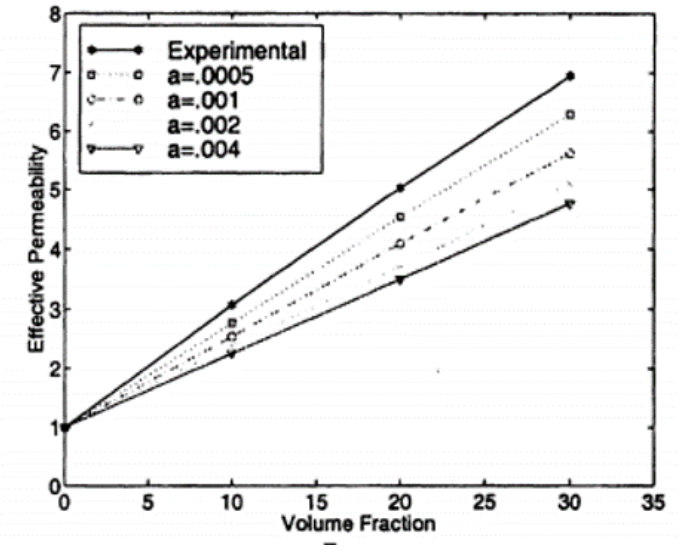

Figure 7.2: The experimental results for the effective permeability ($\mu(x^m)/\mu_0$) of MR fluids at different volume fraction of magnetic particles [13]

$$\phi_a = \phi_b \tag{7.18}$$

$$\mathbf{H}_a \times \mathbf{n} = \mathbf{H}_b \times \mathbf{n} \tag{7.19}$$

$$\mathbf{B}_a \cdot \mathbf{n} = \mathbf{B}_b \cdot \mathbf{n} \tag{7.20}$$

where, ϕ_a, $\mathbf{H}_a$, $\mathbf{B}_a$ and ϕ_b, $\mathbf{H}_b$, $\mathbf{B}_b$ are the magnetic potential, H-field and B-field on the opposite sides of the domain divided by the interface respectively and $\mathbf{n}$ is the normal to the interface.

7.2.3 Magnetic Body Forces, Body Couples and Energy Production

Electromagnetic fields interact with matter, applying forces and couples onto the media. They also cause energy production in the material through interaction. Microscopically, the electromagnetic fields interact with the electrons and protons in the material

[166, 167]. Body forces, body couples and energy production observed in the macroscopic scale is the volume average of this microscopic interaction in the material [167].

In the literature, generally the electromagnetic forces are modeled as body forces ($\mathbf{b}_{mag}$) as postulated by Lorentz or Maxwell. The same force can also be represented in the form of stress that can be computed using the relationship given in equation 7.21. This stress is called as Maxwell Stress ($\mathbf{T}_M$) was introduced by Maxwell in his treatise [163].

$$div(\mathbf{T}_M) = \mathbf{b}_{mag} \tag{7.21}$$

The magnetic force will be considered as a body force ($\mathbf{b}_{mag}$) in the entire development of the model in this thesis, as it is easier to compute the effect of the Maxwell stress on the mechanical state variables are essentially the same as the electromagnetic body forces. The electromagnetic forces, couples and energy production in this thesis are computed using the dipole-current circuit model for electrodynamics in moving media [164, 167]. This model of electromagnetic forces was used in modeling electro-rheological materials by Rajagopal and Ruzika [168] and modeling magneto-rheological fluids by Brigadnov and Dorfmann [133].

The electromagnetic body force ($\mathbf{b}_{mag}$), body couple ($\mathbf{C}_{mag}$) and the magnetic energy production (w_{mag}) produced in an electromagnetic media in the presence of electromagnetic fields modeled through the Dipole-Current Circuit Model [164] is given in the equations below,

$$\begin{aligned} b_{mag} = \rho_e \mathbf{E} + \mathbf{J}_e \times \mathbf{B} + grad(\mathbf{E})^T \mathbf{P}_e + \ grad(\mathbf{B})^T \mathbf{M} \\ \frac{\partial(\mathbf{P}_e \times \mathbf{B})}{\partial t} + div((\mathbf{P}_e \times \mathbf{B}) \otimes \mathbf{v}) \\ \mathbf{C}_{mag} = \mathbf{P}_e \times \mathbf{E} + \mathbf{M} \times \mathbf{B} + \mathbf{v} \times \mathbf{P}_e \times \mathbf{B} \end{aligned}$$

$$w_{mag} = \mathbf{J}_e \cdot \mathbf{E} + \mathbf{E} \cdot \frac{\partial \mathbf{P}_e}{\partial t} - \mathbf{M} \cdot \frac{\partial \mathbf{B}}{\partial t} + div((\mathbf{P}_e \cdot \mathbf{E})\mathbf{v})$$

where, $\mathbf{v}$ is the velocity of the media, ρ_e is the free charge density, $\mathbf{E}$ is the electric field, $\mathbf{B}$ is the B-field, $\mathbf{J}_e$ is the current density and $\mathbf{P}_e$ is the polarization of electric dipoles in the media. Considering the same assumptions that were discussed above, we consider that the electric field, electric displacement, polarization and the current in the fluid to be zero. Thus, the final form of the magnetic body force ($\mathbf{b}_{mag}$), body couple ($\mathbf{C}_{mag}$) and the magnetic power energy production (w_{mag}) as given below,

$$b_{mag} = \ grad(\mathbf{B})^T \mathbf{M} \tag{7.22}$$

$$\mathbf{C}_{mag} = \mathbf{M} \times \mathbf{B} \tag{7.23}$$

$$w_{mag} = -\mathbf{M} \cdot \frac{\partial \mathbf{B}}{\partial t} \tag{7.24}$$

These forces, couples and energy production shown in equations 7.22 to 7.24 will be used later in the chapter to model the flow equations of the polishing mixture.

7.3 Field Theory and Balance Laws of the mixture

In this thesis, the polishing fluid is modeled using mixture theory. Modeling the polishing fluid as a mixture helps in modeling the segregation of the fluid during the polishing process. Mixture theory has been used for modeling the flow of slurries by Ravindran et al.[119]. Mixture theory has also been used for modeling electro-rheological fluids by Rajagopal et al. [134]. In these models, the solid particles have been assumed a single continuum component mixed with the base fluid as the other component. Considering a similar approach, the magneto-rheological polishing fluid needs to be modeled as a mixture of three continua, (a) magnetic particle component, (b) abrasive particle component and (c) the base fluid component.But, for these magnetic polishing slurries in confined

regions, we have observed that the particles essentially behave like wet granular media where each particle being coated by a layer of viscous fluid that convects with it. We will therefore assume the mixture to be essentially consisting of two types of constituents, one a magnetic slurry with high concentration of magnetic particles and the other an abrasive slurry with high concentration of polishing abrasives, mixed to get the magnetic polishing mixture. This idea of the description of the mixture is illustrated in the schematic given in figure 7.3. Such an approach simplifies the flow problem to just two components, easing the modeling and simulation complexity.

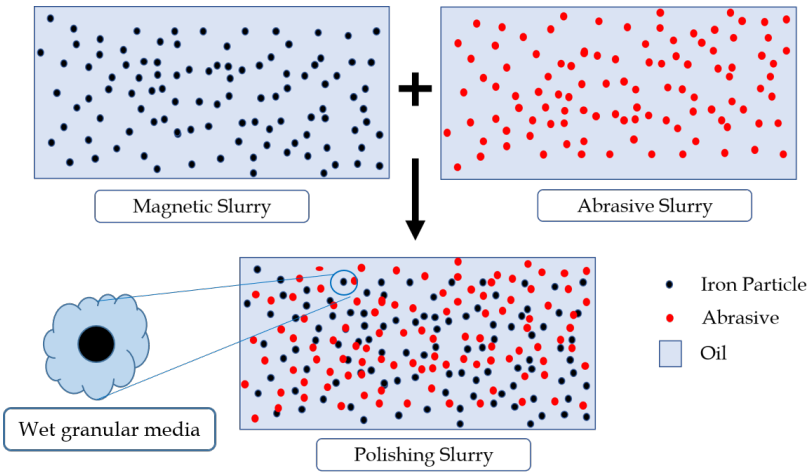

Figure 7.3: Schematic showing the formation of the polishing slurry through mixing of the component slurries, namely the magnetic slurry and the abrasive slurry

In this thesis, we study the mixture in the presence of magnetic fields in purely eulerian perspective, where the variables describing the properties of the fluids are simply modeled as fields in space. Specifically, we do not follow the particles to find the macro behavior of the fluid, rather study the flow and change of a state variable at a particular region in space. The motivation behind this approach is to ensure that the description of the fluid

properties are consistent with the description of electromagnetic fields, which are entirely in eulerian or field theoretic descriptions.

The mechanical state variables are those quantities defined at a point in the domain of the fluid which on integration through the whole volume of the domain will yield the extensive properties of the fluid. The state variables considered in this approach include density, momentum, entropy and energy of the fluid which upon integration on the whole domain yields the mass, total momentum, total entropy and total energy in the fluid. In order for the analysis and discussion of the evolution of these variables, we consider a small differential volume of the mixture, referred to as a representative volume element (RVE), in space and consider the change of these state variables over time.

Let us consider, a state variable (ϵ) in a RVE of the mixture. The rate of change of the state variable in the RVE can be evaluated using the following general balance equation,

$$\frac{\partial \epsilon}{\partial t} + div(\epsilon \mathbf{v}) + div(\mathbf{J}) = \mathbf{R} \tag{7.25}$$

where, $\mathbf{v}$ is the velocity of the fluid and $\mathbf{J}$ is the state variable's flux. Here, the first term in the equation is the production of state variable such as production of chemical species due to chemical reactions, entropy production, energy and momentum production due to external body force in the material in the RVE. The second term is the net outflow of the state variable due to the transportation of the field carrying continuum. And, the last term is the net outflow of the state variable due to the flux of the state variable which occurs due to diffusion, contact stress, conduction of heat, etc. at the boundaries of the RVE.

7.3.1 Balance Laws of the Mixture

We assume that any point in space can be occupied by the magnetic slurry component as well as the abrasive slurry component. Let us assign index '*m*' to the magnetic slurry component of the mixture and index '*a*' to the abrasive slurry component of the fluid. The

state of the mixture is defined through density (ρ^i), momentum ($\mathbf{p}^i$) and energy (u^i) fields of the 2 constituents, B-field ($\mathbf{B}$) acting on the space and the entropy (s) of the bulk fluid. The balance laws for the density, momentum, angular momentum, entropy and energy of the components in the mixture are given below [169]. These equations are of the structure described in equation 7.25.

$$\frac{\partial \rho^i}{\partial t} + div(\rho^i \mathbf{v}^i) = 0 \quad \forall\, i = m, a \tag{7.26}$$

$$\frac{\partial \mathbf{p}^i}{\partial t} + div(\mathbf{p}^i \otimes \mathbf{v}^i) - div(\mathbf{T^i}) = \mathbf{b}^i_{mag} + \mathbf{f}^i \quad \forall\, i = m, a \tag{7.27}$$

$$\frac{\partial (\mathbf{r} \times \mathbf{p}^i)}{\partial t} + div(\mathbf{r} \times \mathbf{p}^i \otimes \mathbf{v}^i) = div(\mathbf{r} \times \mathbf{T^i}) + \mathbf{r} \times (\mathbf{b}^i_{mag} + \mathbf{f}^i) + \mathbf{C}^i_{mag} \quad \forall\, i = m, a \tag{7.28}$$

$$\frac{\partial s}{\partial t} + div(s\mathbf{v}) + div(\mathbf{h}) = \xi \tag{7.29}$$

$$\frac{\partial u^i}{\partial t} + div(u^i \mathbf{v}^i) + div(\mathbf{Q}^i) = w^i_{int} + w^i_{mag} \quad \forall\, i = m, a \tag{7.30}$$

where, t is time, $\mathbf{v^i}$ is the velocity of the component *i*, $\mathbf{T^i}$ is the stress, $\mathbf{b}^i_{mag}$ is the magnetic body force, $\mathbf{f^i}$ is the interaction force, $\mathbf{C}^i_{mag}$ is the body couple w^i_{mag} is the magnetic energy supplied of the component *i*, $\mathbf{v}$ is the velocity, $\mathbf{h}$ is the entropy flux, $\mathbf{Q}$ is the energy flux and ξ is the entropy production of the mixture. Since, the magnetic component of the mixture is magnetizable and responds to the magnetic fields, $\mathbf{b}^m_{mag}$, $\mathbf{C}^m_{mag}$ and w^m_{mag} are computed using equations 7.22 to 7.24 and $\mathbf{b}^a_{mag}$, $\mathbf{C}^a_{mag}$ and w^a_{mag} are taken as zero.

7.3.2 Solution to Balance of Angular Momentum

In this section, we look into the balance of angular momentum equations of the components given in equation 7.28. First, let us consider the body couples applied onto the components of the mixture by the magnetic fields. Since we model the magnetic component to get magnetized in the direction of the magnetic fields, we get the following

derivation.

$$\begin{aligned}\mathbf{C}^m_{mag} &= \mathbf{M} \times \mathbf{B} \\ &= x^m \chi^m \mathbf{H} \times \mu \mathbf{H} \\ &= \mathbf{0} \qquad (7.31)\end{aligned}$$

$$\mathbf{C}^a_{mag} = \mathbf{0} \qquad (7.32)$$

Substituting the above equations for the body couples into the balance of angular momentum equations, and additionally substituting equation 7.27 into the angular momentum balance law gives the following derivation for the stress of each component.

$$\begin{aligned}\frac{\partial(\mathbf{r} \times \mathbf{p}^i)}{\partial t} + div(\mathbf{r} \times \mathbf{p}^i \otimes \mathbf{v}^i) &= div(\mathbf{r} \times \mathbf{T}^{\mathbf{i}}) + \mathbf{r} \times (\mathbf{b}^i_{mag} + \mathbf{f}^i) \\ \implies \mathbf{r} \times \frac{\partial \mathbf{p}^i}{\partial t} + \mathbf{v}^i \times \mathbf{p}^i + \mathbf{r} \times div(\mathbf{p}^i \otimes \mathbf{v}^i) &= \epsilon : \mathbf{T}^{iT} + \mathbf{r} \times div(\mathbf{T}^i) \\ &\quad + \mathbf{r} \times (\mathbf{b}^i_{mag} + \mathbf{f}^i) \\ \implies \epsilon : \mathbf{T}^{iT} &= \mathbf{r} \times (\mathbf{0}) \\ &= 0 \qquad (7.33)\end{aligned}$$

From equation 7.33, we can infer that the stress of the components of the mixture is symmetric.

7.3.3 Remarks

As observed here in equations 7.26 to 7.30, the conservation of mass, momentum and energy of the fluid is written for both the components individually, but the equation on the production of entropy is taken for the whole bulk of the fluid. A more comprehensive approach would be to posit these laws for each component separately rather than the bulk fluid [169]. However, we propose to simplify the situation by assuming one entropy and

one temperature for all the constituents. This will considerably ease the application of the second law in the form of the Clausius-Duhem inequality. This in turn helps in constructing constitutive equations that are consistent with the second law of thermodynamics. The formulation and simulations are designed to ensure that the conservation equations given in 7.26 to 7.30 are satisfied by the components but executed using the bulk flow as the primary flow and the relative motion of the individual components to be secondary in nature. The details of this approach to modeling are discussed in section 7.4.

7.4 Modeling Approach

The standard approach in mixture modeling is to use the conservation equations for individual components in the mixture to calculate the state variable of these components. The bulk behavior of the fluid is then calculated using mixture equations. However, in application, we are primarily interested in the flow behavior of the bulk mixture and segregation behavior of the magnetic component. Experiments studying the mixtures evaluate the bulk properties of the mixture rather than individual components. Moreover, the bulk output of the fluid is of importance to the polishing process. Hence, in this thesis, we study the bulk flow behavior of the fluid and separate the interaction behavior of the fluid in the mixture and study them individually.

The bulk properties of the mixture depend upon how the state, flux and production variables of the bulk mixture are modeled with respect to the individual components from equations 7.26 and 7.27. Some variables can be computed with additive properties and some using rule of mixtures. Variables such as the density (ρ), momentum ($\mathbf{p}$), stress ($\mathbf{T}$), traction ($\mathbf{t}$), net interaction force ($\mathbf{f}$), energy (u), energy flux ($\mathbf{Q}$) and net interaction energy (w_{int}) can be modeled as the sum of the corresponding variables of the individual

components as shown in the equations below,

$$\rho = \rho^m + \rho^a \tag{7.34}$$

$$\mathbf{p} = \mathbf{p}^m + \mathbf{p}^a \tag{7.35}$$

$$\mathbf{T} = \mathbf{T}^m + \mathbf{T}^a \tag{7.36}$$

$$\mathbf{t} = \mathbf{t}^m + \mathbf{t}^a \tag{7.37}$$

$$\mathbf{f} = \mathbf{f}^m + \mathbf{f}^a = 0 \tag{7.38}$$

$$u = u^m + u^a \tag{7.39}$$

$$\mathbf{Q} = \mathbf{Q}^m + \mathbf{Q}^a \tag{7.40}$$

$$w_{int} = w_{int}^m + w_{int}^a = 0 \tag{7.41}$$

where, t^m and t^a are the partial traction in the components. Since the interaction forces are internal forces between the components, we take the net interaction force on the bulk fluid ($\mathbf{f}$) to be zero [169]. This means that the production of momentum in individual components are due to both the interaction forces and the body forces (external forces), whereas the momentum production in the bulk fluid is entirely due to the magnetic body forces acting on the fluid. Furthermore, note that the stress $\mathbf{T}$ is the actual stress acting on the fluid mixture and the stresses $\mathbf{T^m}$ and $\mathbf{T^a}$ are the partial stresses acting on the components. The net interaction energy (w_{int}) of the bulk fluid is also taken as zero. The individual component's interaction energies include the energy supplied by the interaction forces in the components.

7.4.1 Mass and Volume Concentration of the components

Using the above equations, we can define the mass concentration (c^i) and volume concentration (x^i) of the components as follows,

$$c^i = \frac{\rho^i}{\rho} \tag{7.42}$$

$$x^i = \frac{\rho^i}{\rho^i_*} \quad \forall\, i = m, a \tag{7.43}$$

where, ρ^i_* is the filled density of component 'i' i.e., the density of the mixture or component when the whole volume is 'filled' by the component 'i' ($x^i = 0$). This value is constant for a fixed domain of the mixture and is dependent on the density and size of the particles along with the density of the oil.

7.4.2 Bulk velocity formulation

Generally, the velocity ($\mathbf{v}$) of the bulk fluid is calculated from the bulk momentum in the literature using the equation below[169],

$$\begin{aligned} \mathbf{v} &= \frac{\mathbf{p}}{\rho} \\ &= c^m \mathbf{v^m} + c^a \mathbf{v}^a \end{aligned} \tag{7.44}$$

However, in this thesis, we do not use the above definition. We develop an approach based on a general rule of mixtures. At this stage, we introduce two scalars α^m and α^a and use a mixture average velocity for the bulk as given below.

$$\begin{aligned} \mathbf{v} &= \alpha^m \mathbf{v}^m + \alpha^a \mathbf{v}^a \\ \text{where,} \quad \alpha^m, \alpha^a \geq & 0 \quad \text{and} \quad \alpha^m + \alpha^a = 0 \end{aligned} \tag{7.45}$$

where, α^m and α^a are the weights (not to be mistaken for the force of gravity) used to calculate the average velocity for the bulk. The choice of the appropriate weights for the mixture velocity is discussed in section 7.5. With this approach, we can compare different methods for assigning the average mixture properties (by choosing different definitions for α^i). Specifically, we will compare the differences in the formulations when the weights are chosen to be the mass concentration (c^i) as compared to the volume concentrations (x^i) and show that the volume additivity constraint is more easily and intuitively enforced by using the volume averaged velocity.

In the mixture, with the definition of the bulk fluid velocity given in equation 7.45, we can define a relative velocity to each component in the mixture. This relative velocity of the components with respect to the bulk flow results in stratification of the components in the mixture. The relative velocity ($\hat{\mathbf{v}}^i$) of the components in the bulk is defined below.

$$\hat{\mathbf{v}}^i = \mathbf{v}^i - \mathbf{v} \tag{7.46}$$

Therefore, the individual velocities of the components can be expressed using the bulk velocity and the relative velocity as given below,

$$\mathbf{v}^i = \mathbf{v} + \hat{\mathbf{v}}^{\mathbf{i}} \tag{7.47}$$

Substituting the equation 7.46 in equation 7.45, we get the following relation, which is a useful property that can be used in relating the relative velocities of the individual components.

$$\alpha^m \hat{\mathbf{v}}^m + \alpha^a \hat{\mathbf{v}}^a = 0 \tag{7.48}$$

This definition for the bulk velocity of the fluid does not change the definition of the bulk momentum given in equation 7.35, rather redefines it into the following form.

$$\mathbf{p} = \rho\mathbf{v} + \rho^m\hat{\mathbf{v}}^m + \rho^a\hat{\mathbf{v}}^a \tag{7.49}$$

Using the above definitions for the bulk fluid, we compute the balance laws for the bulk and diffusive velocities in the mixture. The derivation and description of these balance laws are discussed in section 7.8.

7.5 Kinematic Constraint: Volume Additivity Constraint

Volume additivity constraint, which means that the sum of the volumes of the components of a mixture is constant, ensures the incompressibility of the overall bulk fluid. We apply this condition as both the constituents of the mixture are incompressible in nature. As a result, even though the volume of the constituents in a particular RVE of bulk fluid changes with time, the sum of the volumes of the constituents in the constituents will be constant. Hence, we can derive the following relationship between the densities of the constituents using the definition of the volume concentrations (x^m and x^a) given in equation 7.43.

$$\begin{aligned} V^m + V^a &= V \\ \implies x^m + x^a &= 1 \\ \implies \frac{\rho^m}{\rho^m_*} + \frac{\rho^a}{\rho^a_*} &= 1 \end{aligned} \tag{7.50}$$

The filled densities of both the magnetic and abrasive fluid constituents are constants, as both the constituents are incompressible in nature. The filled densities for the constituents ρ^m_* and ρ^a_* form a constraint on the densities of the components.

Now, to find the constraints in bulk velocity and diffusive velocities that this relation

leads to, we need to first partially differentiate equation 7.50 with respect to time. Later, upon substitution of equation 7.26 into the relation will give the constraint as shown below.

$$\begin{aligned} \frac{\partial}{\partial t}(\frac{\rho^m}{\rho^m_*} + \frac{\rho^a}{\rho^a_*}) &= \frac{\partial(1)}{\partial t} \\ \implies \frac{1}{\rho^m_*}\frac{\partial \rho^m}{\partial t} + \frac{1}{\rho^a_*}\frac{\partial \rho^a}{\partial t} &= 0 \\ \implies -\frac{div(\rho^m \mathbf{v^m})}{\rho^m_*} - \frac{div(\rho^m \mathbf{v^m})}{\rho^a_*} &= 0 \\ \implies div(x^m \mathbf{v^m} + x^a \mathbf{v^a}) &= 0 \end{aligned} \tag{7.51}$$

Equation 7.51 is the primary equation that constraints flow velocities of the 2 components and ensures the incompressibility of the components and the bulk fluid. In this study, the constraint is calculated in terms of the bulk velocity and diffusive velocity of the magnetic component. The derivation of the constraint of this form is as follows,

$$\begin{aligned} & div(x^m \mathbf{v} + x^m \hat{\mathbf{v}}^{\mathbf{m}} + x^a \mathbf{v} + x^a \hat{\mathbf{v}}^{\mathbf{a}}) = 0 \\ \implies & div(\mathbf{v}) + div(x^m \hat{\mathbf{v}}^{\mathbf{m}} + x^a \hat{\mathbf{v}}^{\mathbf{a}}) = 0 \end{aligned} \tag{7.52}$$

Now substituting equation 7.48 into the above constraint relation, we get the following,

$$div(\mathbf{v}) + div(\frac{x^m \alpha^a - x^a \alpha^m}{\alpha^a} \hat{\mathbf{v}}^{\mathbf{m}}) = 0 \tag{7.53}$$

The equation above is the volume addititivity constraint, expressed in terms of the bulk velocity and the relative velocity of the magnetic constituent. Here, the choice of the weights for calculating the bulk mixture's velocity will give an appropriate constraint on the bulk and the relative velocities. If the weights α^i are assumed to be the mass concentration c^i of the components, then the relationship is derived to be the following

[169].

$$
\begin{aligned}
& div(\mathbf{v}) + div(\frac{x^m c^a - x^a c^m}{c^a}\hat{\mathbf{v}}^{\mathbf{m}}) = 0 \\
\implies & div(\mathbf{v}) + div((\frac{\rho^m \rho^a}{\rho_*^m \rho} - \frac{\rho^m \rho^a}{\rho_*^a \rho})\frac{\rho}{\rho^a}\hat{\mathbf{v}}^{\mathbf{m}}) = 0 \\
\implies & div(\mathbf{v}) + div((\frac{1}{\rho_*^m} - \frac{1}{\rho_*^a})\rho^m \hat{\mathbf{v}}^{\mathbf{m}}) = 0 \\
\implies & div(\mathbf{v}) + div((1 - \frac{\rho_*^m}{\rho_*^a})\hat{\mathbf{q}}^{\mathbf{m}}) = 0
\end{aligned} \tag{7.54}
$$

If the weights α^i are assumed to be the volume concentration x^i of the components, then the relationship is derived to be the following.

$$
\begin{aligned}
& div(\mathbf{v}) + div(\frac{x^m x^a - x^a x^m}{x^a}\hat{\mathbf{v}}^{\mathbf{m}}) = 0 \\
\implies & div(\mathbf{v}) = 0
\end{aligned} \tag{7.55}
$$

Out of the 2 possibilities discussed above, the choice of the weights determine the constraint equation for the mixture. As shown in equation 7.54, if we choose α^i to be the mass concentration (c^i) then the resultant bulk fluid will be compressible. This does not mean that the mixture is compressible, but that the bulk fluid thus chosen through mixture theory is of a compressible form. Hence, the constitutive model that needs to be chosen for such a bulk fluid needs to reflect such a behavior. If we choose α^i to be the volume concentration (x^i) of the components, then the bulk fluid needs to follow the incompressibility constraint. In the literature experimenting on such mixtures, the bulk fluid is usually modeled as an incompressible fluid. In this study, the same form of constitutive model for bulk is studied in detail. Hence, we choose the weights (α^i) to be the volume concentration (x^i) of the

components for modeling the bulk fluid of the mixture as given below,

$$\mathbf{v} = x^m \mathbf{v^m} + x^a \mathbf{v^a} \tag{7.56}$$

7.6 Balance Laws: Bulk and Magnetic Fluid (Relative Flow)

In this section, we employ the modeling approach discussed in section 7.4 to the governing equations of the mixture given in equations 7.26, 7.27 and 7.30. This will result in the balance laws for the bulk mixture and the magnetic component of the mixture.

7.6.1 Conservation of Mass

The conservation of mass for the bulk fluid is calculated by adding the conservation equations for the individual constituents (see equation 7.26) to obtain the conservation equation for the bulk fluid.

$$\begin{aligned} &\frac{\partial \rho}{\partial t} + div(\rho \mathbf{v}) + div(\rho^m \hat{\mathbf{v}}^{\mathbf{m}} + \rho^a \hat{\mathbf{v}}^{\mathbf{a}}) = 0 \\ \implies &\frac{\partial \rho}{\partial t} + div(\rho \mathbf{v}) + (\rho^m_* - \rho^a_*) div(\hat{\mathbf{q}}^{\mathbf{m}}) = 0 \qquad (7.57) \\ &\text{where,} \quad \hat{\mathbf{q}}^{\mathbf{m}} = x^m \hat{\mathbf{v}}^{\mathbf{m}} \qquad (7.58) \end{aligned}$$

The balance equation for the volume concentration of the magnetic constituent can be evaluated by dividing equation 7.26 of the magnetic component, with ρ^m_* which is a constant.

$$\begin{aligned} &\frac{\partial \rho^m}{\partial t} + div(\rho^m \mathbf{v}) + div(\rho^m \hat{\mathbf{v}}^{\mathbf{m}}) = 0 \\ \implies &\frac{\partial x^m}{\partial t} + div(x^m \mathbf{v}) + div(\hat{\mathbf{q}}^{\mathbf{m}}) = 0 \qquad (7.59) \end{aligned}$$

7.6.2 Momentum Balance Laws

Using the same approach for the momentum balance laws, we can compute the balance law for the bulk fluid. First, we divide the equations for the components with their filled densities(ρ_*^i).

$$\frac{\partial \mathbf{p}^i}{\partial t} + div(\mathbf{p}^i \otimes \mathbf{v}^i) = div(\mathbf{T^i}) + \mathbf{b}^i_{mag} + \mathbf{f}^i \quad \forall\, i = m, a$$
$$\implies \frac{\partial x^i \mathbf{v}^i}{\partial t} + div(x^i \mathbf{v}^i \otimes \mathbf{v}^i) = \frac{1}{\rho_*^i}[div(\mathbf{T^i}) + \mathbf{b}^i_{mag} + \mathbf{f}^i] \quad \forall\, i = m, a$$

Upon summing the equations for $i = m, a$ the derivation for the equation velocity of the bulk fluid can be calculated as follows,

$$\frac{\partial(x^m \mathbf{v^m} + x^a \mathbf{v^a})}{\partial t} + div(x^m \mathbf{v^m} \otimes \mathbf{v^m} + x^a \mathbf{v^a} \otimes \mathbf{v^a}) = \frac{div(\mathbf{T^m})}{\rho_*^m} + \frac{div(\mathbf{T^a})}{\rho_*^a} + \frac{\mathbf{b}^m_{mag}}{\rho_*^m} + \frac{\mathbf{f}^m}{\rho_*^m} + \frac{\mathbf{f}^a}{\rho_*^a}$$

Evaluating the left hand side (LHS) of the above equation, we get

$$\begin{aligned}
LHS &= \frac{\partial(x^m \mathbf{v^m} + x^a \mathbf{v^a})}{\partial t} + div(x^m \mathbf{v^m} \otimes \mathbf{v^m} + x^a \mathbf{v^a} \otimes \mathbf{v^a}) \\
&= \frac{\partial \mathbf{v}}{\partial t} + div((x^m \mathbf{v^m} + x^a \mathbf{v^a}) \otimes \mathbf{v}) + div(x^m \mathbf{v^m} \otimes \hat{\mathbf{v}}^\mathbf{m} + x^a \mathbf{v^a} \otimes \hat{\mathbf{v}}^\mathbf{a}) \\
&= \frac{\partial \mathbf{v}}{\partial t} + div(\mathbf{v} \otimes \mathbf{v}) + div(\mathbf{v^m} \otimes (x^m \hat{\mathbf{v}}^\mathbf{m}) + \mathbf{v^a} \otimes (x^a \hat{\mathbf{v}}^\mathbf{a})) \\
&= \frac{\partial \mathbf{v}}{\partial t} + div(\mathbf{v} \otimes \mathbf{v}) + div((\mathbf{v^m} - \mathbf{v^a}) \otimes (x^m \hat{\mathbf{v}}^\mathbf{m})) \\
&= \frac{\partial \mathbf{v}}{\partial t} + div(\mathbf{v} \otimes \mathbf{v}) + div((\hat{\mathbf{v}}^\mathbf{m} - (-\frac{x^m}{x^a})\hat{\mathbf{v}}^\mathbf{m})) \otimes (x^m \hat{\mathbf{v}}^\mathbf{m})) \\
&= \frac{\partial \mathbf{v}}{\partial t} + div(\mathbf{v} \otimes \mathbf{v}) + div(\frac{x^m \hat{\mathbf{v}}^\mathbf{m} \otimes \hat{\mathbf{v}}^\mathbf{m}}{x^a})
\end{aligned}$$

Evaluating the right hand side (RHS) of the equation, we get

$$\begin{aligned} RHS &= \frac{div(\mathbf{T^m})}{\rho_*^m} + \frac{div(\mathbf{T}-\mathbf{T^m})}{\rho_*^a} + \frac{\mathbf{b}_{mag}^m}{\rho_*^m} + \frac{\mathbf{f}^m}{\rho_*^m} - \frac{\mathbf{f}^m}{\rho_*^a} \\ &= \frac{1}{\rho_*^a} div(\mathbf{T}) + (\frac{1}{\rho_*^m} - \frac{1}{\rho_*^a}) div(\mathbf{T^m}) + \frac{\mathbf{b}_{mag}^m}{\rho_*^m} + (\frac{1}{\rho_*^m} - \frac{1}{\rho_*^a})\mathbf{f}^m \end{aligned}$$

The final equation for the velocity of the bulk fluid evaluated by substituting the LHS and the RHS into the original equation comes out to be,

$$\begin{aligned} \frac{\partial \mathbf{v}}{\partial t} + div(\mathbf{v}\otimes\mathbf{v}) = \frac{1}{\rho_*^a} div(\mathbf{T}) + (\frac{1}{\rho_*^m} - \frac{1}{\rho_*^a}) div(\mathbf{T^m}) + \frac{\mathbf{b}_{mag}^m}{\rho_*^m} \\ + (\frac{1}{\rho_*^m} - \frac{1}{\rho_*^a})\mathbf{f}^m + div(\hat{\mathbf{v}}^{\mathbf{m}} \otimes \hat{\mathbf{v}}^{\mathbf{a}}) \end{aligned} \tag{7.60}$$

In order to calculate the equation of flux of particles ($\hat{q}^m$) in the fluid, we start with the momentum balance equation for the constituent. The momentum contribution through the bulk fluid to the constituent is separated through substitution of the bulk momentum equation given in equation 7.60 into the equation given below. The derivation of the equation is given below,

$$\frac{\partial x^m \mathbf{v}^m}{\partial t} + div(x^m \mathbf{v}^m \otimes \mathbf{v}^m) = \frac{1}{\rho_*^m}[div(\mathbf{T^m}) + \mathbf{b}_{mag}^m + \mathbf{f}^m]$$

Simplifying the LHS of the above equation, we get the following derivation,

$$\begin{aligned} LHS &= \frac{\partial x^m \mathbf{v}^m}{\partial t} + div(x^m \mathbf{v}^m \otimes \mathbf{v}^m) \\ &= \frac{\partial x^m (\mathbf{v}+\hat{\mathbf{v}}^m)}{\partial t} + div(x^m(\mathbf{v}+\hat{\mathbf{v}}^m)\otimes(\mathbf{v}+\hat{\mathbf{v}}^m)) \\ &= \frac{\partial x^m \mathbf{v}}{\partial t} + div(\mathbf{v}\otimes x^m\mathbf{v}) + \frac{\partial \hat{\mathbf{q}}^m}{\partial t} + div(\hat{\mathbf{q}}^m \otimes \mathbf{v}) + div(\mathbf{v}\otimes\hat{\mathbf{q}}^m) + div(\hat{\mathbf{q}}^m \otimes \hat{\mathbf{v}^m}) \\ &= (\frac{\partial x^m}{\partial t} + div(x^m\mathbf{v}) + div(\hat{\mathbf{q}}^m))\mathbf{v} + x^m \frac{\partial \mathbf{v}}{\partial t} + grad(\mathbf{v})(x^m\mathbf{v} + \hat{\mathbf{q}}^m) \end{aligned}$$

$$+ \frac{\partial \hat{\mathbf{q}}^m}{\partial t} + div(\hat{\mathbf{q}}^m \otimes \mathbf{v}) + div(\hat{\mathbf{q}}^m \otimes \hat{\mathbf{v}^m})$$

On substituting equations 7.59 and 7.60 into the equation given above, we get the following form for the LHS.

$$\begin{aligned}
LHS &= (0)\mathbf{v} + x^m(-div(\mathbf{v}\otimes\mathbf{v}) + \frac{1}{\rho_*^a}div(\mathbf{T}) + (\frac{1}{\rho_*^m} - \frac{1}{\rho_*^a})div(\mathbf{T^m}) + \frac{\mathbf{b}_{mag}^m}{\rho_*^m} \\
&\quad + (\frac{1}{\rho_*^m} - \frac{1}{\rho_*^a})\mathbf{f}^m + div(\hat{\mathbf{v}}^\mathbf{m} \otimes \hat{\mathbf{v}}^\mathbf{a})) + grad(\mathbf{v})(x^m\mathbf{v} + \hat{\mathbf{q}}^m) \\
&\quad + \frac{\partial \hat{\mathbf{q}}^m}{\partial t} + div(\hat{\mathbf{q}}^m \otimes \mathbf{v}) + div(\hat{\mathbf{q}}^m \otimes \hat{\mathbf{v}^m}) \\
&= \frac{\partial \hat{\mathbf{q}}^m}{\partial t} + div(\hat{\mathbf{q}}^m \otimes \mathbf{v}) + x^m div(\hat{\mathbf{v}}^\mathbf{m} \otimes \hat{\mathbf{v}}^\mathbf{a}) + grad(\mathbf{v})\hat{\mathbf{q}}^m + div(\hat{\mathbf{q}}^m \otimes \hat{\mathbf{v}}^m) \\
&\quad + x^m(\frac{1}{\rho_*^a}div(\mathbf{T}) + (\frac{1}{\rho_*^m} - \frac{1}{\rho_*^a})div(\mathbf{T^m}) + \frac{\mathbf{b}_{mag}^m}{\rho_*^m} + (\frac{1}{\rho_*^m} - \frac{1}{\rho_*^a})\mathbf{f}^m)
\end{aligned}$$

Substituting the above equation into the original equation, we get

$$\begin{aligned}
&\frac{\partial \hat{\mathbf{q}}^m}{\partial t} + div(\hat{\mathbf{q}}^m \otimes \mathbf{v}) + x^m div(\hat{\mathbf{v}}^\mathbf{m} \otimes \hat{\mathbf{v}}^\mathbf{a}) + grad(\mathbf{v})\hat{\mathbf{q}}^m + div(\hat{\mathbf{q}}^m \otimes \hat{\mathbf{v}}^m) \\
&\quad = \frac{1}{\rho_*^m}[div(\mathbf{T^m}) + \mathbf{b}_{mag}^m + \mathbf{f}^m] \\
&\qquad - x^m(\frac{1}{\rho_*^a}div(\mathbf{T}) + (\frac{1}{\rho_*^m} - \frac{1}{\rho_*^a})div(\mathbf{T^m}) + \frac{\mathbf{b}_{mag}^m}{\rho_*^m} + (\frac{1}{\rho_*^m} - \frac{1}{\rho_*^a})\mathbf{f}^m) \\
&\quad = (\frac{x^a}{\rho_*^m} + \frac{x^m}{\rho_*^a})div(\mathbf{T^m}) - \frac{x^m}{\rho_*^a}div(\mathbf{T}) + x^a\frac{\mathbf{b}_{mag}^m}{\rho_*^m} + (\frac{x^a}{\rho_*^m} + \frac{x^m}{\rho_*^a})\mathbf{f}^m \\
&\quad = \frac{\rho}{\rho_*^m\rho_*^a}div(\mathbf{T^m}) - \frac{x^m}{\rho_*^a}div(\mathbf{T}) + x^a\frac{\mathbf{b}_{mag}^m}{\rho_*^m} + \frac{\rho}{\rho_*^m\rho_*^a}\mathbf{f}^m
\end{aligned}$$

The final equation for the rate of change of flux of the magnetic constituent in the mixture is given by the equation below.

$$\begin{aligned}
&\frac{\partial \hat{\mathbf{q}}^m}{\partial t} + div(\hat{\mathbf{q}}^m \otimes \mathbf{v}) + x^m div(\hat{\mathbf{v}}^\mathbf{m} \otimes \hat{\mathbf{v}}^\mathbf{a}) + grad(\mathbf{v})\hat{\mathbf{q}}^m + div(\hat{\mathbf{q}}^m \otimes \hat{\mathbf{v}}^m) \\
&\quad = \frac{\rho}{\rho_*^m\rho_*^a}div(\mathbf{T^m}) - \frac{x^m}{\rho_*^a}div(\mathbf{T}) + x^a\frac{\mathbf{b}_{mag}^m}{\rho_*^m} + \frac{\rho}{\rho_*^m\rho_*^a}\mathbf{f}^m
\end{aligned} \tag{7.61}$$

7.6.3 Energy Balance Equations

The balance laws for the energy of the components given in equation 7.30 is considered to compute the energy balance law for the bulk mixture. We calculate the bulk fluid's energy conservation equation by adding the energy equations of the constituents, as given below.

$$\frac{\partial u^m}{\partial t} + div(u^m \mathbf{v}^m) + div(\mathbf{Q}^m) + \frac{\partial u^a}{\partial t} + div(u^a \mathbf{v}^a) + div(\mathbf{Q}^a) = w^m_{int} + w_{mag} + w^a_{int}$$

$$\implies \frac{\partial u}{\partial t} + div(u^m \mathbf{v}^m + u^a \mathbf{v}^a) + div(\mathbf{Q}) = w_{mag} \tag{7.62}$$

The balance of energy equation developed above is used in the following section to compute the production of entropy in the system and further develop constitutive models for the mixture.

7.7 Constitutive Modeling of the Mixture

7.7.1 Energy Function

The first step to finding the constitutive equations is to define an energy function for the mixture. In general, this energy function for the mixture is the sum of the internal energy and the kinetic energy of the constituents of the mixture. The kinetic energy of the mixture can be written as the sum of the kinetic energies of the constituents of the mixture, as there is no interactive kinetic energy to the mixture. But, the internal energy is defined as a single function for the mixture which depends upon the density of the constituents and the entropy of the system and a magnetic energy that depends upon the density of the magnetic constituent and the B-field in the mixture. The shape of the mixture is not considered in this assumption for the energy equation, as the slurry is assumed to be a fluid that doesn't store energy in its shape. The energy function for the components can be

chosen as follows,

$$u^m = x^m u_0(\rho^m, \rho^a, s) + u_{mag}(\rho^m, \mathbf{B}) + \frac{\mathbf{p^m} \cdot \mathbf{p^m}}{2\rho^m} \tag{7.63}$$

$$u^a = x^a u_0(\rho^m, \rho^a, s) + \frac{\mathbf{p^a} \cdot \mathbf{p^a}}{2\rho^a} \tag{7.64}$$

When we add the energies of the constituents given in equations 7.63 and 7.64 we get the energy of the bulk fluid as follows,

$$\begin{aligned} u &= (x^m + x^a) u_0(\rho^m, \rho^a, s) + \frac{\mathbf{p^m} \cdot \mathbf{p^m}}{2\rho^m} + \frac{\mathbf{p^a} \cdot \mathbf{p^a}}{2\rho^a} + u_{mag}(\rho^m, \mathbf{B}) \\ &= u_0(\rho^m, \rho^a, s) + \frac{\mathbf{p^m} \cdot \mathbf{p^m}}{2\rho^m} + \frac{\mathbf{p^a} \cdot \mathbf{p^a}}{2\rho^a} + u_{mag}(\rho^m, \mathbf{B}) \end{aligned} \tag{7.65}$$

With the form of the energy function given above in equation 7.65, the driving forces for each of the state variables ($\epsilon = [\rho^i, s, \mathbf{p}^i, \mathbf{B}]$), that include the density and momenta of the constituents and the entropy of the mixture, can be computed by differentiating the energy function with respect to the state variables. The driving forces (Π) for each of the state variables (ϵ) thus computed is given below,

$$\begin{aligned} \Pi &:= \frac{\partial u}{\partial \epsilon} \\ A^i &:= \frac{\partial u}{\partial \rho^i} \\ &= \frac{\partial u_0}{\partial \rho^i} - \frac{\mathbf{p^i} \cdot \mathbf{p^i}}{2(\rho^i)^2} + \frac{\partial u_{mag}}{\partial \rho^i} \\ &= A_0^i - \frac{\mathbf{p^i} \cdot \mathbf{p^i}}{2(\rho^i)^2} + A_{mag}^i \end{aligned} \tag{7.66}$$

$$\begin{aligned} \mathbf{v^i} &:= \frac{\partial u}{\partial \mathbf{p^i}} \\ &= \frac{\mathbf{p^i}}{\rho^i} \end{aligned} \tag{7.67}$$

$$\theta := \frac{\partial u}{\partial s} \tag{7.68}$$

$$\begin{aligned} \bar{\mathbf{M}} &:= \frac{\partial u}{\partial \mathbf{B}} \\ &= \frac{\partial u_{mag}}{\partial \mathbf{B}} \end{aligned} \tag{7.69}$$

where, A^i is the chemical potential of the constituents, θ is the temperature in the bulk fluid and $\bar{\mathbf{M}}$ is the magnetic driving force in the fluid. These relations for the driving forces are used to calculate the entropy production in the mixture and compute the primary constraint on the flux state variables in the mixture. We also use these to compute the final constitutive models for the dependent variables from a form of the potential energy that we assume for u_0.

7.7.2 Clausius-Duhem Inequality for the Mixture

The second law of thermodynamics states that the entropy of the universe at the end of every process cycle will either increase or remain constant. Hence, assuming that a material's entropy through any process is non-negative ensures that all processes with the material complies by the second law of thermodynamics. In order to ensure this we assume that in the mixture the net entropy production in particular RVE of the material as a result of local change in entropy, entropy added due to transportation and due to the flux of entropy in the RVE is non-negative. This approach of constraining the entropy production locally has been discussed in detail by Rajagopal and Tao [169]. This results in the inequality given below,

$$\xi \geq 0 \tag{7.70}$$

$$\theta\xi \geq 0 \tag{7.71}$$

The inequality given above is achieved as the temperature of the mixture is always non-negative. Hence, we compute the expression for $\theta\xi$ and enforce the inequality given in equation 7.71 to ensure that the mixture follows the second law of thermodynamics for all processes.

Now let's look at the conservation equations given in equations 7.26,7.27, 7.29 and 7.30 and split the individual velocities in the transportation terms to sum of bulk velocity ($\mathbf{v}$) and individual relative velocities ($\hat{\mathbf{v}}^i$) in the mixture. The relative velocities thus separated are included into the flux of the state variables. This assumption helps in considering the terms $\rho^i\hat{\mathbf{v}}^i$ and $\mathbf{p}^i \otimes \hat{\mathbf{v}}^i$ as diffusing flux of mass and momentum respectively and assuming constitutive model for inter-diffusion of the constituents in the mixture (section 7.7.3). It also eases the derivation by assuming a universal transportation velocity for all the state variables in the mixture. Hence, we get the following form for the balance equations of the mechanical state variables.

$$
\begin{aligned}
&\frac{\partial \rho^i}{\partial t} + div(\rho^i \mathbf{v}) + div(\rho^i \hat{\mathbf{v}}^i) = 0 && \forall\, i = m, a \\
&\frac{\partial \mathbf{p}^i}{\partial t} + div(\mathbf{p}^i \otimes \mathbf{v}) + div(\mathbf{p}^i \otimes \hat{\mathbf{v}}^i - \mathbf{T}^i) = \mathbf{b}^i_{mag} + \mathbf{f}^i && \forall\, i = m, a \\
&\underbrace{\frac{\partial s}{\partial t}}_{\frac{\partial \tilde{\epsilon}_{(j)}}{\partial t}} + \underbrace{div(s\mathbf{v})}_{div(\tilde{\epsilon}_{(j)}\mathbf{v})} + \underbrace{div(\mathbf{h})}_{div(\tilde{\mathbf{Q}}_{(j)})} = \underbrace{\xi}_{\tilde{r}_{(j)}}
\end{aligned}
$$

From the form of the equations written above, we can write a general form for the balance equations of the mechanical state variables ($\tilde{\epsilon} = [\rho^m, \rho^a, \mathbf{p}^m_1, \mathbf{p}^m_2, \mathbf{p}^m_3, \mathbf{p}^a_1, \mathbf{p}^a_2, \mathbf{p}^a_3, s]^T$) in terms of bulk fluxes ($\tilde{\mathbf{Q}} = [\rho^m\hat{\mathbf{v}}^m, \rho^a\hat{\mathbf{v}}^a, \mathbf{p}^m_1\hat{\mathbf{v}}^m - \mathbf{T}^m_1, \mathbf{p}^m_2\hat{\mathbf{v}}^m - \mathbf{T}^m_2, \mathbf{p}^m_3\hat{\mathbf{v}}^m - \mathbf{T}^m_3, \mathbf{p}^a_1\hat{\mathbf{v}}^a - \mathbf{T}^a_1, \mathbf{p}^a_2\hat{\mathbf{v}}^a - \mathbf{T}^a_2, \mathbf{p}^a_3\hat{\mathbf{v}}^a - \mathbf{T}^a_3, \mathbf{h}]^T$) and production rates ($\tilde{r} = [0, 0, \mathbf{b}^m_{mag(1)} + \mathbf{f}^m_1, \mathbf{b}^m_{mag(2)} + \mathbf{f}^m_2, \mathbf{b}^m_{mag(3)} + \mathbf{f}^m_3, \mathbf{f}^a_1, \mathbf{f}^a_2, \mathbf{f}^a_3, \xi]^T$) as given below. This assumes that transportation of the state variables occur only due to the bulk velocity ($\mathbf{v}$).

$$\frac{\partial}{\partial t}\underbrace{\begin{bmatrix}\rho^m\\ \rho^a\\ \mathbf{p}_1^m\\ \mathbf{p}_2^m\\ \mathbf{p}_3^m\\ \mathbf{p}_1^a\\ \mathbf{p}_2^a\\ \mathbf{p}_3^a\\ s\end{bmatrix}}_{\tilde{\epsilon}} + div\Big(\underbrace{\begin{bmatrix}\rho^m\\ \rho^a\\ \mathbf{p}_1^m\\ \mathbf{p}_2^m\\ \mathbf{p}_3^m\\ \mathbf{p}_1^a\\ \mathbf{p}_2^a\\ \mathbf{p}_3^a\\ s\end{bmatrix}}_{\tilde{\epsilon}\otimes\mathbf{v}} \otimes \begin{bmatrix}\mathbf{v}_1\\ \mathbf{v}_2\\ \mathbf{v}_3\end{bmatrix}\Big)$$

$$+div\Big(\underbrace{\begin{bmatrix}\rho^m\hat{\mathbf{v}}_1^m & \rho^m\hat{\mathbf{v}}_2^m & \rho^m\hat{\mathbf{v}}_3^m\\ \rho^a\hat{\mathbf{v}}_1^a & \rho^a\hat{\mathbf{v}}_2^a & \rho^a\hat{\mathbf{v}}_3^a\\ \mathbf{p}_1^m\hat{\mathbf{v}}_1^m-\mathbf{T}_{11}^m & \mathbf{p}_1^m\hat{\mathbf{v}}_2^m-\mathbf{T}_{12}^m & \mathbf{p}_1^m\hat{\mathbf{v}}_3^m-\mathbf{T}_{13}^m\\ \mathbf{p}_2^m\hat{\mathbf{v}}_1^m-\mathbf{T}_{21}^m & \mathbf{p}_2^m\hat{\mathbf{v}}_2^m-\mathbf{T}_{22}^m & \mathbf{p}_2^m\hat{\mathbf{v}}_3^m-\mathbf{T}_{23}^m\\ \mathbf{p}_3^m\hat{\mathbf{v}}_1^m-\mathbf{T}_{31}^m & \mathbf{p}_3^m\hat{\mathbf{v}}_2^m-\mathbf{T}_{32}^m & \mathbf{p}_3^m\hat{\mathbf{v}}_3^m-\mathbf{T}_{33}^m\\ \mathbf{p}_1^a\hat{\mathbf{v}}_1^a-\mathbf{T}_{11}^a & \mathbf{p}_1^a\hat{\mathbf{v}}_2^a-\mathbf{T}_{12}^a & \mathbf{p}_1^a\hat{\mathbf{v}}_3^a-\mathbf{T}_{13}^a\\ \mathbf{p}_2^a\hat{\mathbf{v}}_1^a-\mathbf{T}_{21}^a & \mathbf{p}_2^a\hat{\mathbf{v}}_2^a-\mathbf{T}_{22}^a & \mathbf{p}_2^a\hat{\mathbf{v}}_3^a-\mathbf{T}_{23}^a\\ \mathbf{p}_3^a\hat{\mathbf{v}}_1^a-\mathbf{T}_{31}^a & \mathbf{p}_3^a\hat{\mathbf{v}}_2^a-\mathbf{T}_{32}^a & \mathbf{p}_3^a\hat{\mathbf{v}}_3^a-\mathbf{T}_{33}^a\\ \mathbf{h}_1 & \mathbf{h}_2 & \mathbf{h}_3\end{bmatrix}}_{\tilde{\mathbf{Q}}}\Big) = \underbrace{\begin{bmatrix}0\\ 0\\ \mathbf{b}_{mag(1)}^m+\mathbf{f}_1^m\\ \mathbf{b}_{mag(2)}^m+\mathbf{f}_2^m\\ \mathbf{b}_{mag(3)}^m+\mathbf{f}_3^m\\ \mathbf{f}_1^a\\ \mathbf{f}_2^a\\ \mathbf{f}_3^a\\ \xi\end{bmatrix}}_{\tilde{\mathbf{r}}} \tag{7.72}$$

Hence, the balance law for the individual component $\tilde{\epsilon}_{(j)}$ is of the form given in equation 7.73 below.

$$\frac{\partial\tilde{\epsilon}_{(j)}}{\partial t} + div(\tilde{\epsilon}_{(j)}\mathbf{v}) + div(\tilde{\mathbf{Q}}_{(j)}) = \tilde{r}_{(j)} \quad \forall\, j = 1, 2, ..., 9 \tag{7.73}$$

We can also write the balance equation of the energy of the bulk mixture similarly, as the transportation due to the bulk flow velocity and a composite flux due to both the relative velocity of the individual constituents and their fluxes.

$$\begin{aligned} \frac{\partial u}{\partial t} + div(u^m \mathbf{v}^m + u^a \mathbf{v}^a) + div(\mathbf{Q}_u) &= w_{mag} \\ \implies \frac{\partial u}{\partial t} + div(u\mathbf{v}) + div(\underbrace{u^m \hat{\mathbf{v}}^m + u^a \hat{\mathbf{v}}^a + \mathbf{Q}_u}_{=\tilde{\mathbf{Q}}_u}) &= w_{mag} \end{aligned} \tag{7.74}$$

With this form of the balance equation for the energy of the mixture, we perform the following derivation of the energy equation using the understanding that the energy of the mixture is a function of the state variables as defined in section 7.7.1. Here, the magnetic energy supplied by the magnetic fields given in equation 7.24 is substituted.

$$\begin{aligned} \frac{\partial u}{\partial t} + div(u\mathbf{v}) + div(\tilde{\mathbf{Q}}_u) &= w_{mag} \\ \implies \sum \Pi^j \frac{\partial \epsilon^j}{\partial t} + div(u\mathbf{v}) + div(\tilde{\mathbf{Q}}_u) &= w_{mag} \\ \implies \sum_{j=1}^{9} \tilde{\Pi}_{(j)} \frac{\partial \tilde{\epsilon}_{(j)}}{\partial t} + \bar{\mathbf{M}} \cdot \frac{\partial \mathbf{B}}{\partial t} + div(u\mathbf{v}) + div(\tilde{\mathbf{Q}}_u) &= -\mathbf{M} \cdot \frac{\partial \mathbf{B}}{\partial t} \\ \implies \sum_{j=1}^{9} \tilde{\Pi}_{(j)} \frac{\partial \tilde{\epsilon}_{(j)}}{\partial t} + (\bar{\mathbf{M}} + \mathbf{M}) \cdot \frac{\partial \mathbf{B}}{\partial t} + div(u\mathbf{v}) + div(\tilde{\mathbf{Q}}_u) &= 0 \end{aligned}$$

Now, substituting the equation for the rate of change of the state variable ($\tilde{\epsilon}_{(j)}$) from equation 7.73 into the equation above, we get the following form for the energy balance equation.

$$\begin{aligned} &\sum_{j=1}^{9} \tilde{\Pi}_{(j)} (\tilde{r}_{(j)} - div(\tilde{\epsilon}_{(j)}\mathbf{v}) - div(\tilde{\mathbf{Q}}_{(j)})) \\ &+ (\bar{\mathbf{M}} + \mathbf{M}) \cdot \frac{\partial \mathbf{B}}{\partial t} + div(u\mathbf{v}) + div(\tilde{\mathbf{Q}}_u) = 0 \end{aligned}$$

$$\implies (\bar{\mathbf{M}} + \mathbf{M}) \cdot \frac{\partial \mathbf{B}}{\partial t} + \sum_{j=1}^{9} \tilde{\Pi}_{(j)} \tilde{r}_{(j)}$$

$$+div(u\mathbf{v}) - \sum_{j=1}^{9} \tilde{\Pi}_{(j)} div(\tilde{\epsilon}_{(j)}\mathbf{v}) + div(\tilde{\mathbf{Q}}_u) - \sum_{j=1}^{9} \tilde{\Pi}_{(j)} div(\tilde{\mathbf{Q}}_{(j)}) = 0$$

$$\implies (\bar{\mathbf{M}} + \mathbf{M}) \cdot \frac{\partial \mathbf{B}}{\partial t} + \sum_{j=1}^{9} \tilde{\Pi}_{(j)} \tilde{r}_{(j)}$$

$$+(u - \sum_{j=1}^{9} \tilde{\Pi}_{(j)} \tilde{\epsilon}_{(j)}) div(\mathbf{v}) + (grad(u) - \sum_{j=1}^{9} \tilde{\Pi}_{(j)} grad(\tilde{\epsilon}_{(j)})) \cdot \mathbf{v}$$

$$+div(\tilde{\mathbf{Q}}_u - \sum_{j=1}^{9} \tilde{\Pi}_{(j)} \tilde{\mathbf{Q}}_{(j)}) + \sum_{j=1}^{9} grad(\tilde{\Pi}_{(j)}) \cdot \tilde{\mathbf{Q}}_{(j)} = 0 \tag{7.75}$$

In equation 7.75, we get the net energy balance in the bulk mixture due to the individual state variables in the mixture. Here, each summation terms in the equation indicate different phenomenon due to the behavior of the state variables of the constituents in the mixture. $(\bar{\mathbf{M}} + \mathbf{M}) \cdot \frac{\partial \mathbf{B}}{\partial t}$ is the net energy produced or dissipated in the RVE of the bulk fluid due to the change in magnetic induction in the mixture. Here, the model for the driving force ($\bar{\mathbf{M}}$) quantifies the amount of energy dissipated due to eddy currents developed in the mixture. As discussed in section 7.2, this energy is taken as zero as we assume that no eddy currents are produced in the mixture (magneto quasistatics). $\sum_{j=1}^{9} \tilde{\Pi}_{(j)} \tilde{r}_{(j)}$ is the total energy produced in the bulk fluid due to the production of the state variables in the RVE. $(u - \sum_{j=1}^{9} \tilde{\Pi}_{(j)} \tilde{\epsilon}_{(j)}) div(\mathbf{v})$ and $(grad(u) - \sum_{j=1}^{9} \tilde{\Pi}_{(j)} grad(\tilde{\epsilon}_{(j)})) \cdot \mathbf{v}$ are the net energy lost due to the convection of the bulk fluid in the RVE. $div(\tilde{\mathbf{Q}}_u - \sum_{j=1}^{9} \tilde{\Pi}_{(j)} \tilde{\mathbf{Q}}_{(j)})$ is the net work done on the RVE due to flux of the state variables at the boundaries. $\sum_{j=1}^{9} grad(\tilde{\Pi}_{(j)}) \cdot \tilde{\mathbf{Q}}_{(j)}$ is the net internal energy dissipated due to the interaction between the flux and the driving forces in the RVE.

Now, we compute the summation terms individually and substitute them into the balance equation to get the final balance equation in terms of the state variables, their driving

forces and fluxes. This is expressed in terms of the bulk velocity and the relative velocity of the magnetic constituent. This will be useful in the ensuring the Clausius-Duhem inequality under the constitutive models designed for the bulk flow behavior and magnetic constituent behavior. Now, first we work on the energy produced by the production of the state variables in the RVE. We compute the summation and compute the energy production in terms of the bulk velocity ($\mathbf{v}$) and the relative velocity of the magnetic media.

$$\begin{aligned}
\sum_{j=1}^{9} \tilde{\Pi}_{(j)}\tilde{r}_{(j)} &= A^m(0) + A^a(0) + \mathbf{v}^m \cdot (\mathbf{b}^m_{mag} + \mathbf{f}^m) + \mathbf{v}^a \cdot \mathbf{f}^a + \theta\xi \\
&= \theta\xi + (\mathbf{b}^m_{mag} + \mathbf{f}^m + \mathbf{f}^a) \cdot \mathbf{v} + (\mathbf{b}^m_{mag} + \mathbf{f}^m) \cdot \hat{\mathbf{v}}^m + \mathbf{f}^a \cdot \hat{\mathbf{v}}^a \\
&= \theta\xi + \mathbf{b}^m_{mag} \cdot \mathbf{v} + (\mathbf{b}^m_{mag} + \mathbf{f}^m) \cdot \hat{\mathbf{v}}^m - \mathbf{f}^a \cdot \frac{x^m}{x^a}\hat{\mathbf{v}}^m \\
&= \theta\xi + \mathbf{b}^m_{mag} \cdot \mathbf{v} + (\mathbf{b}^m_{mag} + \mathbf{f}^m - \frac{x^m}{x^a}\mathbf{f}^a) \cdot \hat{\mathbf{v}}^m \\
&= \theta\xi + \mathbf{b}^m_{mag} \cdot \mathbf{v} + (\mathbf{b}^m_{mag} + (1 + \frac{x^m}{x^a})\mathbf{f}^m) \cdot \hat{\mathbf{v}}^m \\
&= \theta\xi + \mathbf{b}^m_{mag} \cdot \mathbf{v} + (\mathbf{b}^m_{mag} + \frac{\mathbf{f}^m}{x^a}) \cdot \hat{\mathbf{v}}^m
\end{aligned} \tag{7.76}$$

Now let's look at the pressure energy produced in the RVE due to the expansion and contraction of the bulk fluid in transportation. We can define a thermodynamic pressure in the bulk fluid due to the mechanical co-energy in the bulk fluid as follows,

$$(u - \sum_{j=1}^{9} \tilde{\Pi}_{(j)}\tilde{\epsilon}_{(j)})div(\mathbf{v}) = -\hat{p}\, div(\mathbf{v}) \tag{7.77}$$

$$\text{where,} \quad \hat{p} = \sum_{j=1}^{9} \tilde{\Pi}_{(j)}\tilde{\epsilon}_{(j)} - u$$

Now, let's evaluate the net external transportation energy at the boundaries of the bulk

RVE. At first, let's compute the gradient of total energy($u(\rho^i, \mathbf{p}^i, s, \mathbf{B})$) in the bulk fluid.

$$\begin{aligned} grad(u) &= \sum_{j=1}^{9} \tilde{\Pi}_{(j)} grad(\tilde{\epsilon}_{(j)}) + grad(\mathbf{B})^T \frac{\partial u}{\partial \mathbf{B}} \\ &= \sum_{j=1}^{9} \tilde{\Pi}_{(j)} grad(\tilde{\epsilon}_{(j)}) + grad(\mathbf{B})^T \bar{\mathbf{M}} \end{aligned}$$

Thus, the production of the net external transportation energy at the boundaries of the RVE is as follows,

$$(grad(u) - \sum_{j=1}^{9} \tilde{\Pi}_{(j)} grad(\tilde{\epsilon}_{(j)})) \cdot \mathbf{v} = grad(\mathbf{B})^T \bar{\mathbf{M}} \cdot \mathbf{v} \tag{7.78}$$

Now, let's evaluate the net external work done in the RVE of the bulk fluid due to material, momentum, entropy and energy fluxes into the bulk RVE. We start by computing the net energy flux into the RVE.

$$\begin{aligned} \tilde{\mathbf{Q}}_u - \sum_{j=1}^{9} \tilde{\Pi}_{(j)} \tilde{\mathbf{Q}}_{(j)} &= \mathbf{Q}_u + \sum_{i \in \{m,a\}} u^i \hat{\mathbf{v}}^i - (\sum_{i \in \{m,a\}} (A^i \rho^i \hat{\mathbf{v}}^i + (\mathbf{p}^i \otimes \hat{\mathbf{v}}^i - \mathbf{T}^i)^T \mathbf{v}^i) + \theta \mathbf{h}) \\ &= \mathbf{Q}_u + \sum_{i \in \{m,a\}} u^i \hat{\mathbf{v}}^i - (\sum_{i \in \{m,a\}} ((A_0^i + A_m^i - \frac{\mathbf{p}^i \cdot \mathbf{p}^i}{2(\rho^i)^2}) \rho^i \hat{\mathbf{v}}^i \\ &\quad + (\mathbf{p}^i \otimes \hat{\mathbf{v}}^i - \mathbf{T}^i)^T \mathbf{v}^i) + \theta \mathbf{h}) \\ &= \mathbf{Q}_u - (\sum_{i \in \{m,a\}} (A_0^i \rho^i \hat{\mathbf{v}}^i - \mathbf{T}^{iT} \mathbf{v}^i) + \theta \mathbf{h}) \\ &\quad + \sum_{i \in \{m,a\}} (u^i \hat{\mathbf{v}}^i - (A_m^i - \frac{\mathbf{p}^i \cdot \mathbf{p}^i}{2(\rho^i)^2}) \rho^i \hat{\mathbf{v}}^i - (\mathbf{p}^i \otimes \hat{\mathbf{v}}^i)^T \mathbf{v}^i) \end{aligned}$$

The flux of energy into the RVE is defined as the flux of energies due to all the fluxes of the individual state variables into the RVE. This is the external work done by the fluxes onto the RVE at its boundaries. This also mean that we assume that only mechanical state variables of the system does external work on the RVE and the magnetic fields does an

internal work through the production term (w_{mag}) assumed earlier in the energy balance equation.

$$\mathbf{Q}_u = \sum_{i\in\{m,a\}} (A_0^i \rho^i \hat{\mathbf{v}}^i - \mathbf{T}^{iT}\mathbf{v}^i) + \theta\mathbf{h} \tag{7.79}$$

Substituting this form of the energy flux ($\mathbf{Q_u}$), given in equation 7.79, into the net external flux expression, $\tilde{\mathbf{Q}}_u - \sum_{j=1}^{9} \tilde{\Pi}_{(j)}\tilde{\mathbf{Q}}_{(j)}$, to compute the following derivation. Into this expression we also substitute the expressions for the energy of the constituents, given in equations 7.63 and 7.64, to get the final form of the expression.

$$\begin{aligned}
\tilde{\mathbf{Q}}_u - \sum_{j=1}^{9} \tilde{\Pi}_{(j)}\tilde{\mathbf{Q}}_{(j)} &= \sum_{i\in\{m,a\}} (u^i\hat{\mathbf{v}}^i - (A_m^i - \frac{\mathbf{p}^i\cdot\mathbf{p}^i}{2(\rho^i)^2})\rho^i\hat{\mathbf{v}}^i - (\mathbf{p}^i\otimes\hat{\mathbf{v}}^i)^T\mathbf{v}^i) \\
&= \sum_{i\in\{m,a\}} ((x^i u_0 + \frac{\mathbf{p^i}\cdot\mathbf{p^i}}{2\rho^i})\hat{\mathbf{v}}^i - A_m^i\rho^i\hat{\mathbf{v}}^i - (\mathbf{p}^i\cdot\mathbf{v}^i - \frac{1}{2}\mathbf{p}^i\cdot\mathbf{v}^i))\hat{\mathbf{v}}^i) \\
&\quad + u_{mag}\hat{\mathbf{v}}^m \\
&= u_0 \sum_{i\in\{m,a\}} x^i\hat{\mathbf{v}}^i + \sum_{i\in\{m,a\}} (\frac{1}{2}\mathbf{p}^i\cdot\mathbf{v}^i - \frac{1}{2}\mathbf{p}^i\cdot\mathbf{v}^i)\hat{\mathbf{v}}^i) \\
&\quad + u_{mag}\hat{\mathbf{v}}^m - A_m^m\rho^m\hat{\mathbf{v}}^m \\
&= (u_{mag} - A_m^m\rho^m)\hat{\mathbf{v}}^m
\end{aligned}$$

Now calculating the divergence of the net external flux into the RVE we get the final form of the net external flux into the RVE.

$$\begin{aligned}
div(\tilde{\mathbf{Q}}_u - \sum_{j=1}^{9} \tilde{\Pi}_{(j)}\tilde{\mathbf{Q}}_{(j)}) &= div((u_{mag} - A_m^m\rho^m)\hat{\mathbf{v}}^m) \\
&= grad(u_{mag} - A_m^m\rho^m)\cdot\hat{\mathbf{v}}^m + (u_{mag} - A_m^m\rho^m)\, div(\hat{\mathbf{v}}^m) \\
&= (\frac{\partial u_{mag}}{\partial\rho^m} grad(\rho^m) + grad(\mathbf{B})^T\frac{\partial u_{mag}}{\partial\mathbf{B}} - \rho^m\, grad(A_m^m)
\end{aligned}$$

$$
\begin{aligned}
&- A_m^m \, grad(\rho^m)) \cdot \hat{\mathbf{v}}^m - \hat{p}_m \, div(\hat{\mathbf{v}}^m) \\
&= (grad(\mathbf{B})^T \bar{\mathbf{M}} - \rho^m \, grad(A_m^m)) \cdot \hat{\mathbf{v}}^m - \hat{p}_m \, div(\hat{\mathbf{v}}^m) \quad (7.80)
\end{aligned}
$$

Now, let's evaluate the internal work done by the interaction of the fluxes with the driving forces of the state variables.

$$
\begin{aligned}
\sum_{j=1}^{9} grad(\tilde{\Pi}_{(j)}) \cdot \tilde{\mathbf{Q}}_{(j)} &= \sum_{i \in \{m,a\}} (grad(A^i) \cdot (\rho^i \hat{\mathbf{v}}^i) + grad(\mathbf{v}^i) \cdot (\mathbf{p}^i \otimes \hat{\mathbf{v}}^i - \mathbf{T}^i)) \\
&\quad + grad(\theta) \cdot \mathbf{h} \\
&= \sum_{i \in \{m,a\}} (grad(A_0^i + A_m^i - \frac{\mathbf{p}^i \cdot \mathbf{p}^i}{2(\rho^i)^2}) \cdot (\rho^i \hat{\mathbf{v}}^i) \\
&\quad + grad(\mathbf{v}^i) \cdot (\mathbf{p}^i \otimes \hat{\mathbf{v}}^i - \mathbf{T}^i)) + grad(\theta) \cdot \mathbf{h} \\
&= \sum_{i \in \{m,a\}} (grad(A_0^i) \cdot (\rho^i \hat{\mathbf{v}}^i) - grad(\mathbf{v}^i) \cdot \mathbf{T}^i) + grad(\theta) \cdot \mathbf{h} \\
&\quad + grad(A_m^m) \cdot \rho^m \hat{\mathbf{v}}^m - \sum_{i \in \{m,a\}} grad(\frac{\mathbf{v}^i \cdot \mathbf{v}^i}{2}) \cdot (\rho^i \hat{\mathbf{v}}^i) \\
&\quad + \sum_{i \in \{m,a\}} grad(\mathbf{v}^i) \cdot (\mathbf{p}^i \otimes \hat{\mathbf{v}}^i) \\
&= \sum_{i \in \{m,a\}} (grad(A_0^i) \cdot (\rho^i \hat{\mathbf{v}}^i) - grad(\mathbf{v}^i) \cdot \mathbf{T}^i) + grad(\theta) \cdot \mathbf{h} \\
&\quad \sum_{i \in \{m,a\}} (grad(\mathbf{v}^i) \hat{\mathbf{v}}^i \cdot \mathbf{p}^i - \frac{1}{2} 2 grad(\mathbf{v}^i)^T \mathbf{v}^i \cdot (\rho^i \hat{\mathbf{v}}^i)) \\
&\quad + grad(A_m^m) \cdot \rho^m \hat{\mathbf{v}}^m \\
&= \sum_{i \in \{m,a\}} (grad(A_0^i) \cdot (\rho^i \hat{\mathbf{v}}^i) - grad(\mathbf{v}^i) \cdot \mathbf{T}^i) + grad(\theta) \cdot \mathbf{h} \\
&\quad + grad(A_m^m) \cdot \rho^m \hat{\mathbf{v}}^m
\end{aligned}
$$

Now changing the above expression to the form of bulk and relative velocity of the

magnetic medium.

$$\begin{aligned}\sum_{j=1}^{9} grad\tilde{\Pi}_{(j)} \cdot \tilde{\mathbf{Q}}_{(j)} &= grad(A_0^m) \cdot (\rho^m \hat{\mathbf{v}}^m) + grad(A_0^a) \cdot (\rho^a \hat{\mathbf{v}}^a) - grad(\mathbf{v}^m) \cdot \mathbf{T}^m \\ &\quad - grad(\mathbf{v}^a) \cdot \mathbf{T}^a + grad(\theta) \cdot \mathbf{h} + grad(A_m^m) \cdot \rho^m \hat{\mathbf{v}}^m \\ &= \rho^m \, grad(A_0^m) \cdot \hat{\mathbf{v}}^m - \rho^a \, grad(A_0^a) \cdot \frac{x^m}{x^a} \hat{\mathbf{v}}^m - grad(\mathbf{v}) \cdot \mathbf{T}^m \\ &\quad - grad(\mathbf{v}) \cdot \mathbf{T}^a - grad(\hat{\mathbf{v}}^m) \cdot \mathbf{T}^m - grad(-\frac{x^m}{x^a} \hat{\mathbf{v}}^m) \cdot \mathbf{T}^a \\ &\quad + grad(\theta) \cdot \mathbf{h} + \rho^m grad(A_m^m) \cdot \hat{\mathbf{v}}^m \\ &= (\rho^m \, grad(A_0^m) + \rho^m \, grad(A_m^m) - \rho^a \frac{x^m}{x^a} \, grad(A_0^a)) \cdot \hat{\mathbf{v}}^m \\ &\quad - grad(\mathbf{v}) \cdot \mathbf{T} - grad(\hat{\mathbf{v}}^m) \cdot \mathbf{T}^m + grad(\frac{x^m}{x^a} \hat{\mathbf{v}}^m) \cdot \mathbf{T}^a \\ &\quad + grad(\theta) \cdot \mathbf{h}\end{aligned}$$

Considering the relationship between the volume concentrations of the constituents, the following relationship can be computed.

$$\begin{aligned} x^m + x^a &= 1 \\ \implies grad(x^m) + grad(x^a) &= 0 \\ \implies grad(x^a) &= -grad(x^m) \end{aligned}$$

Substituting the above equations into the internal work relationship.

$$\begin{aligned}\sum_{j=1}^{9} grad\tilde{\Pi}_{(j)}) \cdot \tilde{\mathbf{Q}}_{(j)} &= (\rho^m \, grad(A_0^m) + \rho^m \, grad(A_m^m) - \rho^a \frac{x^m}{x^a} \, grad(A_0^a)) \cdot \hat{\mathbf{v}}^m \\ &\quad - grad(\mathbf{v}) \cdot \mathbf{T} - grad(\hat{\mathbf{v}}^m) \cdot \mathbf{T}^m + \frac{x^m}{x^a} grad(\hat{\mathbf{v}}^m) \cdot \mathbf{T}^a \\ &\quad + \hat{\mathbf{v}}^m \otimes grad(\frac{1}{x^a} - 1) \cdot \mathbf{T}^a + grad(\theta) \cdot \mathbf{h}\end{aligned}$$

$$
\begin{aligned}
&= (\rho^m\ grad(A_0^m) + \rho^m\ grad(A_m^m) - \rho^a \frac{x^m}{x^a}\ grad(A_0^a) \\
&\quad - \frac{1}{(x^a)^2}\mathbf{T}^a grad(x^a)) \cdot \hat{\mathbf{v}}^m - grad(\mathbf{v}) \cdot \mathbf{T} \\
&\quad - grad(\hat{\mathbf{v}}^m) \cdot (\mathbf{T}^m - \frac{x^m}{x^a}(\mathbf{T} - \mathbf{T}^m)) + grad(\theta) \cdot \mathbf{h} \\
&= (\rho^m\ grad(A_0^m) + \rho^m\ grad(A_m^m) - \rho^a \frac{x^m}{x^a}\ grad(A_0^a) \\
&\quad + \frac{\mathbf{T} - \mathbf{T}^m}{(x^a)^2} grad(x^m)) \cdot \hat{\mathbf{v}}^m - grad(\mathbf{v}) \cdot \mathbf{T} \\
&\quad - grad(\hat{\mathbf{v}}^m) \cdot \frac{(\mathbf{T}^m - x^m\mathbf{T})}{x^a} + grad(\theta) \cdot \mathbf{h}
\end{aligned} \tag{7.81}
$$

Substituting equations 7.76, 7.77, 7.78, 7.80 and 7.81into the original balance of energy equation, given in equation 7.75, we get the following derivation for the form of the balance equation.

$$
\begin{aligned}
&(\bar{\mathbf{M}} + \mathbf{M}) \cdot \frac{\partial \mathbf{B}}{\partial t} + \sum_{j=1}^{9} \tilde{\Pi}_{(j)} \tilde{r}_{(j)} \\
&+(u - \sum_{j=1}^{9} \tilde{\Pi}_{(j)} \tilde{\epsilon}_{(j)}) div(\mathbf{v}) + (grad(u) - \sum_{j=1}^{9} \tilde{\Pi}_{(j)} grad(\tilde{\epsilon}_{(j)})) \cdot \mathbf{v} \\
&+div(\tilde{\mathbf{Q}}_u - \sum_{j=1}^{9} \tilde{\Pi}_{(j)} \tilde{\mathbf{Q}}_{(j)}) + \sum_{j=1}^{9} grad(\tilde{\Pi}_{(j)}) \cdot \tilde{\mathbf{Q}}_{(j)} = 0 \\
&\implies (\bar{\mathbf{M}} + \mathbf{M}) \cdot \frac{\partial \mathbf{B}}{\partial t} + \theta\xi + \mathbf{b}_{mag}^m \cdot \mathbf{v} + (\mathbf{b}_{mag}^m + \frac{\mathbf{f}^m}{x^a}) \cdot \hat{\mathbf{v}}^m \\
&-\hat{p}\ div(\mathbf{v}) + grad(\mathbf{B})^T \bar{\mathbf{M}} \cdot \mathbf{v} + (grad(\mathbf{B})^T \bar{\mathbf{M}} - \rho^m\ grad(A_m^m)) \cdot \hat{\mathbf{v}}^m \\
&-\hat{p}_m\ div(\hat{\mathbf{v}}^m) + (\rho^m\ grad(A_0^m) + \rho^m\ grad(A_m^m) - \rho^a \frac{x^m}{x^a}\ grad(A_0^a) \\
&+\frac{\mathbf{T} - \mathbf{T}^m}{(x^a)^2} grad(x^m)) \cdot \hat{\mathbf{v}}^m - grad(\mathbf{v}) \cdot \mathbf{T} - grad(\hat{\mathbf{v}}^m) \cdot \frac{(\mathbf{T}^m - x^m\mathbf{T})}{x^a} \\
&+grad(\theta) \cdot \mathbf{h} = 0 \\
&\implies \theta\xi + grad(\theta) \cdot \mathbf{h} - grad(\mathbf{v}) \cdot (\mathbf{T} + \hat{p}\mathbf{I}) - grad(\hat{\mathbf{v}}^m) \cdot (\frac{\mathbf{T}^m - x^m\mathbf{T}}{x^a} \\
&+\hat{p}_m\mathbf{I}) + (\bar{\mathbf{M}} + \mathbf{M}) \cdot \frac{\partial \mathbf{B}}{\partial t} + (\mathbf{b}_{mag}^m + grad(\mathbf{B})^T \bar{\mathbf{M}}) \cdot \mathbf{v} + (\mathbf{b}_{mag}^m
\end{aligned}
$$

$$
\begin{aligned}
&+grad(\mathbf{B})^T\bar{\mathbf{M}} + \frac{\mathbf{f}^m}{x^a} - \rho^m\, grad(A_m^m) + \rho^m\, grad(A_m^m) \\
&+\rho^m\, grad(A_0^m) - \rho^a \frac{x^m}{x^a}\, grad(A_0^a) + \frac{\mathbf{T}-\mathbf{T}^m}{(x^a)^2} grad(x^m)) \cdot \hat{\mathbf{v}}^m = 0 \\
\implies\ &\theta\xi + grad(\theta)\cdot\mathbf{h} - grad(\mathbf{v})\cdot(\mathbf{T}+\hat{p}\mathbf{I}) - grad(\hat{\mathbf{v}}^m)\cdot(\frac{\mathbf{T}^m - x^m\mathbf{T}}{x^a} + \hat{p}_m\mathbf{I}) \\
&+(\bar{\mathbf{M}}+\mathbf{M})\cdot\frac{\partial\mathbf{B}}{\partial t} + (\mathbf{b}_{mag}^m + grad(\mathbf{B})^T\bar{\mathbf{M}})\cdot\mathbf{v} + (\mathbf{b}_{mag}^m + grad(\mathbf{B})^T\bar{\mathbf{M}} \\
&+\frac{\mathbf{f}^m}{x^a} + \rho^m\, grad(A_0^m) - \rho^a\frac{x^m}{x^a}\, grad(A_0^a) + \frac{\mathbf{T}-\mathbf{T}^m}{(x^a)^2} grad(x^m))\cdot\hat{\mathbf{v}}^m = 0
\end{aligned}
$$

From this, we calculate the entropy energy produced in the RVE as follows

$$
\begin{aligned}
\theta\xi = &-grad(\theta)\cdot\mathbf{h} + grad(\mathbf{v})\cdot(\mathbf{T}+\hat{p}\mathbf{I}) + grad(\hat{\mathbf{v}}^m)\cdot(\frac{\mathbf{T}^m - x^m\mathbf{T}}{x^a} + \hat{p}_m\mathbf{I}) \\
&-(\bar{\mathbf{M}}+\mathbf{M})\cdot\frac{\partial\mathbf{B}}{\partial t} - (\mathbf{b}_{mag}^m + grad(\mathbf{B})^T\bar{\mathbf{M}})\cdot\mathbf{v} - ((\mathbf{b}_{mag}^m + grad(\mathbf{B})^T\bar{\mathbf{M}})x^a \\
&+\mathbf{f}^m + \rho^m x^a\, grad(A_0^m) - \rho^a x^m\, grad(A_0^a) + \frac{\mathbf{T}-\mathbf{T}^m}{x^a} grad(x^m))\cdot\frac{\hat{\mathbf{v}}^m}{x^a}
\end{aligned}
\tag{7.82}
$$

Equation 7.82 is the final expression developed for $\theta\xi$ from the energy balance equation after considering the form of the energy function and the energy flux in the mixture. This expression is represented in terms of the bulk velocity ($\mathbf{v}$) and the diffusive velocity of the magnetic component ($\hat{\mathbf{v}}^{\mathbf{m}}$). To this expression we apply the Clausius-Duhem inequality to ensure that the mixture always undergoes processes with non-negative production of entropy given in equation 7.71. The final inequality thus computed is given below.

$$
\begin{aligned}
&-grad(\theta)\cdot\mathbf{h} + grad(\mathbf{v})\cdot(\mathbf{T}+\hat{p}\mathbf{I}) + grad(\hat{\mathbf{v}}^m)\cdot(\frac{\mathbf{T}^m - x^m\mathbf{T}}{x^a} + \hat{p}_m\mathbf{I}) \\
&-(\bar{\mathbf{M}}+\mathbf{M})\cdot\frac{\partial\mathbf{B}}{\partial t} - (\mathbf{b}_{mag}^m + grad(\mathbf{B})^T\bar{\mathbf{M}})\cdot\mathbf{v} - ((\mathbf{b}_{mag}^m + grad(\mathbf{B})^T\bar{\mathbf{M}})x^a \\
&+\mathbf{f}^m + \rho^m x^a\, grad(A_0^m) - \rho^a x^m\, grad(A_0^a) + \frac{\mathbf{T}-\mathbf{T}^m}{x^a} grad(x^m))\cdot\frac{\hat{\mathbf{v}}^m}{x^a} \geq 0
\end{aligned}
\tag{7.83}
$$

The inequality given in 7.83 acts as a constraint to the constitutive models for the

fluxes $\mathbf{h}$, $\mathbf{T}$, A^i and the interactive force $\mathbf{f}^m$ in the mixture. This constraint is the entropy constraint on the mixture, which ensures that the constitutive models of the mixture follows the second law of thermodynamics.

7.7.3 Constitutive Models

The constitutive models for the mixture are to be defined such that both the Clausius-Duhem inequality in equation 7.83 and the volume additivity constraint given in equation 7.55 are satisfied. Thus, we define the following inequality where the volume additivity constraint is added to the original inequality with a Legendre Multiplier (λ) creating the mixture's inequality constraint that all constitutive models in the mixture needs to satisfy.

$$\begin{aligned}
&-grad(\theta)\cdot\mathbf{h} + grad(\mathbf{v})\cdot(\mathbf{T}+\hat{p}\mathbf{I}) + grad(\hat{\mathbf{v}}^m)\cdot(\frac{\mathbf{T}^m - x^m\mathbf{T}}{x^a} + \hat{p}_m\mathbf{I})\\
&-(\bar{\mathbf{M}}+\mathbf{M})\cdot\frac{\partial\mathbf{B}}{\partial t} - (\mathbf{b}^m_{mag} + grad(\mathbf{B})^T\bar{\mathbf{M}})\cdot\mathbf{v} - ((\mathbf{b}^m_{mag} + grad(\mathbf{B})^T\bar{\mathbf{M}})x^a\\
&+\mathbf{f}^m + \rho^m x^a\, grad(A^m_0) - \rho^a x^m\, grad(A^a_0) + \frac{\mathbf{T}-\mathbf{T}^m}{x^a}grad(x^m))\cdot\frac{\hat{\mathbf{v}}^m}{x^a}\\
&+\lambda\, div(\mathbf{v}) \geq 0\\
&-grad(\theta)\cdot\mathbf{h} + grad(\mathbf{v})\cdot(\mathbf{T}+(\hat{p}+\lambda)\mathbf{I}) + grad(\hat{\mathbf{v}}^m)\cdot(\frac{\mathbf{T}^m - x^m\mathbf{T}}{x^a} + \hat{p}_m\mathbf{I})\\
&-(\bar{\mathbf{M}}+\mathbf{M})\cdot\frac{\partial\mathbf{B}}{\partial t} - (\mathbf{b}^m_{mag} + grad(\mathbf{B})^T\bar{\mathbf{M}})\cdot\mathbf{v} - ((\mathbf{b}^m_{mag} + grad(\mathbf{B})^T\bar{\mathbf{M}})x^a\\
&+\mathbf{f}^m + \rho^m x^a\, grad(A^m_0) - \rho^a x^m\, grad(A^a_0) + \frac{\mathbf{T}-\mathbf{T}^m}{x^a}grad(x^m))\cdot\frac{\hat{\mathbf{v}}^m}{x^a} \geq 0
\end{aligned} \tag{7.84}$$

As discussed earlier, this inequality is applied locally in the mixture. This will ensure that the inequality is satisfied globally by the whole mixture. A set of models for the fluxes can be assumed that satisfies only the above equation, resulting in a thermodynamically consistent set of models that are coupled. It is already discussed in section 7.7.2 that this is a stricter approach as we ensure the inequality locally at every point on the domain rather than on the global entropy production of the mixture.

In this thesis, a much simpler approach is taken by assuming that each term in the above equation satisfies the inequality individually [169]. This approach gives a simple form for the constitutive equation that can be globally satisfied by the mixture. Such an approach will also uncouple the models in such a way that any subset of the models assumed will also satisfy the second law of thermodynamics. Also, in order to ensure that the models satisfy Galilean Invariance, the term of the equation dependent on the velocity of the bulk fluid is to be assumed as zero. Hence, with the above assumption, the set of constraints on the models that can be assumed for the mixture is given below.

$$-(\bar{\mathbf{M}} + \mathbf{M}) \cdot \frac{\partial \mathbf{B}}{\partial t} \geq 0 \quad (7.85)$$

$$-(\mathbf{b}^m_{mag} + grad(\mathbf{B})^T \bar{\mathbf{M}}) \cdot \mathbf{v} = 0 \quad (7.86)$$

$$-grad(\theta) \cdot \mathbf{h} \geq 0 \quad (7.87)$$

$$grad(\mathbf{v}) \cdot (\mathbf{T} + (\hat{p} + \lambda)\mathbf{I}) \geq 0 \quad (7.88)$$

$$grad(\hat{\mathbf{v}}^{\mathbf{m}}) \cdot (\frac{(\mathbf{T}^{\mathbf{m}} - x^m \mathbf{T})}{x^a} + \hat{p}_m \mathbf{I}) \geq 0 \quad (7.89)$$

$$-\frac{1}{x^a}[(\mathbf{b}^m_{mag} + grad(\mathbf{B})^T \bar{\mathbf{M}})x^a + \mathbf{f}^m + \rho^m x^a grad(A^m_0) - \rho^a x^m grad(A^a_0) + \frac{(\mathbf{T} - \mathbf{T}^{\mathbf{m}})}{x^a} \cdot grad(x^m)] \cdot \hat{\mathbf{v}}^{\mathbf{m}} \geq 0 \quad (7.90)$$

$$div(\mathbf{v}) = 0 \quad (7.91)$$

Thus, constitutive models are chosen for the mixture such that they reflect the expected behavior from the fluid too and also satisfy the inequalities given in equations 7.85 to 7.90. This is achieved by choosing appropriate energy functions for the mixture. Discussions on models that are more general are given by Rajagopal and Tao [169], Rajagopal and Wineman [170], Brigadnov and Dorfmann [133], etc. In this thesis, we consider a set of simple models that qualitatively reflect the behavior of the polishing fluid.

7.7.3.1 Magnetic Model

In order to model the magnetic behavior of the mixture, we assume a model such that the no entropy is produced due to the magnetic driving force in the mixture. That is, the internal energy due to the magnetic behavior is conservative in nature. Hence, we get the following model for $\bar{\mathbf{M}}$.

$$\bar{\mathbf{M}} = -\mathbf{M} \tag{7.92}$$

The model above means that we take the driving force in the magnetic fluid to be the negative of the magnetization of the magnetic fluid in the presence of an external magnetic field. Assuming such a model for the driving force gives the following derivation for the magnetic energy (u_{mag}) in the magnetic media.

$$\begin{aligned} \bar{\mathbf{M}} &= \frac{\partial u_{mag}}{\partial \mathbf{B}} \\ \implies \frac{\partial u_{mag}}{\partial \mathbf{B}} &= -\mathbf{M} \\ &= -\frac{\mu_0\, \chi(\rho^m)}{\mu(\rho^m)}\, \mathbf{B} \\ \implies u_{mag} &= -\frac{1}{2}\, \frac{\chi(\rho^m)}{1+\chi(\rho^m)} \mathbf{B}^2 \end{aligned} \tag{7.93}$$

where, $\chi(\rho^m)$ is the magnetic susceptibility of the magnetic component of the mixture. This depends on the density of the magnetic particles in the mixture. In this thesis, we assume a linear model for the susceptibility of the magnetic media.

Now let's consider the model for the magnetic force developed in the mixture. This model has to satisfy the equality given an equation 7.86 to satisfy Galealian Invariance.

The model for the magnetic force is given below.

$$\begin{aligned} \mathbf{b}^{m}_{mag} &= -grad(\mathbf{B})^{T}\bar{\mathbf{M}} \\ &= grad(\mathbf{B})^{T}\mathbf{M} \end{aligned} \tag{7.94}$$

Note that the above model for the magnetic body force ($\mathbf{b}^{m}_{mag}$) is not a new constitutive model developed for the mixture, but rather reflects upon the internal consistency of the Dipole-current circuit model developed for electromagnetic media discussed in section 7.2. Such an entropy conserving model is assumed for this material to be consistent with the earlier works given in the literature for magnetic polishing [133, 171, 168].

7.7.3.2 Entropy Flux

Secondly, we model the entropy flux in the mixture. In the scope of this simulation, we do not study or compute the entropy in the mixture. Hence, the simplest possible model for entropy flux ($\mathbf{h}$) is used, as given below.

$$\mathbf{h} = -k_{\theta} grad(\theta) \tag{7.95}$$

The model given in equation 7.95 gives the simplest form that the no entropy flux into the mixture is directly proportional to the gradient of temperature in the bulk fluid. This is the simplest model chosen as entropy evolution in the mixture is not of interest in this study and this model on substitution satisfies the inequality in equation 7.87.

7.7.3.3 Bulk Rheology

Next, we model the flow behavior of the bulk fluid as an incompressible fluid, whose deviatoric stress is dependent on the rate of Deformation Tensor ($\mathbf{D}$) of the bulk mixture,

B-field ($\mathbf{B}$) and concentration (x^m) of the magnetic component, as given below,

$$\begin{aligned} & \mathbf{T} = -P\mathbf{I} + \mathbf{T}_E(\mathbf{D}, \mathbf{B}, x^m) \\ \text{where,} \qquad & \mathbf{D} = \frac{1}{2}(grad(\mathbf{v}) + (grad(\mathbf{v}))^T) \\ & P \geq 0 \end{aligned} \tag{7.96}$$

where, P is the pressure in the fluid and $\mathbf{T}_E$ is the extra stress in the fluid. The above model gives an incompressible fluid behavior which is compatible with the model for the bulk fluid velocity taken in equation 7.56. In the above model on substitution of inequality 7.88, we get the following.

$$\begin{aligned} grad(\mathbf{v}) : (\mathbf{T} + (\hat{p} + \lambda)\mathbf{I}) &= grad(\mathbf{v}) : (-P\mathbf{I} + \mathbf{T}_E(\mathbf{D}, \mathbf{B}, x^m) + (\hat{p} + \lambda)\mathbf{I}) \\ &= \mathbf{T}_E(\mathbf{D}, \mathbf{B}, x^m) : \mathbf{D} + div(\mathbf{v})(\hat{p} + \lambda - P) \\ &= \mathbf{T}_E(\mathbf{D}, \mathbf{B}, x^m) : \mathbf{D} \geq 0 \end{aligned} \tag{7.97}$$

The above model allows us to choose different incompressible models for the bulk mixture such that the constraint given in equation 7.97 is satisfied. Different models that can be used for the bulk mixture include, power-law model, Bingham model and Herschel-Bulkley model that were discussed in detail in chapter 6. These models are symmetric models for the rheology of the bulk mixture. We can assume that due to the coupled effects of the magnetic fields on the fluid. The materials constants of the bulk fluid model to be a dependent on the magnitude of the magnetic field acting upon it. Several experiments study this effect of the magnetic field on the rheological material constants. This would again result in symmetric dependence of the rheological behavior on the magnetic fields. But, it is also observed that the direction of the magnetic field has significant effect on the rheological behavior of the fluid as well [172, 173]. We ignore this effect of the direction

of the magnetic field in this thesis to keep the model simple. Another important behavior of the magnetic fluid mixtures is the slip and friction behavior at the boundaries. We do not discuss these models in this thesis, as we are interested in the behavior of the fluid in known flow. However, this is an important characteristic to be considered to study the polishing effects of these fluids.

7.7.3.4 Stress in Magnetic Component

Next, we model the flow behavior of the magnetic fluid in the mixture. Here, we take the following model for the stress ($\mathbf{T^m}$),

$$\mathbf{T^m} = x^m \mathbf{T} - \hat{p}_m \mathbf{I} \tag{7.98}$$

Computing the magnetic thermodynamic pressure acting on the magnetic component of the fluid we get the following derivation.

$$\begin{aligned} \hat{p}_m &= u_{mag} - \frac{\partial u_{mag}}{\partial \rho^m} \rho^m \\ &= -\frac{1}{2} \mu_0 \, x^m \chi^m \, \mathbf{B}^2 - (-\frac{1}{2\rho_*^m} \mu_0 \, \chi^m \, \mathbf{B}^2) \rho^m \\ &= 0 \end{aligned} \tag{7.99}$$

Therefore, the model for the stress in the magnetic constituent of the mixture reduces to the following form.

$$\mathbf{T^m} = x^m \mathbf{T} \tag{7.100}$$

This model considers that the partial stress acting on constituent 1 is the volume fraction times the total stress caused by the bulk fluid. As a result, this means that diffusive velocity of the magnetic fluid is not caused by the partial stress in the magnetic fluid. This

is the simplest model that can be taken for the magnetic fluid. It can be understood by substituting the model into the inequality given in equation 7.89 as evaluated below.

$$grad(\hat{\mathbf{v}}^{\mathbf{m}}) \cdot \frac{(\mathbf{T^m} - x^m\mathbf{T})}{x^a} = grad(\hat{\mathbf{v}}^{\mathbf{m}}) \cdot \frac{(x^m\mathbf{T} - x^m\mathbf{T})}{x^a}$$
$$= 0 \tag{7.101}$$

Thus, this model uncouples the relative velocity from the stress in the mixture. Hence, the diffusive velocity in the mixture in this model is caused by the interactive forces ($\mathbf{f^i}$) between the constituents.

7.7.3.5 Interaction Forces in Magnetic Component

The model chosen for the interactive forces is given below,

$$\begin{aligned}\mathbf{f^m} &= -k_1\hat{\mathbf{q}}^{\mathbf{m}} - (\rho^m x^a grad(A_0^m) - x^m\rho^a grad(A_0^a)) \\ &\quad - \frac{(1-x^m)\mathbf{T}}{x^a} \cdot grad(x^m) \\ &= -k_1\hat{\mathbf{q}}^{\mathbf{m}} - (\rho^m x^a grad(A_0^m) - x^m\rho^a grad(A_0^a)) - \mathbf{T}grad(x^m) \end{aligned} \tag{7.102}$$

where, $\hat{\mathbf{q}}^{\mathbf{m}} = x^m\hat{\mathbf{v}}^{\mathbf{m}}$

Equation 7.102 gives a model for the interactive forces that are dependent on the chemical potential of the constituents, the partial stress in constituent 2 and the diffusive flux of the constituents in the mixture. On substituting this model in the inequality 7.90, we get the following,

$$\begin{aligned}&-\frac{1}{x^a}[(\mathbf{b}^m_{mag} + grad(\mathbf{B})^T\bar{\mathbf{M}})x^a + \mathbf{f}^m + \rho^m x^a grad(A_0^m) - \rho^a x^m grad(A_0^a) \\ &+ \frac{(\mathbf{T} - \mathbf{T^m})}{x^a} \cdot grad(x^m)] \cdot \hat{\mathbf{v}}^{\mathbf{i}} \\ &= k_1\frac{x^m}{x^a}\hat{\mathbf{v}}^{\mathbf{m}} \cdot \hat{\mathbf{v}}^{\mathbf{m}} \geq 0\end{aligned} \tag{7.103}$$

The above inequality suggests a model for the interactive forces that are diffusive in nature. The forces are currently modeled in terms of the chemical potential A_0^i, whose model is dependent on the function chosen for the internal energy function u_0. Hence, we choose an appropriate model for the internal energy u_0 to derive the equations for the final form of the interactive forces. The internal energy has 3 components, (a) the energy due to formation of a mixture, (b) the interfacial energy due to formation of boundaries between phases [174] and (c) the thermal energy in the mixture. The internal energy thus chosen is as follows,

$$\begin{aligned} u_0(\rho^i, s) &= k_2\Big(\sum_{i\in\{m,a\}} \frac{\rho^i}{\rho_*^i} ln(\frac{\rho^i}{\rho_*^i})\Big) - \frac{k_3}{2}\sum_{i\in\{m,a\}} grad(\frac{\rho^m}{\rho_*^m})\cdot grad(\frac{\rho^a}{\rho_*^a}) + \theta s \\ &= k_2\Big(\sum_{i\in\{m,a\}} x^i ln(x^i)\Big) - \frac{k_3}{2} grad(x^m)\cdot grad(x^a) + \theta s \end{aligned} \tag{7.104}$$

where, k_2 and k_3 are diffusive material constants associated with homogeneous and inhomogeneous distribution of constituents in the bulk mixture. Calculating the chemical potentials (A_0^i) and their gradients ($grad(A_0^i)$) from equation 7.104 we get,

$$\begin{aligned} A_0^m &= \frac{\partial u_0}{\partial \rho^m} - div(\frac{\partial u_0}{\partial grad(\rho^m)}) \\ &= k_2(ln(x^m)\frac{\partial x^m}{\partial \rho^m} + x^m\frac{1}{x^m}\frac{\partial x^m}{\partial \rho^m} - 0 + 0) + \frac{k_3}{2} div(grad(x^a)\frac{\partial grad(x^m)}{\partial grad(\rho^m)}) \\ &= k_2(ln(x^m)+1)\frac{\partial x^m}{\partial \rho^m} + \frac{k_3}{2}\, div(grad(x^a))\frac{\partial x^m}{\partial \rho^m} \\ &= \frac{k_2}{\rho_*^m}(ln(x^m)+1) + \frac{k_3}{2\rho_*^m}\, div(grad(x^a)) \end{aligned} \tag{7.105}$$

$$grad(A_0^m) = \frac{k_2}{\rho_*^m x^m} grad(x^m) + \frac{k_3}{2\rho_*^m}\, grad(div(grad(x^a)))$$

$$= \frac{k_2\ grad(x^m)}{\rho_*^m x^m} + \frac{k_3}{2\rho_*^m}\ grad(div(grad(x^a))) \tag{7.106}$$

Similarly, the expressions for the abrasive constituent are derived as follows,

$$A_0^a = \frac{k_2}{\rho_*^a}(ln(x^a)+1) + \frac{k_3}{2\rho_*^a}\ div(grad(x^m)) \tag{7.107}$$

$$grad(A_0^a) = \frac{k_2\ grad(x^a)}{\rho_*^a x^a} + \frac{k_3}{2\rho_*^a}\ grad(div(grad(x^m))) \tag{7.108}$$

Now, let's evaluate the component of interactive forces generated due to the chemical potential in the constituents, as described in equation 7.102.

$$\begin{aligned}
&(\rho^m x^a grad(A_0^m) - x^m \rho^a grad(A_0^a)) \\
&\quad = x^m x^a(\rho_*^m grad(A_0^m) - \rho_*^a grad(A_0^a)) \\
&\quad = x^m x^a(\rho_*^m(\frac{k_2\ grad(x^m)}{\rho_*^m x^m} + \frac{k_3}{2\rho_*^m}\ grad(div(grad(x^a)))) \\
&\qquad - \rho_*^a(\frac{k_2\ grad(x^a)}{\rho_*^a x^a} + \frac{k_3}{2\rho_*^a}\ grad(div(grad(x^m)))) \\
&\quad = x^a k_2\ grad(x^m) - x^m k_2\ grad(x^a) + \frac{k_3 x^m x^a}{2}\ grad(div(grad(x^a))) \\
&\quad - \frac{k_3 x^m x^a}{2}\ grad(div(grad(x^m))) \\
&\quad = k_2\ grad(x^m) - k_3\ x^m x^a grad(div(grad(x^m)))
\end{aligned} \tag{7.109}$$

Hence, the final constitutive equation for the interactive forces developed in the magnetic component of the mixture is as shown below.

$$\mathbf{f^m} = -k_1\hat{\mathbf{q}}^{\mathbf{m}} - k_2\ grad(x^m) + k_3 x^m x^a grad(div(grad(x^m))) - \mathbf{T}grad(x^m) \tag{7.110}$$

Based on the constitutive models chosen above for the fluid the simulations will reflect dissipation behavior of the mixture due to viscous flow of the bulk fluid and diffusion of

the constituents due to the interactive forces. Any dissipation due to the relative flow of individual constituents and their individual stresses are assumed to be zero in this model. Such a bare minimum simple model is possible here due to the approach of taking the bulk of the mixture and the diffusion of magnetic constituent as the governing equations rather than considering individual constituents separately in the mixture equations. The final form of the energy function(u) for the bulk mixture assumed for modeling the polishing mixture is given below,

$$\begin{aligned} u(\rho^m, \rho^a, \mathbf{p}^m, \mathbf{p}^a, s, \mathbf{B}) &= u_0(\rho^m, \rho^a, s) + \frac{\mathbf{p^m} \cdot \mathbf{p^m}}{2\rho^m} + \frac{\mathbf{p^a} \cdot \mathbf{p^a}}{2\rho^a} + u_{mag}(\rho^m, \mathbf{B}) \\ &= k_2(\sum_{i \in \{m,a\}} x^i ln(x^i)) - \frac{k_3}{2} grad(x^m) \cdot grad(x^a) + \theta s \\ &\quad + \frac{\mathbf{p^m} \cdot \mathbf{p^m}}{2\rho^m} + \frac{\mathbf{p^a} \cdot \mathbf{p^a}}{2\rho^a} - \frac{1}{2} \frac{\chi(\rho^m)}{1 + \chi(\rho^m)} \mathbf{B}^2 \end{aligned} \tag{7.111}$$

7.8 Field Equations of the Polishing Fluid

The final form of the balance equations were computed in section 7.6. The models for the mixture are also computed in section 7.7. The interest of this thesis is to study the stratification and the flow behavior of the mixture. Hence, the mass and momentum balance equations along with the magnetic field equations and the associated models are of primary interest of study in the thesis. A simplified form of the flow equations of the mixture can be achieved by substituting the models of the magnetic fluid (stress ($\mathbf{T^m}$) and interaction force ($\mathbf{f^m}$)) into the momentum balance equations.

Substituting the models for stress in the magnetic component ($\mathbf{T^m}$) and interaction force ($\mathbf{f^m}$) in the magnetic fluid into the momentum balance equation of the bulk fluid we get the following derivation for the bulk momentum balance equation.

$$\frac{\partial \mathbf{v}}{\partial t} + div(\mathbf{v} \otimes \mathbf{v}) = \frac{1}{\rho^a_*} div(\mathbf{T}) + (\frac{1}{\rho^m_*} - \frac{1}{\rho^a_*}) div(\mathbf{T^m}) + \frac{\mathbf{b}^m_{mag}}{\rho^m_*}$$

$$
\begin{aligned}
&+ (\frac{1}{\rho_*^m} - \frac{1}{\rho_*^a})\mathbf{f}^m + div(\hat{\mathbf{v}}^{\mathbf{m}} \otimes \hat{\mathbf{v}}^{\mathbf{a}}) \\
&= \frac{1}{\rho_*^a} div(\mathbf{T}) + (\frac{1}{\rho_*^m} - \frac{1}{\rho_*^a}) div(x^m \mathbf{T}) + \frac{\mathbf{b}_{mag}^m}{\rho_*^m} \\
&+ (\frac{1}{\rho_*^m} - \frac{1}{\rho_*^a})(-k_1 \hat{\mathbf{q}}^{\mathbf{m}} - k_2\ grad(x^m) + k_3 x^m x^a grad(div(grad(x^m))) \\
&- \mathbf{T} grad(x^m)) + div(\hat{\mathbf{v}}^{\mathbf{m}} \otimes \hat{\mathbf{v}}^{\mathbf{a}}) \\
&= \frac{1}{\rho_*^a} div(\mathbf{T}) + (\frac{1}{\rho_*^m} - \frac{1}{\rho_*^a}) x^m\ div(\mathbf{T}) + (\frac{1}{\rho_*^m} - \frac{1}{\rho_*^a}) \mathbf{T}^{\mathbf{T}} grad(x^m) \\
&- (\frac{1}{\rho_*^m} - \frac{1}{\rho_*^a}) \mathbf{T} grad(x^m) + \frac{\mathbf{b}_{mag}^m}{\rho_*^m} + div(\hat{\mathbf{v}}^{\mathbf{m}} \otimes \hat{\mathbf{v}}^{\mathbf{a}}) \\
&+ (\frac{1}{\rho_*^m} - \frac{1}{\rho_*^a})(-k_1 \hat{\mathbf{q}}^{\mathbf{m}} - k_2\ grad(x^m) + k_3 x^m x^a grad(div(grad(x^m)))) \\
&= (\frac{x^m}{\rho_*^m} + \frac{x^a}{\rho_*^a}) div(\mathbf{T}) + \frac{\mathbf{b}_{mag}^m}{\rho_*^m} + div(\hat{\mathbf{v}}^{\mathbf{m}} \otimes \hat{\mathbf{v}}^{\mathbf{a}}) \\
&- (\frac{1}{\rho_*^m} - \frac{1}{\rho_*^a})(k_1 \hat{\mathbf{q}}^{\mathbf{m}} + k_2\ grad(x^m) - k_3 x^m x^a grad(div(grad(x^m))))
\end{aligned}
\tag{7.112}
$$

Upon substituting the models for stress ($\mathbf{T}^{\mathbf{m}}$) and interaction force ($\mathbf{f}^{\mathbf{m}}$) in the magnetic fluid into the momentum balance equation of the bulk fluid we get the following derivation for the balance of flux in the mixture.

$$
\begin{aligned}
&\frac{\partial \hat{\mathbf{q}}^m}{\partial t} + div(\hat{\mathbf{q}}^m \otimes \mathbf{v}) + x^m div(\hat{\mathbf{v}}^{\mathbf{m}} \otimes \hat{\mathbf{v}}^{\mathbf{a}}) + grad(\mathbf{v}) \hat{\mathbf{q}}^m + div(\hat{\mathbf{q}}^m \otimes \hat{\mathbf{v}}^m) \\
&\quad = \frac{\rho}{\rho_*^m \rho_*^a} div(\mathbf{T}^{\mathbf{m}}) - \frac{x^m}{\rho_*^a} div(\mathbf{T}) + x^a \frac{\mathbf{b}_{mag}^m}{\rho_*^m} + \frac{\rho}{\rho_*^m \rho_*^a} \mathbf{f}^m \\
&\quad = \frac{\rho}{\rho_*^m \rho_*^a} div(x^m \mathbf{T}) - \frac{x^m}{\rho_*^a} div(\mathbf{T}) + x^a \frac{\mathbf{b}_{mag}^m}{\rho_*^m} \\
&\qquad + \frac{\rho}{\rho_*^m \rho_*^a}(-k_1 \hat{\mathbf{q}}^{\mathbf{m}} - k_2\ grad(x^m) + k_3 x^m x^a grad(div(grad(x^m))) - \mathbf{T} grad(x^m)) \\
&\quad = \frac{x^m}{\rho_*^a}(\frac{\rho}{\rho_*^m} - 1) div(\mathbf{T}) + \frac{\rho}{\rho_*^m \rho_*^a} \mathbf{T}^{\mathbf{T}}\ grad(x^m) + x^a \frac{\mathbf{b}_{mag}^m}{\rho_*^m} - \frac{\rho}{\rho_*^m \rho_*^a} \mathbf{T}\ grad(x^m) \\
&\qquad - \frac{\rho}{\rho_*^m \rho_*^a}(k_1 \hat{\mathbf{q}}^{\mathbf{m}} + k_2\ grad(x^m) - k_3 x^m x^a grad(div(grad(x^m))))
\end{aligned}
$$

$$
\begin{aligned}
&= \frac{x^m}{\rho_*^a}(\frac{x^m\rho_*^m + x^a\rho_*^a}{\rho_*^m} - 1)div(\mathbf{T}) + x^a\frac{\mathbf{b}_{mag}^m}{\rho_*^m} \\
&\quad - \frac{\rho}{\rho_*^m\rho_*^a}(k_1\hat{\mathbf{q}}^{\mathbf{m}} + k_2\ grad(x^m) - k_3x^mx^agrad(div(grad(x^m)))) \\
&= \frac{x^m}{\rho_*^a}(\frac{x^a\rho_*^a}{\rho_*^m} - x^a)div(\mathbf{T}) + x^a\frac{\mathbf{b}_{mag}^m}{\rho_*^m} \\
&\quad - \frac{\rho}{\rho_*^m\rho_*^a}(k_1\hat{\mathbf{q}}^{\mathbf{m}} + k_2\ grad(x^m) - k_3x^mx^agrad(div(grad(x^m)))) \\
&= x^mx^a(\frac{1}{\rho_*^m} - \frac{1}{\rho_*^a})div(\mathbf{T}) + x^a\frac{\mathbf{b}_{mag}^m}{\rho_*^m} \\
&\quad - \frac{\rho}{\rho_*^m\rho_*^a}(k_1\hat{\mathbf{q}}^{\mathbf{m}} + k_2\ grad(x^m) - k_3x^mx^agrad(div(grad(x^m))))
\end{aligned}
$$

$$
\begin{aligned}
\implies \frac{\partial\hat{\mathbf{q}}^m}{\partial t} + div(\hat{\mathbf{q}}^m \otimes \mathbf{v}) + x^m div(\hat{\mathbf{v}}^{\mathbf{m}} \otimes \hat{\mathbf{v}}^{\mathbf{a}}) + grad(\mathbf{v})\hat{\mathbf{q}}^m + div(\hat{\mathbf{q}}^m \otimes \hat{\mathbf{v}}^m) \\
+\frac{\rho}{\rho_*^m\rho_*^a}k_1\hat{\mathbf{q}}^{\mathbf{m}} = x^mx^a(\frac{1}{\rho_*^m} - \frac{1}{\rho_*^a})div(\mathbf{T}) + x^a\frac{\mathbf{b}_{mag}^m}{\rho_*^m} \\
- \frac{\rho}{\rho_*^m\rho_*^a}(k_2\ grad(x^m) - k_3x^mx^agrad(div(grad(x^m))))
\end{aligned}
\tag{7.113}
$$

Ultimately, for a general polishing mixture with magnetic and abrasive constituents, the final set of the field equations needed to solve for the state variables $[\rho, x^m, \mathbf{v}, \hat{\mathbf{q}}^{\mathbf{m}}]$ are given below. These are a collected form of all the field equations developed in the sections above. These state variables can be used to compute the state variables of the constituents ($[\rho^m, \rho^a, \mathbf{p}^m, \mathbf{p}^a]$).

The field equations for the mixture are,

$$
\begin{aligned}
curl(\mathbf{H}) &= 0 \\
div(\mathbf{B}) &= \mathbf{0} \\
\frac{\partial\rho}{\partial t} + div(\rho\mathbf{v}) &= -(\rho_*^m - \rho_*^a)div(\hat{\mathbf{q}}^{\mathbf{m}})
\end{aligned}
$$

$$
\begin{aligned}
\frac{\partial \mathbf{v}}{\partial t} + div(\mathbf{v} \otimes \mathbf{v}) &= (\frac{x^m}{\rho_*^m} + \frac{x^a}{\rho_*^a}) div(\mathbf{T}) + \frac{\mathbf{b}_{mag}^m}{\rho_*^m} \\
&\quad - (\frac{1}{\rho_*^m} - \frac{1}{\rho_*^a})(k_1 \hat{\mathbf{q}}^{\mathbf{m}} + k_2\, grad(x^m) - k_3 x^m x^a grad(div(grad(x^m)))) \\
&\quad + div(\hat{\mathbf{v}}^{\mathbf{m}} \otimes \hat{\mathbf{v}}^{\mathbf{a}}) \\
\frac{\partial x^m}{\partial t} + div(x^m \mathbf{v}) &= -div(\hat{\mathbf{q}}^{\mathbf{m}}) \\
\frac{\partial \hat{\mathbf{q}}^m}{\partial t} + div(\hat{\mathbf{q}}^m \otimes \mathbf{v}) + x^m div(\hat{\mathbf{v}}^{\mathbf{m}} \otimes \hat{\mathbf{v}}^{\mathbf{a}}) + grad(\mathbf{v}) \hat{\mathbf{q}}^m + div(\hat{\mathbf{q}}^m \otimes \hat{\mathbf{v}}^m) & \\
+ \frac{\rho}{\rho_*^m \rho_*^a} k_1 \hat{\mathbf{q}}^{\mathbf{m}} &= x^m x^a (\frac{1}{\rho_*^m} - \frac{1}{\rho_*^a}) div(\mathbf{T}) + x^a \frac{\mathbf{b}_{mag}^m}{\rho_*^m} \\
&\quad - \frac{\rho}{\rho_*^m \rho_*^a} (k_2\, grad(x^m) - k_3 x^m x^a grad(div(grad(x^m))))
\end{aligned}
$$

subject to the constraint,

$$
div(\mathbf{v}) = 0
$$

where,

$$
\begin{aligned}
\mathbf{B} &= \mu_0 (1 + x^m \chi^m) \mathbf{H} \\
\hat{\mathbf{q}}^{\mathbf{m}} &= x^m \hat{\mathbf{v}}^{\mathbf{m}} \\
x^a &= 1 - x^m \\
\hat{\mathbf{v}}^a &= -\frac{x^m}{x^a} \hat{\mathbf{v}}^m \\
\mathbf{T} &= -P\mathbf{I} + \mathbf{T}_E(\mathbf{D}, \mathbf{B}, x^m) \\
\mathbf{b}_{mag}^m &= \chi^m\, x^m\, grad(\mathbf{B})^T \mathbf{H}
\end{aligned}
$$

7.9 Some Special Cases

7.9.1 Flow Equations for Creeping Flow

In this section, we focus on the diffusion and flow of the magnetorheological fluids under creeping flow, where the velocity of the fluid is small. Since, the velocity of the fluid is small, we can assume the convective components of the momentum and the diffusive flux equations to be zero. Also, we neglect the body force due to gravity on the fluid as the magnetic forces are assumed to be much greater in comparison. This results in the body force in the magnetic constituent ($\mathbf{b}^m_{mag}$) to be solely contributed by the attraction forces acting on the particles due to the magnetic field and the body force in the abrasive constituent (b^a) to be zero. Hence, we achieve the following set of final equations for the fluid.

$$\frac{\partial \rho}{\partial t} + div(\rho \mathbf{v}) = -(\rho^m_* - \rho^a_*) div(\hat{\mathbf{q}}^{\mathbf{m}}) \tag{7.114}$$

$$\begin{aligned} \frac{\partial \mathbf{v}}{\partial t} = {} & (\frac{x^m}{\rho^m_*} + \frac{x^a}{\rho^a_*}) div(\mathbf{T}) + \frac{\mathbf{b}^m_{mag}}{\rho^m_*} \\ & - (\frac{1}{\rho^m_*} - \frac{1}{\rho^a_*})(k_1 \hat{\mathbf{q}}^{\mathbf{m}} + k_2\, grad(x^m) \\ & - k_3 x^m x^a grad(div(grad(x^m)))) \end{aligned} \tag{7.115}$$

$$\frac{\partial x^m}{\partial t} + div(x^m \mathbf{v}) = -div(\hat{\mathbf{q}}^{\mathbf{m}}) \tag{7.116}$$

$$\begin{aligned} \frac{\partial \hat{\mathbf{q}}^m}{\partial t} + \frac{\rho}{\rho^m_* \rho^a_*} k_1 \hat{\mathbf{q}}^{\mathbf{m}} = {} & x^m x^a (\frac{1}{\rho^m_*} - \frac{1}{\rho^a_*}) div(\mathbf{T}) + x^a \frac{\mathbf{b}^m_{mag}}{\rho^m_*} \\ & - \frac{\rho}{\rho^m_* \rho^a_*} (k_2\, grad(x^m) - k_3 x^m x^a grad(div(grad(x^m)))) \end{aligned} \tag{7.117}$$

where,

$$\hat{\mathbf{q}}^{\mathbf{m}} = x^m \hat{\mathbf{v}}^{\mathbf{m}}$$

$$\mathbf{T} = -P\mathbf{I} + \mathbf{T}_E(\mathbf{D}, \mathbf{B}, x^m)$$

(7.118)

7.9.2 Diffusion in a Stationary Fluid

In this case, we assume a mixture which is stationary in the presence of magnetic field. In such a fluid, the bulk velocity of the fluid is assumed to be zero. Substituting the zero bulk velocity into the balance equations of fluid we get the following equations.

$$\frac{\partial \rho}{\partial t} = -(\rho_*^m - \rho_*^a) div(\hat{\mathbf{q}}^{\mathbf{m}}) \tag{7.119}$$

$$\begin{aligned}(\frac{x^m}{\rho_*^m} + \frac{x^a}{\rho_*^a}) grad(P) = \frac{\mathbf{b}_{mag}^m}{\rho_*^m} - (\frac{1}{\rho_*^m} - \frac{1}{\rho_*^a})(k_1 \hat{\mathbf{q}}^{\mathbf{m}} + k_2\, grad(x^m) \\ - k_3 x^m x^a grad(div(grad(x^m)))) \end{aligned} \tag{7.120}$$

$$\frac{\partial x^m}{\partial t} = -div(\hat{\mathbf{q}}^{\mathbf{m}}) \tag{7.121}$$

$$\begin{aligned}\frac{\partial \hat{\mathbf{q}}^m}{\partial t} + \frac{\rho}{\rho_*^m \rho_*^a} k_1 \hat{\mathbf{q}}^{\mathbf{m}} = -x^m x^a (\frac{1}{\rho_*^m} - \frac{1}{\rho_*^a}) grad(P) + x^a \frac{\mathbf{b}_{mag}^m}{\rho_*^m} \\ - \frac{\rho}{\rho_*^m \rho_*^a} (k_2\, grad(x^m) - k_3 x^m x^a grad(div(grad(x^m))))\end{aligned} \tag{7.122}$$

7.9.3 Constituents with Equal Densities

When both the constituents are of same density while they occupy the whole fluid volume, the mixture flow behavior is simplified and leads to the following equations. This is relevant only in some specific cases in polishing fluid when the filled densities of both the magnetic and abrasive particles are similar in the mixture.

$$\rho_*^m = \rho_*^a \tag{7.123}$$

$$\begin{aligned}\rho &= x^m \rho_*^m + x^a \rho_*^a \\ &= \rho_*^m\end{aligned} \tag{7.124}$$

$$
\begin{aligned}
c^i &= \frac{\rho^i}{\rho} \\
&= \frac{\rho^i}{\rho^i_*} = x^i
\end{aligned} \tag{7.125}
$$

This simplification results in the following balance equations for the mixture.

$$\frac{\partial \rho}{\partial t} + div(\rho \mathbf{v}) = 0 \tag{7.126}$$

$$\rho^m_* \frac{\partial \mathbf{v}}{\partial t} = div(\mathbf{T}) + \mathbf{b}^m_{mag} \tag{7.127}$$

$$\frac{\partial x^m}{\partial t} + div(x^m \mathbf{v}) = -div(\hat{\mathbf{q}}^{\mathbf{m}}) \tag{7.128}$$

$$
\begin{aligned}
\rho^m_* \frac{\partial \hat{\mathbf{q}}^m}{\partial t} + k_1 \hat{\mathbf{q}}^{\mathbf{m}} &= x^a \mathbf{b}^m_{mag} - k_2 \, grad(x^m) \\
&\quad + k_3 x^m x^a grad(div(grad(x^m)))
\end{aligned} \tag{7.129}
$$

7.10 Conclusions

In this chapter, we modeled the behavior of a magnetorheological polishing fluid using Mixture Theory. The polishing fluid was assumed to be a mixture of magnetic slurry component and abrasive slurry component. Dipole-current circuit model was used to model the magnetic behavior of the polishing fluid. The field equations of the components have been resolved into the field equations for the bulk mixture and relative flow of the magnetic component. Through this, the field equations for the bulk mixture fluid and the relative flow of the magnetic component were derived. Thermodynamically consistent constitutive models were developed for the fluid to exhibit segregation through diffusion and flow of the bulk mixture during the polishing process. It was identified that a mixture model for the bulk flow velocity formulated using the volume concentration of the component provides field equations and constraints for the bulk mixture, where simpler incompressible constitutive models can be used to model the flow of the bulk mixture. The constitutive

models chosen for the mixture assumes a dissipative nature for the shearing of the bulk fluid, diffusion flow of the components during segregation and flow of heat in the mixture. This set of field equations have been used in chapter 8 to simulate the behavior of the polishing fluid under different conditions.

8. SIMULATION OF CONVECTION-DIFFUSION AND STRATIFICATION IN STATIC FLUID

8.1 Finite Element Formulation

The finite element analysis for the simulation of the slurry mixture is carried out using FEniCS (Finite Element 'ni' Computational Software) [175, 176]. This is an open source computing platform where partial differential equations can be solved in a general sense. Conventional CFD based methods such as OpenFoam, Fluent [177] and StarCCM+ implement only second order partial differential equations (PDEs) whereas FEniCS allows using higher-order PDEs as well, which are essential in this case.

All the field equations for the behavior of the polishing fluid described in section 7.9.1 are used here to develop a weak formulation of the differential equations. These equations are used to solve for the state variables in the problem. Note that the field equations are dynamic in nature. The fields, thus, are not only functions of space but also of time. If one attempts to compute the state variables simultaneously, one may need to first discretize the time domain using finite difference method (Crank–Nicolson Method) and then solve for the space domain using finite element discretization. Let us consider that for every time step, the state of the system at time t is known and the state at time $t + \Delta t$ is of interest for computation. The time discretized form of the field equations for the system are given in the following equations.

$$div(\mu(x^m_{t+\frac{\Delta t}{2}})\ grad(\phi_{t+\Delta t/2})) = \mathbf{0}$$

$$\frac{\mathbf{v}_{t+\Delta t} - \mathbf{v}_t}{\Delta t} - (\frac{x^m_{t+\frac{\Delta t}{2}}}{\rho^m_*} + \frac{x^a_{t+\frac{\Delta t}{2}}}{\rho^a_*})div(\mathbf{T}_{t+\frac{\Delta t}{2}}) - \frac{\mathbf{b}^m_{mag\ t+\frac{\Delta t}{2}}}{\rho^m_*}$$

$$-(\frac{1}{\rho^m_*} - \frac{1}{\rho^a_*})(k_1\hat{\mathbf{q}}^{\mathbf{m}}_{\mathbf{t}+\frac{\mathbf{\Delta t}}{\mathbf{2}}} + k_2\ grad(x^m_{t+\frac{\Delta t}{2}}) - k_3 x^m_{t+\frac{\Delta t}{2}} x^a_{t+\frac{\Delta t}{2}} grad(div(grad(x^m_{t+\frac{\Delta t}{2}}))) = \mathbf{0}$$

$$\frac{x^m_{t+\Delta t} - x^m_t}{\Delta t} + div(x^m_{t+\frac{\Delta t}{2}} \mathbf{v}_{t+\frac{\Delta t}{2}}) + div(\hat{\mathbf{q}}^{\mathbf{m}}_{\mathbf{t}+\frac{\mathbf{\Delta t}}{\mathbf{2}}}) = 0$$

$$\frac{\hat{\mathbf{q}}^m_{t+\Delta t} - \hat{\mathbf{q}}^m_t}{\Delta t} - x^m_{t+\frac{\Delta t}{2}} x^a_{t+\frac{\Delta t}{2}} (\frac{1}{\rho^m_*} - \frac{1}{\rho^a_*}) div(\mathbf{T}_{t+\frac{\Delta t}{2}}) - x^a_{t+\frac{\Delta t}{2}} \frac{\mathbf{b}^m_{mag\ t+\frac{\Delta t}{2}}}{\rho^m_*}$$

$$+ \frac{\rho_{t+\frac{\Delta t}{2}}}{\rho^m_* \rho^a_*} (k_1 \hat{\mathbf{q}}^{\mathbf{m}}_{\mathbf{t}+\frac{\mathbf{\Delta t}}{\mathbf{2}}} + k_2\ grad(x^m_{t+\frac{\Delta t}{2}}) - k_3 x^m_{t+\frac{\Delta t}{2}} x^a_{t+\frac{\Delta t}{2}} grad(div(grad(x^m_{t+\frac{\Delta t}{2}}))) = 0$$

In the above equations, we need to solve for $x^m_{t+\Delta t}$, $\mathbf{v}_{t+\Delta t}$ and $\phi_{t+\Delta t}$ simultaneously at every time step. Moreover, the equations are nonlinear in terms of the concentration of the magnetic constituent. This makes the computation of the state variables quite complicated. Hence, we perform a serial operator splitting of the equations and variables [178] in the problem like Alternate Direction Implicit (ADI) methods [179]. A flowchart describing the approach to the simulation is given in figure 8.1. In the flowchart, we may note that for any time step the current concentration of the magnetic particles are used to compute the magnetic fields and the magnetic field thus computed is used to solve the convection-diffusion problem, computing the new concentration and magnetic particle flux at the end of the time step. This updated new concentration field is then used to compute the magnetic fields for the next time step. Since the class of simulations in this thesis assume the flow field of the bulk fluid, the momentum balance equation is not solved in any time step. The pressure field or stress state at the steady state or in any required time step is directly computed using the concentration field at that time by solving the momentum balance equation. We will further simplify the balance equations to solve for the evolution of the concentration under the influence of magnetic fields for a known flow. In order to do this, we will simplify the balance laws further to eliminate the need to calculate the bulk velocity as described in section 8.3.

The magnetic and convection-diffusion problems are solved by an adaptive time step strategy. At each time step, the solution is first computed directly using the time step Δt. Then the solution is recomputed by halving the time step and the results are compared. If

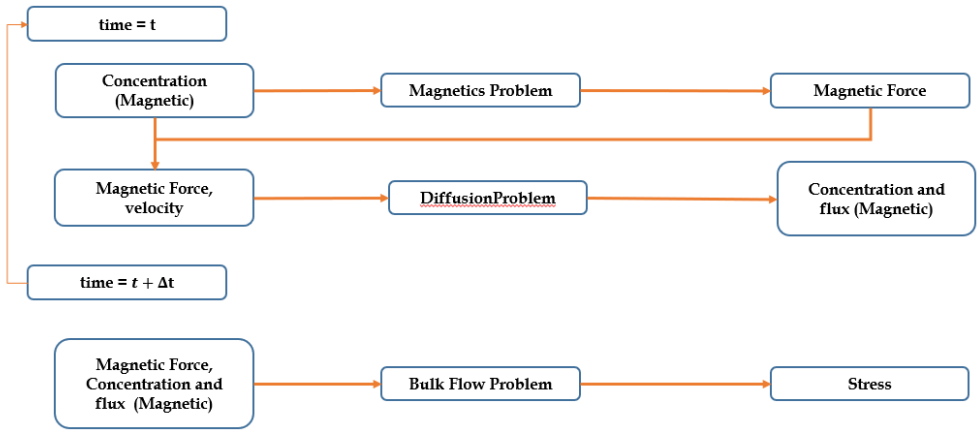

Figure 8.1: A basic flowchart showing the simulation strategy employed to compute the concentration distribution of the magnetic particles in the mixture. Note that the magnetic fields and concentration are not computed simultaneously, but rather operator split of the variables are used to compute the variables one after another as shown in the figure.

the results are deemed to be sufficiently close, we proceed to the next time step; otherwise, the time step is halved and the process is repeated. For the simulations discussed in this chapter, the solutions are considered close if the L2 norm of their difference is less than 5×10^{-5}, else the time step is halved. If the L2 norm is less than 8×10^{-6}, the time step is doubled for the subsequent time-step. For these values, the simulations were observed to be stable.

8.2 Organization of the chapter

In this chapter, section 8.3 describes the simplification of the balance equations to make them appropriate for a simplified weak form. Section 8.4 describes the weak form developed for the differential equations. Section 8.5 describes the general boundary conditions for the problems considered in the chapter. Section 8.6 describes the material parameters considered for the magnetic polishing mixture in the simulations. Section 8.7 describes the general non-dimensionalization of the differential equations. Section 8.8 describes the

mesh convergence study performed to choose an appropriate mesh for the simulations. Section 8.9 describes the segregation simulations computed for a polishing mixture with stationary bulk fluid under different magnetic fields. Section 8.11 describes the simulations computed for a polishing mixture with bulk fluid under known shear flow. Finally, section 8.12 draws conclusions on the modeling of the magnetic polishing mixture under different flows in the presence of magnetic field.

8.3 Simplified form of the Differential Equations

In this thesis, we work with the behavior of the polishing fluids in known bulk flow in the presence of the magnetic fields. Since the bulk flow is already known in these class of problems, the bulk velocity and momentum is not required to be solved for every time step. Hence, we can simplify the set of equations to solve only the magnetics problem and the convection-diffusion problem. The bulk momentum equation is only solved to compute the stress state of the bulk mixture at necessary time steps, reducing the complexity of the differential equations. Thus, we simplify the convection-diffusion equation by substituting for $div(\mathbf{T})$ from the bulk momentum equation. This development of the convection-diffusion equation is discussed in this section. Consider the set of bulk momentum and convection-diffusion equations given below from equations 7.114 to 7.117.

$$\frac{\partial \rho}{\partial t} + div(\rho \mathbf{v}) = -(\rho_*^m - \rho_*^a) div(\hat{\mathbf{q}}^{\mathbf{m}}) \tag{8.1}$$

$$\begin{aligned} \frac{\partial \mathbf{v}}{\partial t} = &(\frac{x^m}{\rho_*^m} + \frac{x^a}{\rho_*^a}) div(\mathbf{T}) + \frac{\mathbf{b}_{mag}^m}{\rho_*^m} \\ &- (\frac{1}{\rho_*^m} - \frac{1}{\rho_*^a})(k_1 \hat{\mathbf{q}}^{\mathbf{m}} + k_2 \, grad(x^m) \\ &- k_3 x^m x^a grad(div(grad(x^m)))) \end{aligned} \tag{8.2}$$

$$\frac{\partial x^m}{\partial t} + div(x^m \mathbf{v}) = -div(\hat{\mathbf{q}}^{\mathbf{m}}) \tag{8.3}$$

$$\frac{\partial \hat{\mathbf{q}}^m}{\partial t} + \frac{\rho}{\rho_*^m \rho_*^a} k_1 \hat{\mathbf{q}}^{\mathbf{m}} = x^m x^a (\frac{1}{\rho_*^m} - \frac{1}{\rho_*^a}) div(\mathbf{T}) + x^a \frac{\mathbf{b}_{mag}^m}{\rho_*^m} - \frac{\rho}{\rho_*^m \rho_*^a} \{k_2\ grad(x^m) - k_3 x^m x^a grad(div(grad(x^m)))\} \quad (8.4)$$

Here, equation 8.1 is not needed to be solved, as we can compute the bulk density directly from the concentration of the magnetic constituents in the fluid. Computing the expression for $div(\mathbf{T})$ from equation 8.2, we get the following

$$\begin{aligned} div(\mathbf{T}) =& \frac{1}{x^m + x^a \rho_r} [\rho_*^m \frac{\partial \mathbf{v}}{\partial t} - \mathbf{b}_{mag}^m + (1 - \rho_r)\{k_1 \mathbf{q}^m + k_2 grad(x^m) \\ & - k_3 x^m x^a grad(div(grad(x^m)))\}] \quad (8.5) \\ \text{where,} \quad & \rho_r = \frac{\rho_*^m}{\rho_*^a} \end{aligned}$$

We can further simplify the equations by substituting the expression for $div(\mathbf{T})$ (from equation 8.5) into the differential equation for the flux, $\mathbf{q^m}$ (equation 8.4). The resulting evolution equation for $\mathbf{q^m}$ are derived as follows,

$$\begin{aligned} & \rho_*^m \frac{\partial \hat{\mathbf{q}}^m}{\partial t} - x^m x^a (1 - \rho_r) div(\mathbf{T}) - x^a \mathbf{b}_{mag}^m \\ & + (x^m \rho_r + x^a)\{k_1 \hat{\mathbf{q}}^{\mathbf{m}} + k_2\ grad(x^m) - k_3 x^m x^a grad(div(grad(x^m)))\} = 0 \\ \implies & \rho_*^m \frac{\partial \hat{\mathbf{q}}^m}{\partial t} - x^a \mathbf{b}_{mag}^m - \frac{x^m x^a (1 - \rho_r)}{x^m + x^a \rho_r} [\rho_*^m \frac{\partial \mathbf{v}}{\partial t} - \mathbf{b}_{mag}^m \\ & + (1 - \rho_r)\{k_1 \mathbf{q}^m + k_2 grad(x^m) - k_3 x^m x^a grad(div(grad(x^m)))\}] \\ & + (x^m \rho_r + x^a)\{k_1 \hat{\mathbf{q}}^{\mathbf{m}} + k_2\ grad(x^m) - k_3 x^m x^a grad(div(grad(x^m)))\} = 0 \\ \implies & \rho_*^m (x^m + x^a \rho_r) \frac{\partial \hat{\mathbf{q}}^m}{\partial t} - \rho_*^m x^m x^a (1 - \rho_r) \frac{\partial \mathbf{v}}{\partial t} \\ & - (x^m + x^a \rho_r - x^m (1 - \rho_r)) x^a \mathbf{b}_{mag}^m \end{aligned}$$

$$
\begin{aligned}
&+\{(x^m\rho_r + x^a)(x^m + x^a\rho_r) - x^m x^a(1-\rho_r)^2\} \\
&\{k_1\hat{\mathbf{q}}^{\mathbf{m}} + k_2\ grad(x^m) - k_3 x^m x^a grad(div(grad(x^m)))\} = 0 \\
\implies\ &\rho_*^m(x^m + x^a\rho_r)\frac{\partial\hat{\mathbf{q}}^m}{\partial t} - \rho_*^m x^m x^a(1-\rho_r)\frac{\partial\mathbf{v}}{\partial t} - \rho_r x^a\mathbf{b}_{mag}^m \\
&+\rho_r\{k_1\hat{\mathbf{q}}^{\mathbf{m}} + k_2\ grad(x^m) - k_3 x^m x^a grad(div(grad(x^m)))\} = 0 \\
\implies\ &(x^m\rho_*^a + x^a\rho_*^m)\frac{\partial\hat{\mathbf{q}}^m}{\partial t} - \rho_*^a x^m x^a(1-\rho_r)\frac{\partial\mathbf{v}}{\partial t} - x^a\mathbf{b}_{mag}^m \\
&+\{k_1\hat{\mathbf{q}}^{\mathbf{m}} + k_2\ grad(x^m) - k_3 x^m x^a grad(div(grad(x^m)))\} = 0 \qquad (8.6)
\end{aligned}
$$

Equation 8.6 gives the final form of the evolution of the flux of the magnetic component when the bulk momentum or velocity is known. Hence, the final set of equations being solved including the magnetics problem is as follows,

$$div(\mu(x^m)\ grad(\phi)) = 0 \qquad (8.7)$$

$$\frac{\partial x^m}{\partial t} + div(x^m\mathbf{v}) = -div(\hat{\mathbf{q}}^m) \qquad (8.8)$$

$$
\begin{aligned}
(x^m\rho_*^a + x^a\rho_*^m)\frac{\partial\hat{\mathbf{q}}^m}{\partial t} + k_1\hat{\mathbf{q}}^{\mathbf{m}} &= \rho_*^a x^m x^a(1-\rho_r)\frac{\partial\mathbf{v}}{\partial t} + x^a\mathbf{b}_{mag}^m \\
&\quad - \{k_2\ grad(x^m) - k_3 x^m x^a grad(div(grad(x^m)))\}
\end{aligned} \qquad (8.9)
$$

$$
\begin{aligned}
div(\mathbf{T}) =& \frac{1}{x^m + x^a\rho_r}[\rho_*^m\frac{\partial\mathbf{v}}{\partial t} - \mathbf{b}_{mag}^m + (1-\rho_r)\{k_1\mathbf{q}^m + k_2 grad(x^m) \\
&- k_3 x^m x^a grad(div(grad(x^m)))\}] \qquad (8.10)
\end{aligned}
$$

8.4 Weak Form of the Differential Equations for a Stationary Fluid

In the following subsections, we develop the weak formulation of the PDEs discussed above. In order to develop the weak formulation of the equations, test functions ($\phi^\dagger, x^\dagger$ and $\mathbf{v}^\dagger$) defined in the same function space as the corresponding state variables are considered. The operator split allows us to consider the coupled problem as a sequence of

magnetic and convection-diffusion problems that are solved independently. The magnetic and convection-diffusion problems are solved by an adaptive time step strategy, as discussed earlier.

8.4.1 Magnetics Problem

In order to solve the magnetics problem in the magnetic domain (Ω_M) we use equation 8.7 for the scalar potential (ϕ) such that the H-field is the gradient of this potential as described in section 7.2. Since we solve for magnetic fields in the beginning of the time step, the known concentration distribution (x_t^m) computed in the earlier time step is used, making it a differential equation of a single variable.

$$div(\mu(x_t^m)\ grad(\phi_{t+\Delta t})) = 0 \tag{8.11}$$

The weak form of the magnetic equation given above is computed using a scalar test function ($\phi^\dagger$).

$$\begin{aligned} &\int_{\Omega_M} div(\mu(x_{(t)}^m)\ grad(\phi_{t+\Delta t}))\phi^\dagger dV = 0 \\ \implies &-\int_{\Omega_M} \mu(x_{(t)}^m)\ grad(\phi_{t+\Delta t}) \cdot grad(\phi^\dagger) dV + \int_{\partial\Omega_M} \phi^\dagger \mathbf{B}_b \cdot d\mathbf{A} = 0 \end{aligned} \tag{8.12}$$

The body force due to the magnetic field in the system is computed as follows,

$$\begin{aligned} \mathbf{b}_{mag\ t+\Delta t}^m &= x_t^m\ \chi^m\ grad(\mathbf{B_{t+\Delta t}})^T \mathbf{H_{t+\Delta t}} \\ &= \frac{1}{2} \frac{x_t^m\ \chi^m}{\mu(x_t^m)}\ grad(\mathbf{B_{t+\Delta t}} \cdot \mathbf{B_{t+\Delta t}}) \end{aligned} \tag{8.13}$$

where,

$$\mathbf{B_{t+\Delta t}} = \mu(x_t^m)\ grad(\phi_{t+\Delta t}) \tag{8.14}$$

8.4.2 Convection-Diffusion Problem

The convection-diffusion problem is the most critical problem among all the field equations for the polishing mixture. The equation evolution of the concentration of the magnetic particle is non-linear and constrained by the condition, $0 \leq x^m \leq 1$. The equations for the flux and the concentration of the magnetic component of the fluid need to be solved simultaneously.

Hence, an operator split is again employed here with the concentration (x^m, x^a) at time, t, considered for the coefficients of the magnetic force and the differential terms whereas concentration at time, $t+\Delta t$ inside the gradient terms resulting in a semi-implicit formulation for the convection-diffusion problem. Thus, a simple linear equation for convection-diffusion of the constituents in the mixture is achieved. The strong form of the finite difference form of the equations is given below,

$$\begin{aligned}
\frac{x_{t+\Delta t}^m - x_t^m}{\Delta t} &= -div(\hat{\mathbf{q}}^{\mathbf{m}}_{t+\Delta t}) \\
(x_t^m \rho_*^a + x_t^a \rho_*^m)\frac{\hat{\mathbf{q}}_{t+\Delta t}^m - \hat{\mathbf{q}}_t^m}{\Delta t} + k_1 \hat{\mathbf{q}}^{\mathbf{m}}_{\mathbf{t+\Delta t}} &= x_t^a \mathbf{b}^m_{mag\ t+\Delta t} \\
&\quad - k_2\ grad(x^m_{t+\Delta t}) \\
&\quad + k_3 x_t^m x_t^a grad(div(grad(x^m_{t+\Delta t})))
\end{aligned} \tag{8.15}$$

The flux can be computed directly from the finite difference scheme given in equation 8.15. The equation for the magnetic component ($\mathbf{q}^m$) is a third order differential equation in terms of concentration of the magnetic component (x^m). This will make the concentration evolution equation to be a fourth order differential equation. In order to reduce

the complexity of the problem, an additional variable, κ, is introduced and the problem is solved using mixed formulation. The definition of κ is given below,

$$\kappa = div(grad(x^m_{t+\Delta t})) \tag{8.16}$$

It is important to note that the component of the chemical potential in the fluid that minimizes the interface energy in the fluid as given in equation 7.105 is directly proportional to the variable κ defined above. Hence, we simplify the equations by using a mixed formulation with this κ and x^m.

The weak form, thus, derived for the evolution of the concentration of the magnetic component is given below.

$$\int_{\Omega_f} \frac{x^m_{t+\Delta t} - x^m_t}{\Delta t} x^\dagger dV - \int_{\Omega_f} \hat{\mathbf{q}}^m_{t+\Delta t} \cdot grad(x^\dagger) dV + \int_{\partial\Omega_f} x^\dagger \hat{\mathbf{q}}^m_{t+\Delta t} \cdot d\mathbf{A} = 0 \tag{8.17}$$

$$\begin{aligned} \hat{\mathbf{q}}^m_{t+\Delta t} = \frac{1}{k_1 \Delta t + x^m_t \rho^a_* + x^a_t \rho^m_*} [(x^m_t \rho^a_* + x^a_t \rho^m_*) \mathbf{q}^m_t \\ + \Delta t(-k_2\, grad(x^m_{t+\Delta t}) + k_3 x^m_t x^a_t grad(\kappa)))] \end{aligned} \tag{8.18}$$

$$\int_{\Omega_f} \kappa\, \kappa^\dagger dV + \int_{\Omega_f} grad(x^m_{t+\Delta t}) \cdot grad(\kappa^\dagger) dV - \int_{\partial\Omega_f} \kappa^\dagger grad(x^m_{t+\Delta t}) \cdot d\mathbf{A} = 0 \tag{8.19}$$

8.4.3 Velocity - Pressure Problem

The pressure-velocity problem of the fluid is defined using the solutions computed earlier in the convection-diffusion problem. Generally, this problem is not solved in every time step for problems of stationary fluid or known flow, but rather for problems where evolution of the velocity is necessary. For the problems of known flow, the equation is solved for those instances where the pressure solution is to be computed using the time series data of the solved convection-diffusion problem. For such cases, we compute the velocity field as well along with the pressure and check if the resultant solutions match the

initial assumptions for the fluid flow. A constitutive equation for the stresses is assumed appropriately to match the assumed velocity field in the bulk fluid.

The momentum equation (given in equation 8.2) for the fluid when represented in the finite difference form is shown below. The quadratic terms due to the transportation of the bulk momentum is neglected for the simulations

$$\frac{\mathbf{v}_{t+\Delta t}-\mathbf{v}_t}{\Delta t}-(\frac{x^m_{t+\Delta t}}{\rho^m_*}+\frac{x^a_{t+\Delta t}}{\rho^a_*})div(\mathbf{T}_{t+\Delta t})-\frac{\mathbf{b}^m_{mag\ t+\Delta t}}{\rho^m_*}$$
$$-(\frac{1}{\rho^m_*}-\frac{1}{\rho^a_*})(k_1\hat{\mathbf{q}}^{\mathbf{m}}_{\mathbf{t+\Delta t}}+k_2\ grad(x^m_{t+\Delta t})-k_3x^m_{t+\Delta t}x^a_{t+\Delta t}grad(div(grad(x^m_{t+\Delta t})))=\mathbf{0}$$
$$\Longrightarrow\ \frac{\mathbf{v}_{t+\Delta t}-\mathbf{v}_t}{\Delta t}-(x^m_{t+\Delta t}+x^a_{t+\Delta t}\rho_r)div(\mathbf{T}_{t+\Delta t})-\mathbf{b}^m_{mag\ t+\Delta t}$$
$$-(1-\rho_r)(k_1\hat{\mathbf{q}}^{\mathbf{m}}_{\mathbf{t+\Delta t}}+k_2\ grad(x^m_{t+\Delta t})-k_3x^m_{t+\Delta t}x^a_{t+\Delta t}grad(div(grad(x^m_{t+\Delta t})))=\mathbf{0}$$

$$\text{where,}\quad \rho_r=\frac{\rho^m_*}{\rho^a_*}$$

The weak form for the differential equation is given below,

$$\int_{\Omega_f}(\frac{\mathbf{v}_{t+\Delta t}-\mathbf{v}_t}{\Delta t})\cdot\mathbf{v}^\dagger dV+\int_{\Omega_f}\mathbf{T}_{t+\Delta t}\cdot grad((x^m_{t+\Delta t}+x^a_{t+\Delta t}\rho_r)\mathbf{v}^\dagger)dV$$
$$-\int_{\partial\Omega_f}(x^m_{t+\Delta t}+x^a_{t+\Delta t}\rho_r)\mathbf{T}^T_{t+\Delta t}\mathbf{v}^\dagger\cdot d\mathbf{A}-\int_{\Omega_f}\mathbf{b}^m_{mag\ t+\Delta t}\cdot\mathbf{v}^\dagger dV$$
$$-(1-\rho_r)\int_{\Omega_f}(k_1\hat{\mathbf{q}}^{\mathbf{m}}_{\mathbf{t+\Delta t}}+k_2\ grad(x^m_{t+\Delta t})$$
$$-k_3x^m_{t+\Delta t}x^a_{t+\Delta t}grad(div(grad(x^m_{t+\Delta t})))\cdot\mathbf{v}^\dagger dV=\mathbf{0}$$

(8.20)

8.5 Boundary Conditions

8.5.1 Magnetics Problem

The boundary conditions for the magnetics problem depend upon the type of problem being solved in polishing condition. For a scenario where the magnet is considered along with the polishing fluid, the magnetic domain includes the polishing fluid, the magnet, and air with infinite boundary. In such a case, we need to consider a large domain of air and consider using open boundary condition. This is discussed in detail by Meeker [180]. In such simulations, we take the simplest approach by taking a large domain of air and considering that the potential at the boundary to be zero. When the magnetic domain is considered as the domain of the fluid, we define the boundary conditions for the magnetic fields at the boundary of the fluids. In this thesis, we define the H-field at the boundaries of the domain.

8.5.2 Convection-Diffusion Problem

For the convection-diffusion problem, the flux of the magnetic media at the boundaries are set to zero. It is also assumed that no interfaces are formed at the boundaries, and hence the interface energy at the boundaries are zero. This concludes that the gradient of the concentration of magnetic particles at the boundaries are set to zero. There is also an integral constraint that the average concentration of the magnetic component in the mixture is constant in the whole domain. This integral condition applied in the weak form is as follows,

$$\int_{\Omega_f} x^m_{t+\Delta t} dV = \int_{\Omega_f} x^m_0 dV \tag{8.21}$$

where, x^m is the initial concentration of the magnetic media in the mixture. This condition is not needed in the current simulations as we solve for the evolution of the concentration

in time, where the concentration of the previous time step is used to compute the solution for the next time step. But, the condition is monitored through the progress of the computations to check if errors of computations propagate.

8.5.3 Velocity-Pressure Problem

In this thesis, since the velocity of the bulk fluid is already assumed for the fluid, we use the boundary conditions of the assumed velocity to solve this problem. The pressure at the boundary with high abrasive particle concentration is chosen to be zero initially to solve the problem, and then this solution is readjusted by setting the lowest observed pressure to be zero in the domain.

8.6 Material Parameters for Simulation Studies

In this section, we discuss only the general properties of the polishing mixture used in all the simulations. Some of these properties are universal constants, whereas some of them are chosen for a carbonyl iron and silicon carbide abrasive polishing mixture. We assume the mixture to be composed of a magnetic component(30 % magnetic particles in oil) and an abrasive component (30% abrasive particles in oil).

The material properties of the magnetic fluid used in the simulations in this thesis is given in Table 8.1. The permeability of free space is a universal constant which is given in the table. The magnetic susceptibility of the magnetic fluid of 30% is taken from figure 7.2 which describes the experimental results for the magnetic susceptibility of MR fluids. The filled density of the components is computed from the density of particles, carbonyl iron ($\rho_p^m = 7860\ kg/m^3$) and silicon carbide abrasive ($\rho_p^a = 3210\ kg/m^3$), and the density of the base oil ($\rho_{oil} = 823\ kg/m^3$) using equations 8.22 and 8.23.

$$\rho_*^m = 0.30\rho_p^m + 0.70\rho_{oil} \tag{8.22}$$

$$\rho_*^a = 0.30\rho_p^a + 0.70\rho_{oil} \tag{8.23}$$

It is a difficult task to estimate the material parameters of the mixture without conducting repeatable experiments on the magnetic mixture and evaluating the data with the theoretical assumptions. In this thesis, we assume values for the coefficients which on an order of magnitude closer to the existing theoretical models for particulate fluids and qualitatively exhibit the behavior of the fluid.

The drag coefficient, k_1, determines the stress developed by the resistance to the flux of the components of the mixture with respect to the bulk fluid motion. A value or model for this coefficient is not computed or reported in the literature for the model developed in the dissertation. But, expressions for the drag coefficient exist in the literature for a particulate mixture for relative flow between the particles and the base fluid for dilute mixtures. Equation 8.24 shows the drag coefficient as a function of the viscosity of the base oil (η_f), the particle concentration (x_p) and the average radius of the particles (r_p) as discussed by Massoudi [121]. The same equation has been used here to get an approximate estimation of the drag coefficient and hence, a drag coefficient of $10^7\ Pa\ s/m^2$ was chosen for the components in the fluid. The material parameter, k_2, which determines the mixing energy in the mixture can also be approximated through the expression from the literature [121]. But, using those formulas, we find that the value of k_2 is very small. Hence, the value of k_2 was chosen to be $100\ Pa/m^2$ as an approximation, as this would lead to a mixture which upon simulations proved to be stable without separating and settling for 6-7 hours.

The interfacial energy constant (k_3) is written as a function of the mixing constant (k_2) of the material and a length-scale property (l_i) of the fluid as given in equation 8.25. This will help in the future while non-dimensionalizing the differential equation in determining the length scale for the convection-diffusion problem. Also, l_i determines the thickness

of the interface between the magnetic and abrasive brush media. Since we assume that the components to be a continuum, theoretically the interface between the brushes can be of zero thickness. But, since the actual fluid is made up of particles of finite radii mixed and flowing in the oil, the actual interface will have a finite thickness with a much more gradual variation in concentration. It has been qualitatively observed that abrasive particles are stuck at the boundaries of the brushes, indicating an interface region [181]. But, experimental results have not been reported on the size of the interface region. Hence, we assume an interface thickness of 5 mm is chosen to reflect this effect in the mixture for the sake of simulations.

$$k_1 = \frac{9\eta_f(1 + 6.55x_p)}{2r_p^2} \tag{8.24}$$

$$k_3 = k_2 l_i^2 \tag{8.25}$$

Table 8.1: Material properties assumed for magnetic polishing mixture.

Material Property	**Value**
Permeability (μ_0) of Free Space	$4\pi \times 10^{-7} N/A^2$
Magnetic Susceptibility (χ^m) of MR fluid (30 %)	7
Filled density of magnetic component (ρ_*^m)	$2934\ kg/m^3$
Filled density of the abrasive component (ρ_*^a)	$1540\ kg/m^3$
Material parameter (k_1)	$10^7\ Pa\ s/m^2$
Material parameter (k_2)	$100\ Pa/m^2$
Material parameter (l_i)	5 mm

8.7 Non-Dimensionalization of the Differential Equations

The system of differential equations is non-dimensionalized to study the factors that contribute to the behavior of the magnetic mixture.

The differential equations are as given below,

$$div(\mu(x^m)\ grad(\phi)) = 0 \tag{8.26}$$

$$\frac{\partial x^m}{\partial t} + div(x^m \mathbf{v}) = -div(\hat{\mathbf{q}}^m) \tag{8.27}$$

$$\begin{aligned}(x^m\rho_*^a + x^a\rho_*^m)\frac{\partial \hat{\mathbf{q}}^m}{\partial t} + k_1\hat{\mathbf{q}}^{\mathbf{m}} = \rho_*^a x^m x^a(1-\rho_r)\frac{\partial \mathbf{v}}{\partial t} + x^a\mathbf{b}_{mag}^m - \{k_2\ grad(x^m) \\ - k_3 x^m x^a grad(div(grad(x^m)))\}\end{aligned} \tag{8.28}$$

$$\begin{aligned}(x^m + x^a\rho_r)div(-P\mathbf{I} + \mathbf{T}_E) =& \rho_*^m\frac{\partial \mathbf{v}}{\partial t} - \mathbf{b}_{mag}^m + (1-\rho_r)\{k_1\mathbf{q}^m + k_2 grad(x^m) \\ & - k_3 x^m x^a grad(div(grad(x^m)))\}\end{aligned} \tag{8.29}$$

In equation 8.29 we consider the general model for an incompressible fluid directly for ease of non-dimensionalization. In order to non-dimensionalize the differential equation we use the characteristic magnetic potential (ϕ_0), length (l_0), time (t_0), magnetic particle flux ($\hat{q}_0^m$), bulk velocity (v_0). Since the concentration (x^m) does not have any dimensions, we use it directly in our evaluation. The variables and operators of the differential equations can be written in terms of the non-dimensionalized form of the variables with the characteristic variables as following.

$$t = \bar{t}t_0 \tag{8.30}$$

$$div = \frac{\bar{div}}{l_0} \tag{8.31}$$

$$grad = \frac{\bar{grad}}{l_0} \tag{8.32}$$

$$\phi = \bar{\phi}\phi_0 \tag{8.33}$$

$$\mathbf{v} = \bar{\mathbf{v}}v_0 \tag{8.34}$$

$$\mathbf{T} = -P_0\bar{P}\mathbf{I} + T_{E0}\bar{T_E} \tag{8.35}$$

$$\hat{\mathbf{q}}^{\mathbf{m}} = \bar{\hat{\mathbf{q}}}^{\mathbf{m}}\hat{q}_0^m \tag{8.36}$$

$$\mathbf{b}_{\mathbf{mag}}^{\mathbf{m}} = \bar{\mathbf{b}}_{\mathbf{mag}}^{\mathbf{m}} b_0^m \tag{8.37}$$

Using the above definitions for the variables and non-dimensionalizing the differential equations above, we get the following form of the differential equations in terms of non-dimensinalized variables and operators.

$$\begin{aligned} & div(\mu(x^m)grad(\phi)) = 0 \\ \implies & \frac{\mu_0\phi_0}{l_0^2}\bar{div}(\bar{\mu}(x^m)\ \bar{grad}(\bar{\phi})) = 0 \\ \implies & \bar{div}(\bar{\mu}(x^m)\ \bar{grad}(\bar{\phi})) = 0 \end{aligned} \tag{8.38}$$

Non-dimensionalizing the H-field we get,

$$\begin{aligned} H_0\bar{\mathbf{H}} &= grad(\phi) \\ &= \frac{\phi_0}{l_0}\bar{grad}(\bar{\phi}) \\ \implies \bar{\mathbf{H}} &= \frac{\phi_0}{l_0H_0}\bar{grad}(\bar{\phi}) \end{aligned} \tag{8.39}$$

Non-dimensionalizing the magnetic force we get,

$$\begin{aligned} b_{mag0}^m\bar{\mathbf{b}}_{mag}^m &= \chi^m x^m grad(\mathbf{B})^T\mathbf{H} \\ &= \chi^m x^m grad(\mu(x^m)grad(\phi))^T grad(\phi) \end{aligned}$$

$$= \frac{\mu_0 \phi_0^2 \chi^m}{l_0^3} x^m \bar{grad}(\bar{\mu}(x^m) \bar{grad}(\bar{\phi}))^T \bar{grad}(\bar{\phi})$$

$$\implies \bar{\mathbf{b}}_{mag}^m = \frac{\mu_0 \phi_0^2 \chi^m}{l_0^3 b_{mag0}^m} x^m \bar{grad}(\bar{\mu}(x^m) \bar{grad}(\bar{\phi}))^T \bar{grad}(\bar{\phi}) \tag{8.40}$$

Now, non-dimensionalizing the balance equation for x^m using the definitions given in equations 8.30 to 8.37 we get the following form for the balance equation with the non-dimensionalized quantities.

$$\frac{1}{t_0} \frac{\partial x^m}{\partial \bar{t}} + \frac{v_0}{l_0} \bar{div}(x^m \bar{\mathbf{v}}) = -\frac{\hat{q}_0^m}{l_0} \bar{div}(\bar{\hat{\mathbf{q}}}^m)$$

$$\implies \frac{\partial x^m}{\partial \bar{t}} + \frac{v_0 t_0}{l_0} \bar{div}(x^m \bar{\mathbf{v}}) = -\frac{\hat{q}_0^m t_0}{l_0} \bar{div}(\bar{\hat{\mathbf{q}}}^m) \tag{8.41}$$

Now, again non-dimensionalizing the balance equation for the flux of the magnetic component (given in equation 8.28) using the definitions given in equations 8.30 to 8.37 we get the following derivation.

$$\begin{aligned}
\rho_*^m (x^m \rho_r + x^a) \frac{\hat{q}_0^m}{t_0} \frac{\partial \bar{\hat{\mathbf{q}}}^m}{\partial \bar{t}} + k_1 \hat{q}_0^m \bar{\hat{\mathbf{q}}}^{\mathbf{m}} &= x^a b_{mag0}^m \bar{\mathbf{b}}_{mag}^m \\
&\quad - \frac{k_2}{l_0} \bar{grad}(x^m) \\
&\quad + \frac{k_3}{l_0^3} x^m x^a \bar{grad}(\bar{div}(\bar{grad}(x^m))) \\
\implies \frac{\rho_*^m}{k_1 t_0} (x^m \rho_r + x^a) \frac{\partial \bar{\hat{\mathbf{q}}}^m}{\partial \bar{t}} + \bar{\hat{\mathbf{q}}}^{\mathbf{m}} &= \frac{b_{mag0}^m}{k_1 \hat{q}_0^m} x^a \bar{\mathbf{b}}_{mag}^m \\
&\quad - \frac{k_2}{l_0 k_1 \hat{q}_0^m} \bar{grad}(x^m) \\
&\quad + \frac{k_2 l_i^2}{l_0^3 k_1 \hat{q}_0^m} x^m x^a \bar{grad}(\bar{div}(\bar{grad}(x^m)))
\end{aligned} \tag{8.42}$$

Finally, the non-dimensionalized form of the momentum balance equation (given in 8.29)

using the definitions in equations 8.30 to 8.37 is derived as shown below.

$$\begin{aligned}
\frac{(x^m + x^a\rho_r)}{l_0}\bar{div}(-P_0\bar{P}\mathbf{I} + T_{E0}\bar{\mathbf{T}}_E) =& \frac{\rho_*^m v_0}{t_0}\frac{\partial\bar{\mathbf{v}}}{\partial\bar{t}} - b_{mag0}^m\bar{\mathbf{b}}_{mag}^m + (1-\rho_r)\{k_1\hat{q}_0^m\bar{\hat{\mathbf{q}}}^m \\
&+ \frac{k_2}{l_0}\bar{grad}(x^m) - \frac{k_3}{l_0^3}x^m x^a\bar{grad}(\bar{div}(\bar{grad}(x^m)))\} \\
\implies -\frac{(x^m + x^a\rho_r)P_0}{k_1\hat{q}_0^m l_0}&\bar{grad}(\bar{P}) \\
+\frac{(x^m + x^a\rho_r)T_{E0}}{k_1\hat{q}_0^m l_0}\bar{div}(\bar{\mathbf{T}}_E) =& \frac{\rho_*^m v_0}{k_1\hat{q}_0^m t_0}\frac{\partial\bar{\mathbf{v}}}{\partial\bar{t}} - \frac{b_{mag0}^m}{k_1\hat{q}_0^m}\bar{\mathbf{b}}_{mag}^m + (1-\rho_r)\{\bar{\hat{\mathbf{q}}}^m \\
&+ \frac{k_2}{k_1\hat{q}_0^m l_0}\bar{grad}(x^m) \\
&- \frac{k_3}{k_1\hat{q}_0^m l_0^3}x^m x^a\bar{grad}(\bar{div}(\bar{grad}(x^m)))\} \qquad (8.43)
\end{aligned}$$

We make the following simplifications on the characteristic variables by setting the coefficients of some processes to 1. This will reduce the complexity of the problem and set the equations in terms of the few important control characteristic values that we set for the problem. First, let's set the coefficient of $\bar{\phi}$ to 1 in equation 8.39.

$$\begin{aligned}
\frac{\phi_0}{H_0 l_0} &= 1 \\
\implies \phi_0 &= H_0 l_0 \qquad (8.44)
\end{aligned}$$

Now, let's set the coefficient of $x^m\bar{grad}(\bar{\mu}(x^m)\bar{grad}(\bar{\phi}))^T\bar{grad}(\bar{\phi})$ in equation 8.40 to 1. Substituting the expression for ϕ_0 given in equation 8.44 we compute the following expression for b_{mag0}^m.

$$\begin{aligned}
\frac{\mu_0\phi_0^2\chi^m}{l_0^3 b_{mag0}^m} &= 1 \\
\implies b_{mag0}^m &= \frac{\mu_0\phi_0^2\chi^m}{l_0^3} \\
&= \frac{\mu_0 H_0^2\chi^m}{l_0} \qquad (8.45)
\end{aligned}$$

Now, let's set the coefficient of $\bar{div}(\bar{\hat{\mathbf{q}}}^m)$ in equation 8.41 to 1 to compute the following expression for $\hat{q}_0^m$.

$$\begin{aligned} \frac{\hat{q}_0^m t_0}{l_0} &= 1 \\ \implies \hat{q}_0^m &= \frac{l_0}{t_0} \end{aligned} \tag{8.46}$$

Since the type of problems solved in this thesis are either stationary bulk fluid or bulk fluid shearing at a constant known rate, it is useful to define the characteristic speed (v_0) in terms of the shear rate (γ_0) in the bulk fluid as given below.

$$v_0 = \gamma_0 l_0 \tag{8.47}$$

Now, setting the coefficient of $\bar{grad}(x^m)$ and $x^m x^a \bar{grad}(\bar{div}(\bar{grad}(x^m)))$ to 1 in equation 8.42 we compute the following expression for t_0 and l_0.

$$\begin{aligned} \frac{k_2}{l_0 k_1 \hat{q}_0^m} &= 1 \\ \implies \frac{k_2 t_0}{k_1 l_0^2} &= 1 \\ \implies t_0 &= \frac{k_1 l_0^2}{k_2} \end{aligned} \tag{8.48}$$

$$\begin{aligned} \frac{k_2 l_i^2}{l_0^3 k_1 \hat{q}_0^m} &= 1 \\ \implies \frac{k_2 l_i^2 t_0}{l_0^4 k_1} &= 1 \\ \implies \frac{k_2 l_i^2}{l_0^4 k_1} \frac{k_1 l_0^2}{k_2} &= 1 \\ \implies l_0 &= l_i \end{aligned} \tag{8.49}$$

Now, let's assume the coefficient associated with the pressure term in equation 8.43 to

be one to get a characteristic pressure for the system in terms of the material parameters.

$$\begin{aligned}
&\frac{P_0}{k_1 \hat{q}_0^m l_0} = 1 \\
\implies\ & P_0 = k_1 \hat{q}_0^m l_0 \\
&= k_1 \ \frac{l_0}{k_1 l_0^2 / k_2} \ l_0 \\
&= k_2
\end{aligned} \tag{8.50}$$

Finally, assuming the following expression for T_{E0} in terms of an average viscosity (η_0) and the shear rate (γ_0) in the material, we get a rough estimate of the characteristic extra stress for the bulk fluid.

$$T_{E0} = \eta_0 \gamma_0 \tag{8.51}$$

Now, substituting all these expressions for the characteristic terms evaluated in equations 8.44 to 8.51 we get the following simplified form for all the balance equations.

$$\bar{div}(\bar{\mu}(x^m)\ \bar{grad}(\bar{\phi})) = 0 \tag{8.52}$$

$$\frac{\partial x^m}{\partial \bar{t}} + \frac{\gamma_0 k_1 l_i^2}{k_2} \bar{div}(x^m \bar{\mathbf{v}}) = -\bar{div}(\bar{\hat{\mathbf{q}}}^m) \tag{8.53}$$

$$\begin{aligned}
\frac{\rho_*^m k_2}{k_1^2 l_i^2}(x^m \rho_r + x^a) \frac{\partial \bar{\hat{\mathbf{q}}}^m}{\partial \bar{t}} + \bar{\hat{\mathbf{q}}}^{\mathbf{m}} &= \frac{\mu_0 H_0^2 \chi^m}{k_2} x^a \bar{\mathbf{b}}_{mag}^m - \bar{grad}(x^m) \\
&\quad + x^m x^a \bar{grad}(\bar{div}(\bar{grad}(x^m)))
\end{aligned} \tag{8.54}$$

$$\begin{aligned}
&-(x^m + x^a \rho_r) \bar{grad}(\bar{P}) \\
+\frac{(x^m + x^a \rho_r)\eta_0 \gamma_0}{k_2} \bar{div}(\bar{\mathbf{T}}_E) =& \frac{\rho_*^m \gamma_0}{k_1} \frac{\partial \bar{\mathbf{v}}}{\partial \bar{t}} - \frac{\mu_0 H_0^2 \chi^m}{k_2} \bar{\mathbf{b}}_{mag}^m + (1 - \rho_r)\{\bar{\hat{\mathbf{q}}}^m \\
&+ \bar{grad}(x^m) - x^m x^a \bar{grad}(\bar{div}(\bar{grad}(x^m)))\}
\end{aligned} \tag{8.55}$$

Through the simplifications done above, we were finally able to evaluate the non-dimensionalized equations for the balance equations in terms of the material parameters (ρ_*^m, ρ_r, k_1, k_2, l_i, η_0, μ_0 and χ_m) and problem specific characteristic values for the H-field (H_0) and shear rate (γ_0). Now, the values of these coefficients for any specific problem dictates the behavior exhibited by the mixture. Since, we assume a single set of material properties for the mixture, as shown in table 8.1, for all the simulations in this thesis, we can further evaluate and simplify the coefficients as given below. For this analysis, we take a characteristic viscosity of 30 Pas for the bulk fluid from the results of the experiments conducted in Chapter 6. This is an inaccurate assumption, but it suits us to check the relevance of shear forces in the system in comparison with diffusion.

$$\frac{\gamma_0 k_1 l_i^2}{k_2} = 2.5\gamma_0 \tag{8.56}$$

$$\frac{\rho_*^m k_2}{k_1^2 l_i^2} = 1.17 \times 10^{-4} \tag{8.57}$$

$$\frac{\mu_0 H_0^2 \chi^m}{k_2} = 8.796 \times 10^{-8} H_0^2 \tag{8.58}$$

$$\frac{\eta_0 \gamma_0}{k_2} = 0.3\gamma_0 \tag{8.59}$$

$$\frac{\rho_*^m \gamma_0}{k_1} = 2.934 \times 10^{-4}\gamma_0 \tag{8.60}$$

Through this non-dimensionalization scheme, we choose a length scale and time scale for the problem that are normalized to the diffusion process. Hence, we compare every other process, namely the magnetic forces developed, the shear flow of the bulk fluid and inertial forces and the effect of the initial concentration of the magnetic component with respect to this primary process. Now, studying the value of the coefficient computed in equation 8.57 above, we find that the inertial effect of the flux of magnetic component is insignificant in comparison to the diffusion in this fluid. Hence, we may neglect the

inertial effects in the magnetic flux in the fluid. Equation 8.59 shows that the stress in the mixture is significant in the computation of the bulk velocity of the bulk fluid for the shear rates considered in the thesis. The details about the choice of characteristic values and its effect on the behavior is discussed in detail later in this chapter.

8.8 Mesh Convergence Study

The appropriate size of the finite element mesh is found by conducting a mesh convergence study described in the section. Convergence study on the mesh helps in simulating numerical results for the evolution of the magnetic fields and concentrations in the mixture that are independent of the mesh parameters used to compute them. The simulations of the magnetic fields and the concentration of the magnetic particles were conducted on a structured mesh (e.g., refer figure 8.3).

The appropriate mesh size for the mesh was found by comparing the results of final equilibrium solution for infinitely long stationary bulk fluid with perturbed initial concentration of magnetic particles in the presence of a constant H-field. The fluid is assumed to occupy a rectangular domain of size $10\ cm \times 2\ cm$ with periodic boundary conditions in the x direction. The initial distribution of the magnetic particles is given in equation 8.61. The fluid concentration assumed to be distributed sinusoidally in the x direction. The equilibrium solution for the segregated fluid is used to compare the effect of the choice of mesh sizes.

$$x^m = 0.5 + 0.1 * cos(\frac{\pi x}{w_b}) \tag{8.61}$$

where, w_b is the width of the brush with perturbed concentration of magnetic component. The width of the brush here is chosen to be one-sixth of the length of the domain.

The material constants for the problem given in Table 8.1 are considered for the fluid.

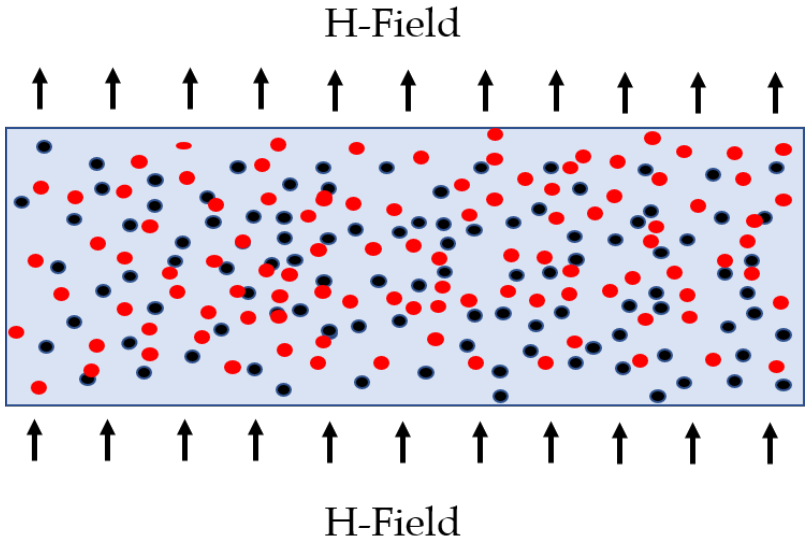

Figure 8.2: Schematic showing the mixture, with a constant H-field at the boundaries, used for conducting a mesh convergence study for the fluid.

The H-field in the material assumed to be constant at the top and bottom boundaries. The H-field is assumed to be $5 \times 10^3\ A/m$.

A schematic of the test problem used for mesh convergence is given in figure 8.2. The mesh used for the simulations is a structured mesh where the domain is divided into rectangular cells which are further divided into two right triangular mesh units as shown in figure 8.3. Since every rectangular cell in the mesh is divided diagonally to form two triangular mesh units, it is the size of the rectangular cells that are altered in this study. The aspect ratio of 1:2 is used as the cell-size for the cells in the mesh. The initial mesh is taken is by assuming 2 cells in the y direction. The aspect ratio of 1:2 results in 20 cells in the x direction. This initial mesh is shown in figure 8.3. For every subsequent simulation, the number of cells in the y direction is doubled. Thus, the simulations were run for the number of cells 20×2, 40×4, 80×8, 160×16 and 32×320 for 5 s to find the equilibrium solution. The equilibrium solution is checked by identifying if the flux ($\mathbf{q}^m$) goes to zero

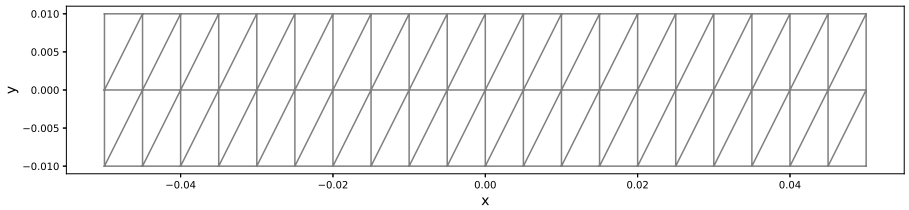

Figure 8.3: The base mesh used to find the convergent mesh for the simulation. Note that the mesh has right triangular cells with an aspect ratio of 1:2 for the sides. In each step, the cell size is reduced to half the earlier size. The center of the coordinates is chosen at the center of the domain.

at 5 s. The maximum pressure in the fluid and the final distribution of the concentration of the magnetic particles are used to find the appropriate mesh for simulations.

The results for the pressure and the final concentration state of the fluid was considered in the domain. The results for the maximum pressure observed with respect to the no. of cells in the y direction for different meshes are given in figure 8.4. Here, it is observed that the maximum pressure for 80×8 mesh is only 0.554 % different from the maximum pressure for 160×16 mesh. Moreover, by further halving the mesh size, the maximum pressure estimated improves only by 0.0001 %. This indicates that mesh becomes convergent at 160×16 cell configuration and further refinement doesn't improve the pressure significantly.

The results for the concentration of magnetic component in the x direction at $y = 0$ is given in figure 8.5. The results have been plotted only between $[-0.025, 0.025]$ for comparison. The concentration distribution across the magnetic brush formed due to magnetic segregation is shown in the figure. The data points for this graph are collected with a gap of $0.1\ mm$ along the x direction. Here, it can be directly observed that even though the results are significantly different for smaller number of cells, there is a very small difference between the results for 80×8 cell mesh and 160×16 cell mesh. It is also observed that the results for 320×32 cell mesh is almost exactly the same as the result for a 160×16 mesh,

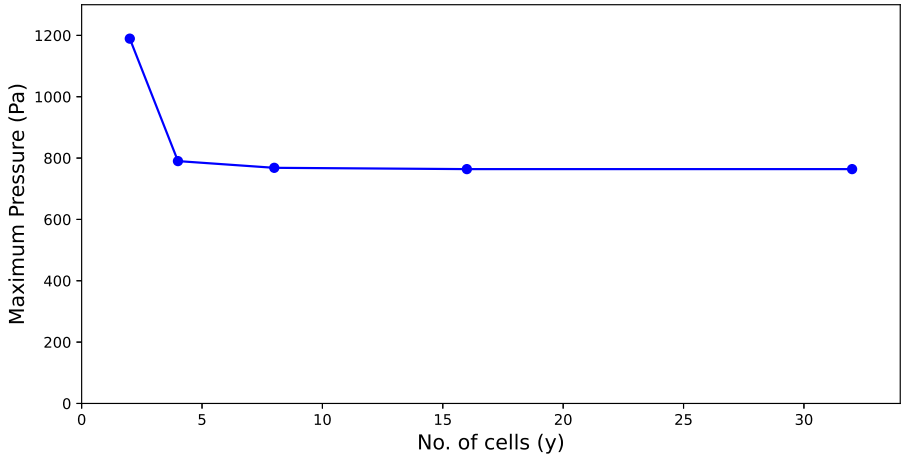

Figure 8.4: The maximum pressure computed in the domain versus the number of cells in the y direction of the mesh. Note that the pressure computed for 80×8 mesh (8 cells in y direction) is only 0.5 % different from the pressure for 160×16 mesh.

indicating that the problem achieves mesh independence at 160×16 cell configuration. Thus, 160×16 cell configuration is chosen as the mesh-independent configuration for the domain. The mesh size for this cell configuration is $0.625\ mm \times 1.25\ mm$.

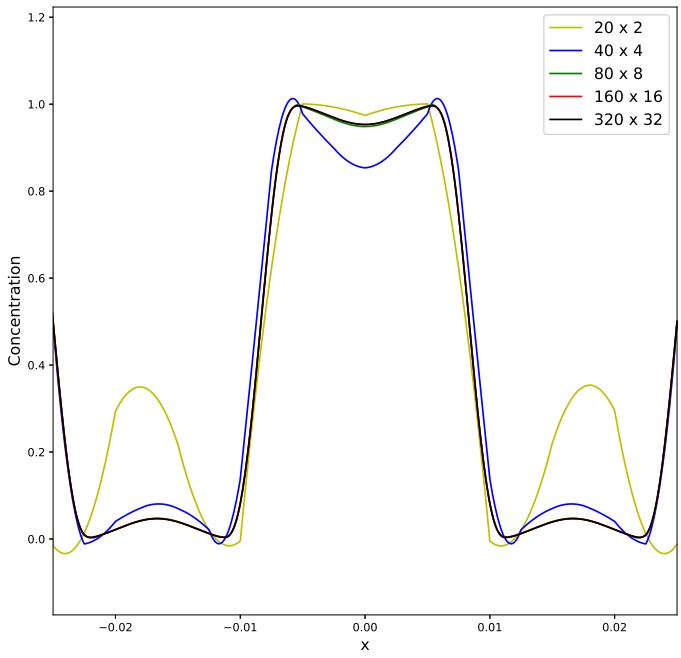

Figure 8.5: Comparison of the concentration of the magnetic particles at y = 0 for the different meshes. Note that the plot from the 320×32 mesh completely coincides with the plot from 160×16 mesh

8.9 Segregation in stationary polishing fluid under magnetic field

In this section, we study if the approach is able to simulate the formation of segregated brushes in the fluid under magnetic fields. In the literature, segregation and formation of brushes are simulated only for MR fluids (no abrasives are considered in the studies). Moreover, the calculation of the distribution, flow behavior etc., based on the magnetic fields assumed in the fluid or calculated based on the initial distribution of the particles [181]. The problems of both the magnetic fields and flow behavior are simulated in a decoupled method, i.e., the solution of flow behavior is assumed to not affect the magnetic fields inside the bulk fluid. A first order coupling of the H-field to the particles is performed for molecular dynamics simulation of dilute MR fluids [182]. Here, we study the results of the distribution achieved by coupling and decoupling the two behaviors as a

continuum formulation for concentrated MR finishing mixtures. This study focuses on the stratification of a stationary mixture (zero bulk velocity) due to different boundary conditions on the fluid and initial conditions for the concentration of the magnetic component in the mixture. The study helps in analyzing the effect of these conditions on the final equilibrium distribution of components and pressure in the mixture.

8.9.1 Test Problem - Stationary Fluid with perturbed concentration

The behavior of a stationary fluid with a perturbed distribution of magnetic component in the presence of a constant H-field is studied in this section. Experiments have been conducted on dilute magnetic particulate fluids in the presence of a constant H-field where, chain like structures are formed by the magnetic particles separating from the base fluid [14]. One such experimental result showing the chains formed in dilute MR fluids are shown in figure 8.6. Segregation study on MR polishing fluid under a uniform magnetic field is not reported in the literature. Experimental observations on the segregated structure of the fluid has been made for magnetic arrangements in polishing setups [15]. Figure 8.7 shows the segregated structure of an MR polishing fluid for a magnetic arrangement using permanent magnets. Since polishing fluids have higher concentration of magnetic particles, the polishing fluid generally segregates into brush like structures. This study simulates this brush like formations in the fluid. The influence of the change in magnetic fields due to the concentration changes in the mixture is studied in this section. For the simulation, if we assume a constant distribution of the components in the fluid, it will result in a constant B-field in the mixture. This leads to zero body forces to segregate the mixture. But, the concentration will never be exactly constant through the volume in practice, rather would be perturbed through the volume. Thus, the initial volume is assumed to be perturbed to observe the effect of perturbation on the stability of the fluid in the presence of a constant H-field. The basic setup is that of a mixture with 50 %

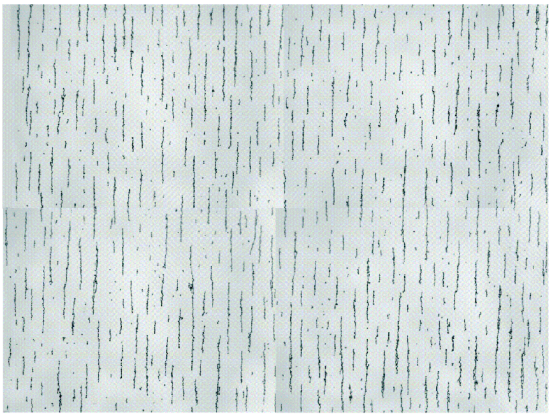

Figure 8.6: Magnetic particle chains formed in a dilute MR fluid under uniform H-field [14]

volume occupied by magnetic slurry in a mixture infinitely long in the x direction. This is simulated using a rectangular domain of dimensions $10\ cm \times 2\ cm$ with periodic boundary conditions in the x direction. A schematic of this setup with the magnetic fields is given in figure 8.8

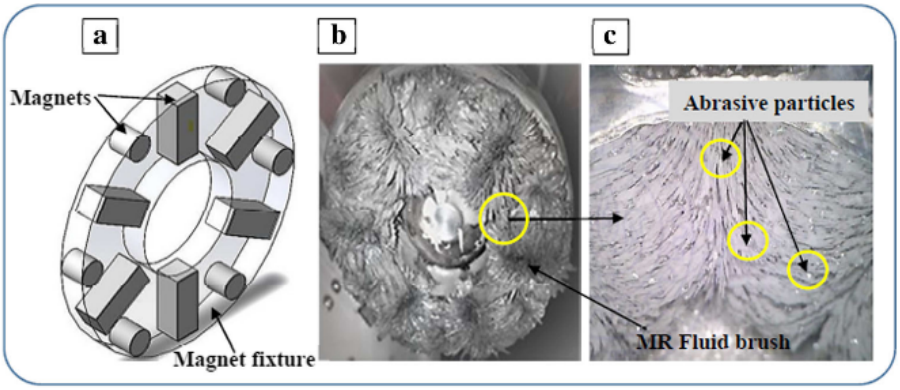

Figure 8.7: a) Magnetic fixture used for polishing, b)Photographic view of tool with the segregated MR finishing fluid and c) Magnified view of MR fluid brushes and abrasives [15]

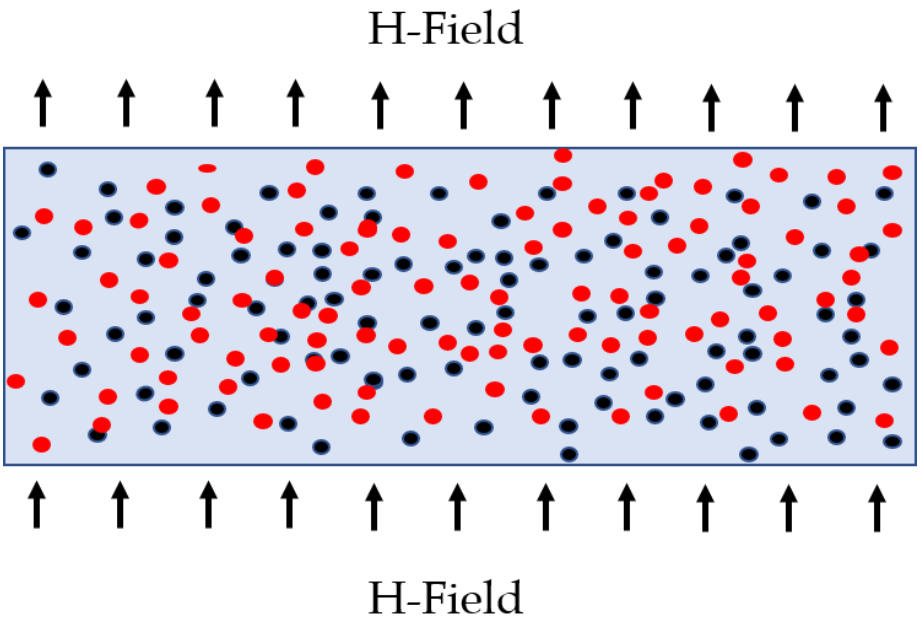

Figure 8.8: Schematic describing the basic setup of the mixture and magnetic fields for the cases being discussed in the section

In this test case, the magnetic particles are assumed to be uniformly distributed in the domain but with a small perturbation in the x direction. The equation defining the concentration of the magnetic component in the domain is given below,

$$x^m = 0.5 + 0.1\ cos(\frac{\pi x}{w_b}) \tag{8.62}$$

where w_b is the width of concentrated regions (brushes) in the fluid. The width of the brush here is chosen to be one-sixth of the length of the domain.

A uniform H-field of $5 \times 10^3\ A/m$ is applied at the top and bottom boundaries of the domain. The setup of the fluid and the H-field at the boundaries are the same as given in figure 8.8. The initial concentration of the magnetic component in the mixture before the magnetic field is applied is given in figure 8.9. The simulations are run in two conditions.

- Decoupled - The magnetic fields for the initial distribution of the magnetic media is computed and assumed to be unchanged throughout the segregation simulation
- Coupled - The magnetic fields are updated as the distribution of the magnetic media in the fluid changes.

The final differential equations for a stationary mixture in the presence of constant H-field is given below.

$$div(\mu(x^m)\ grad(\phi)) = 0 \tag{8.63}$$

$$\frac{\partial x^m}{\partial t} = -div(\hat{\mathbf{q}}^m) \tag{8.64}$$

$$\begin{aligned}(x^m\rho_*^a + x^a\rho_*^m)\frac{\partial \hat{\mathbf{q}}^m}{\partial t} + k_1\hat{\mathbf{q}}^{\mathbf{m}} &= x^a\mathbf{b}_{mag}^m - \{k_2\ grad(x^m) \\ &\quad - k_3x^mx^a grad(div(grad(x^m)))\}\end{aligned} \tag{8.65}$$

$$\begin{aligned}(x^m + x^a\rho_r)div(-P\mathbf{I} + \mathbf{T}_E) &= -\mathbf{b}_{mag}^m + (1-\rho_r)\{k_1\mathbf{q}^m + k_2 grad(x^m) \\ &\quad - k_3x^mx^a grad(div(grad(x^m)))\}\end{aligned} \tag{8.66}$$

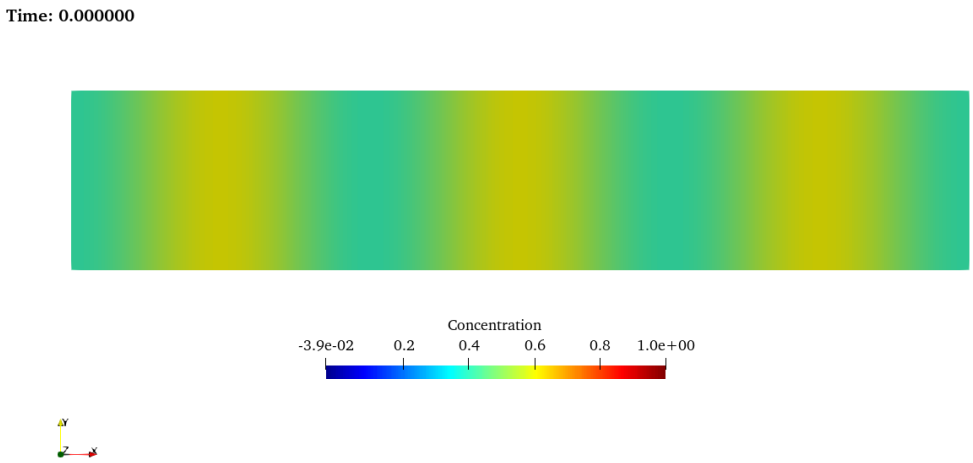

Figure 8.9: Initial Concentration of the perturbed fluid in the presence of a uniform H-field at the boundaries. Note that the regions with higher and lower concentrations of fluid are of brush width w_b.

where,

$$\mathbf{b}^m_{mag} = \chi^m x^m grad(\mathbf{B})^T \mathbf{H} \tag{8.67}$$

The boundary conditions for the fluid are given below. Periodic boundary conditions are applied at the boundaries $x = -l_f/2$ and $x = l_f/2$. The boundary conditions for the constant H-field, zero flux and zero gradient for the concentration of magnetic components are applied at the boundaries $y = -w_f/2$ and $y = w_f/2$.

$$\phi|_{x=-l_f/2} = \phi|_{x=l_f/2}$$

$$x^m|_{x=-l_f/2} = x^m|_{x=l_f/2}$$

$$\hat{\mathbf{q}}^m|_{x=-l_f/2} = \hat{\mathbf{q}}^m|_{x=l_f/2}$$

$$\mathbf{H} \cdot \mathbf{n}|_{y=-w_f/2} = -5 \times 10^3 A/m$$

$$\mathbf{H} \cdot \mathbf{n}|_{y=w_f/2} = 5 \times 10^3 A/m$$

$$\hat{\mathbf{q}}^m \cdot \mathbf{n}|_{y=-w_f/2} = \hat{\mathbf{q}}^m \cdot \mathbf{n}|_{y=w_f/2} = 0$$
$$grad(x^m) \cdot \mathbf{n}|_{y=-w_f/2} = grad(x^m) \cdot \mathbf{n}|_{y=w_f/2} = 0 \tag{8.68}$$

The results of the simulations for the stationary fluid is given in the following section.

8.9.1.1 Results and Discussion

The results for the volume concentration of the polishing mixture after reaching steady state is given in figure 8.10. The segregation of the components in the decoupled scenario is minimal. This is due to smaller body forces developed due to the perturbation in the initial concentration of the magnetic component. From the volume concentration in the coupled simulation results, higher amount of segregation is observed as the change in the magnetic fields are also considered. This indicates that the body forces on the magnetic components change significantly with change in the concentration of the fluid driving the segregation process in the mixture. This results in highly segregated brushes in the mixture. Figure 8.11 shows the concentration of the magnetic component in the fluid at $y = 0$ in the x-direction. This shows the effect of coupling the magnetic field in the simulation of the concentration evolution. Interfaces are formed with high gradients showing the segregation of the components with interface width equal to the characteristic length of the mixture. This effect is observed in the simulations as the perturbations cause a varying B-field in the fluid resulting in segregating that only further drives the segregation of the mixture. The interfacial energy developed at the interfaces of the brushes counteract the body forces, resulting in a smooth interface between the segregated regions. The decoupled simulation computes a low gradient of concentration at the edges of the brushes, resulting in lower segregation. This results in computation of much smaller body forces and pressure in the brushes, which are also an important factor in polishing. Thus, coupled simulations are necessary to predict a more realistic segregated structure of the fluid,

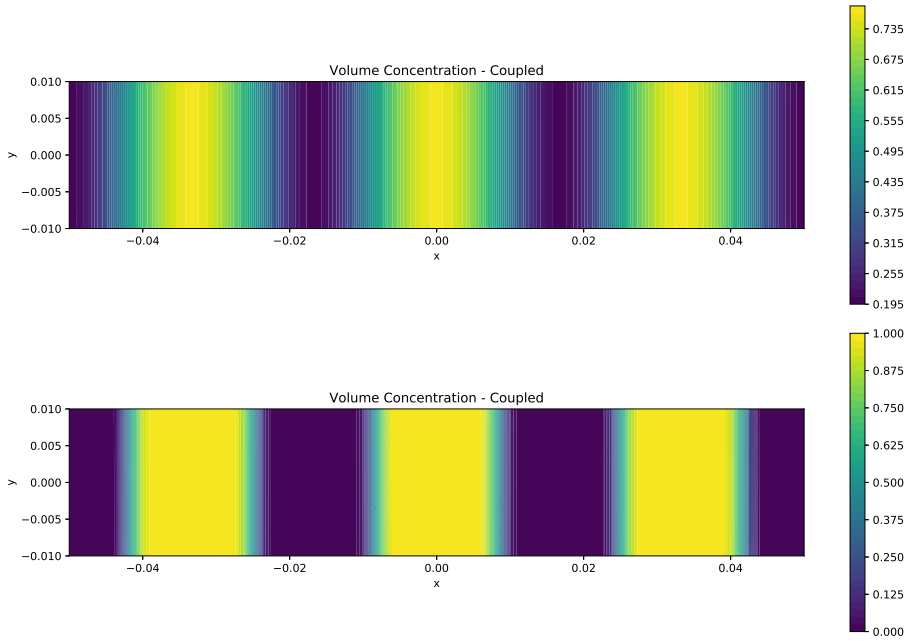

Figure 8.10: Volume Concentration of the magnetic component of the fluid at equilibrium in the mixture under a linearly varying H-field. Note that in the decoupled scenario the fluid doesn't segregate much due to very low body forces from the perturbed initial condition, whereas in the coupled scenario the fluid segregates into brush like formation.

although this is computed in a decoupled approach in the literature.

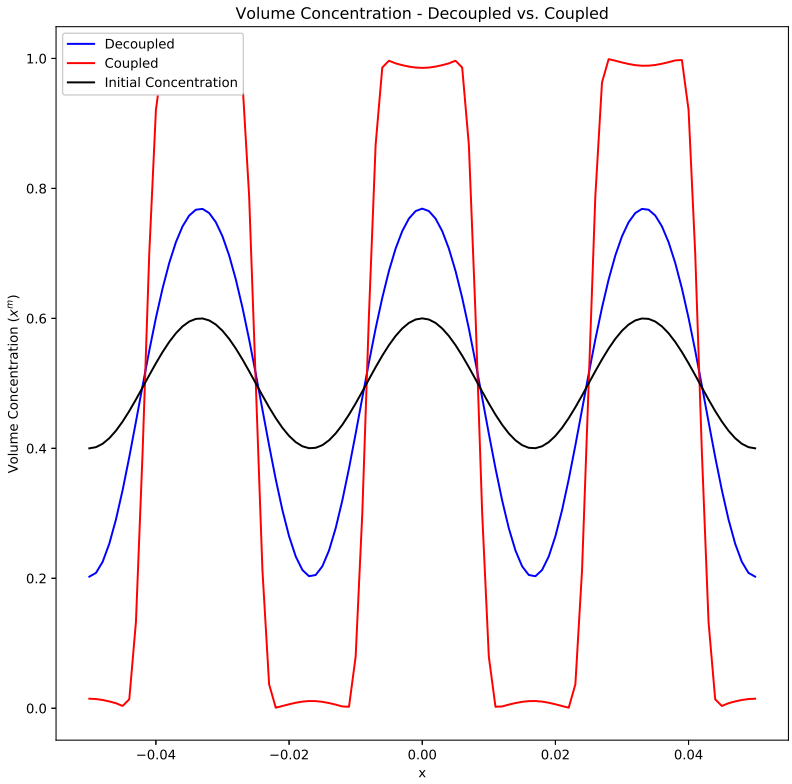

Figure 8.11: Comparison of the volume concentration of magnetic component of the mixture at equilibrium condition with respect to the initial concentration of the component in the mixture. Note that the volume concentration of the magnetic component has a huge gradient at the boundaries of the segregated fluid which leads to the high pressure in the inside the magnetic brushes.

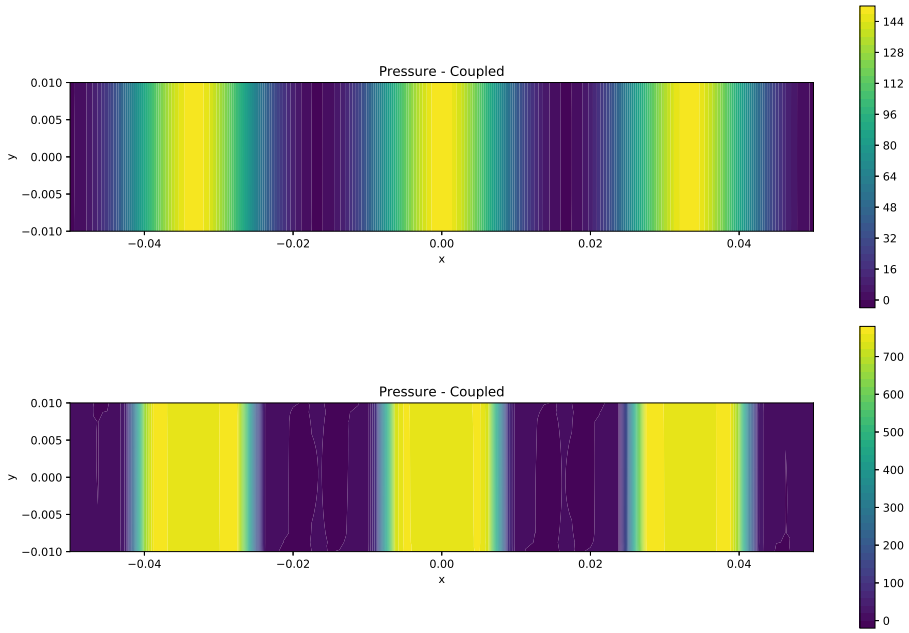

Figure 8.12: Comparison of the pressure in the mixture at equilibrium. Note that the pressure in the coupled simulation is much higher than the pressure in the decoupled simulation. This pressure will result in a normal force on the workpiece at the top boundary

8.9.2 Fringe like H-field at the boundaries

In this scenario, we assume the H-field to vary linearly such that it is a maximum of $5 \times 10^3\ A/m$ at the center and reduces to zero at the ends. The mixture will segregate due to the gradient of the magnetic fields in the mixture. In this section, we study the effect of coupling the magnetic field calculation to the concentration equations on the steady state solution of the segregated fluid. In the earlier section, it was the perturbation of the fluid that primarily drove the segregation process. In this scenario, the objective is to study if the coupling influences the results significantly when the gradient of the external field applied is the primary cause that drives the segregation of the fluid. Thus, a mixture with constant distribution of magnetic particles is studied in the presence of a linearly varying H-field to gauge the influence of coupling the magnetic fields to the concentration

changes. The schematic of this configuration is given in figure 8.13. This scenario is similar to fringe magnetic fields observed close to the edges of two magnets placed next to each other to produce a constant magnetic field at the center. This simulation studies the effect of magnetic gradient perpendicular to the field with change in magnetic component distribution on the segregation and the stresses developed in a stationary fluid.

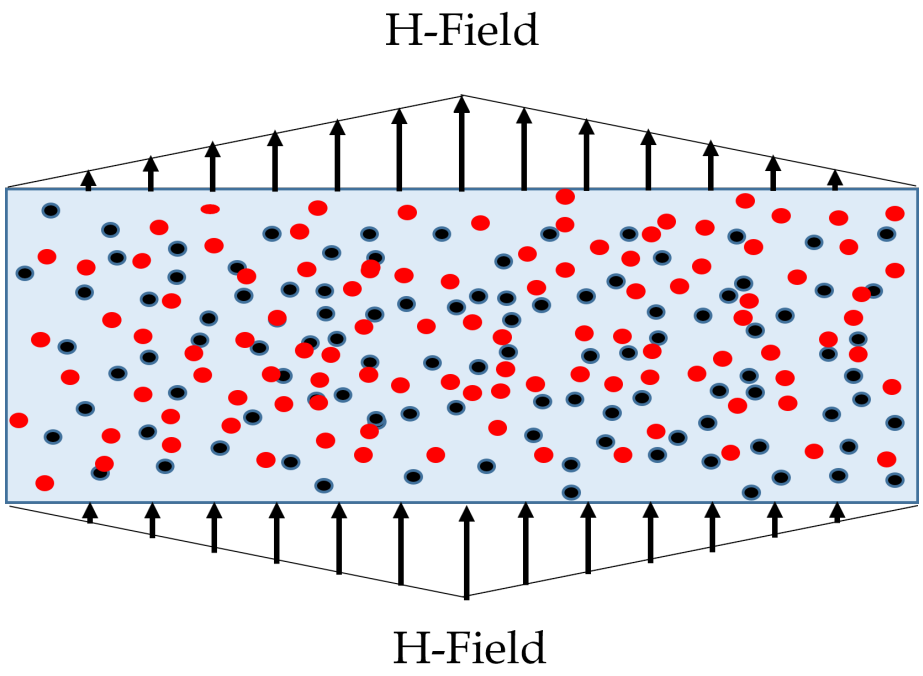

Figure 8.13: Schematic showing the polishing mixture with linearly varying H-field for Case – 1

The simulations were conducted for the following two conditions.

- Decoupled - The magnetic fields for the initial distribution of the magnetic media is computed and assumed to be unchanged throughout the segregation simulation
- Coupled - The magnetic fields are updated as the distribution of the magnetic media

in the fluid changes.

The final differential equations for a stationary mixture in the presence of linearly varying H-field at the boundaries is given below.

$$div(\mu(x^m)\ grad(\phi)) = 0 \tag{8.69}$$

$$\frac{\partial x^m}{\partial t} = -div(\hat{\mathbf{q}}^m) \tag{8.70}$$

$$\begin{aligned}(x^m\rho_*^a + x^a\rho_*^m)\frac{\partial \hat{\mathbf{q}}^m}{\partial t} + k_1\hat{\mathbf{q}}^{\mathbf{m}} &= x^a\mathbf{b}_{mag}^m - \{k_2\ grad(x^m) \\ &\quad - k_3x^mx^a grad(div(grad(x^m)))\}\end{aligned} \tag{8.71}$$

$$\begin{aligned}(x^m + x^a\rho_r)div(-P\mathbf{I} + \mathbf{T}_E) &= -\mathbf{b}_{mag}^m + (1-\rho_r)\{k_1\mathbf{q}^m + k_2 grad(x^m) \\ &\quad - k_3x^mx^a grad(div(grad(x^m)))\}\end{aligned} \tag{8.72}$$

where,

$$\mathbf{b}_{mag}^m = \chi^m x^m grad(\mathbf{B})^T\mathbf{H} \tag{8.73}$$

The boundary conditions for the fluid are given below. The boundary conditions for the constant H-field, zero flux and zero gradient for the concentration of magnetic components are applied at the boundaries $y = -w_f/2$ and $y = w_f/2$.

$$\mathbf{H}\cdot\mathbf{n}|_{x=-l_f/2} = \mathbf{H}\cdot\mathbf{n}|_{x=l_f/2} = 0$$

$$\hat{\mathbf{q}}^m\cdot\mathbf{n}|_{x=-l_f/2} = \hat{\mathbf{q}}^m\cdot\mathbf{n}|_{x=l_f/2} = 0$$

$$\mathbf{H}\cdot\mathbf{n}|_{y=-w_f/2} = -5\times10^3(|x| - l_f/2)$$

$$\mathbf{H}\cdot\mathbf{n}|_{y=w_f/2} = 5\times10^3(|x| - l_f/2)$$

$$\hat{\mathbf{q}}^m\cdot\mathbf{n}|_{y=-w_f/2} = \hat{\mathbf{q}}^m\cdot\mathbf{n}|_{y=w_f/2} = 0$$

$$grad(x^m) \cdot \mathbf{n}|_{y=-w_f/2} = grad(x^m) \cdot \mathbf{n}|_{y=w_f/2} = 0 \tag{8.74}$$

where $\mathbf{n}$ is the normal perpendicular to the boundary of the domain.

8.9.2.1 Results and Discussion

The results of the simulation for these two cases are given in Figures 8.14 to 8.16. Figure 8.14 shows the distribution of the magnetic component of the fluid at steady state. Similar to the earlier example, the segregation is much higher in the coupled simulation in comparison to the decoupled simulations. Fig 8.15 shows that a much higher gradient is observed at the boundary of the segregated fluid. This is observed as the coupled simulations do consider the segregation div en by the concentration also along with the segregation due to magnetic fields. This results in a much higher pressure observed inside the magnetic component, as shown in figure 8.16. Even in this scenario, we observe a 60 % reduction in the pressure in the segregated media when a decoupled magnetic field is assumed to act on the fluid. These results indicate that the concentration of the magnetic component in the mixture significantly affects the stresses and the magnetic fields in the mixture. Hence, it is necessary to consider coupled simulation of the fluid to achieve an accurate simulation of the fluid for all types of external magnetic fields

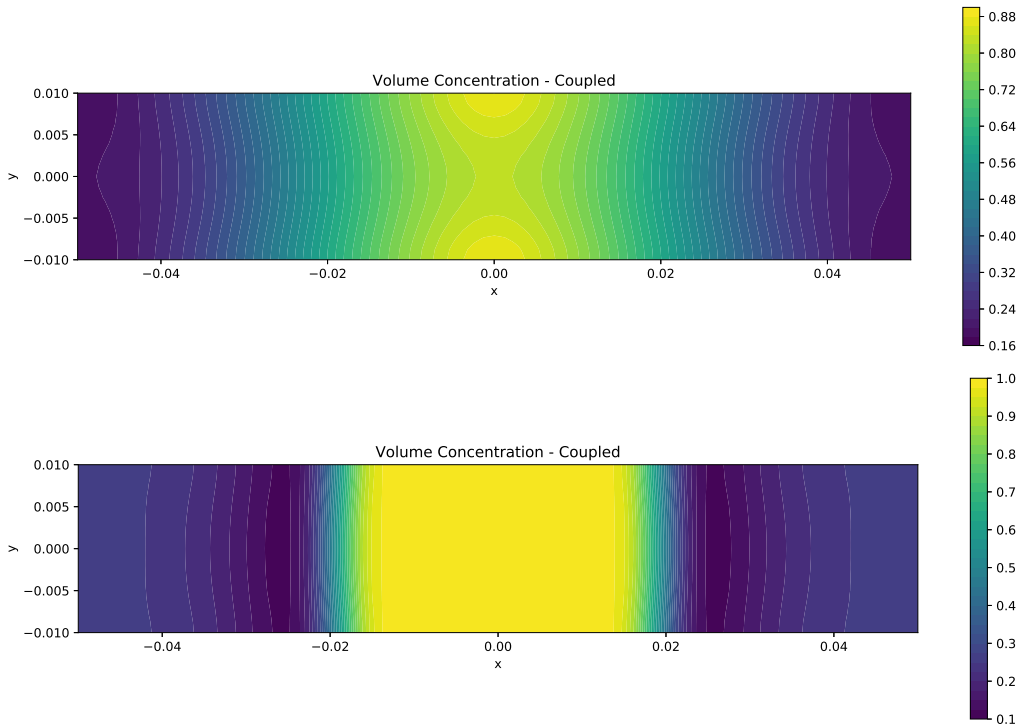

Figure 8.14: The Volume Concentration of the magnetic component of the fluid at equilibrium in the mixture under a linearly varying H-field. Note that the coupled simulation of the fluid gives a more defined segregation of magnetic media in the mixture.

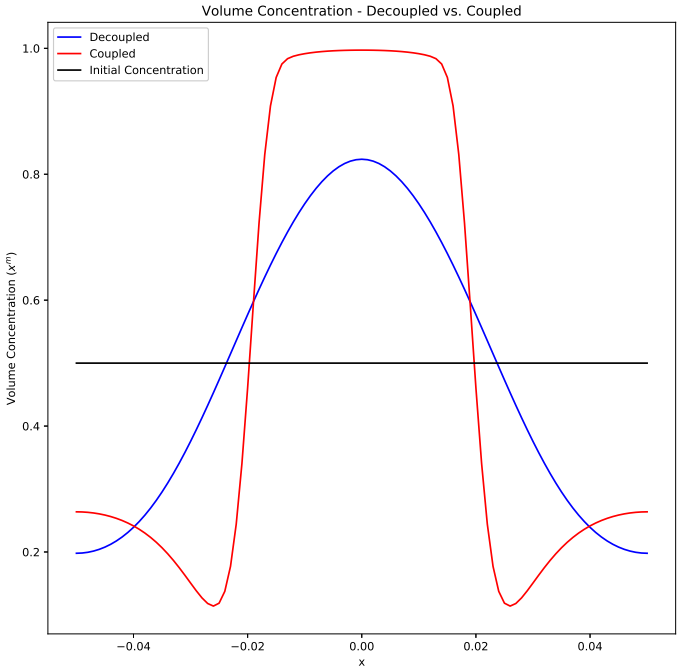

Figure 8.15: Comparison of the volume concentration of the magnetic component of the mixture at $y = 0$. Note that the coupled simulation has a higher gradient than the decoupled simulation at the boundary, as it considers both the effect of permeability change in the mixture along the gradient in the magnetic field.

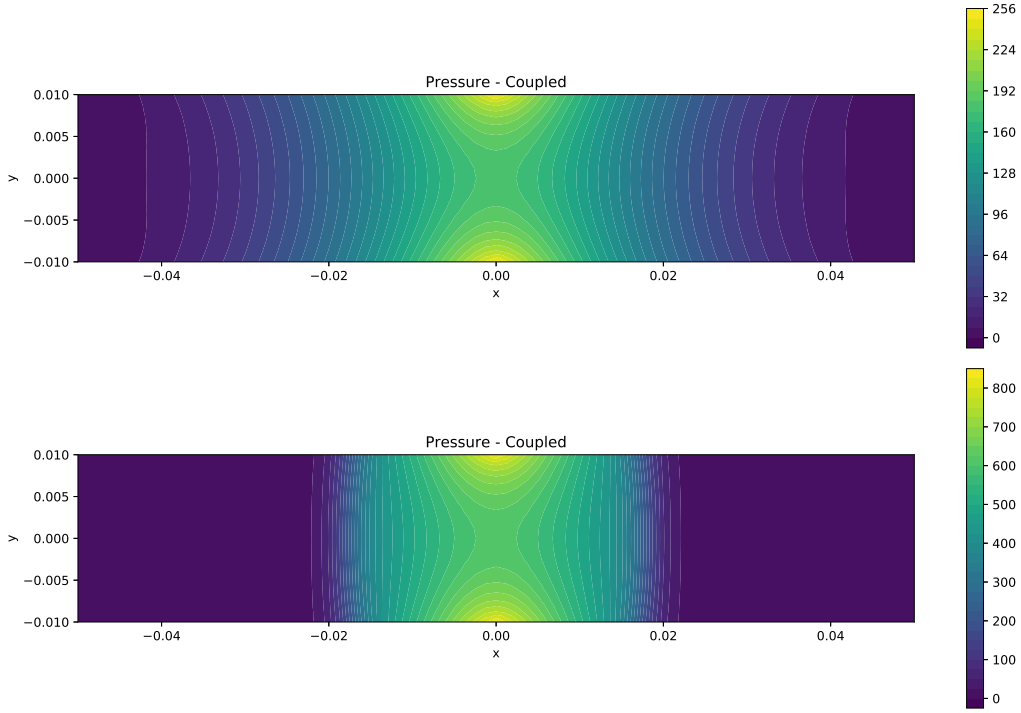

Figure 8.16: Comparison of the Pressure fields in the decoupled and coupled simulations. Note that the maximum pressure observed in the decoupled is much lower(60 %) than the pressure in the coupled simulation

8.10 Non-Dimensionalized study of Perturbed fluid in Constant H-field

In this section, we study the conditions for the segregation and mixing behavior of the magnetic polishing mixture. Upon studying the behavior of fluid, we observe that the fluid segregation behavior is dependent on the initial condition of the fluid and the H-field applied at the boundaries of the fluid. For some perturbation brush widths in the initial distribution, it is observed that the fluid completely segregates to magnetic brushes, whereas for certain brush widths the fluid mixes to form a stable uniform mixture. In this study, we hope to identify the hope to identify the non-dimensional factors in the fluid and the external fields that decide this behavior of the mixture model. The non-dimensionalized form of the differential equations for the stationary fluid problem ($\mathbf{v} = \mathbf{0}$) is given in the equations 8.75 to 8.78 from the equations 8.52 to 8.55. Since we assume that the fluid is stationary, we take the shear rate in the fluid to be zero.

$$\bar{div}(\bar{\mu}(x^m)\ \bar{grad}(\bar{\phi})) = 0 \tag{8.75}$$

$$\frac{\partial x^m}{\partial \bar{t}} = -\bar{div}(\hat{\mathbf{q}}^m) \tag{8.76}$$

$$\begin{aligned}\frac{\rho_*^m k_2}{k_1^2 l_i^2}(x^m\rho_r + x^a)\frac{\partial \bar{\hat{\mathbf{q}}}^m}{\partial \bar{t}} + \bar{\hat{\mathbf{q}}}^{\mathbf{m}} =& \frac{\mu_0 H_0^2 \chi^m}{k_2} x^a \bar{\mathbf{b}}_{mag}^m - \bar{grad}(x^m) \\ &+ x^m x^a \bar{grad}(\bar{div}(\bar{grad}(x^m)))\end{aligned} \tag{8.77}$$

$$\begin{aligned}(x^m + x^a\rho_r)\bar{grad}(\bar{P}) =& \frac{\mu_0 H_0^2 \chi^m}{k_2}\bar{\mathbf{b}}_{mag}^m - (1-\rho_r)\{\bar{\hat{\mathbf{q}}}^m \\ &+ \bar{grad}(x^m) - x^m x^a \bar{grad}(\bar{div}(\bar{grad}(x^m)))\}\end{aligned} \tag{8.78}$$

Now considering the equations for the coefficients given in equations 8.56 to 8.60 for the material used in these simulations, we get the following final form for the non-

dimensionalized differential equations in terms of the characteristic H-field H_0.

$$\begin{aligned}\bar{\hat{\mathbf{q}}}^{\mathbf{m}} &= C_{mag}x^a\bar{\mathbf{b}}^m_{mag} - g\bar{r}ad(x^m) \\ &\quad + x^m x^a g\bar{r}ad(d\bar{i}v(g\bar{r}ad(x^m))) \qquad (8.79)\\ (x^m + x^a\rho_r)g\bar{r}ad(\bar{P}) &= C_{mag}\bar{\mathbf{b}}^m_{mag} - (1-\rho_r)\{\bar{\hat{\mathbf{q}}}^m \\ &\quad + g\bar{r}ad(x^m) - x^m x^a g\bar{r}ad(d\bar{i}v(g\bar{r}ad(x^m)))\} \qquad (8.80)\end{aligned}$$

where, C_{mag} is the magnetic coefficient to $\bar{\mathbf{b}}^m_{mag}$ which is computed for the problem as follows,

$$\begin{aligned}C_{mag} &= \frac{\mu_0 H_0^2 \chi^m}{k_2} \\ &= 8.796 \times 10^{-8} H_0^2 \qquad (8.81)\end{aligned}$$

Now non-dimensionalizing the initial condition for the fluid problem using the characteristic length for the fluid problem as derived below. Defining the x position in terms of the characteristic length as shown in equation 8.82.

$$x = l_i \bar{x} \qquad (8.82)$$

The concentration of the magnetic component (x^m) in terms of the non-dimensional form of the x position is given in the equation below.

$$\begin{aligned}x^m &= 0.5 + 0.1\ cos(\frac{\pi x}{w_b}) \\ &= 0.5 + 0.1\ cos(\frac{\pi \bar{x}}{\bar{w}_b}) \qquad (8.83)\end{aligned}$$

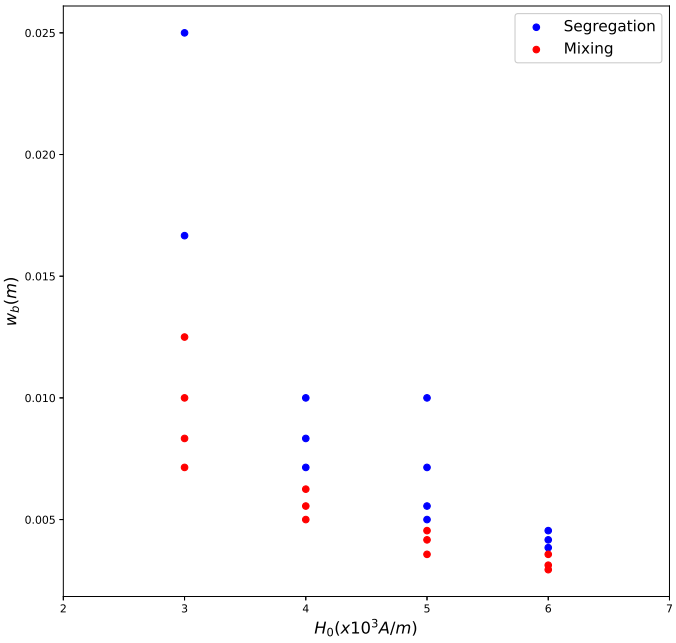

Figure 8.17: Segregation and mixing behavior of magnetic polishing mixture for different magnetic field (H_0) and initial brush width (w_b)

where w_b is the non-dimensionalized form of the width of the brush, as given below.

$$\bar{w_b} = \frac{w_b}{l_i} \tag{8.84}$$

Hence, the problem of the stationary fluid in the presence of constant H-field in the boundaries is simplified to a2 parameter problem, where the characteristics of the behavior of the fluid is governed by the parameters, the H-field at the boundaries (H_0) and the width of perturbation in concentration (brush width) (w_b). Now, comparing the behavior of the fluid for different combinations of H_0 and w_b we get the graph given in figure 8.17.

This behavior of the fluid for different magnetic fields (H_0) and brush width (w_b) indicate that for a mixture with defined properties given by the material parameters, the fluid mixing and segregation is governed by two opposing forces, the magnetic field that tries

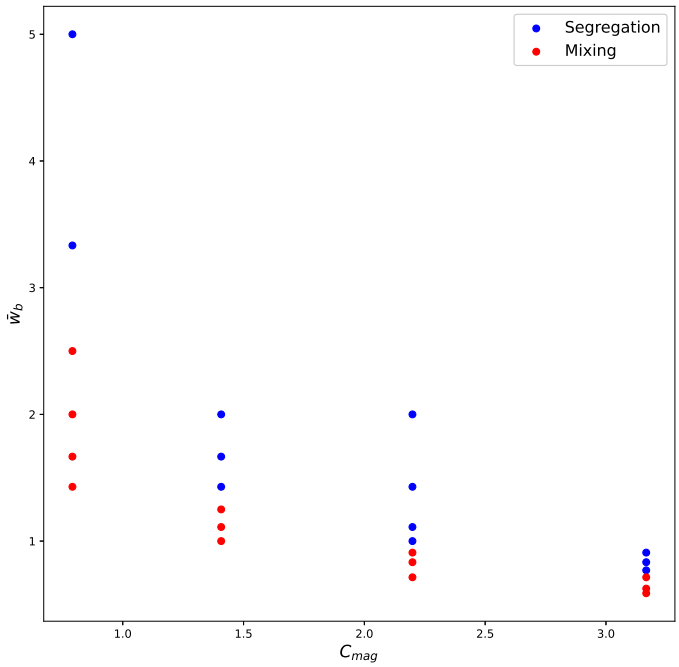

Figure 8.18: Segregation and mixing behavior of the magnetic mixture for different combinations of magnetic coefficients and non-dimensional brush widths for the problem

to segregate the fluid and the internal energy that tires to mix through the fluid through diffusion. The effect of these can be motivated theoretically through substituting the initial condition into the problem and studying the direction of the flux generated for this initial condition. Note that for the initial condition, the concentration only varies in the x direction and is independent of the y coordinate. Therefore, the solution to the magnetics problem (given in equation 8.63) is a linear ϕ field as given below.

$$\phi = H_0 y \tag{8.85}$$

where, H_0 is the constant external H-field applied at the top and bottom boundaries. From

this the non-dimensionalized form of the H-field ($\bar{\mathbf{H}}$) can be computed as follows,

$$\begin{aligned}\bar{\mathbf{H}} &= \frac{1}{H_0} grad(\phi) \\ &= 1\hat{\mathbf{e}}_y \end{aligned} \tag{8.86}$$

The non-dimensionalized magnetic force ($\bar{\mathbf{b}}_{mag}$) is computed as follows,

$$\begin{aligned}\bar{\mathbf{b}}_{mag} &= x^m \bar{grad}(\bar{\mu}(x^m)\bar{\mathbf{H}})^T\bar{\mathbf{H}} \\ &= x^m \frac{1}{2\bar{\mu}(x^m)} \bar{grad}(\bar{\mu}(x^m)^2\bar{\mathbf{H}}\cdot\bar{\mathbf{H}}) \\ &= x^m \bar{grad}(\bar{\mu}(x^m)) \\ &= x^m \bar{grad}(\frac{\mu_0(1+\chi^m x^m)}{\mu_0}) \\ &= x^m \chi^m \bar{grad}(x^m) \end{aligned} \tag{8.87}$$

Now substituting this in equation 8.79 describing the flux in the mixture, we get the following form

$$\begin{aligned}\bar{\hat{\mathbf{q}}}^{\mathbf{m}} &= C_{mag} x^a \bar{\mathbf{b}}^m_{mag} - \bar{grad}(x^m) + x^m x^a \bar{grad}(\bar{div}(\bar{grad}(x^m))) \\ &= C_{mag} x^a x^m \chi^m \bar{grad}(x^m) - \bar{grad}(x^m) + x^m x^a \bar{grad}(\bar{div}(\bar{grad}(x^m))) \end{aligned} \tag{8.88}$$

Now, substituting the initial condition (equation 8.83) into the above equation, we get the following for flux $\bar{\hat{\mathbf{q}}}^{\mathbf{m}}$.

$$\begin{aligned}\bar{\hat{\mathbf{q}}}^{\mathbf{m}} &= [-x^a x^m \chi^m C_{mag} \frac{0.1\pi}{\bar{w}_b} sin(\frac{\pi\bar{x}}{\bar{w}_b}) + \frac{0.1\pi}{\bar{w}_b} sin(\frac{\pi\bar{x}}{\bar{w}_b}) + x^m x^a \frac{0.1\pi^3}{\bar{w}_b^3} sin(\frac{\pi\bar{x}}{\bar{w}_b})]\hat{\mathbf{e}}_x \\ &= [-x^a x^m \chi^m C_{mag} + 1 + x^m x^a \frac{\pi^2}{\bar{w}_b^2}] \frac{0.1\pi}{\bar{w}_b} sin(\frac{\pi\bar{x}}{\bar{w}_b})\hat{\mathbf{e}}_x \end{aligned}$$

$$= [1 + x^m x^a (\frac{\pi^2}{\bar{w}_b^2} - \chi^m C_{mag})] \frac{0.1\pi}{\bar{w}_b} sin(\frac{\pi \bar{x}}{\bar{w}_b}) \hat{\mathbf{e}}_x$$
$$= C_q \frac{0.1\pi}{\bar{w}_b} sin(\frac{\pi \bar{x}}{\bar{w}_b}) \hat{\mathbf{e}}_x \tag{8.89}$$

where,

$$C_q = [1 + x^m x^a (\frac{\pi^2}{\bar{w}_b^2} - \chi^m C_{mag})] \tag{8.90}$$

The direction of the flux of the magnetic component $\hat{\mathbf{q}}^m$ can be studied with respect to the gradient of the concentration in the mixture, given below.

$$grad(x^m) = -\frac{0.1\pi}{\bar{w}_b} sin(\frac{\pi \bar{x}}{\bar{w}_b}) \hat{\mathbf{e}}_x \tag{8.91}$$

The behavior of the mixture can be studied by comparing equations 8.89 and 8.91. When C_q is negative the fluid will segregate as the magnetic component will diffuse along the gradient of the concentration further segregating the fluid, whereas when C_q is positive the magnetic component will diffuse from the higher concentration to the lower concentrations resulting in a mixed fluid. Thus, it can be noted that the segregation behavior of the mixture initially increases with increasing magnetic field and brush width in the mixture. It is observed from the simulations that this behavior of the fluid continues until a stable distribution of the magnetic component is achieved, either in the form of segregated brushes or as a complete mixture. Also note that the amplitude of the perturbation doesn't play a role in deciding the behavior of the fluid. Thus, when a stationary fluid with a perturbed concentration of magnetic component in x direction is subject to a constant magnetic field the fluid segregates for all those brush widths above a brush width decided by the coefficient C_{mag} and susceptibility χ^m of the mixture.

8.11 Magnetic Mixture under shear flow

In this chapter, we primarily consider the magnetic polishing mixture in couette-like motion. This bulk motion of the fluid is prescribed to the fluid and the behavior of the particles under this motion of the fluid is studied to find the formation of magnetic brushes inside the fluid. Breaking and reformation of the brushes have been studied in the literature using methods such as laser spectrometry for dilute magnetic fluids [183]. Chains have been observed to be breaking and reforming for low shear rate, whereas at high shear the chains break completely [183]. Simulations of such dilute single component particulate media have been conducted using molecular dynamics [136]. But, simulations on concentrated multi-component magnetic mixtures where the particles segregate and form brushes are not generally studied in the literature. The effect of different factors such as the field strength and shear rate of the mixture on these brush formations is studied in this section.

8.11.1 Shear flow applied to the segregated fluid

In this section, we discuss a problem where a perturbed fluid is subjected to constant H-field while it is stationary. And then the segregated fluid is subjected to a known constant shear flow to study how the characteristics of the magnetic brushes evolve under shear flow condition. Here, we conduct a one way coupling of the fluid bulk flow behavior to study the segregation behavior of the fluid. The bulk mixture velocity is assumed to be unaffected by the magnetic field. Typically, in the literature [136], the velocity is computed from the magnetic field which is already assumed. In this study, we rather assume the bulk flow and rather consider the coupled effect of the magnetic field on the shearing fluid.

Generally, in polishing, the thickness of the magnetic mixture used is small in comparison to the size of the pad used to polish the work piece. Thus, we assume that the velocity of the bulk fluid along the thickness is zero. Substituting this assumption into the

incompressibility condition gives that the velocity of the fluid is only a function of y (we assume the thickness to be along the y direction) as given below.

$$\begin{aligned} div(\mathbf{v}) &= 0 \\ \implies \frac{\partial v_x}{\partial x} + \frac{\partial v_y}{\partial y} &= 0 \\ \implies \frac{\partial v_x}{\partial x} &= 0 \\ \implies \mathbf{v} &= v_x(y)\hat{\mathbf{e}}_x \end{aligned} \tag{8.92}$$

Also, we take a zeroth order approximation for the extra stress ($\mathbf{T}_E(x^m, H_0, \mathbf{D})$) in the bulk mixture with respect to the concentration of the magnetic component in the fluid as shown in the equation below.

$$\begin{aligned} \mathbf{T}_E(x^m, H_0, \mathbf{D}) &= \mathbf{T}_E(0.5, H_0, \mathbf{D}) + (x^m - 0.5)\frac{\partial \mathbf{T}_E(x^m, H_0, \mathbf{D})}{\partial x^m} \\ &\quad + \frac{(x^m - 0.5)^2}{2!}\frac{\partial^2 \mathbf{T}_E(x^m, H_0, \mathbf{D})}{\partial x^{m2}} + ... \\ &\approx \mathbf{T}_E(0.5, H_0, \mathbf{D}) \end{aligned} \tag{8.93}$$

Now, considering equation 8.54 describing the evolution of the flux, $\hat{\mathbf{q}}^m$ with the value of the coefficient computed in equation 8.57 the following expression can be computed.

$$\begin{aligned} \bar{\hat{\mathbf{q}}}^{\mathbf{m}} &= \frac{\mu_0 H_0^2 \chi^m}{k_2} x^a \bar{\mathbf{b}}^m_{mag} - \bar{grad}(x^m) + x^m x^a \bar{grad}(\bar{div}(\bar{grad}(x^m))) \\ \implies \bar{\hat{\mathbf{q}}}^{\mathbf{m}} &+ \bar{grad}(x^m) - x^m x^a \bar{grad}(\bar{div}(\bar{grad}(x^m))) = C_{mag} x^a \bar{\mathbf{b}}^m_{mag} \end{aligned} \tag{8.94}$$

Now considering equation 8.55 and substituting equation 8.94 into the function, we

get a simplified form of the momentum balance equation. The inertial term in the equation can be ignored, as equation 8.60 suggests that for the shear rates considered in this thesis the inertial coefficient is much smaller than the other terms. Thus, the final equation of momentum balance is given in equation 8.95.

$$\begin{aligned}
&-(x^m + x^a\rho_r)\bar{grad}(\bar{P}) \\
+\frac{(x^m + x^a\rho_r)\eta_0\gamma_0}{k_2}\bar{div}(\bar{\mathbf{T}}_E) =& \frac{\rho_*^m\gamma_0}{k_1}\frac{\partial\bar{\mathbf{v}}}{\partial\bar{t}} - \frac{\mu_0 H_0^2\chi^m}{k_2}\bar{\mathbf{b}}_{mag}^m + (1-\rho_r)\{\bar{\hat{\mathbf{q}}}^m \\
&+ \bar{grad}(x^m) - x^m x^a \bar{grad}(\bar{div}(\bar{grad}(x^m)))\} \\
=& -C_{mag}\bar{\mathbf{b}}_{mag}^m + (1-\rho_r)C_{mag}x^a\bar{\mathbf{b}}_{mag}^m \\
=& -(x^m + x^a\rho_r)C_{mag}\bar{\mathbf{b}}_{mag}^m \\
\implies -\bar{grad}(\bar{P}) + \frac{\eta_0\gamma_0}{k_2}\bar{div}(\bar{\mathbf{T}}_E) =& -C_{mag}\bar{\mathbf{b}}_{mag}^m
\end{aligned} \tag{8.95}$$

Now looking the momentum balance in x direction from equation 8.95 above we get the following,

$$\begin{aligned}
-\frac{\partial\bar{P}}{\partial\bar{x}} + \frac{\eta_0\gamma_0}{k_2}\left(\frac{\partial\bar{\mathbf{T}}_{Exx}}{\partial\bar{x}} + \frac{\partial\bar{\mathbf{T}}_{Exy}}{\partial\bar{y}}\right) &= -C_{mag}\bar{\mathbf{b}}_{magx}^m \\
\implies -\frac{\partial\bar{P}}{\partial\bar{x}} + \frac{\eta_0\gamma_0}{k_2}\frac{\partial\bar{\mathbf{T}}_{Exy}}{\partial\bar{y}} &= -C_{mag}\bar{\mathbf{b}}_{magx}^m
\end{aligned}$$

This implies that,

$$\begin{aligned}
\bar{P} &= C_{mag}\int\bar{\mathbf{b}}_{magx}^m dx + \frac{\eta_0\gamma_0}{k_2}\int\frac{\partial\bar{\mathbf{T}}_{Exy}}{\partial\bar{y}}dx \\
\implies \bar{P} &= C_{mag}\int\bar{\mathbf{b}}_{magx}^m dx + \frac{\eta_0\gamma_0}{k_2}\frac{\partial\bar{\mathbf{T}}_{Exy}}{\partial\bar{y}}x
\end{aligned} \tag{8.96}$$

Since we try to solve the problem for an infinitely long domain in x direction by considering periodic boundary conditions at $x = -l_f/2$ and $x = l_f/2$, $\bar{P}$ and $\int\bar{\mathbf{b}}_{magx}^m dx$ are

equal at the two boundaries. On substituting these conditions into equation 8.96 we get the following derivation for $\bar{\mathbf{T}}_{Exy}$.

$$\begin{aligned} & \frac{\partial \bar{\mathbf{T}}_{Exy}}{\partial \bar{y}} l_f = 0 \\ \implies & \frac{\partial \bar{\mathbf{T}}_{Exy}}{\partial \bar{y}} = 0 \\ \implies & \bar{\mathbf{T}}_{Exy} = c_1 \end{aligned} \tag{8.97}$$

Since $\bar{\mathbf{T}}_{Exy}$ is a function of the gradient of velocity ($\partial v_x / \partial y$), equation 8.97 indicates that the gradient of velocity is constant. Thus, a linear profile for the velocity ($v_x(y)\hat{\mathbf{e}}_x$) in the y direction is a good assumption for the behavior of the fluid under couette type boundary conditions when we ignore the bulk velocity in the y direction.

The initial fluid concentration chosen here is the same as the fluid concentration chosen in the earlier perturbed problem in stationary condition. The equation of the variation of the concentration of the magnetic particles is given in the equation below. In this problem, we assume that the magnetic field is first applied to the static fluid for 5 s when the fluid segregates to form brushes. Then the fluid is sheared at a constant rate to study the evolution of the brushes in the fluid.

$$x^m = 0.5 + 0.1 * cos(\frac{\pi x}{w_b}) \tag{8.98}$$

where x is the position in the x direction and w_b is the width of concentrated regions (brushes) in the fluid. The width of the brush here is chosen to be one-sixth of the length of the domain.

The velocity field in the bulk fluid is assumed to be linearly varying in the y direction, resulting in a fluid shearing at a constant rate. The velocity profile for the fluid is given

below in equation 8.99.

$$\mathbf{v} = \gamma_0 y \, \hat{\mathbf{e}}_x \tag{8.99}$$

The final differential equations for a flowing mixture in the presence of constant H-field, considering a velocity field that is constant with respect to time, is given below.

$$div(\mu(x^m) \, grad(\phi)) = 0 \tag{8.100}$$

$$\frac{\partial x^m}{\partial t} + div(x^m \mathbf{v}) = -div(\hat{\mathbf{q}}^m) \tag{8.101}$$

$$\begin{aligned}(x^m \rho_*^a + x^a \rho_*^m)\frac{\partial \hat{\mathbf{q}}^m}{\partial t} + k_1 \hat{\mathbf{q}}^{\mathbf{m}} &= x^a \mathbf{b}_{mag}^m - \{k_2 \, grad(x^m) \\ &\quad - k_3 x^m x^a grad(div(grad(x^m)))\}\end{aligned} \tag{8.102}$$

$$\begin{aligned}(x^m + x^a \rho_r) div(-P\mathbf{I} + \mathbf{T}_E) &= -\mathbf{b}_{mag}^m + (1 - \rho_r)\{k_1 \mathbf{q}^m + k_2 grad(x^m) \\ &\quad - k_3 x^m x^a grad(div(grad(x^m)))\}\end{aligned} \tag{8.103}$$

where,

$$\mathbf{b}_{mag}^m = \chi^m x^m grad(\mathbf{B})^T \mathbf{H} \tag{8.104}$$

$$\mathbf{v} = \gamma_0 y \, \hat{\mathbf{e}}_x \tag{8.105}$$

The boundary conditions for the fluid are given below. Periodic boundary conditions are applied at the boundaries $x = -l_f/2$ and $x = l_f/2$. The boundary conditions for the constant H-field, zero flux and zero gradient for the concentration of magnetic components are applied at the boundaries $y = -w_f/2$ and $y = w_f/2$.

$$\phi|_{x=-l_f/2} = \phi|_{x=l_f/2}$$

$$x^m|_{x=-l_f/2} = x^m|_{x=l_f/2}$$

$$\hat{\mathbf{q}}^m|_{x=-l_f/2} = \hat{\mathbf{q}}^m|_{x=l_f/2}$$

$$\mathbf{H}\cdot\mathbf{n}|_{y=-w_f/2} = -5\times10^3$$

$$\mathbf{H}\cdot\mathbf{n}|_{y=w_f/2} = 5\times10^3$$

$$\hat{\mathbf{q}}^m\cdot\mathbf{n}|_{y=-w_f/2} = \hat{\mathbf{q}}^m\cdot\mathbf{n}|_{y=w_f/2} = 0$$

$$grad(x^m)\cdot\mathbf{n}|_{y=-w_f/2} = grad(x^m)\cdot\mathbf{n}|_{y=w_f/2} = 0 \tag{8.106}$$

Results obtained by conducting simulations for different shear rates are discussed in the following sections.

8.11.1.1 Bulk shear rate of 1 /s

The results for the evolution of the concentration of magnetic component in the fluid when it is sheared at a rate of 1 /s visualized using Paraview is given in figures 8.19 and 8.20. At first, we can observe that the brushes rotate and stretch due to shearing while maintaining their segregated structure. At 6.62 s, it is observed that the brushes are stretched enough for the segregated structure to become unstable. Due to this instability, the mixing initiates at a point where the distance is minimum between adjacent brushes. This results in diffusive mixing at that local area. But, then this region becomes an area that attracts more magnetic particles due to the altered magnetic fields in the region, resulting in a new brush being formed. As the fluid shears, migration of magnetic component into this region grows and the original brush thickness is also reduced by the shearing action. This results in a new brush being grown out of the magnetic particles moving from the earlier brush to this newly formed brush. We can see that the magnetic brush is able to

shift to the new brush of almost similar width as that of the static segregated mixture. This process keeps continuing periodically. It is important to note that, the fluid doesn't get mixed completely, but rather is able to maintain its segregated behavior while shearing. The segregated fluid keeps breaking and reforming with the adjacent structures at the same pace as the shearing in the fluid.

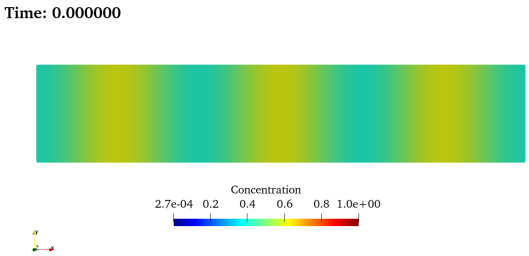

(a) Initial condition, $t = 0\ s$

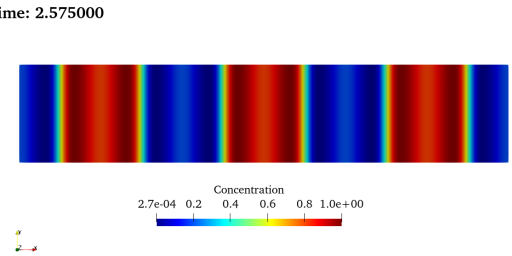

(b) Static segregation, $t = 2.58\ s$

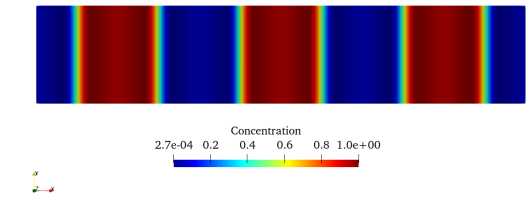

(c) Complete static segregation, $t = 4.88\ s$

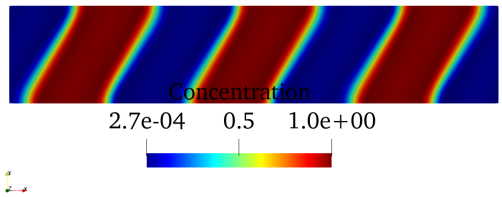

(d) Initial shearing, $t = 5.66\ s$

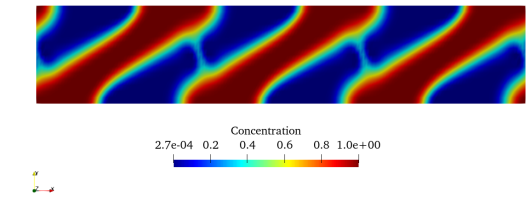

(e) Mixing initiation, $t = 6.62\ s$

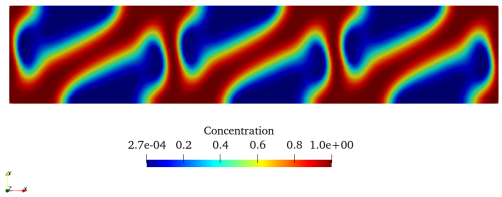

(f) Initiation of new brush, $t = 6.90\ s$

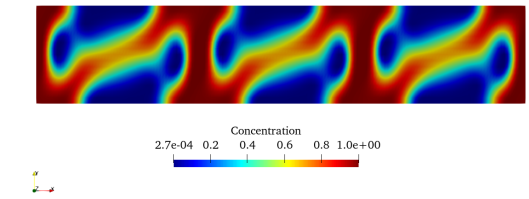

(g) Completion of diffusion to new brushes, $t = 7.25\ s$

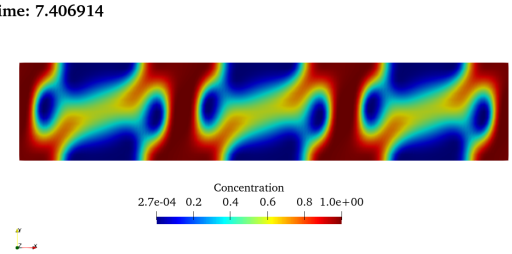

(h) Breakage of old extended brushes, $t = 7.41\ s$

Figure 8.19: Evolution of the concentration of the magnetic particles in the mixture from 0s to 7.4 s.

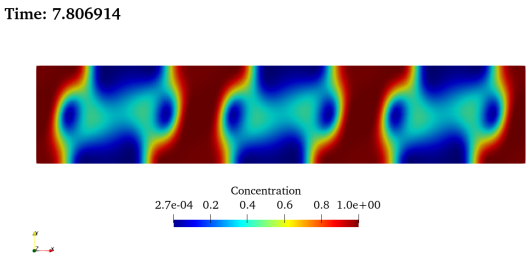

(a) Complete formation of new brushes, $t = 7.81\ s$

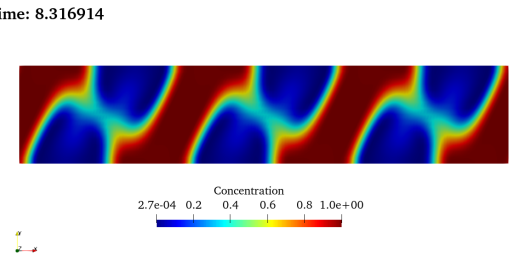

(b) Extension of formation of the next brush, $t = 8.31\ s$

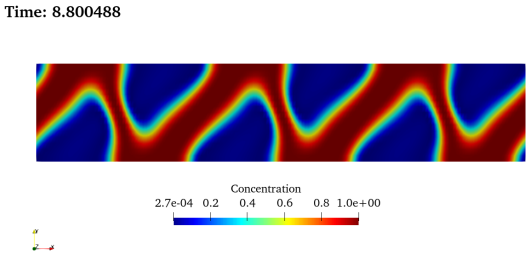

(c) Complete formation of new brushes, $t = 8.8\ s$

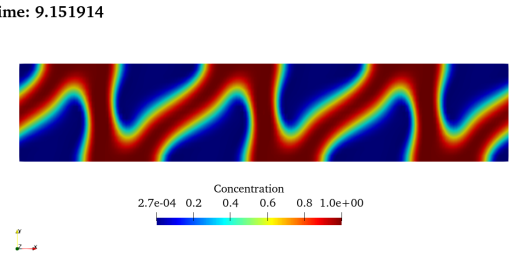

(d) growth of new brush and loss of old brushes, $t = 9.15\ s$

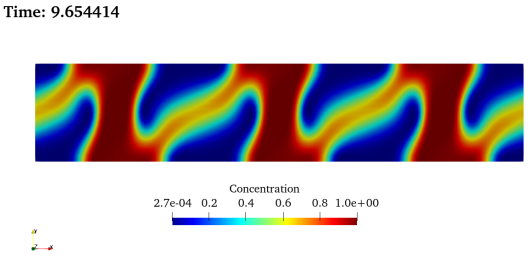

(e) The process of brush switching continues, $t = 9.65\ s$

Figure 8.20: Evolution of the concentration of the magnetic particles in the mixture from 7.8 s to 9.65 s. Note how the switching of the brushes continue as the fluid continues to shear.

8.11.1.2 Bulk shear rate of 5 /s

The evolution of the concentration of the magnetic component in the fluid when sheared at a rate of 5 /s is given in figure 8.21 and 8.22. From the results, it can be observed that, the fluid initially shears by maintaining its segregated structure, leading to stretching and thinning of the brushes. By the time diffusive mixing starts, there are multiple locations where the brushes are unstable. This results in mixing at multiple locations, as shown in figure 8.21e. Thus, new brushes form at these locations. But, as the shearing continues, the components mix at several locations while the most stable new brush formed reforms and grows through the shearing. As shearing continues, the switching behavior of these magnetic components continue, with new brushes that are not formed completely before being mixed through shearing. This results in brushes and a switching pattern similar to the earlier scenario. But, the thickness of the brushes are thinner than the earlier case.

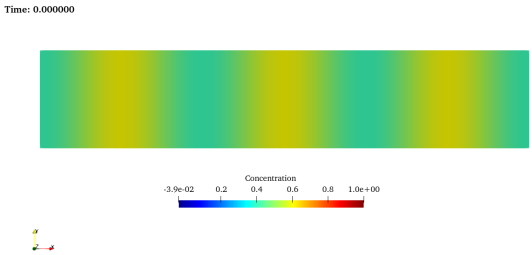

(a) Initial condition, $t = 0\ s$

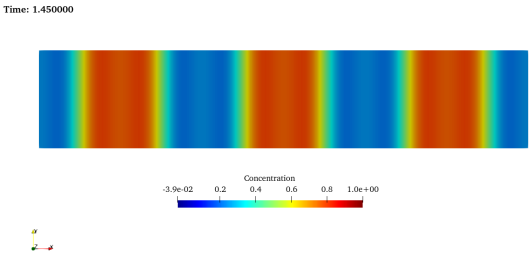

(b) Static segregation, $t = 1.45\ s$

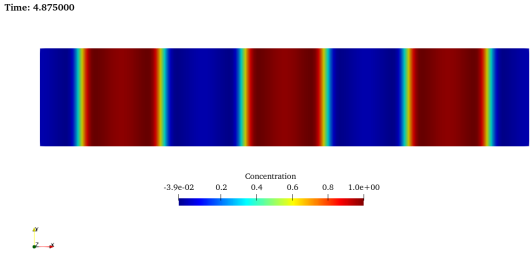

(c) Complete static segregation, $t = 4.875\ s$

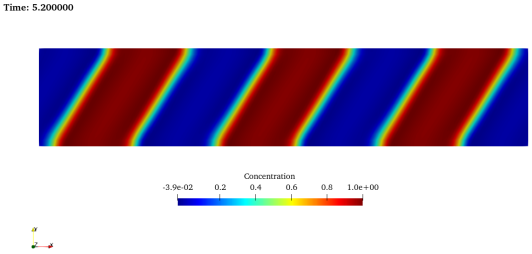

(d) shearing started, $t = 5.2\ s$

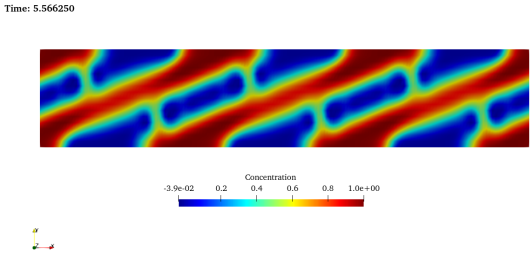

(e) Mixing Initiation at multiple locations, $t = 5.56\ s$

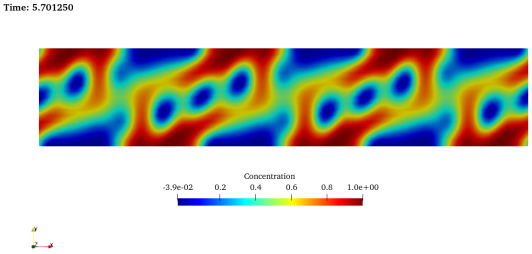

(f) Mixing and diffusion of magnetic component leading to loss of brush structure, $t = 5.7\ s$

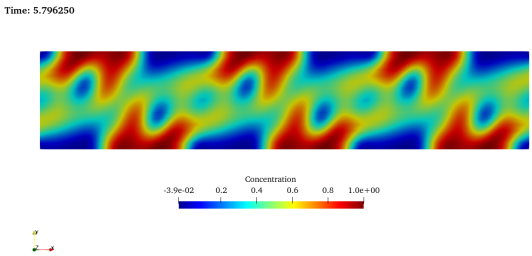

(g) Partial brushes due to mixing, $t = 5.79\ s$

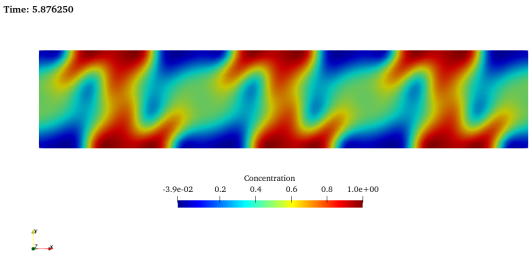

(h) New Brush formation post mixing due to the influence of the magnetic fields, $t = 5.87\ s$

Figure 8.21: Evolution of the concentration of the magnetic component of the fluid from 0 to 5.87 s. Note that in the initial 5 s, the fluid is undergoing segregation while it is stationary. In the following 0.875 s, the fluid undergoes shear

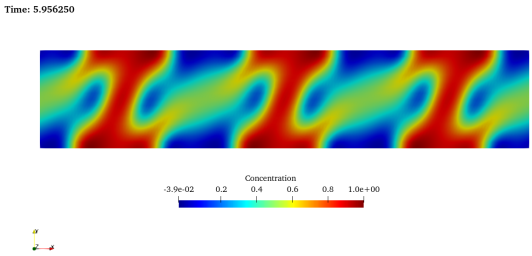

(a) Completion of new brush formation, $t = 5.95\ s$

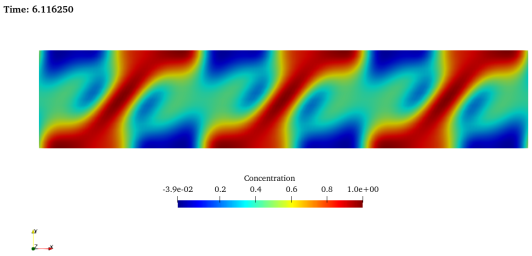

(b) stretching of the brush structure, $t = 6.11\ s$

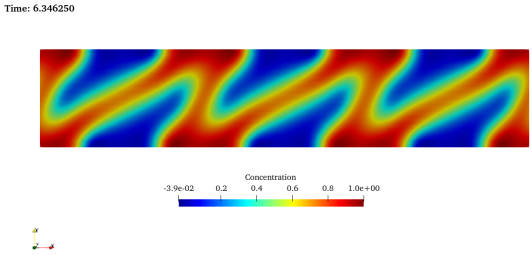

(c) Late formation of new brushes after shearing, $t = 6.34\ s$

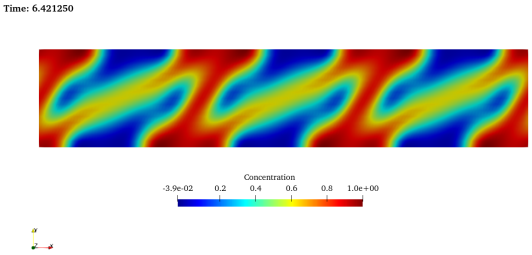

(d) Continuation of shearing and stretching of the newer brushes, $t = 6.42\ s$

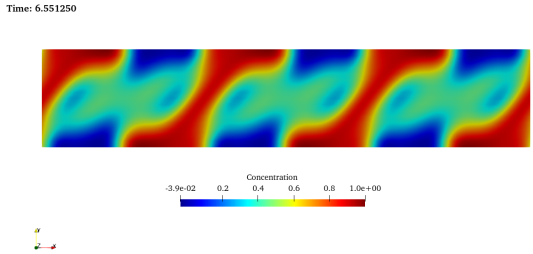

(e) Another set of brushes is formed, $t = 6.55\ s$

Figure 8.22: Evolution of the concentration of the magnetic component of the fluid from 5.95 s to 6.87 s when the fluid is sheared at 5 /s. Note that the magnetic fields through diffusion is able to segregate the magnetic component incompletely, as the diffusion process is much slower in comparison to the shearing process of the bulk fluid. Also note that the magnetic brushes formed are stretched longer and thinner by the shearing process due to this disparity in the processes.

8.11.1.3 Bulk shear rate of 20 /s

The results showing the evolution of the concentration of magnetic particles when the fluid is sheared at a rate of 20 /s are given in figure 8.23. This results in a fluid which initially shears in the same form as the other cases, continuing to stretch. But, when the brushes meet at 5.27 s, instability occurs at all points near the center of the bulk of the mixture. This leads to mixing up of the components at these regions. Compared to earlier cases, the mixing of the components process is not local in the brushes. Thus, instead of new brushes being formed, the components mix and flow as a single mixed fluid. Hence, we can note that the segregated structure is lost in the whole bulk of the fluid due to shearing.

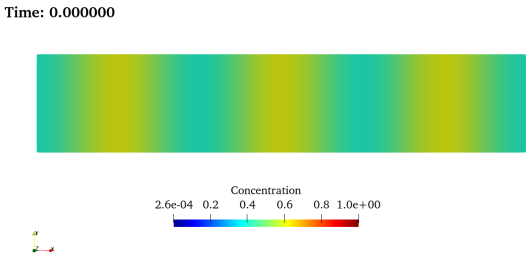

(a) Initial Condition, $t = 0.0\ s$

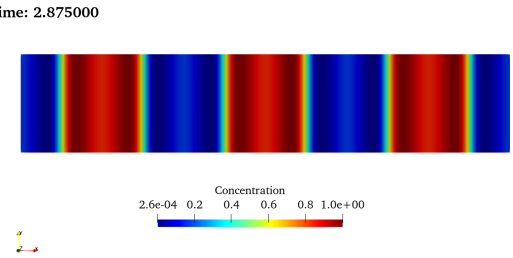

(b) Segregation in progress, $t = 2.85\ s$

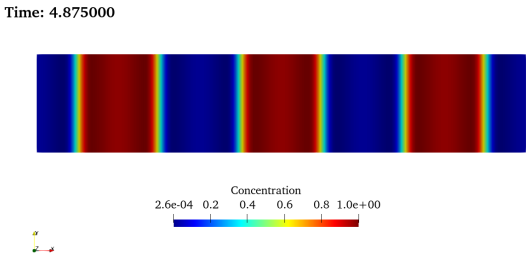

(c) Complete static segregation, $t = 4.88\ s$

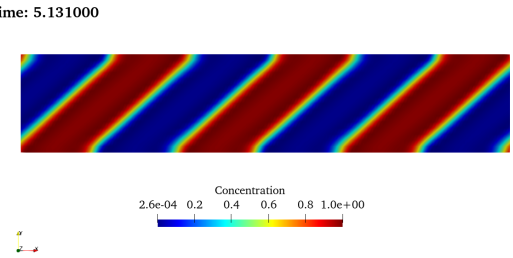

(d) Initial shearing, $t = 5.13\ s$

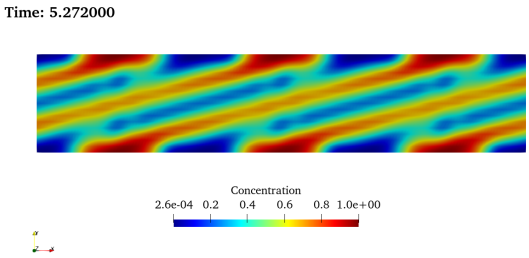

(e) Initiation of mixing at all the locations with overstretched brushes, $t = 5.272\ s$

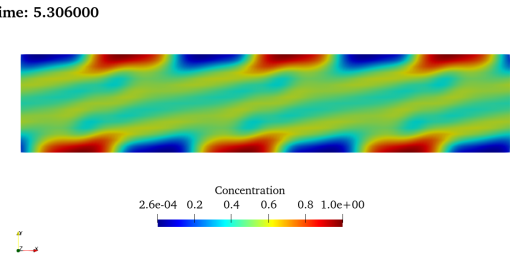

(f) Mixing Continues as the brush structure is highly unstable, $t = 5.30\ s$

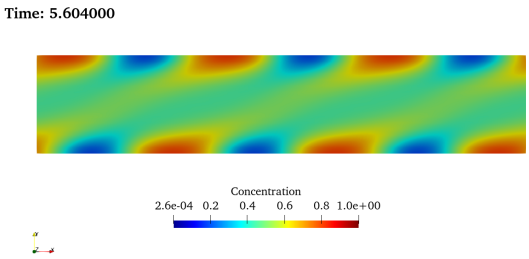

(g) Mixing of the mixture the segregation limited to the boundaries of the fluid, $t = 5.604\ s$

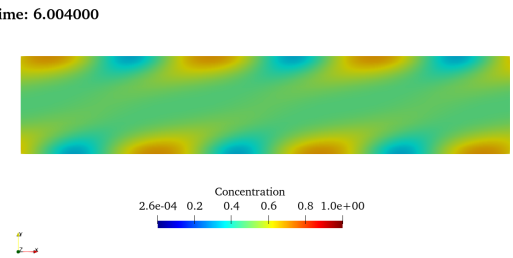

(h) Mixing complete due to shearing, $t = 6.0\ s$

Figure 8.23: Evolution of the concentration of magnetic component in the mixture while being sheared at 20 /s. Note that when the coefficient of transport is much higher than the coefficient of diffusion, the particles are no longer able to switch quickly enough to maintain their segregated brush structure.

8.11.1.4 Discussion

The primary effect in the media is that the fluid once segregated has a tendency to maintain the brush formation even under shear flow due to the magnetic field. But, we can notice that the brushes start to rotate and stretch as the fluid flows. This motion of the fluid reduces the perpendicular distance between the brushes and with time results in brushes with much smaller width. Also, the length of the interface region in the fluid increases due to stretching. Thus, when the brush width reaches a critical value, the fluid starts to mix through the brushes. Note that the nominal brush width at the center of the fluid (given in figure 8.23e) is lesser than the minimum stable segregating width for the fluid as shown in figure 8.17. It is this stretching and thinning behavior of the shearing of the fluid that causes the mixing of the fluid at high shear rates. In the scenarios where the flux due to magnetic fields has comparable response as the shearing process, the mixing initiates only at limited regions on the brushes where the width of the abrasive region is minimum. This localized mixing of the magnetic particles results in new brushes being formed which gets stronger as the fluid shears, which eventually breaks through the same mechanism of shearing. Thus, such a motion results in a periodic behavior in the fluid where the brushes are constantly reformed and broken as the fluid shears.

The mixing and segregation behavior of the mixture under shear can be studied using a coefficient of mixing entropy (C_{mix}) defined as given in equation 8.107. It is defined as the average of the non-dimensionalized form of the mixing free energy in the mixture.

$$C_{mix} = \frac{\int_{\Omega_f} x^m ln(x^m) + x^a ln(x^a) dV}{\int_{\Omega_f} dV} \tag{8.107}$$

This coefficient is compared with shear angle (θ_γ) in the mixture as given below.

$$\theta_\gamma = \gamma_0 t \tag{8.108}$$

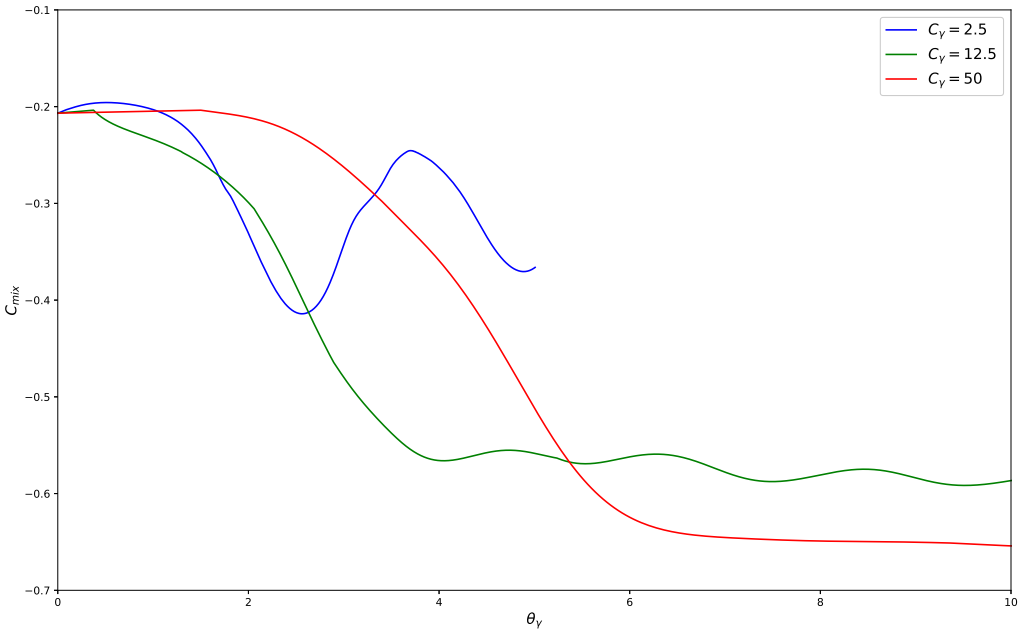

Figure 8.24: Evolution of the average mixing entropy (C_{mix}) with respect to the shear angle (θ_γ) for different coefficients of shear (C_γ). Note that for lower value of C_γ, C_{mix} increases as new brushes are formed periodically through shearing. But, for higher values of C_γ, C_{mix} reduces much more due to mixing from shearing.

This evolution of C_{mix} is studied for different values of the coefficient of shear rate (C_γ) which is the coefficient of $\bar{div}(x^m \bar{\mathbf{v}})$ in equation 8.53. This is the ratio of the shear process with respect to the diffusion process in the mixture.

$$C_\gamma = \frac{\gamma_0 k_1 l_i^2}{k_2} = 2.5\gamma_0 \tag{8.109}$$

The evolution of the average mixing entropy (C_{mix}) with respect to the shear angle of the mixture (θ_γ) for different coefficients of shear rate (C_γ) is shown in figure 8.24. C_{mix} takes a value of 0 for a fully segregated fluid with infinitely small interface between the bushes and a value of -0.69 for a fully mixed fluid. When the fluid segregates, it forms a finite sized interface between the brushes, leading to a C_{mix} value of -0.2 for the mixture. As the fluid is sheared, C_{mix} reduces due to the stretching and thinning of the brushes as observed in the figure. In all the cases, the slope of the reduction of C_{mix} increases when the brushes start to mix. The segregated mixture starts to mix across the brushes at a shear angle of 1.62 radians, 2.8 radians and 5.2 radians for C_γ values of 2.5, 12.5 and 50 respectively. For a C_γ value of 2.5, where the shearing process is comparable speed to the diffusion process, the diffusion mixing of the brushes locally leads to a significant reduction in C_{mix}. As the fluid shears the brushes start to reform leading to the reformation of the brushes and segregation of the mixture as indicated by the increase in C_{mix}. The periodical variation of C_{mix} indicates the breaking and reformation of the brushes in the mixture. It can also be observed that the mixture maintains the segregated behavior to some extent. For a C_γ value of 12.5, where the shearing process is 12.5 faster than the diffusion process, the diffusion mixing occurs at multiple points on the brushes, leading to a huge reduction in C_{mix}. But, since the diffusion process is still able to cope with the shearing process, the mixture doesn't completely mix but rather continues to form thinner brushes which break and reform through the shearing process. For a C_γ value of 50, where

the shearing process is much faster than the diffusion process, the mixing of the brushes occur at multiple regions, resulting in an almost mixed state of the bulk fluid. As indicated in figure 8.24 for a high value of C_γ both the high shearing process and diffusive mixing leads to completely mixed state of the fluid resulting in a low value of C_{mix} which cannot be recovered as the mixing process from shearing is much higher. Thus, the coefficient of shear rate (C_γ) of the fluid plays an important role in determining the segregation and the thickness of brushes while shearing. The critical values of C_γ that govern behavior of the segregated structure is dependent on C_{mag} as well as it governs the scale of non-dimensional flux, $\bar{\hat{\mathbf{q}}}^m$.

8.12 Conclusions

A polishing mixture with a magnetic component concentration of 50 % is considered for simulations. The fluid concentration was initially perturbed in the presence of a uniform H-field for the first simulation. The same fluid was considered in a linearly varying magnetic field in the second case. On comparing the simulation results from the decoupled and coupled scenarios, one can observe that higher amount of segregation occurs for the coupled scenario for both test cases. The magnetic component of the fluid has relative permeability of 7 with respect to the abrasive component. This high a difference between the magnetic behavior of the fluid gives a characteristic change in the magnetic field distribution in the mixture as segregation occurs. This further leads to segregation, resulting in the brush like formation that is observed in practice (figure 8.7). Thus, the body forces developed in the fluid are closer to the simulation results captured by the coupled scenario. This phenomenon can only be captured in simulation when the effect of segregation of the mixture on the magnetic field and body forces is considered in the simulations. A considerable difference in the results of the pressure is also observed in both the cases. The pressure observed in the regions with the higher concentration of magnetic particles is

much higher than the pressure in the abrasive regions. This pressure is observed as normal force acting on the workpiece during polishing, thus, plays an important role in the material removal from the surface of the workpiece. It is also to be noted that it is the abrasives trapped at the interfaces at a much lower concentration that result in the material removal in polishing.

Studying the evolution of the concentration of the magnetic component when the segregated fluid is sheared under constant H-field indicate that the shearing process destabilizes the brush structure of the fluid by stretching and thinning of the regions. If the diffusion process is able to respond to this effect of shearing at a comparable rate, the segregation of the fluid is maintained through formation of new brushes as the fluid shears. When the shearing process is much higher to the diffusion process, the fluid is able to maintain a segregated structure but with much thinner magnetic brushes and higher amount of mixing, as indicated by the lower value of C_{mix} while shearing. And when the diffusion is unable to respond to the shearing behavior this will lead to unstable structure in the fluid leading to mixing of the fluid components destroying the segregated structure. This indicates that there is a limit to the shearing rate that can be induced into the fluid through polishing dictated by the material parameters and the magnetic field applied to the fluid beyond which the segregated brush like formation critical to the polishing of the workpiece cannot be achieved in the fluid.

9. CONCLUSIONS

The research conducted in this thesis can be divided into 2 parts, experimental study on polishing fluids to identify appropriate models and mixture modeling of the magneto-rheological polishing fluid to simulate the segregation of a magneto-rheological polishing mixture while flowing under magnetic fields.

In the experimental study, torsional flow experiments conducted using a non-traditional test cell is modeled using analytical and CFD approaches, for power law, Bingham fluid and Herschel-Bulkley models, to study its rheological behavior. It was identified that, the idealization about the flow of the fluid and neglecting the flow of fluid in the gap of the setup can have a significant impact on the properties obtained for the fluid. Thus, the assumption that the wall effect on the fluid flow being negligible may not be a good assumption to follow in cases where experiments are conducted on non-idealistic geometries. In such cases, a method that uses the simulations will provide a more accurate estimation of the parameters for the models of the fluid. Akaike Information Criterion was used to select an appropriate model for the fluid. The high Akaike weights and lower standard deviation in the CFD based estimation of models show the higher predictability of the fluid achieved through the CFD based analysis of the fluid behavior.

Mixture theory was chosen to model the segregation and flow behavior of MR finishing mixture. Dipole-current circuit model was used to model the magnetic behavior of the polishing fluid. The field equations for the bulk mixture fluid and the relative flow of the magnetic component were derived. Thermodynamically consistent constitutive models were developed for the fluid to exhibit segregation through diffusion and flow of the bulk mixture during the polishing process. It was identified that a mixture model for the bulk flow velocity formulated using the volume concentrations of the component as weights,

provide field equations and constraints for the bulk mixture where simpler incompressible constitutive models can be used to model the flow of the bulk mixture.

For the purpose of simulations, a polishing mixture with a magnetic component concentration of 50 % is considered. The fluid concentration was initially perturbed in the presence of a uniform H field for a stationary fluid. The same fluid was considered in a linearly varying magnetic field in the second case. On comparing the simulation results from the decoupled and coupled scenarios, it was identified that segregation of the magnetic component with a relative permeability of 7 with respect to the abrasive component altered the magnetic forces significantly, resulting in a more pronounced segregation into brush like formations. This phenomenon can only be captured in the simulation when the influence of segregation mixture is taken into consideration in the simulations. Thus, coupled simulations of the polishing fluid are necessary to simulate the segregation and the pressure that arise in the fluid due to body forces from the magnetic field.

A non-dimensionalized study on the perturbed stationary fluid identified that for a fluid with defined material parameters that is subject to a uniform magnetic field, the fluid segregated or mixed based on the width of the brush for the initial concentration of the fluid. There is a critical value of brush width below which the fluid mixed into a completely mixed fluid and above which the fluid segregated completely to form brushes. This critical brush width is a function of the magnetic coefficient (C_{mag}) of the mixture.

Simulations were performed for an infinitely long segregated fluid shearing in the presence of a uniform magnetic field. The simulations studied the evolution of the segregated structure in the presence of a fixed magnetic field while being sheared at different rates. It is observed that for low values of C_γ the mixture maintains its segregated brushes periodically which gets broken and reformed through shearing. For higher values of C_γ, the fluid gets mixed at major regions, but the brush like segregation is maintained to some extent by the mixture. At really high shear rates the fluid gets completely mixed with shearing

and diffusive mixing through the brushes. The fluid behavior slowly transitions from the segregated brush structure to completely mixed fluid as the shear rate increases in the fluid.

9.1 Recommendations for future work

The following research topics need attention in this subject: Experimental studies on the material properties of MR polishing fluid. Simulations that study the influence of magnetic field along with the shear rate and the brush width on the behavior of the fluid. Two-way coupling of the velocity and concentration of the magnetic component, where the influence of concentration distribution on both the magnetic fields and the velocity field of the bulk fluid is taken into consideration. Inclusion of slip conditions at the boundaries of the fluid where the fluid is in contact with the workpiece. Experimental studies on the local shear and normal forces developed by MR polishing fluids under polishing conditions.

REFERENCES

[1] R. Pan, Z.-Z. Wang, T. Jiang, Z.-S. Wang, and Y.-B. Guo, "A novel method for aspheric polishing based on abrasive trajectories analysis on contact region," *Proceedings of the Institution of Mechanical Engineers, Part B: Journal of Engineering Manufacture*, vol. 229, no. 2, pp. 275–285, 2015.

[2] M. S. Cheema, G. Venkatesh, A. Dvivedi, and A. K. Sharma, "Developments in abrasive flow machining: a review on experimental investigations using abrasive flow machining variants and media," *Proceedings of the Institution of Mechanical Engineers, Part B: Journal of Engineering Manufacture*, vol. 226, no. 12, pp. 1951–1962, 2012.

[3] M. R. Sankar, J. Ramkumar, and V. K. Jain, "Experimental investigation and mechanism of material removal in nano finishing of MMCs using abrasive flow finishing (AFF) process," *Wear*, vol. 266, no. 7-8, pp. 688–698, 2009.

[4] S. Singh, H. S. Shan, and P. Kumar, "Wear behavior of materials in magnetically assisted abrasive flow machining," *Journal of Materials Processing Technology*, vol. 128, no. 1, pp. 155–161, 2002.

[5] M. K. Reddy, A. K. Sharma, and P. Kumar, "Some aspects of centrifugal force assisted abrasive flow machining of 2014 Al alloy," *Proceedings of the Institution of Mechanical Engineers, Part B: Journal of Engineering Manufacture*, vol. 222, no. 7, pp. 773–783, 2008.

[6] D. W. Kim and S.-W. Kim, "Static tool influence function for fabrication simulation of hexagonal mirror segments for extremely large telescopes," *Optics Express*, vol. 13, no. 3, pp. 910–917, 2005.

[7] S. Y. Zeng and L. Blunt, "Experimental investigation and analytical modelling of the effects of process parameters on material removal rate for bonnet polishing of cobalt chrome alloy," *Precision Engineering-Journal of the International Societies for Precision Engineering and Nanotechnology*, vol. 38, no. 2, pp. 348–355, 2014.

[8] C. R. Dunn and D. D. Walker, "Pseudo-random tool paths for CNC sub-aperture polishing and other applications," *Optics Express*, vol. 16, no. 23, pp. 18942–18949, 2008.

[9] W. I. Kordonski and S. D. Jacobs, "Magnetorheological finishing," *International Journal of Modern Physics B*, vol. 10, no. 23-24, pp. 2837–2848, 1996.

[10] V. K. Jain, "Magnetic field assisted abrasive based micro-/nano-finishing," *Journal of Materials Processing Technology*, vol. 209, no. 20, pp. 6022–6038, 2009.

[11] T. Mori, K. Hirota, and Y. Kawashima, "Clarification of magnetic abrasive finishing mechanism," *Journal of Materials Processing Technology*, vol. 143, pp. 682–686, 2003.

[12] S. Mueller, E. W. Llewellin, and H. M. Mader, "The rheology of suspensions of solid particles," *Proceedings of the Royal Society A: Mathematical, Physical and Engineering Sciences*, vol. 466, pp. 1201–1228, 2010.

[13] T. M. Simon, K. Ito, H. T. Banksa, F. Reitich, and M. R. Jolly, "Estimation of the Effective Permeability in Magnetorheological Fluids," *Journal of Intelligent Material Systems and Structures*, vol. 10, pp. 872–879, 11 1999.

[14] F. Donado, P. Miranda-Romagnoli, and R. Agustín-Serrano, "Phenomenological model for yield stress based on the distribution of chain lengths in a dilute magnetorheological fluid under an oscillatory magnetic field," *Revista Mexicana de Física*, vol. 59, pp. 131–140, 2013.

[15] G. Parameswari, V. K. Jain, J. Ramkumar, and L. Nagdeve, "Experimental investigations into nanofinishing of Ti6Al4V flat disc using magnetorheological finishing process,"

[16] E. Strait, G. McGimpsey, and T. Bradford, "Limb Prosthetics Services and Devices," *White Paper*, no. January, pp. 1–35, 2006.

[17] T. M. Research, "Rising Need of Medical Implants to Drive Biomaterials Market for Implantable Devices to US$33,600 million by 2019 : Transparency Market Research," 2014.

[18] J. R. Davis, "Overview of biomaterials and their use in medical devices," *Handbook of materials for medical devices. Illustrated edition, Ohio: ASM International*, pp. 1–11, 2003.

[19] H. Hermawan, D. Ramdan, and J. R. P. Djuansjah, *Metals for biomedical applications*. INTECH Open Access Publisher, 2011.

[20] R. Z. Legeros and R. G. Craig, "Strategies to affect bone remodeling: osteointegration," *Journal of Bone and Mineral Research*, vol. 8, no. S2, pp. S583–S596, 1993.

[21] M. M. Shalabi, A. Gortemaker, M. A. Van't Hof, J. A. Jansen, and N. H. J. Creugers, "Implant surface roughness and bone healing: a systematic review," *Journal of dental research*, vol. 85, no. 6, pp. 496–500, 2006.

[22] K. Anselme and M. Bigerelle, "Topography effects of pure titanium substrates on human osteoblast long-term adhesion," *Acta biomaterialia*, vol. 1, no. 2, pp. 211–222, 2005.

[23] A. Wennerberg and T. Albrektsson, "Suggested guidelines for the topographic evaluation of implant surfaces," *The International journal of oral & maxillofacial im-*

plants, vol. 15, no. 3, pp. 331–344, 1999.

[24] H. E. Götz, M. Müller, A. Emmel, U. Holzwarth, R. G. Erben, and R. Stangl, "Effect of surface finish on the osseointegration of laser-treated titanium alloy implants," *Biomaterials*, vol. 25, no. 18, pp. 4057–4064, 2004.

[25] Aniket, R. Reid, B. Hall, I. Marriott, and A. El-Ghannam, "Early osteoblast responses to orthopedic implants: Synergy of surface roughness and chemistry of bioactive ceramic coating," *Journal of Biomedical Materials Research Part A*, vol. 103, no. 6, pp. 1961–1973, 2015.

[26] A. Lundgren, D. Lundgren, A. Wennerberg, C. H. F. Hämmerle, and S. Nyman, "Influence of Surface Roughness of Barrier Walls on Guided Bone Augmentation: Experimental Study in Rabbits," *Clinical Implant Dentistry and Related Research*, vol. 1, no. 1, pp. 41–48, 1999.

[27] Y. Deng, X. Liu, A. Xu, L. Wang, Z. Luo, Y. Zheng, F. Deng, J. Wei, Z. Tang, and S. Wei, "Effect of surface roughness on osteogenesis in vitro and osseointegration in vivo of carbon fiber-reinforced polyetheretherketone– Nanohydroxyapatite composite," *International Journal of Nanomedicine*, vol. 10, pp. 1425–1447, 2 2015.

[28] K. S. Katti, "Biomaterials in total joint replacement," *Colloids and Surfaces B: Biointerfaces*, vol. 39, no. 3, pp. 133–142, 2004.

[29] T. Karachalios and G. Karydakis, "Bearing Surfaces," in *European Instructional Lectures, Vol 11* (G. Bentley, ed.), vol. 11, pp. 133–140, Dordrecht: Springer, 2011.

[30] N. Kumar, G. N. C. Arora, and B. Datta, "Bearing surfaces in hip replacement - Evolution and likely future," *Medical journal, Armed Forces India*, vol. 70, no. 4, pp. 371–376, 2014.

[31] J.-D. Chang, "Future bearing surfaces in total hip arthroplasty," *Clinics in orthopedic surgery*, vol. 6, no. 1, pp. 110–116, 2014.

[32] D. Dowson and Z. M. Jin, "Metal-on-metal hip joint tribology," *Proceedings of the Institution of Mechanical Engineers, Part H: Journal of Engineering in Medicine*, vol. 220, no. 2, pp. 107–118, 2006.

[33] R. K. Alla, K. Ginjupalli, N. Upadhya, M. Shammas, R. K. Ravi, and R. Sekhar, "Surface roughness of implants: a review," *Trends in Biomaterials and Artificial Organs*, vol. 25, no. 3, pp. 112–118, 2011.

[34] K.-I. Jang, J. Seok, B.-K. Min, and S. J. Lee, "An electrochemomechanical polishing process using magnetorheological fluid," *International Journal of Machine Tools and Manufacture*, vol. 50, no. 10, pp. 869–881, 2010.

[35] B. M. Basol, "Method and apparatus for localized material removal by electrochemical polishing," 2006.

[36] J. Fischer, A. Schott, and S. Märtin, "Surface micro-structuring of zirconia dental implants," *Clinical oral implants research*, 2015.

[37] Y. Taga, K. Kawai, and T. Nokubi, "New method for divesting cobalt-chromium alloy castings: Sandblasting with a mixed abrasive powder," *J Prosthet Dent*, vol. 85, no. 4, pp. 357–362, 2001.

[38] C. Aparicio, F. J. Gil, C. Fonseca, M. Barbosa, and J. A. Planell, "Corrosion behaviour of commercially pure titanium shot blasted with different materials and sizes of shot particles for dental implant applications," *Biomaterials*, vol. 24, no. 2, pp. 263–273, 2003.

[39] K. Subramanian, N. Balashanmugam, and P. Shashi Kumar, "Nanometric Finishing on Biomedical Implants by Abrasive Flow Finishing," *Journal of The Institution of*

Engineers (India): Series C, pp. 1–7, 2015.

[40] D. D. Walker, A. T. H. Beaucamp, D. Brooks, R. Freeman, A. King, G. McCavana, R. Morten, D. Riley, and J. Simms, "Novel CNC polishing process for control of form and texture on aspheric surfaces," in *Current Developments in Lens Design and Optical Engineering Iii* (R. E. Fischer, W. J. Smith, and R. B. Johnson, eds.), vol. 4767, pp. 99–105, Bellingham: Spie-Int Soc Optical Engineering, 2002.

[41] D. Walker, D. Brooks, A. King, R. Freeman, R. Morton, G. McCavana, and S.-W. Kim, "The "Precessions" tooling for polishing and figuring flat, spherical and aspheric surfaces," *Optics Express*, vol. 11, no. 8, pp. 958–964, 2003.

[42] S. Zeng, L. Blunt, and R. Racasan, "An investigation of the viability of bonnet polishing as a possible method to manufacture hip prostheses with multi-radius femoral heads," *The International Journal of Advanced Manufacturing Technology*, vol. 70, no. 1-4, pp. 583–590, 2014.

[43] D. W. Kim and J. H. Burge, "Rigid conformal polishing tool using non-linear viscoelastic effect," *Optics Express*, vol. 18, no. 3, pp. 2242–2257, 2010.

[44] T. Akahori, T. Ashizawa, K. Hirai, M. Kurihara, M. Yoshida, and Y. Kurata, "CMP abrasive, liquid additive for CMP abrasive and method for polishing substrate," 2004.

[45] M. Yoshida, T. Ashizawa, H. Terazaki, Y. Kurata, J. Matsuzawa, K. Tanno, and Y. Ootuki, "Cerium oxide abrasive and method of polishing substrates," 2001.

[46] S. Zeng, L. Blunt, and X. Jiang, "The investigation of material removal in bonnet polishing of CoCr alloy artificial joints," 2012.

[47] A. M. Sidpara and V. K. Jain, "Nanofinishing of freeform surfaces of prosthetic knee joint implant," *Proceedings of the Institution of Mechanical Engineers Part*

B-Journal of Engineering Manufacture, vol. 226, no. A11, pp. 1833–1846, 2012.

[48] C. Sittig, M. Textor, N. D. Spencer, M. Wieland, and P. H. Vallotton, "Surface characterization of implant materials c.p. Ti, Ti-6Al-7Nb and Ti-6Al-4V with different pretreatments," *Journal of Materials Science: Materials in Medicine*, vol. 10, pp. 35–46, 1 1999.

[49] C. Larsson, P. Thomsen, B. O. Aronsson, M. Rodahl, J. Lausmaa, B. Kasemo, and L. E. Ericson, "Bone response to surface-modified titanium implants: studies on the early tissue response to machined and electropolished implants with different oxide thicknesses," *Biomaterials*, vol. 17, no. 6, pp. 605–616, 1996.

[50] A. Latifi, M. Imani, M. T. Khorasani, and M. D. Joupari, "Electrochemical and chemical methods for improving surface characteristics of 316L stainless steel for biomedical applications," *Surface & Coatings Technology*, vol. 221, pp. 1–12, 2013.

[51] T. Hryniewicz, R. Rokicki, and K. Rokosz, "Surface characterization of AISI 316L biomaterials obtained by electropolishing in a magnetic field," *Surface and coatings technology*, vol. 202, no. 9, pp. 1668–1673, 2008.

[52] R. S. Faeda, H. S. Tavares, R. Sartori, A. C. Guastaldi, and E. Marcantonio, "Evaluation of titanium implants with surface modification by laser beam. Biomechanical study in rabbit tibias," *Brazilian Oral Research*, vol. 23, no. 2, pp. 137–143, 2009.

[53] D. D. Walker, A. T. Beaucamp, D. Brooks, V. Doubrovski, M. D. Cassie, C. Dunn, R. R. Freeman, A. King, M. Libert, and G. McCavana, "Recent developments of Precessions polishing for larger components and free-form surfaces," in *Optical Science and Technology, the SPIE 49th Annual Meeting*, pp. 281–289, International Society for Optics and Photonics, 2004.

[54] L. Zhang, J.-L. Zhuang, X.-Z. Ma, J. Tang, and Z.-W. Tian, "Microstructuring of p-Si (100) by localized electrochemical polishing using patterned agarose as a stamp," *Electrochemistry Communications*, vol. 9, no. 10, pp. 2529–2533, 2007.

[55] R. W. McCarty, "Method of Honing by Extruding," 1968.

[56] L. Rhoades, "Abrasive flow machining: a case study," *Journal of Materials Processing Technology*, vol. 28, no. 1, pp. 107–116, 1991.

[57] H. S. Mali and A. Manna, "Current status and application of abrasive flow finishing processes: a review," *Proceedings of the Institution of Mechanical Engineers Part B-Journal of Engineering Manufacture*, vol. 223, no. 7, pp. 809–820, 2009.

[58] R. Minear and N. Nokovich, "Machine for abrading by extruding," 1974.

[59] L. J. Rhoades, T. A. Kohut, N. P. Nokovich, and D. W. Yanda, "Unidirectional abrasive flow machining," 1994.

[60] J. R. Gilmore and L. J. Rhoades, "Self-forming tooling for an orbital polishing machine and method for producing," 2002.

[61] V. K. Gorana, V. K. Jain, and G. K. Lal, "Prediction of surface roughness during abrasive flow machining," *The International Journal of Advanced Manufacturing Technology*, vol. 31, no. 3-4, pp. 258–267, 2006.

[62] W. B. Perry, "Honing media," 1993.

[63] V. K. Gorana, V. K. Jain, and G. K. Lal, "Experimental investigation into cutting forces and active grain density during abrasive flow machining," *International Journal of Machine Tools and Manufacture*, vol. 44, no. 2–3, pp. 201–211, 2004.

[64] A. C. Wang and S. H. Weng, "Developing the polymer abrasive gels in AFM processs," *Journal of Materials Processing Technology*, vol. 192–193, pp. 486–490, 2007.

[65] A. R. Jones and J. B. Hull, "Ultrasonic flow polishing," *Ultrasonics*, vol. 36, no. 1–5, pp. 97–101, 1998.

[66] D. Walker, A. Beaucamp, and C. Dunn, "Computer controlled work tool apparatus and method," 2008.

[67] X. Chen, "Corrective Abrasive Polishing Processes for Freeform Surface," in *Progress in Abrasive and Grinding Technology* (X. Xu, ed.), vol. 404, pp. 103–112, Stafa-Zurich: Trans Tech Publications Ltd, 2009.

[68] C. F. Cheung, L. B. Kong, L. T. Ho, and S. To, "Modelling and simulation of structure surface generation using computer controlled ultra-precision polishing," *Precision Engineering*, vol. 35, no. 4, pp. 574–590, 2011.

[69] R. Pan, Y. Zhang, C. Cao, M. Sun, Z. Wang, and Y. Peng, "Modeling of material removal in dynamic deterministic polishing," *The International Journal of Advanced Manufacturing Technology*, pp. 1–12, 2015.

[70] PRESTON and F. W., "The Theory and Design of Plate Glass Polishing Machines," *Journal of Glass Technology*, vol. 11, no. 44, pp. 214–256, 1927.

[71] R. G. Bingham, D. D. Walker, D.-H. Kim, D. Brooks, R. Freeman, and D. Riley, "Novel automated process for aspheric surfaces," in *Current Developments in Lens Design and Optical Systems Engineenng* (W. H. Swantner, ed.), vol. 4093, pp. 445–450, 2000.

[72] D. Walker, G. Yu, H. Li, W. Messelink, R. Evans, and A. Beaucamp, "Edges in CNC polishing: from mirror-segments towards semiconductors, paper 1: edges on processing the global surface," *Optics Express*, vol. 20, no. 18, pp. 19787–19798, 2012.

[73] A. Beaucamp and Y. Namba, "Super-smooth finishing of diamond turned hard X-ray molding dies by combined fluid jet and bonnet polishing," *CIRP Annals-Manufacturing Technology*, vol. 62, no. 1, pp. 315–318, 2013.

[74] A. T. H. Beaucamp, R. R. Freeman, A. Matsumoto, and Y. Namba, "Fluid jet and bonnet polishing of optical moulds for application from visible to x-ray," in *Proceedings of SPIE*, vol. 8126, pp. 81260U–81260U–8, 2011.

[75] H. P. Coats, "Method of and apparatus for polishing containers," 8 1940.

[76] SHIMADA and K., "Hydrodynamic and Magnetized Characteristics of MCF (Magnetic Compound Fluid)," *Journal of the Japan Society of Mechanical Engineers (C)*, vol. 67, no. 664, pp. 122–128, 2001.

[77] T. Shinmura, K. Takazawa, E. Hatano, M. Matsunaga, and T. Matsuo, "Study on Magnetic Abrasive Finishing," *CIRP Annals - Manufacturing Technology*, vol. 39, pp. 325–328, 1 1990.

[78] M. Fox, K. Agrawal, T. Shinmura, and R. Komanduri, "Magnetic Abrasive Finishing of Rollers," *CIRP Annals - Manufacturing Technology*, vol. 43, pp. 181–184, 1 1994.

[79] J. D. Kim, Y. H. Kang, Y. H. Bae, and S. W. Lee, "Development of a magnetic abrasive jet machining system for precision internal polishing of circular tubes," *Journal of Materials Processing Technology*, vol. 71, pp. 384–393, 11 1997.

[80] A. C. Wang, L. Tsai, C. H. Liu, K. Z. Liang, and S. J. Lee, "Elucidating the Optimal Parameters in Magnetic Finishing with Gel Abrasive," *Materials and Manufacturing Processes*, vol. 26, no. 5, pp. 786–791, 2011.

[81] A. C. Wang and S. J. Lee, "Study the characteristics of magnetic finishing with gel abrasive," *International Journal of Machine Tools and Manufacture*, vol. 49,

pp. 1063–1069, 11 2009.

[82] D. C. Harris, "History of magnetorheological finishing," in *SPIE Defense, Security, and Sensing*, pp. 80160N–80160N–22, International Society for Optics and Photonics, 2011.

[83] H. Yamaguchi and T. Shinmura, "Study of an internal magnetic abrasive finishing using a pole rotation system: Discussion of the characteristic abrasive behavior," *Precision Engineering*, vol. 24, no. 3, pp. 237–244, 2000.

[84] Y. Tani, K. Kawata, and K. Nakayama, "Development of High-Efficient Fine Finishing Process Using Magnetic Fluid," *CIRP Annals - Manufacturing Technology*, vol. 33, no. 1, pp. 217–220, 1984.

[85] A. Sidpara and V. K. Jain, "Magnetorheological and Allied Finishing Processes," in *Micromanufacturing Processes* (V. K. Jain, ed.), pp. 133–153, CRC Press (Taylor and Francis), 2012.

[86] A. Shorey, "Mechanisms of material removal in magnetorheological finishing (MRF) of glass.," 2001.

[87] A. B. Shorey, *Mechanisms of material removal in magnetorheological finishing (MRF) of glass*. PhD thesis, Rochester, 2000.

[88] C. Miao, S. N. Shafrir, J. C. Lambropoulos, J. Mici, and S. D. Jacobs, "Shear stress in magnetorheological finishing for glasses," *Applied Optics*, vol. 48, no. 13, pp. 2585–2594, 2009.

[89] V. H. Bulsara, Y. Ahn, S. Chandrasekar, and T. N. Farris, "Mechanics of Polishing," *Journal of Applied Mechanics*, vol. 65, no. 2, pp. 410–416, 1998.

[90] S. D. Jacobs and I. V. Prokhorov, "Magnetorheological finishing of edges of optical elements," 1997.

[91] W. Kordonski, S. Gorodkin, and A. Sekeres, "System for magnetorheological finishing of substrates," 2013.

[92] W. I. Kordonski, "Apparatus and method for abrasive jet finishing of deeply concave surfaces using magnetorheological fluid," 2003.

[93] L.-J. Liao, "Ultra-low temperature magnetic polishing machine," 2013.

[94] R. Komanduri, N. Umehara, and M. Raghunandan, "On the possibility of chemo-mechanical action in magnetic float polishing of silicon nitride," *Journal of tribology*, vol. 118, no. 4, pp. 721–727, 1996.

[95] J. Seok, Y.-J. Kim, K.-I. Jang, B.-K. Min, and S. J. Lee, "A study on the fabrication of curved surfaces using magnetorheological fluid finishing," *International Journal of Machine Tools and Manufacture*, vol. 47, no. 14, pp. 2077–2090, 2007.

[96] T. Mori, K. Hirota, and Y. Kawashima, "Clarification of magnetic abrasive finishing mechanism," in *Journal of Materials Processing Technology*, vol. 143-144, pp. 682–686, Elsevier, 12 2003.

[97] S. Bando, A. Tsukada, and Y. Kondo, "A Study on Precision Internal Finishing for Alumina Ceramics Tube," *Journal of the Japan Society for Abrasive Technology*, vol. 45, no. 1, pp. 46–59, 2001.

[98] H. Yamaguchi and T. Shinmura, "Internal finishing process for alumina ceramic components by a magnetic field assisted finishing process," *Precision Engineering*, vol. 28, no. 2, pp. 135–142, 2004.

[99] J. Huang, J. Q. Zhang, and J. N. Liu, "EFFECT OF MAGNETIC FIELD ON PROPERTIES OF MR FLUIDS," *International Journal of Modern Physics B: Condensed Matter Physics; Statistical Physics; Applied Physics*, vol. 19, no. 1-3, pp. 597–601, 2005.

[100] G.-W. Chang, B.-H. Yan, and R.-T. Hsu, "Study on cylindrical magnetic abrasive finishing using unbonded magnetic abrasives," *International Journal of Machine Tools and Manufacture*, vol. 42, no. 5, pp. 575–583, 2002.

[101] A. K. Singh, S. Jha, and P. M. Pandey, "Design and development of nanofinishing process for 3D surfaces using ball end MR finishing tool," *International Journal of Machine Tools & Manufacture*, vol. 51, no. 2, pp. 142–151, 2011.

[102] H. Yamaguchi, T. Shinmura, and A. Kobayashi, "Development of an Internal Magnetic Abrasive Finishing Process for Nonferromagnetic Complex Shaped Tubes," *JSME International Journal Series C*, vol. 44, no. 1, pp. 275–281, 2001.

[103] H. Yamaguchi and T. Shinmura, "Study of the surface modification resulting from an internal magnetic abrasive finishing process," *Wear*, vol. 225, pp. 246–255, 1999.

[104] V. K. Jain, P. Kumar, P. K. Behera, and S. C. Jayswal, "Effect of working gap and circumferential speed on the performance of magnetic abrasive finishing process," *Wear*, vol. 250, no. 1, pp. 384–390, 2001.

[105] B.-H. Yan, G.-W. Chang, T.-J. Cheng, and R.-T. Hsu, "Electrolytic magnetic abrasive finishing," *International Journal of Machine Tools and Manufacture*, vol. 43, no. 13, pp. 1355–1366, 2003.

[106] S. Yin and T. Shinmura, "Vertical vibration-assisted magnetic abrasive finishing and deburring for magnesium alloy," *International Journal of Machine Tools and Manufacture*, vol. 44, no. 12, pp. 1297–1303, 2004.

[107] D. K. Singh, V. K. Jain, and V. Raghuram, "Experimental investigations into forces acting during a magnetic abrasive finishing process," *The International Journal of Advanced Manufacturing Technology*, vol. 30, no. 7-8, pp. 652–662, 2006.

[108] R. S. Mulik and P. M. Pandey, "Mechanism of surface finishing in ultrasonic-assisted magnetic abrasive finishing process," *Materials and Manufacturing Processes*, vol. 25, no. 12, pp. 1418–1427, 2010.

[109] J. K. Sutton, "Orthopaedic component manufacturing method and equipment," 2011.

[110] H. Yamaguchi and A. A. Graziano, "Surface finishing of cobalt chromium alloy femoral knee components," *CIRP Annals - Manufacturing Technology*, vol. 63, no. 1, pp. 309–312, 2014.

[111] A. Einstein, "Eine neue Bestimmung der Moleküldimensionen," *Annalen der Physik*, vol. 324, no. 2, pp. 289–306, 1906.

[112] M. Mooney, "The viscosity of a concentrated suspension of spherical particles," *Journal of Colloid Science*, vol. 6, pp. 162–170, 4 1951.

[113] D. G. Thomas, "TRANSPORT CHARACTERISTICS OF SUSPENSION': VIII. A NOTE ON THE VISCOSITY OF NEWTONIAN SUSPENSIONS OF UNIFORM SPHERICAL PARTICLES," *JOURNAL OF COLLOID SCIENCE*, vol. 0, pp. 267–277, 1965.

[114] T. B. Lewis and L. E. Nielsen, "Viscosity of dispersed and aggregated suspensions of spheres viscosity of dispersed and aggregated suspensions of spheres*," *Transactions of the Society of Rheology*, vol. 12, no. 3, pp. 421–443, 1968.

[115] I. M. Krieger, "Rheology of monodisperse latices," *Advances in Colloid and Interface Science*, vol. 3, no. 2, pp. 111–136, 1972.

[116] J. J. Stickel and R. L. Powell, "Fluid mechanics and rheology of dense suspensions," *Annual Review of Fluid Mechanics*, vol. 37, pp. 129–149, 1 2005.

[117] W. H. Herschel and R. Bulkley, "Konsistenzmessungen von Gummi-Benzollösungen," *Kolloid-Zeitschrift*, vol. 39, pp. 291–300, 8 1926.

[118] S. H. Maron and P. E. Pierce, "Application of ree-eyring generalized flow theory to suspensions of spherical particles," *Journal of Colloid Science*, vol. 11, pp. 80–95, 2 1956.

[119] P. RAVINDRAN, N. K. ANAND, and M. MASSOUDI, "Steady Free Surface Flow of a Fluid-Solid Mixture Down an Inclined Plane," *Particulate Science and Technology*, vol. 22, pp. 253–273, 7 2004.

[120] G. Johnson+, M. Massoudi, and K. R. Rajagopal ', "FLOW OF A FLUID-SOLID MIXTURE BETWEEN FLAT PLATES," *Chemzeal E " glnewmg science*, vol. 46, no. 7, pp. 1713–1723, 1991.

[121] M. Massoudi, "A mixture theory formulation for hydraulic or pneumatic transport of solid particles," *International Journal of Engineering Science*, vol. 48, pp. 1440–1461, 11 2010.

[122] J. Rabinow, "The magnetic fluid clutch," *Transactions of the American Institute of Electrical Engineers*, vol. 67, no. 2, pp. 1308–1315, 1948.

[123] A. Ghaffari and S. Hashemabadi, "A review on the simulation and modeling of magnetorheological fluids," *Journal of Intelligent*, 2015.

[124] H. M. Laun, C. Kormann, and N. Willenbacher, "Rheometry on magnetorheological (MR) fluids," *Rheologica Acta*, vol. 35, no. 5, pp. 417–432, 1996.

[125] J. Claracq, J. Sarrazin, and J.-P. Montfort, "Viscoelastic properties of magnetorheological fluids," *Rheologica Acta*, vol. 43, pp. 38–49, 2 2004.

[126] H. M. Laun, C. Gabriel, and G. Schmidt, "Primary and secondary normal stress differences of a magnetorheological fluid (MRF) up to magnetic flux densities of

1 T," *Journal of Non-Newtonian Fluid Mechanics*, vol. 148, no. 1–3, pp. 47–56, 2008.

[127] F. Ahmadkhanlou, M. Mahboob, S. Bechtel, and G. Washington, "An Improved Model for Magnetorheological Fluid-Based Actuators and Sensors:," *http://dx.doi.org/10.1177/1045389X09350330*, vol. 21, pp. 3–18, 11 2009.

[128] K. Han, Y. T. Feng, and D. R. J. Owen, "Three-dimensional modelling and simulation of magnetorheological fluids," *International Journal for Numerical Methods in Engineering*, vol. 84, pp. 1273–1302, 12 2010.

[129] J. De Vicente, D. J. Klingenberg, and R. Hidalgo-Alvarez, "Magnetorheological fluids: a review,"

[130] J. Ramos, D. J. Klingenberg, R. Hidalgo-Alvarez, and J. de Vicente, "Steady shear magnetorheology of inverse ferrofluids," *Journal of Rheology*, vol. 55, no. 1, p. 127, 2011.

[131] G. Bossis, S. Lacis, A. Meunier, and O. Volkova, "Magnetorheological fluids," *Journal of magnetism and*, 2002.

[132] B. D. Chin, J. H. Park, M. H. Kwon, and O. O. Park, "Rheological properties and dispersion stability of magnetorheological (MR) suspensions," *Rheologica Acta*, vol. 40, no. 3, pp. 211–219, 2001.

[133] I. A. Brigadnov and A. Dorfmann, "Mathematical modeling of magnetorheological fluids," *Continuum Mechanics and Thermodynamics*, vol. 17, no. 1, pp. 29–42, 2005.

[134] K. R. Rajagopal, R. C. Yalamanchili, and A. S. Wineman, "Modeling electrorheological materials through mixture theory," *International Journal of Engineering Science*, vol. 32, pp. 481–500, 3 1994.

[135] J. Xu, J. Li, P. Zhu, B. Li, and C. Zhao, "Coarse-grained molecular dynamics simulations of particle behaviors in magnetorheological polishing fluid," *Computational Materials Science*, vol. 163, pp. 68–81, 6 2019.

[136] T. Liu, R. Gu, X. Gong, S. Xuan, H. Wu, and Z. Zhang, "STRUCTURAL AND RHEOLOGICAL STUDY OF MAGNETIC FLUIDS USING MOLECULAR DYNAMICS," *MAGNETOHYDRODYNAMICS*, vol. 46, no. 3, pp. 257–269, 2010.

[137] G. Schramm, *A practical approach to rheology and rheometry*. 1994.

[138] B. D. Coleman, H. Markovitz, and W. Noll, *Viscometric Flows of Non-Newtonian Fluids : Theory and Experiment*. Berlin, Heidelberg : Springer Berlin Heidelberg, 1966., 1966.

[139] "Standard Practice for Static Calibration of Electronic Transducer-Based Pressure Measurement Systems for Geotechnical Purposes," 2009.

[140] N. Thomas, A. I. Sikandar, S. T. Bukkapatnam, and A. R. Srinivasa, "Nanofinishing of Biomedical Implants," in *Nanofinishing Science and Technology: Basic and Advanced Finishing and Polishing Processes* (V. K. Jain, ed.), ch. Nanofinish, pp. 549–598, CRC Press, 1 ed., 2016.

[141] T. Kuntzsch, U. Witnik, M. Hollatz, M. Stintz, and S. Ripperger, "Characterization of Slurries Used for Chemical-Mechanical Polishing (CMP) in the Semiconductor Industry," *Chemical Engineering & Technology*, vol. 26, pp. 1235–1239, 12 2003.

[142] T. S. Bedi and A. K. Singh, "Magnetorheological methods for nanofinishing – a review," *Particulate Science and Technology*, vol. 34, pp. 412–422, 7 2016.

[143] A. C. Petare and N. K. Jain, "A critical review of past research and advances in abrasive flow finishing process," 7 2018.

[144] G. Nanz and L. E. Camilletti, "Modeling of Chemical—Mechanical Polishing: A Review," *IEEE Transactions on Semiconductor Manufacturing*, vol. 8, no. 4, pp. 382–389, 1995.

[145] J. V. Robinson, "THE VISCOSITY OF SUSPENSIONS OF SPHERES," Tech. Rep. 4, 1932.

[146] Q. D. Nguyen and D. V. Boger, "Measuring the flow properties of yield stress fluids," *Annual Review of Fluid Mechanics*, vol. 24, pp. 47–88, 1992.

[147] K. Lu, E. E. Brodsky, and H. P. Kavehpour, "Shear-weakening of the transitional regime for granular flow," *Journal of Fluid Mechanics*, vol. 587, pp. 347–372, 2007.

[148] S. Baek, K. R. Rajagopal, and A. R. Srinivasa, "Measurements related to the flow of granular material in a torsional rheometer," *Particulate Science and Technology*, vol. 19, no. 2, pp. 175–186, 2001.

[149] R. M. Turian, T. W. Ma, F. L. Hsu, and D. J. Sung, "Characterization, settling, and rheology of concentrated fine particulate mineral slurries," *Powder Technology*, vol. 93, pp. 219–233, 10 1997.

[150] A. C. Pipkin, "Controllable viscometric flows," *Quarterly of Applied Mathematics*, vol. 26, pp. 87–100, 1968.

[151] S. Avril, M. Bonnet, A.-S. Bretelle, M. Grédiac, F. Hild, P. Ienny, F. Latourte, D. Lemosse, S. Pagano, E. Pagnacco, F. Pierron, A.-S. Bretelle, P. Ienny, M. Grédiac, F. Hild, F. Latourte, S. Pagano, D. Lemosse, and E. Pagnacco, "Overview of Identification Methods of Mechanical Parameters Based on Full-field Measurements," *Experimental Mechanics*, vol. 48, pp. 381–402, 2008.

[152] H. Schmid, M. P. Nash, A. A. Young, and P. J. Hunter, "Myocardial material parameter estimation - A comparative study for simple shear," *Journal of Biomechanical*

Engineering, vol. 128, pp. 742–750, 10 2006.

[153] D. Guan, F. Ahmad, P. Theobald, S. Soe, X. Luo, and H. Gao, "On the AIC-based model reduction for the general Holzapfel–Ogden myocardial constitutive law," *Biomechanics and Modeling in Mechanobiology*, vol. 18, pp. 1213–1232, 8 2019.

[154] K. P. Burnham and D. R. Anderson, *Model Selection and Multimodel Inference*. New York, NY: Springer New York, 2004.

[155] A. S. Margotta, "MODEL SELECTION IN RHEOLOGY: PROVIDING A PRACTICAL FRAMEWORK, SURVEYING THE FIELD, AND ASSESSING THE USES AND LIMITATIONS OF BIC," tech. rep., 11 2019.

[156] J. B. Freund and R. H. Ewoldt, "Quantitative rheological model selection: Good fits versus credible models using Bayesian inference," *Journal of Rheology*, vol. 59, pp. 667–701, 5 2015.

[157] A. Sutherland, R. Haldenwang, R. Chhabra, and E. Van Den Heever, "SELECTING THE BEST RHEOLOGICAL AND PIPE TURBULENT FLOW PREDICTION MODELS FOR NON-NEWTONIAN FLUIDS-USE OF RMSE and R 2 vs. AIC,"

[158] J. A. Nelder and R. Mead, "A simplex method for function minimization," *The Computer Journal*, vol. 7, pp. 308–313, 1 1965.

[159] H. Akaike, "A new look at the statistical model identification," *IEEE Transactions on Automatic Control*, vol. 19, pp. 716–723, 12 1974.

[160] Gideon Schwarz, "Estimating the dimension of a model," *The Annals of Statistics*, vol. 6, no. 2, pp. 461–464, 1978.

[161] K. P. Burnham and D. R. Anderson, "Multimodel Inference," *Sociological Methods & Research*, vol. 33, pp. 261–304, 11 2004.

[162] D. D. Cook and D. J. Robertson, "The generic modeling fallacy: Average biomechanical models often produce non-average results!," 11 2016.

[163] M. James Clerk, *A treatise on electricity and magnetism*, vol. 1. Oxford: Clarendon Press, 1873.

[164] Y. H. Pao and Y. H., "Electromagnetic forces in deformable continua," *meto*, vol. 4, pp. 209–305, 1978.

[165] P. Dular, J. F. Remacle, F. Henrotte, A. Genon, and W. Legros, "Magnetostatic and magnetodynamic mixed formulations compared with conventional formulations," *IEEE Transactions on Magnetics*, vol. 33, no. 2 PART 2, pp. 1302–1305, 1997.

[166] Y. H. Pao and K. Hutter, "Electrodynamics for Moving Elastic Solids and Viscous Fluids," *Proceedings of the IEEE*, vol. 63, no. 7, pp. 1011–1021, 1975.

[167] A. C. Eringen and G. A. Maugin, *Electrodynamics of Continua I*. Springer New York, 1990.

[168] K. R. Rajagopal and M. Růžička, "On the modeling of electrorheological materials," *Mechanics Research Communications*, vol. 23, no. 4, pp. 401–407, 1996.

[169] K. R. Rajagopal and L. Tao, *Mechanics of Mixtures*, vol. 35 of *Series on Advances in Mathematics for Applied Sciences*. WORLD SCIENTIFIC, 10 1995.

[170] K. R. Rajagopal and A. S. Wineman, "Flow of electro-rheological materials," *Acta Mechanica*, vol. 91, pp. 57–75, 3 1992.

[171] I. A. Brigadnov and A. Dorfmann, "Mathematical modeling of magneto-sensitive elastomers," *International Journal of Solids and Structures*, vol. 40, no. 18, pp. 4659–4674, 2003.

[172] A. Grants, A. Irbitis, G. Kroņkalns, and M. M. Maiorov, "Rheological properties of magnetite magnetic fluid," *Journal of Magnetism and Magnetic Materials*, vol. 85, pp. 129–132, 4 1990.

[173] M. Kröger, P. Ilg, and S. Hess, "Magnetoviscous model fluids," *Journal of Physics: Condensed Matter*, vol. 15, p. S1403, 4 2003.

[174] M. Heida, J. Málek, and K. R. Rajagopal, "On the development and generalizations of Cahn-Hilliard equations within a thermodynamic framework," *Zeitschrift fur Angewandte Mathematik und Physik*, vol. 63, pp. 145–169, 7 2012.

[175] M. Alnæs, J. Blechta, J. Hake, A. Johansson, B. Kehlet, A. Logg, C. Richardson, J. Ring, M. E. Rognes, and G. N. Wells, "The FEniCS Project Version 1.5," *The FEniCS Project Version 1.5*, vol. 3, pp. 9–23, 12 2015.

[176] A. Logg, K. A. Mardal, and G. Wells, *Automated Solution of Differential Equations by the Finite Element Method: The FEniCS Book (Lecture Notes in Computational Science and Engineering)*, vol. 84. 2012.

[177] C. Xì, *ANSYS CFX-Solver Theory Guide ANSYS CFX Release 11.0*. 2006.

[178] J. Geiser, E. Martínez, and J. L. Hueso, "Serial and Parallel Iterative Splitting Methods: Algorithms and Applications to Fractional Convection-Diffusion Equations," *Mathematics 2020, Vol. 8, Page 1950*, vol. 8, p. 1950, 11 2020.

[179] T. P. Witelski and M. Bowen, "ADI schemes for higher-order nonlinear diffusion equations," *Applied Numerical Mathematics*, vol. 45, pp. 331–351, 5 2003.

[180] D. Meeker, "Improvised Open Boundary Conditions for Magnetic Finite Elements," *IEEE Transactions on Magnetics*, vol. 49, pp. 5243–5247, 10 2013.

[181] M. Das, V. K. Jain, and P. S. Ghoshdastidar, "A 2D CFD simulation of MR polishing medium in magnetic field-assisted finishing process using electromagnet," *The In-*

ternational Journal of Advanced Manufacturing Technology, vol. 76, pp. 173–187, 1 2015.

[182] Lei Pei, Haoming Pang, Xiaohui Ruan, Xinglong Gong, and Shouhu Xuan, "Magnetorheology of a magnetic fluid based on Fe 3 O 4 immobilized SiO 2 core–shell nanospheres: experiments and molecular dynamics simulations," *RSC Advances*, vol. 7, pp. 8142–8150, 1 2017.

[183] D. Y. Borin, C. Bergmann, and S. Odenbach, "Characterization of a magnetic fluid exposed to a shear flow and external magnetic field using small angle laser scattering," *Journal of Magnetism and Magnetic Materials*, vol. 497, p. 165959, 3 2020.

APPENDIX A

RELATIONSHIP BETWEEN THE MASS AND VOLUME CONCENTRATIONS

In the formulation and simulation of the mixture, we see the use of two types of concentrations namely the mass concentration (c^i) and the volume concentration (x^i) of the components. Even though in the formulation and simulation we use the the volume concentration as the primary state variable for calculating the presence of a particular component in the mixture. We may need to calculate and use the mass concentration of a component at a certain point. In this section we study the relationship of these concentrations to the bulk density (ρ) and among themselves.

We can define the bulk density(ρ) as a function of both the volume concentration(x^i) and mass concentration (c^i) using the equations given below,

$$\rho = \sum_i x^i \rho^i_* \qquad = x^m \rho^m_* + x^a \rho^a_* \tag{A.1}$$

$$\rho = \sum_i c^i \rho^i \qquad = c^m \rho^m + c^a \rho^a \tag{A.2}$$

where, ρ^m_* and ρ^a_* are the filled densities of the magnetic and abrasive components and ρ^m and ρ^a are the densities of the magnetic and abrasive components.

As per the modeling approach, discussed in Chapter 7, the relation between x^m and c^m is of importance and x^a and c^a can be calculated by taking its complement with respect to 1. Using the definition of c^m given in equation 7.42 and substituting the relationship given above we get the following expression for c^m in terms of x^m.

$$
\begin{aligned}
c^m &= \frac{\rho^m}{\rho} \\
&= \frac{x^m \rho_*^m}{x^m \rho_*^m + (1 - x^m)\rho_*^a} \\
&= \frac{x^m}{\rho_r + (1 - \rho_r)x^m} \qquad \text{(A.3)}
\end{aligned}
$$

$$
\text{where,} \qquad \rho_r = \frac{\rho_*^a}{\rho_*^m} \qquad \text{(A.4)}
$$

Rearranging equation A.3, we can also express x^m in terms of c^m as given below,

$$
x^m = \frac{\rho_r c^m}{1 - (1 - \rho_r)c^m} \qquad \text{(A.5)}
$$

As we use the gradients of the concentrations in our formulation, the relationship of the gradients of the concentrations are also of importance in the study. This relationship can be computed by taking the gradient of equation A.3. Note that ρ_r is constant as the filled densities of the components are constant.

$$
\begin{aligned}
& grad(x^m) = \rho_r grad(c^m) + (1 - \rho_r)(c^m grad(x^m) + x^m grad(c^m)) \\
\implies & [1 - (1 - \rho_r)c^m] grad(x^m) = [\rho_r + (1 - \rho_r)x^m] grad(c^m) \\
\implies & \frac{\rho_r c^m}{x^m} grad(x^m) = \frac{x^m}{c^m} grad(c^m) \\
\implies & \rho_r \frac{grad(x^m)}{(x^m)^2} = \frac{grad(c^m)}{(c^m)^2} \qquad \text{(A.6)}
\end{aligned}
$$

The relationships thus developed in equations A.3 and A.6, are useful to calculate the mass or volume concentration in the mixture at any particular point when the other is known in the mixture.